POZNAŃ 2020

Rafał Białek

Purple bacteria reaction centers in photovoltaic applications

PURPLE BACTERIA REACTION CENTERS IN PHOTOVOLTAIC APPLICATIONS

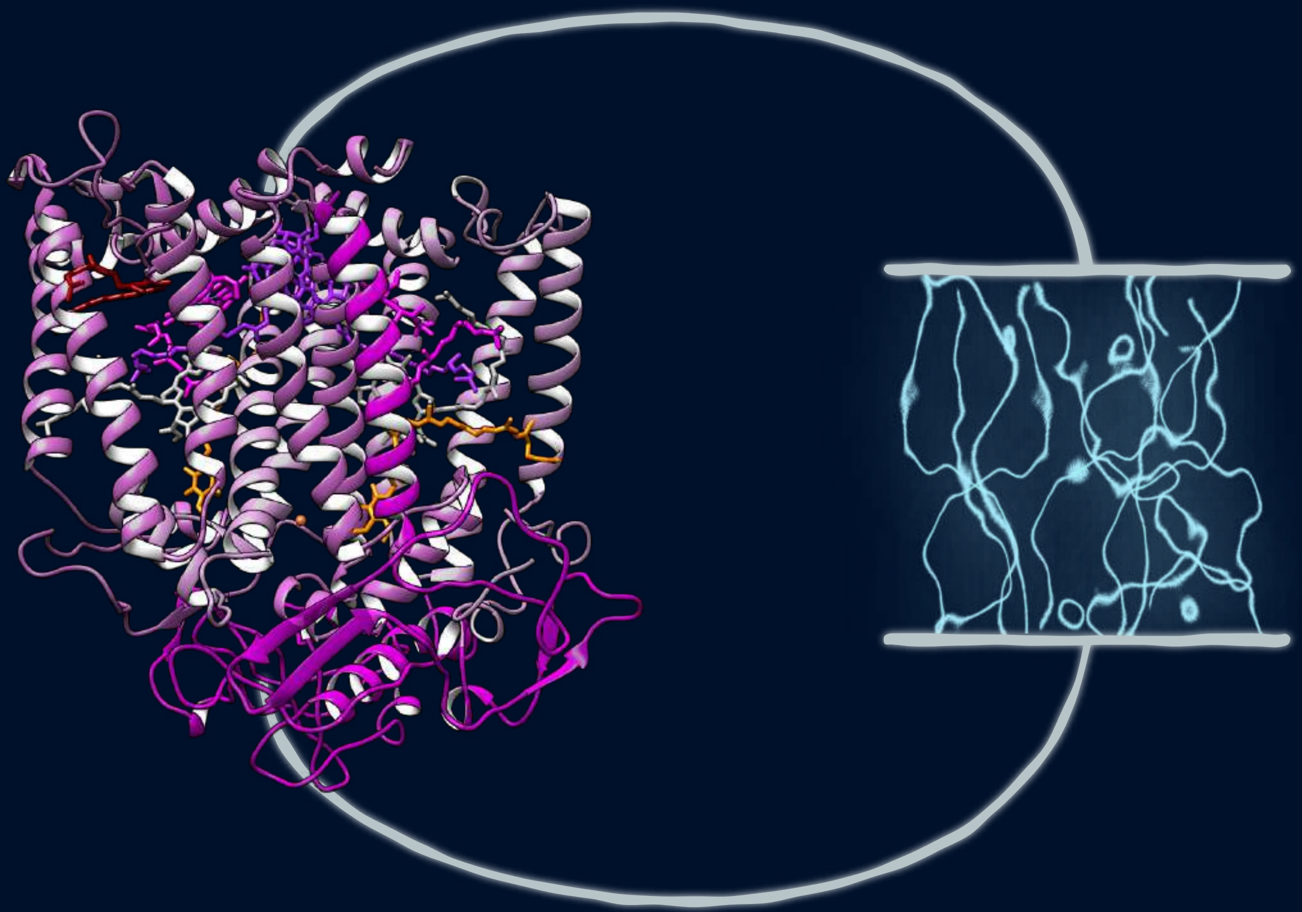

Rafał Białek

Adam Mickiewicz University, Poznań
Faculty of Physics
Department of Molecular Biophysics

Purple bacteria reaction centers in photovoltaic applications

PhD thesis based on original publications

Rafał Białek

Supervisor:

dr hab. Krzysztof Gibasiewicz, prof. UAM

Poznań, 2020

ACKNOWLEDGEMENTS

First of all, I would like to thank my wife Kasia for her constant support, especially in the final stage of writing the thesis.

I would like to express my gratitude towards my supervisor, prof. UAM dr hab. Krzysztof Gibasiewicz for guiding me in my journey through fundamental and applied photosynthesis research since the early stages of my undergraduate level and gave me a lot of freedom, which allowed me to learn how to conduct research independently.

I would like to thank all co-authors of my papers, as without them I would not be able to do most of my work.

Another person to acknowledge is Dr Vincent Friebe from VU University, Amsterdam, who helped mi a lot with his advices and connected me with the right people to start new collaborations.

I would also like to thank all colleagues from the Faculty of Physics at Adam Mickiewicz University, Poznań for creating a cordial working environment, especially those with which we had time to conduct many “scientific” discussions during lunch breaks and “Very Official Meetings”.

I would not probably even choose to study physics if to was not for my high school physics teachers: Grażyna and Jarosław Linder, thus I am thankful to them for instilling a love for physics in me.

And last but not least, I would like to thank my parents and rest of the family, as their influence shaped me as a person I am now.

Work presented in the publications [RB1-2] was supported by the National Science Center (project entitled “Bio-semiconductor hybrids for photovoltaic cells” No. 2012/07/B/NZ1/02639) while the publications [RB3-4] were supported by Polish Ministry of Science and Higher Education (project entitled: “Construction of solar cells based on purple bacteria Reaction Centers and polymer hydrogels” no. 0129/DIA/2016/45 within a “Diamentowy Grant” program).

TABLE OF CONTENTS

ABSTRACT

Nature had billions of years to optimize the processes occurring in living organisms, which makes it a perfect example to follow and source of inspiration for humanity for centuries. One of this examples is photosynthesis, which is a natural solar energy conversion process, whose first steps are nothing else but the conversion of light energy to the flow of electrons (electrical current). This occurs in photosynthetic proteins (such as purple bacteria reaction centers) embedded in membranes.

One of the strategies to utilize Nature's optimization achievement is to isolate photosynthetic proteins and use them as photoactive material in biohybrid photovoltaic devices. This approach might not have a significant probability of creation of an applicable design, however, knowledge about the operation of biological solar energy harvesting components gathered along the way will be invaluable in the improvement of synthetic photovoltaic devices. This knowledge lays on the border of multiple disciplines, such as biochemistry, electrochemistry, spectroscopy, and solid-state physics.

In this thesis, the focus is put on the understanding of the operation of *Rhodobacter sphaeroides* reaction centers (RCs) with possible applications in biohybrid photoelectrochemical devices. First, the recombination (or back electron transport) processes within the isolated RC were investigated, which gave insight into the protein scaffold dynamics. It is important information in designing of biohybrid devices, as the interaction with other parts of the system may have an influence on mechanical properties of the protein.

First biohybrid system presented in this work is based on TiO_2 mesoporous layer as a substrate for RCs immobilization. It resulted in relatively low photocurrents, but generated in both cathodic and anodic ways. It suggested that there are multiple processes occurring in the studied electrode, which inspired preparation of mathematical model revealing bottlenecks of photocurrent generation.

Second studied system is a redox-active hydrogel (built with Os-complex based polymers) with embedded RCs. This was characterized by generation of photocurrent with significant internal quantum efficiency ($50 \pm 12\,\%$). This high efficiency encouraged further characterization of this system using spectroscopy techniques, such as steady-state UV-vis absorption spectroelectrochemistry and transient absorption spectroscopy. The former technique was applied *in situ* in the operational electrode and revealed a shift of the RCs primary electron donor potential towards positive values in such conditions, in comparison to that measured in solution and reported earlier in literature. The latter technique, on the other hand, was applied to the mixture of polymer (as an electron donor), proteins and electron acceptors in solution. It allowed determination of time constants of primary donor reduction by redox centers in the polymer. The values of these time constants span from a few microseconds to a millisecond and change with the concentration of both polymer and RCs.

To summarize, work presented in this thesis contributed to understanding of the operation of biohybrid devices, which along with work of other researchers in the field, might create a fully understood picture of it in the future.

STRESZCZENIE

Natura przez miliardy lat optymalizuje procesy zachodzące w żywych organizmach, co czyni ją idealnym wzorem do naśladowania i źródłem inspiracji dla ludzkości od wieków. Jednym z przykładów jest fotosynteza, będąca naturalnym procesem konwersji energii słonecznej, której pierwsze etapy są niczym innym jak przekształcaniem energii słonecznej na przepływ elektronów (prąd elektryczny). Proces ten zachodzi w białkach fotosyntetycznych (takich jak centra reakcji bakterii purpurowych) występujących w błonach biologicznych.

Jedną ze strategii wykorzystania osiągnieć optymalizacyjnych natury jest użycie izolowanych białek fotosyntetycznych jako materiału pochłaniającego światło w biohybrydowych urządzeniach fotowoltaicznych. Pomimo niskich szans na bezpośrednie zastosowanie tego podejścia, uzyskiwane informacje o działaniu narzędzi natury do przekształcania energii słonecznej jest niezwykle istotna. Wiedza ta, z zakresu wielu dziedzin, takich jak: biochemia, elektrochemia, spektroskopia czy fizyka ciała stałego, jest bezcenna w ulepszaniu syntetycznych urządzeń fotowoltaicznych.

W tej rozprawie doktorskiej nacisk kładziony jest na zrozumienie działania centrów reakcji *Rhodobacter sphaeroides* z możliwym zastosowaniem w biohybrydowych urządzeniach fotoelektrochemicznych. W pierwszej kolejności zbadane zostały procesy rekombinacyjne (transportu wstecznego elektronu) wewnątrz izolowanych centrów reakcji. Dało to wgląd w dynamikę szkieletu białkowego. Są to ważne informacje przy projektowaniu urządzeń biohybrydowych, jako że oddziaływanie z innymi elementami układu może mieć wpływ na mechaniczne właściwości białka.

Pierwszą opisaną w pracy elektrodą biohybrydową jest układ oparty na mezoporowatej warstwie TiO_2 użytej jako baza do przyłączenia centrów reakcji. Wartości fotoprądów dla opisanej konstrukcji okazały się względnie niskie, lecz ich przepływ możliwy był w obu kierunkach (prąd katodowy lub anodowy). Wynik ten zasugerował, że w badanym układzie zachodzi wiele różnych procesów, co zainspirowało do przygotowania modelu matematycznego wskazującego wąskie gardła w generacji fotoprądu.

Drugim zaprezentowanym układem jest hydrożel o właściwościach redoks (zbudowany z polimeru z centrami osmowymi) z unieruchomionymi w nim centrami reakcji. Zaobserwowano wysoką wydajność kwantową ($50 \pm 12\,\%$) generacji fotoprądu w tych układach. Ta wysoka wydajność zachęciła do dalszego badania układu z użyciem technik spektroskopowych, takich jak stacjonarna spektroelektrochemia UV-vis i spektroskopia absorpcji przejściowej. Pierwsza z tych technik była zastosowana *in situ* w działającej elektrodzie i pokazała przesunięcie potencjału redoks pierwotnego donora w centrach reakcji w stronę bardziej pozytywnych wartości w porównaniu do literaturowych wartości uzyskanych w izolowanych centrach reakcji. Druga z technik została zastosowana do pomiarów mieszaniny polimeru (donora elektronu), białek i akceptorów elektronów w roztworze. Pozwoliło to na określenie stałych czasowych redukcji pierwotnego donora elektronu centrów reakcji

przez centra redoks w polimerze. Wartości tych stałych czasowych znajdowały się w przedziale od kilku mikrosekund do milisekundy i zależały od zmian stężenia zarówno polimeru jak i centrów reakcji.

Podsumowując, praca zaprezentowana w tej rozprawie przyczyniła się do lepszego zrozumienia działania układów biohybrydowych, co razem z wynikami innych grup badawczych może w przyszłości ukazać kompletny, w pełni zrozumiały obraz działania tych urządzeń.

LIST OF PUBLICATIONS CONSTITUTING THE THESIS

In chronological order:

[RB1]

Gibasiewicz K, **Białek R**, Pajzderska M, Karolczak J, Burdziński G, Jones MR, Brettel K.

Weak Temperature Dependence of $P^+H_A^-$ Recombination in Mutant *Rhodobacter sphaeroides* Reaction Centers.

Photosynth Res 2016;**128**:243–58. https://doi.org/10.1007/s11120-016-0239-9.

Ministerial points: **100** $IF_{5\text{-year}(2019)}$: **3.630** IF_{2019}: **3.216**

[RB2]

Białek R, Swainsbury DJK, Wiesner M, Jones MR, Gibasiewicz K.

Modelling of the Cathodic and Anodic Photocurrents from *Rhodobacter sphaeroides* Reaction Centres Immobilized on Titanium Dioxide.

Photosynth Res 2018;**138**:103–14. https://doi.org/10.1007/s11120-018-0550-8.

Ministerial points: **100** $IF_{5\text{-year}(2019)}$: **3.630** IF_{2019}: **3.216**

[RB3]

Białek R, Friebe V, Ruff A, Jones MR, Frese R, Gibasiewicz K.

In situ Spectroelectrochemical Investigation of a Biophotoelectrode Based on Photoreaction Centers Embedded in a Redox Hydrogel.

Electrochim Acta 2020;**330**:135190. https://doi.org/10.1016/j.electacta.2019.135190.

Ministerial points: **100** $IF_{5\text{-year}(2019)}$: **5.478** IF_{2019}: **6.215**

[RB4]

Białek R, Thakur K, Ruff A, Jones MR, Schuhmann W, Ramanan C, Gibasiewicz K.

Insight in the Electron Transfer from a Redox Polymer to a Photoactive Protein.

J Phys Chem B https://doi.org/10.1021/acs.jpcb.0c08714. just accepted

Ministerial points: **140** $IF_{5\text{-year}(2019)}$: **2.880** IF_{2019}: **2.857**

OTHER PUBLICATIONS

1. **Białek R**, Burdziński G, Jones MR, Gibasiewicz K.
   Bacteriopheophytin Triplet State in *Rhodobacter sphaeroides* Reaction Centers.
   Photosynth Res 2016;**129**:205–16. https://doi.org/10.1007/s11120-016-0290-6.
   Ministerial points: **100** $\mathrm{IF}_{5\text{-year}(2019)}$: **3.630** IF_{2019}: **3.216**

2. Szewczyk S, Giera W, **Białek R**, Burdziński G, Gibasiewicz K.
   Acceleration of the Excitation Decay in Photosystem I Immobilized on Glass Surface.
   Photosynth Res 2018;**136**:171–81. https://doi.org/10.1007/s11120-017-0454-z.
   Ministerial points: **100** $\mathrm{IF}_{5\text{-year}(2019)}$: **3.630** IF_{2019}: **3.216**

3. Szewczyk S, **Białek R**, Giera W, Burdziński G, van Grondelle R, Gibasiewicz K.
   Excitation Dynamics in Photosystem I Trapped in TiO_2 Mesopores.
   Photosynth Res 2020;**144**:235–45. https://doi.org/10.1007/s11120-020-00730-1.
   Ministerial points: **100** $\mathrm{IF}_{5\text{-year}(2019)}$: **3.630** IF_{2019}: **3.216**

4. Szewczyk S, **Białek R**, Burdziński G, Gibasiewicz K.
   Photovoltaic Activity of Electrodes Based on Intact Photosystem I Electrodeposited on Bare Conducting Glass.
   Photosynth Res 2020;**144**:1–12. https://doi.org/10.1007/s11120-020-00722-1.
   Ministerial points: **100** $\mathrm{IF}_{5\text{-year}(2019)}$: **3.630** IF_{2019}: **3.216**

5. Abram M[‡], **Białek R**[‡], Szewczyk S, Karolczak J, Gibasiewicz K, Kargul J.
   Remodeling of Excitation Energy Transfer in Extremophilic Red Algal PSI-LHCI Complex During Light Adaptation.
   Biochim Biophys Acta - Bioenerg 2020;**1861**:148093.
   https://doi.org/10.1016/j.bbabio.2019.148093.
   Minis terial points: **100** $\mathrm{IF}_{5\text{-year}(2019)}$: **4.579** IF_{2019}: **3.465**

6. Szewczyk S, Abram M, **Białek R**, Haniewicz P, Karolczak J, Gapiński J, Kargul J, Gibasiewicz K.
   On the Nature of Uncoupled Chlorophylls in the Extremophilic Photosystem I-Light Harvesting I Supercomplex.
   Biochim Biophys Acta - Bioenerg 2020;**1861**:148136.
   https://doi.org/10.1016/j.bbabio.2019.148136.
   Ministerial points: **100** $\mathrm{IF}_{5\text{-year}(2019)}$: **4.579** IF_{2019}: **3.465**

[‡] Joint first authorship

1 INTRODUCTION AND MOTIVATION

The global energy consumption has been growing steadily for the last decades[1], as is the global human population.[2] It poses a lot of challenges for us as humanity, for which scientists are expected to find solutions. The growth of energy consumption with the current usage of fossil fuels results in an increase of CO_2 release into the atmosphere[1] contributing to the global temperature rise, which poses a serious threat for a human civilization as we know it now. Planet Earth and its environment per se have already survived many climate changes, however humankind may not be that resistant. Possible solution for this problem is a shift towards renewable energy sources. One of the first natural choices for this is solar energy. However, the current state of technology in this field is far from being perfect with either low efficiency or high cost-to-performance ratio.

On the other hand, Nature has already mastered solar energy utilization in the process called photosynthesis, which is used by plants and some lower organisms (*e.g.,* algae or cyanobacteria) to convert light energy into a chemical one. In photosynthetic systems, the quantum efficiency of absorbed photon-to-electron conversion reaches even 100 %,[3] which is rarely the case in artificial systems. Scientists have tried to incorporate photosynthetic proteins in artificial systems for a few decades now[4–6] but it was the last few years when the most breakthroughs were achieved.[7–10] However, there is still a lot to be done in this field, especially in terms of understanding of electron and energy transfer processes within constructed electrodes and whole devices.

One of the most studied photosynthetic proteins is the reaction center (RC) from a purple bacterium *Rhodobacter sphaeroides*.[11–13] Knowledge we have about its operational and structural principles and its relative robustness make it a perfect candidate for the preparation of model biophotoelectrodes. Moreover, its spectral properties (distinct absorption bands for different cofactors) make it a perfect specimen for transient absorption observation of electron and energy transfer.[14]

There are many different approaches of wiring the protein to the electrode. In this work, two of them are being used: based on protein interaction with mesoporous titanium dioxide and redox-active polymer hydrogel. These two were chosen due to their relative simplicity in preparation and comprehensive description in literature[10,15–20] making it easier to have a deeper insight into the mechanisms.

2 THE AIMS OF THE THESIS

The general goal of the thesis was fabrication and characterization of photovoltaic activity of photoelectrodes comprising photosynthetic proteins, purple bacteria reaction centers (RCs), incorporated into non-biological matrices. Specific objectives achieved in this work were the following:

1. Description of the dynamics of back electron transfer processes within the purified RCs potentially limiting their photovoltaic performance.
2. Description and modelling of electron transfer between different parts of the biophotovoltaic system comprising RCs and TiO_2.
3. Development of the spectroelectrochemical method for *in situ* determination of midpoint redox potentials of different parts of the biophotoelectrode comprising RCs and redox-active polymer.
4. Description of the kinetics of the electron transfer between RCs and redox-active polymers.

3 BIOPHYSICAL DESCRIPTION OF PHOTOSYNTHESIS

3.1 BASIC PRINCIPLE OF OPERATION

Photosynthesis is a natural process used by green plants and certain other groups of organisms (*e.g.*, purple bacteria) to convert light energy into chemical energy available for the organism to store and use for its metabolism. Photosynthesis is a multistep process, which traditionally is divided into two main phases: 1) light-dependent reactions and 2) light-independent reactions (Figure 3.1). The first phase is a process of light energy harvesting followed by an electron transfer occurring along the cofactors chain, the transfer being coupled to proton pumping across the photosynthetic membrane. The individual steps of the light-dependent phase occur within (or in the vicinity of) the photosynthetic membrane and result in the creation of high-energy, short-lived intermediates. There are multiple different membrane and water-soluble proteins involved in this process that pose various roles, including reaction centers (primary charge separation), antennas (light energy harvesting and its transfer to reaction centers), cytochromes (electron transfer) and ATP synthase (synthesis of adenosine triphosphate using the proton gradient across the photosynthetic membrane).[12]

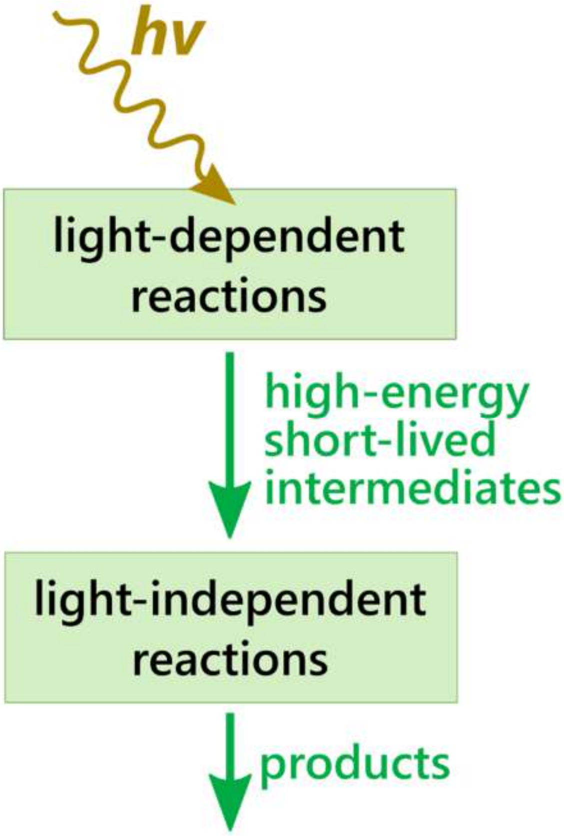

Figure 3.1 General scheme of photosynthesis.

The details of each phase of photosynthesis depend on the species. Here, an emphasis is placed on the light-dependent reactions in the purple bacterium *Rhodobacter (Rba.) sphearoides* as it lays within the scope of this thesis. Whole spectrum of detailed information on photosynthesis is available in literature.[12]

3.2 PHOTOSYNTHESIS OF PURPLE BACTERIA

3.2.1 Electron transfer chain

Photosynthesis of purple bacterium *Rba. sphaeroides* is of the anoxygenic type, meaning that there is no oxygen generated as a byproduct. However, purple bacteria can grow in both aerobic and anaerobic conditions. In general, their electron transfer chain in light reactions of photosynthesis follows the cyclic electron transfer scheme, meaning that the electron flow initialized by the primary charge separation ultimately leads to the rereduction of the primary electron donor within a closed cycle of redox reactions. It is on the contrary to green plants photosynthesis, in which the noncyclic electron transfer chain is employed and the primary electron donor is reduced with an electron coming from an external electron donor (water molecule).[12]

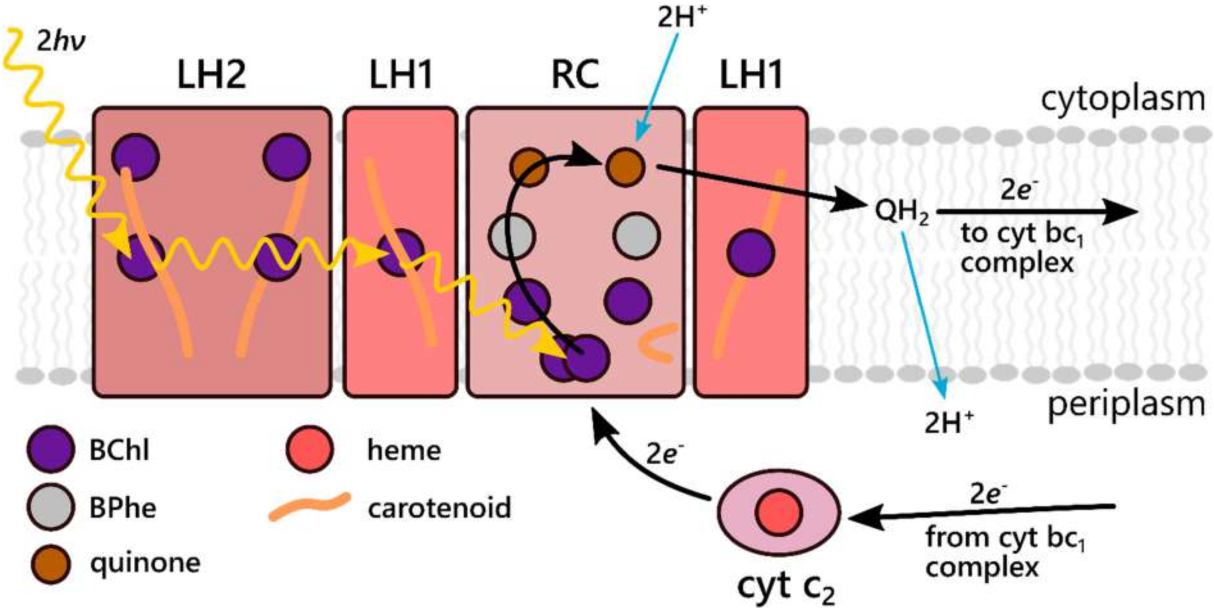

Figure 3.2 Scheme of the Rba. sphaeroides photosynthetic membrane cross-section with cyt bc_1 complex omitted for clarity. LH1 is a ring surrounding RC. There is excitation energy transfer (yellow arrows), electron transfer (black arrows), and trans-membrane hydrogen transport (blue arrows) presented. Prepared based on refs. 11,12,21.

Detailed scheme of the electron and energy transfer within the photosynthetic membrane of *Rba. sphaeroides* is presented in Figure 3.2, while the electron transfer chain cofactors of RC are shown in Figure 3.3. Light energy is harvested by three types of proteins: two types of antennas (LH1 and LH2) and RC, and all the harvested energy is eventually transferred to RC. As a result, the excited state of the primary electron donor, P_{870}*, is formed. This energy is then used for multistep charge separation with the final electron acceptor being quinone Q_B. This ET occurs with quantum efficiency (electron per absorbed photon) near 100 %.[3] Details on the charge separation within RC are given in chapter 3.2.2. The quinone Q_B, after being doubly reduced, diffuses out of its pocket in the protein into the membrane and is oxidized by the cyt bc_1 complex. Subsequently, electron transfer within cytochrome bc_1 finally leads to the reduction of the water-soluble cyt c_2. Cyt c_2 in its reduced state is finally able to rereduce the primary donor P_{870}^+ in RC, closing the cyclic electron transfer scheme. Protons, which were pumped across the membrane during the electron transfer, form an electrochemical gradient, which is then used as a driving force for ATP synthesis by the ATP synthase. ATP can be then used to power cellular processes and synthesize organic compounds in light-independent reactions of photosynthesis.

3.2.2 Reaction centers

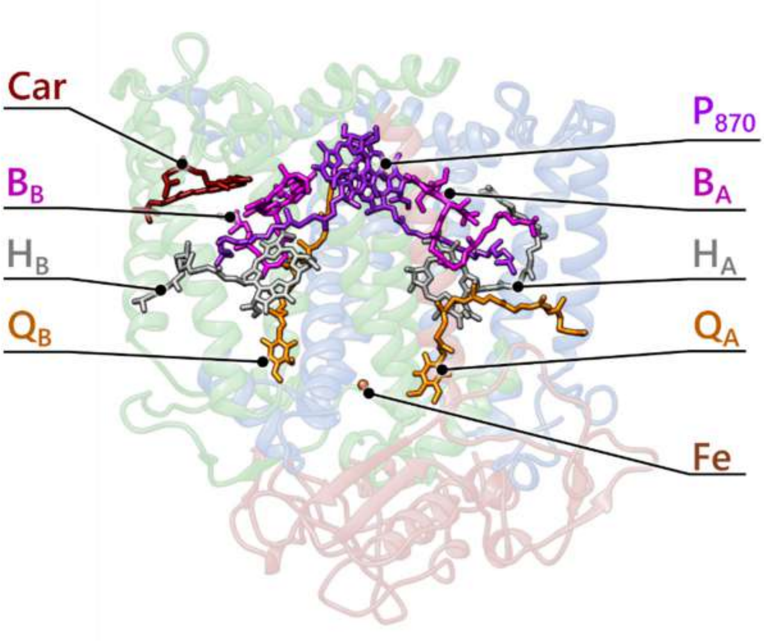

Figure 3.3 Scheme of the structure of the Rba. sphaeroides RC with all the cofactors annotated. Colors of the ribbon in the background depict different protein subunits: blue – L subunit, green – M subunit and red – H subunit. Crystallographic taken from PDB database, code: 1PCR.[22]

Reaction center of *Rba. sphaeroides* is a membrane protein, which has been thoroughly examined both structurally (by x-ray crystallography) and functionally (by various methods including time-resolved absorption and fluorescence spectroscopy).[11,13] The protein scaffold of the RC consists of 3 polypeptide chains (L, M and H) and there is a set of cofactors buried inside forming two branches (A and B; Figure 3.3). Only branch A is active in electron transfer, while the pigments in the branch B serve a photoprotective function,[23–25] but might also play another, still unknown, role.[12] The cofactors are: four bacteriochlorophylls a (BChl), two of which form the excitonically coupled dimer and act as a primary electron donor (P_{870} or shortly P) and remaining two act as accessory bacteriochlorophylls (B_A and B_B); two bacteriopheophytins a (BPhe; H_A and H_B); two ubiquinones (Q_A and Q_B); carotenoid (Car), which is either spheroidene of spheroidenone depending on the bacteria growing conditions; iron ion (Fe). Detailed structure of each of the cofactors is presented in Figure 3.4.

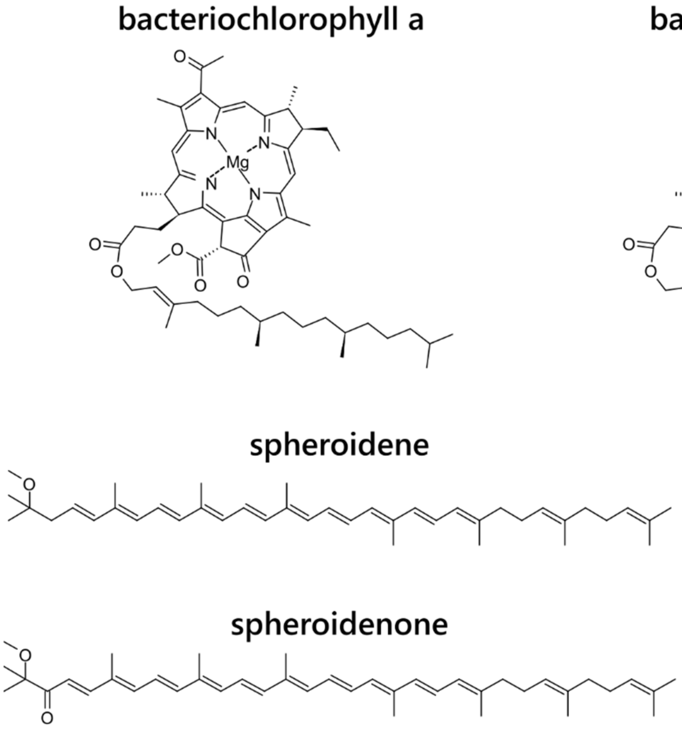

bacteriochlorophyll a

bacteriopheophytin a

spheroidene

spheroidenone

ubiquinone-10

Figure 3.4 Chemical structures of cofactors from the Rba. sphaeroides RCs.

Nonprotein components of the RC and their interaction with polypeptide chains strictly determine the absorption properties of the whole complex in the vis-NIR region. The steady-state absorption spectrum of RCs is known (Figure 3.5) and all of its bands can be attributed to specific cofactors. One of the distinct features of the spectrum are the three bands at around 750-870 nm, where each band corresponds to one of the cofactor types. This features of the spectrum are especially valuable in transient absorption spectroscopy (TAS) experiments, where one can follow an electron transfer by observation of changes in each of the bands.

As mentioned above, primary function of RC is to perform a charge separation after excitation. Energy stored in an excited state of the primary donor P_{870}* leads to the charge-separated state $P_{870}^{+}H_{A}^{-}$ within ~3 ps via the transient formation of the $P_{870}^{+}B_{A}^{-}$ state. The next steps depend on the state of the RC. There are two of those possible, named in the literature as “open” or “closed”. In closed RCs, further electron transfer from H_{A}^{-} is blocked by either reduction or depletion of Q_A, while in open RCs, all cofactors are initially in their neutral form, and electron can go further from H_{A}^{-}. Closing of RCs is achieved in the laboratory either by depletion of quinone Q_A with genetic engineering/chemical methods or by providing a supply of electrons to the P_{870} (*e.g.* sodium ascorbate) without accepting electrons from the Q-side of RC under light conditions, leading to the formation of the $P_{870}Q_{A}^{-}$ state.

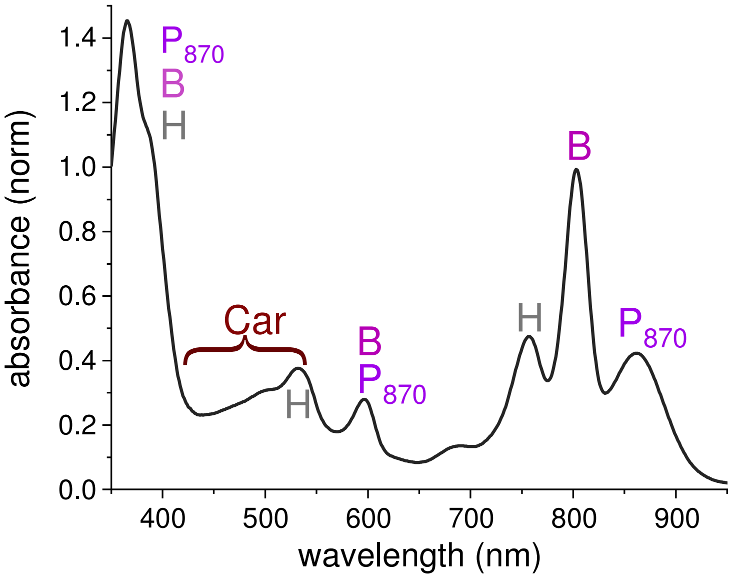

Figure 3.5 Steady-state absorption spectrum of RCs solubilized in a buffered aqueous solution with each band assigned to certain RC cofactors.

Thus, in closed RCs, the state $P_{870}^{+}H_{A}^{-}$ can be depopulated only by back electron transfer or charge recombination, which occurs within the nanosecond time scale and is a multiexponential process, whose mechanism is still under scientific debate and is a scope of one of the papers constituting this thesis[RB1]. There are two main possible results of the charge recombination: the ground state P_{870}, leaving RCs in the initial state, or the triplet excited state $^{3}P_{870}$. Triplet state is formed with ~15 % quantum yield in wild type RCs.[26] The lifetime of $^{3}P_{870}$ is of the order of 10-100 µs,[23,25] which might be long enough for electron injection from it into the electrode. In general, triplet states formation within biological organisms pose a great threat to the stability of its compounds due to the possible formation of reactive oxygen species (ROS) by it.[27] To mitigate this problem, purple bacteria developed a mechanism of quenching of the triplet energy of $^{3}P_{870}$ by the Car, forming ^{3}Car via an intermediate $^{3}B_{B}$ within ~25 ns.[23,25] The lifetime of ^{3}Car is of the order of a few microseconds which is 1-2 orders of magnitude less than that of $^{3}P_{870}$. Moreover, the energy level of ^{3}Car is lower than that of $^{3}P_{870}$. These two facts lower the probability of creation of ROS and thus increase the robustness and lifetime of the whole RC complex.

On the other hand, in open RCs, the electron is transferred further from H_{A} to Q_{A} within ~200 ps.[28] The charge separated state $P_{870}^{+}Q_{A}^{-}$ is already relatively long-lived (~100 ms recombination lifetime), and thus is potentially interesting as a source of electrons in biohybrid devices. Further electron transfer process in RCs bound to the membrane is more complex, as the quinone Q_{B} needs to be reduced twice by electron from Q_{A}, after two separate full excitations. It occurs within ~0.1 ms (first electron) or ~1 ms (second electron).[29] Then it diffuses out of its pocket into the quinone pool in the membrane and is replaced by the oxidized quinone. However, in RCs solubilized in solution, the Q_B pocket might be empty and $P_{870}^{+}Q_A^{-}$ is the final charge separated state. Percentage of occupied Q_B pockets depends on the protein purification procedure.[30]

All the charge separation steps presented above occur in accordance with the change of redox potential (Figure 3.6). Similarly, the possibility of the RC to donate or accept electrons to/from external acceptors or donors is governed by redox potentials of the involved species. It is, along with the ET recombination lifetime of each step, an essential factor influencing the current generation in biohybrid devices with RC as a photoactive material.

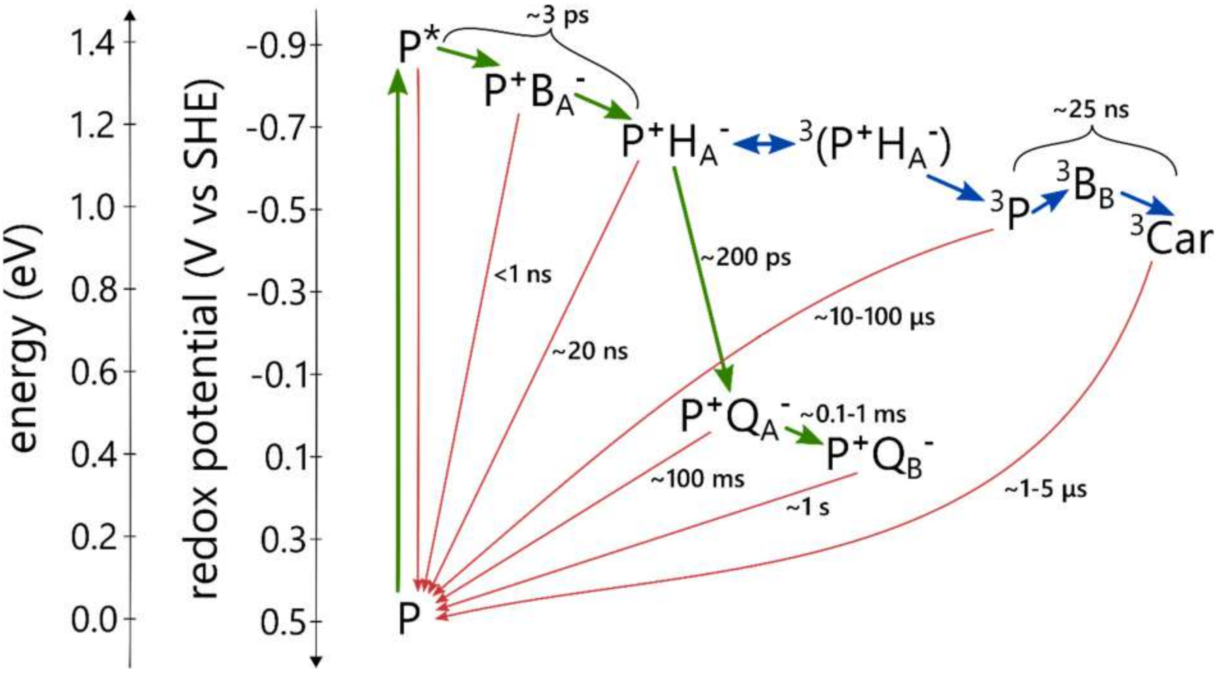

Figure 3.6 Scheme of the charge separation (green), charge recombination (red), and triplet energy transfer (blue) steps within RC. Energy of the states is presented in reference to the ground state. Redox potentials concern oxidation reactions of presented species. Based on refs. 14,23–25,29,31.

4 (BIO)PHOTOVOLTAICS

4.1 PHOTOVOLTAICS

Photovoltaics is a field of science and technology focusing on transforming visible electromagnetic radiation energy into electrical one. Photovoltaic devices can be classified in three categories called generations.[32] First generation solar cells are the oldest, but the most common on the market with the main representative as single-crystal silicon solar cells. Their main problem is the cost of production. In the second generation of solar cells a few technologies were proposed, such as amorphous silicon cells, which are cheap, but have much lower efficiency than single-crystal ones. The third generation cells are currently developed in laboratories using various approaches. These constructions are meant to address both issues of earlier photovoltaics: high costs and low efficiencies. Proposed constructions are, for example: organic, dye-sensitized, perovskite, quantum dots or biohybrid solar cells. One of the most important parameters of solar cells is their efficiency under illumination of standardized solar light. In order to compare it between different devices independently, all record cells are investigated by, among others, National Renewable Energy Laboratory (NREL) in the United States. NREL keeps track of all the record efficiencies of different technology devices in a form of a chart updated regularly and available on-line.[33] Figure 4.1 shows this chart with emerging (3rd generation) photovoltaics highlighted. One can see that some of them (especially perovskite ones) approach efficiencies similar to that of silicon solar cells, being cheaper in construction. Biohybrid devices have not yet been able to find their place on this chart, however there are multiple literature reports on those, and they are described in more detail in further paragraphs.

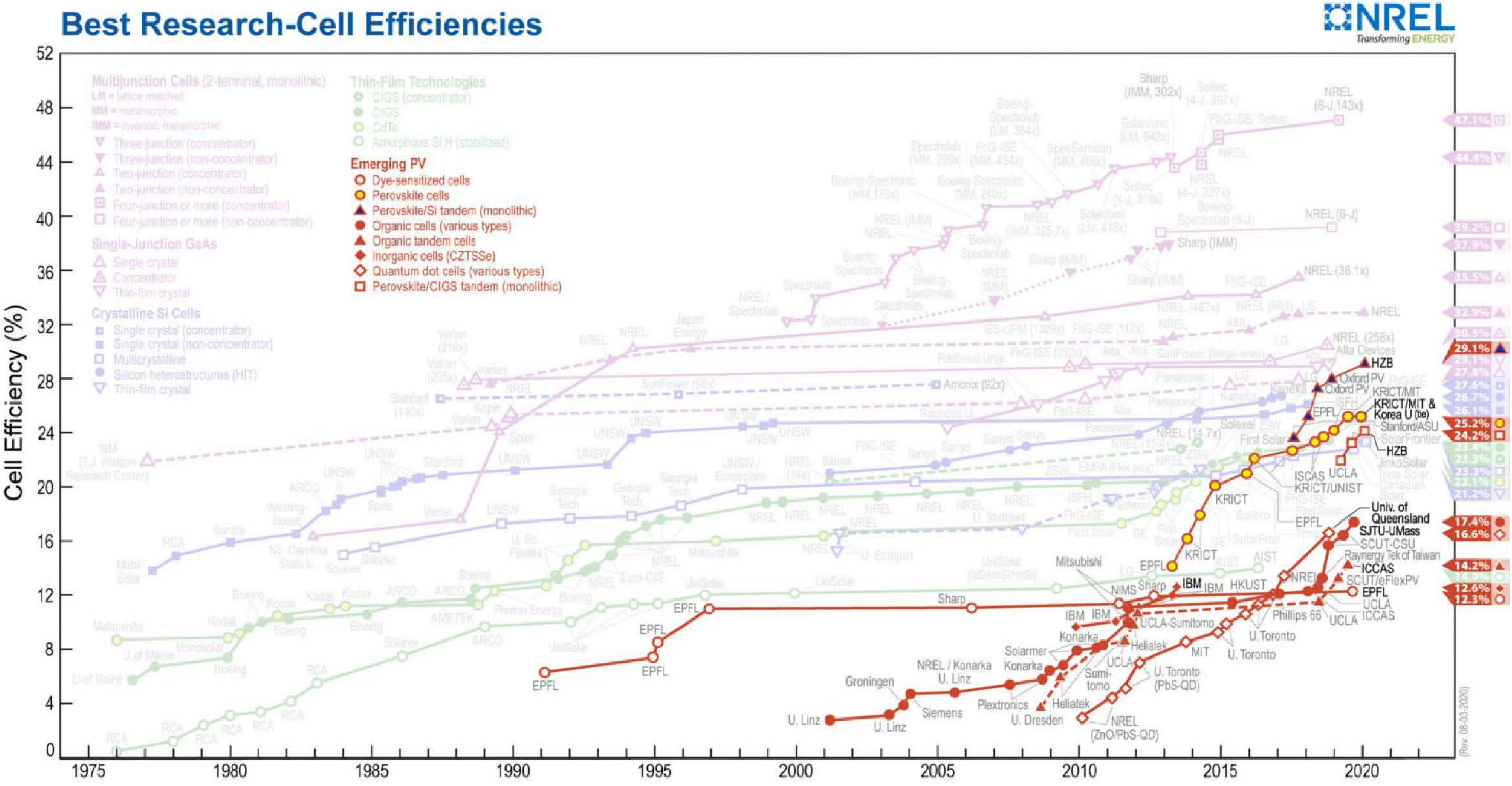

Figure 4.1 Chart of best research solar cell efficiencies tested by the NREL with emerging photovoltaics highlighted. Reproduced from ref. 33.

4.2 BIOHYBRID APPROACH

The trend of building biohybrid devices for solar energy conversion comes from the fact that Nature has excelled this for use in the process of photosynthesis. Closer look at the operation of photosynthetic reaction centers shows that they are solar cells in nanoscale generating electric potential from the energy of light with quantum efficiency close to 100 %. Thus, there is a temptation to take advantage of this efficiency in a human-made device. The first approaches toward utilization of photosynthetic membranes and proteins were reported in the end of 1970s.[4,34] However, the state of the knowledge and methods available at that time did not allow a full investigation of this topic and it got researchers' attention again in the last two decades resulting in many reports on various constructions.[7–10,35–39] There are many challenges in designing biohybrid photovoltaic devices, but they can be summarized in three main groups: 1) choice of biological material, 2) wiring of protein to the working electrode and 3) choice of the electron mediator between the protein and counter electrode. The factors that affect the choice of protein are its cost of production, robustness, absorption spectrum, redox potentials that have to match other parts of the system, and surface properties which affect the interaction with other components of the system. Wiring of the protein to the electrode has to maintain its functional intactness while providing efficient conduction of electrons. Some of the wiring procedures may additionally increase the stability of the protein. Mediator can be either in solution or in solid-state configuration and it should provide fast and efficient electron transfer to/from protein without significant recombination with the working electrode. Further paragraphs summarize different approaches to address these problems reported recently.

The simplest approach is usage of proteins solubilized in solution without adsorbing them on the working electrode. Such system was constructed already for *Rba. sphaeroides* RCs.[40–43] For such device, there is a question: why is there any photocurrent generated?, or in other words: why one electrode is favored over the other in accepting/giving electrons from/to RCs? It is provided either by different properties of the electrodes (for example one being clean fluorine-doped tin oxide (FTO) glass and the other covered with platinum[40]) and/or application of proper external bias.[40–43] Such systems are not capable of generation of record efficiencies, but the simplicity of the system allows exact modelling.[43]

Most of the reported biohybrid devices designs are based on proteins immobilized on the surface of the electrode in contact with a liquid electrolyte. Here two of such constructions will be discussed: 1) with metal oxides[RB2] and 2) with redox-active polymers in hydrogel phase[RB3-4].

The usage of metal oxides in solar cell designs is already well established with Dye Sensitized Solar Cells (DSSC) as an example, in which mesoporous TiO_2 or ZnO layers are used as a matrix for organic dyes.[44–46] The dye can be replaced with proteins in biohybrid approach. Porosity of the substrate gives high surface area for immobilization of protein remaining in a direct contact with the electrolyte, possibly allowing high efficiency of the device. There are multiple reports of such constructions with both purple bacteria RCs[15,47] and higher organisms photosystems,[10,16,48,49] even with one of the record efficiencies (0.08 %) by Mershin *et al.*[16] using ZnO nanostructured electrode and photosystem I as a photoactive material. Similar approach to this is use of inverse opal indium-tin oxide (ITO) porous layers instead of TiO_2 or ZnO for protein immobilization, which allowed creation of bigger pores with better protein penetration into the electrode volume.[19,50]

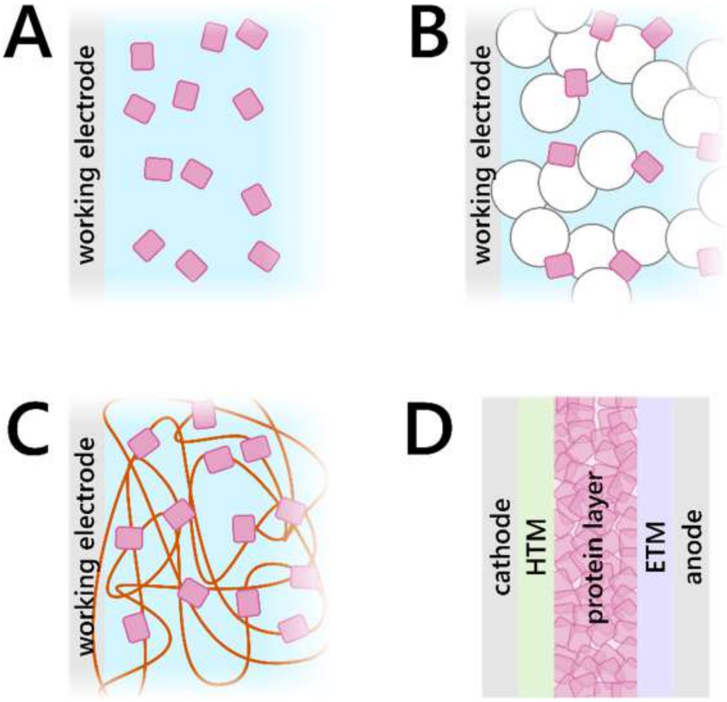

Figure 4.2 Schematic representation of different biohybrid electrodes (A-C) and device (D). (A) Proteins in solution surrounding the working electrode. (B) Proteins immobilized on the surface of a mesoporous layer of metal oxide. (C) Proteins immobilized in a hydrogel matrix. (D) Sample solid-state device with a sandwich-like configuration. HTM – hole transporting material, ETM – electron transporting material.

The usage of redox-active hydrogel matrix is another approach to facilitate the packing of protein on the electrode while maintaining proper electrical contact with both electrode and electrolyte. There are multiple reports of this designs utilizing photosystems[17,51–53] and purple bacteria RCs.[54] Its advantage over metal-oxide electrodes is possibility to tune redox potential of the hydrogel matrix to fit redox potentials of proteins almost freely using different chemical modifications. Moreover, proteins in hydrogel remain in an environment more similar to the native one than when immobilized on solid-state metal oxides.

One of the weak points of abovementioned designs is the liquid electrolyte, which can evaporate or leak during operation, leaving the cell unusable. Thus, there were a few approaches to incorporate photosynthetic proteins in solid-state devices.[37,55–57] However, none of these construction were able to outperform the efficiency of the best freshly prepared cells with liquid electrolyte.

Another problem of biophotovoltaic devices is the stability of the biological part (proteins). One of the highest stabilities of biohybrid devices so far was reported by Gizzie *et al.*[55] for photosystem I solid state device, and amounted 3x12 h of illumination which is still enormously less than desired 10 years of minimal operability of a photovoltaic device. To mitigate this problem, one can use the best repairing device available for biological materials: living organisms. There are multiple reports on utilization of whole living photosynthetic cells directly generating photocurrents while immobilized on electrodes.[7,58,59] In such designs the lifetime of the device is increasing significantly, but the obtained photocurrent densities are much lower. Moreover, the exact mechanism of photocurrent generation in such configurations is not yet known. However, this might be the proper approach if one needs to power some low-current device for long time in a remote location without any other source of electrical energy.

4.3 MODELLING OF BIOHYBRID ELECTRODES

Proper understanding of operation mechanism of biohybrid devices is often not that straight-forward. Thus, there is a need of preparation of mathematical models. However, there were very few attempts to do this reported in literature.[43,60] Most probably, due to the fact that modeling needs proper knowledge of as many as possible kinetic and thermodynamic parameters of both intra- and extraprotein reactions, which might be not available experimentally yet. Nevertheless, those reports, which are available, cover systems of proteins freely diffusing[43] in solution and those immobilized in a hydrogel matrix[60]. Moreover, an article on modelling devices with RCs immobilized on a TiO_2 electrode is part of this thesis.[RB2] All of these models are capable of showing the bottlenecks of the photocurrent generation and allow rational design of better constructions.

5 SAMPLES

Compositions and methods of preparation of samples are described in the papers constituting the thesis. However, in the scientific publications, procedure descriptions are usually brief and hard to follow while redoing experiments, thus I wanted to describe them here in more details giving justification to particular decisions made.

5.1 CELLS BASED ON TiO_2

Preparation of the cells based on mesoporous TiO_2 layers was performed on the basis of the procedures known for DSSC. The most common and simplest method of preparation of TiO_2 substrate is deposition of a thin layer of the paste containing TiO_2 on the conductive glass (FTO or ITO) followed by sintering in an oven (at not less than 450 °C). Basic principles of this procedure appear to be simple, however, small details at each step make a difference in a final outcome.

First, there are multiple possible compositions and preparation procedures of the paste. Size and type of nanoparticles used can determine the size of pores, surface properties of the film as well as the conduction band energy level. Additives in the paste can influence the porosity, thickness and surface properties of the film. Although there was a choice of pastes commercially available to be used in construction of DSSC at the time of preparation of the publication being part of this thesis,[61] none of them was suitable for its objectives. All of them were tuned to be used with small, monomolecular dyes and small-molecule (iodide) electrolyte, with the resultant pore size ≤ 20 nm. This porosity was not enough for the protein such as RC with the diameter of ~7 nm to efficiently diffuse deeply into the porous layer. Thus, there was a need for preparation of custom paste. Pastes were prepared from the commercially available TiO_2 nanoparticles and chemicals. There were two suppliers of nanoparticles chosen: PlasmaChem (P25 nanoparticles with diameter of 21±10 nm and mixed rutile (20 %) and anatase (80 %) phase) and mkNANO (pure anatase nanoparticles of diameters: 5, 10, 15 and 50 nm). All of the nanoparticles were used for preparation of pastes using two procedures: one by Woronowicz *et al.*[62] and the other one by Ito *et al.*[63]

The procedure by Woronowicz *et al.* was a simpler one. The whole preparation was done in a mortar. First, 6 g of TiO_2 nanoparticles were ground with 2 ml of double-distilled water with 0.2 ml of acetylacetone. The mixture was slowly diluted with addition of 8 ml of double-distilled water mixed with 0.1 ml of Triton X-100 (detergent). The resulting paste was viscous and relatively grainy (it was hard to properly remove all aggregates from the paste). Moreover, the shelf-life of the paste was relatively short (no more than a few weeks) due to creation of aggregates and evaporation of water.

The preparation of the paste using Ito *et al.* method was significantly more labor intensive but created the paste of higher quality and much longer shelf-life (even years). First, 3 g of TiO_2 powder was ground with 0.5 ml of acetic acid for 5 min. Next, while grinding, water (2.5 ml) and then ethanol (15 ml) were added in small portions. Afterwards, the mixture was transferred to a beaker using 50 ml of ethanol and stirred with magnetic stir bar alternating with sonication with ultrasonic horn. In the meantime 10 g of terpineol and 1.5 g of ethyl cellulose (15 g of 10 % solution in methanol) were added. The final step was evaporation of ethanol leaving only nanoparticles, terpineol and ethyl cellulose. Terpineol is the key ingredient for long shelf-life of the paste.[63] The usage of three-roller mill described by Ito *et al.* was not possible in our laboratory due to lack of equipment.

There are 3 methods of application of the paste on the surface of the electrode described in literature: doctor-blading, screen-printing and spin-coating.[64] Only the former two were used in reported work. Doctor-blading is the simplest method and can be used with both types of pastes prepared and results in the layer thickness defined by the scotch tape (see Figure 5.1 for resulting layers). Screen-printing, on the other hand, can be used only with the paste prepared with the procedure by Ito *et al.*, as the aggregates in the other paste may clog the pores in the mesh. It creates a uniform layer (more uniform than that from doctor-blading) and its thickness is defined by the mesh. In general, the usage of screen-printing method resulted in creation of more translucent layers, which was preferred for transmission experiments. No matter which method was used, the substrate was FTO and the samples were sintered in an oven for 30 min at 570 °C after warming up within 25 min. For some of the slides covered with TiO_2, additional treatment with $TiCl_4$ solution was performed. Slides were immersed in a 50 mM $TiCl_4$ aqueous solution for 30 min at 70 °C. The aim of the $TiCl_4$ treatment was to cover the mesoporous TiO_2 structure, and any bare areas of FTO glass, with an additional thin layer of TiO_2.[65]

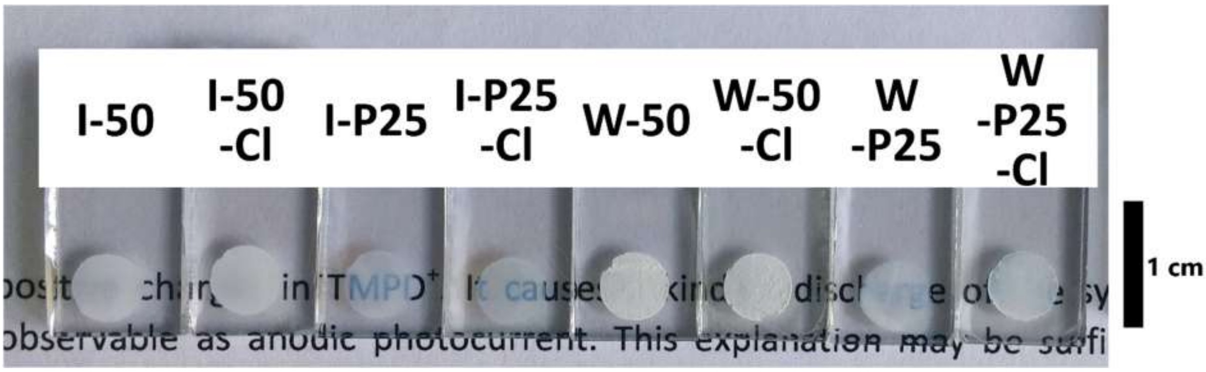

Figure 5.1 Photography of the sintered layers of TiO_2 prepared using doctor-blading technique. The I- and W- prefixes depict procedures by Ito et al.[63] and Woronowicz et al.,[62] respectively. P25 means the P25 type nanoparticles, while 50 means mkNANO nanoparticles of 50 nm diameter. -Cl suffix means additional $TiCl_4$ treatment.

The next step after sintering the TiO_2 is immobilization of RCs on its surface. There are multiple methods of protein immobilization on electrode surface such as immersing the electrode in the solution of proteins for some time, electrodeposition or drop-casting (in ambient conditions or under low pressure to assist drying). All of this methods can rely on simple physisorption of protein to the surface (*e.g.* by electrostatic interaction), covalent bonding via linkers (*e.g.* alkanethiols self-assembled monolayers) or immobilization in some kind of matrix (such as hydrogel).[66] In the presented work with TiO_2 the simple drop-casting of 1 µl of concentrated RCs solution was used. [RB2] This method was chosen as it wastes relatively small amount of precious RCs sample and RCs used were genetically engineered to efficiently and quickly bind to TiO_2, so prolonged immersion was not needed.[61]

The final part of the cell is the electrolyte. Although the iodide one in acetonitrile (typical for DSSC) was used in a work by Mershin *et al.*,[16] it might be too harsh for proteins. Thus, in the presented work water-based electrolyte was used with TMPD (*N,N,N′,N′*-tetramethyl-*p*-phenylenediamine) as a redox agent. This chemical was used as it had already proven its value in biophotovoltaics with RCs.[40]

5.2 CELLS BASED ON HYDROGELS

Deposition of the redox-active hydrogel with a protein is usually done within one step of drop-casting the mixture of polymer, protein, and cross-linker in a proper buffer solution onto the surface of the electrode. The polymer used was poly(vinyl imidazole-co-ally amine)-$[Os(II)(bpy)_2Cl]^+$, which has already proven its usage in biohybrid electrodes.[20,51,52] The gelation process occurs in room temperature over several hours along with drying of an excess of water. The solution contained PEGDGE (poly(ethylene glycol) diglycidyl ether) which is a cross-linker ensuring the formation of stable polymer-protein film. Exact composition of the solution can be found in the paper constituting this thesis.[RB3] As the redox mediator, for photocurrent measurements, the water soluble quinone was used (2,3-dimethoxy-5-methyl-*p*-benzoquinone). It was chosen due to its high specificity in redox reactions with the Q-side of RCs. This specificity is caused by enzymatic activity of the Q_B side of RC in reducing quinones. Moreover, this reduction reaction is coupled with protonation, which lowers efficiency of its occurrence at the bare electrode or the polymer redox sites. Thus, it was used to limit the recombination process between the mediator and the working electrode and eventually increase the net photocurrent.

6 METHODS

6.1 ELECTROCHEMISTRY

Electrochemistry is a field of science laying at the edge of physics and chemistry. It focuses on studies of redox (reduction and oxidation) chemical reactions by observation of electrical phenomena in the system. From electrochemists' point of view, redox reactions can be divided in two types: homo- and heterogenous. Former ones, are those which occur in the volume of the analyzed solution, while the latter ones – on the surface of electrode. Heterogenous reactions can be studied directly via electrochemical methods, as they rely on donation or acceptance of electrons to/from electrode, and thus electrical current flowing through the cell.

6.1.1 Theory of electrode potentials

Let us analyze, from the thermodynamical point of view, a simple reduction reaction 6.1 occurring at the electrode surface.

$$A_{ox} + z\, e^{-} \rightarrow A_{red} \tag{6.1}$$

Where: $A_{ox/red}$ – oxidized/reduced species A, z – number of electrons taking part in the reaction, e^{-} – electron.

It is known, that each chemical reaction is connected with the change of the free Gibbs energy of the system.[67] It is described accurately by equation 6.2.

$$\Delta G = \Delta G^{0} + RT \ln \frac{a_{A_{red}}}{a_{A_{ox}}} \tag{6.2}$$

Where: ΔG – actual change of the Gibbs free energy, ΔG^{0} – change of the Gibbs free energy in the standard conditions, R – universal gas constant ($R \cong 8.314\ J\ mol^{-1}K^{-1}$), T – temperature (in kelvins), $a_{A_{red/ox}}$ – activity of reduced/oxidized species.

In many experimental conditions (low ionic strengths) activities can be simply replaced by molar concentrations giving equation 6.3.

$$\Delta G = \Delta G^{0} + RT \ln \frac{[A_{red}]}{[A_{ox}]} \tag{6.3}$$

Where: $[X]$ – molar concentration of species X.

Electrochemical potential of a chemical reaction is related to the Gibbs free energy change as in equation 6.4.

$$\Delta G = -z\, F\, E \tag{6.4}$$

Where: F – Faraday constant ($F \cong 96485\ C\ mol^{-1}$), E – electrochemical (redox) potential.

By applying equation 6.4 to equation 6.3 one gets equation 6.5, which is nothing else but a Nernst equation – most basic equation of electrochemistry.

$$E = E^0 - \frac{RT}{zF}\ln\frac{[A_{red}]}{[A_{ox}]} \tag{6.5}$$

Where: E^0 *– standard redox potential.*

Analyzed electrode reaction is just half of the whole electrochemical experimental system. In order to measure potentials or currents, at least two electrodes are needed. Combination of an electrode and reactants from the electrolyte is called a half-cell, and its potential is described by a Nernst equation (6.5). To get the value of the voltage of the whole cell (two half-cells connected electrically) one can use an equation 6.6.

$$E_{cell} = E_{half-cell\,1} - E_{half-cell\,2} \tag{6.6}$$

Resulting cell voltage can be measured and its sign determines a spontaneous direction of the reaction.

6.1.2 Experimental setup

As mentioned above, there are at least two electrodes needed for an electrochemical experiment. In such situation one of them would be called anode and the other: cathode. Anode is an electrode, at which reactant's oxidation takes place, while the reduction takes place at the cathode. Described reactions can either occur spontaneously (in the galvanic cells) or due to applied potential (in the electrolytic cells). However, usage of two electrodes in an analytical setup in order to study half-cells reactions is possible only in low-current situations. Flow of significant current (> microamperes) causes change in the electrode potential and thus determination of redox potentials of each half-cells becomes impossible.[68] Thus, a three-electrode setup was introduced, consisting of: working electrode (WE), reference electrode (RE) and counter (auxiliary) electrode (CE). Working electrode is that one of the studied half-cell, and it can serve as both cathode or anode depending on the conditions. Reference electrode is a standard half-cell, such as Ag/AgCl, usually enclosed in a glass tube filled with proper electrolyte (such as 3 M KCl), with a frit in the end, providing electrical contact with the studied solution, but preventing the solutions from mixing. And finally, counter electrode is used for current flow from working electrode instead of reference electrode, to keep the reference potential steady. Counter electrode is usually a high-surface-area, inert conductor, such as Pt wire. If reference and counter electrode are chosen properly, only the processes at the working electrode influence the results of measurements described in further chapters.

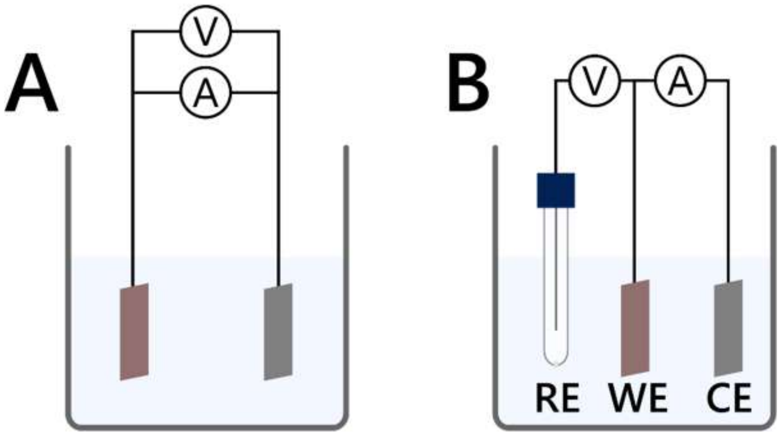

Figure 6.1 Schematic representation of 2- and 3-electrode setups used in electrochemical experiments.

In modern electrochemical experimental setups the whole measurement is conducted using potentiostat. It is a device, which can apply potential to the working electrode in reference to the reference electrode and measure current between working and counter electrodes. Most of the commercially available potentiostats are also capable of working in galvanostat mode, in which the current between working and counter electrodes is kept steady while potentials between working and reference electrodes is measured.

In electrochemistry there are two conventions of plotting potentials and currents (Figure 6.2): international (set by IUPAC) and classical (polarographic, used mainly in US). In this thesis, all results are shown in agreement with the IUPAC convention.

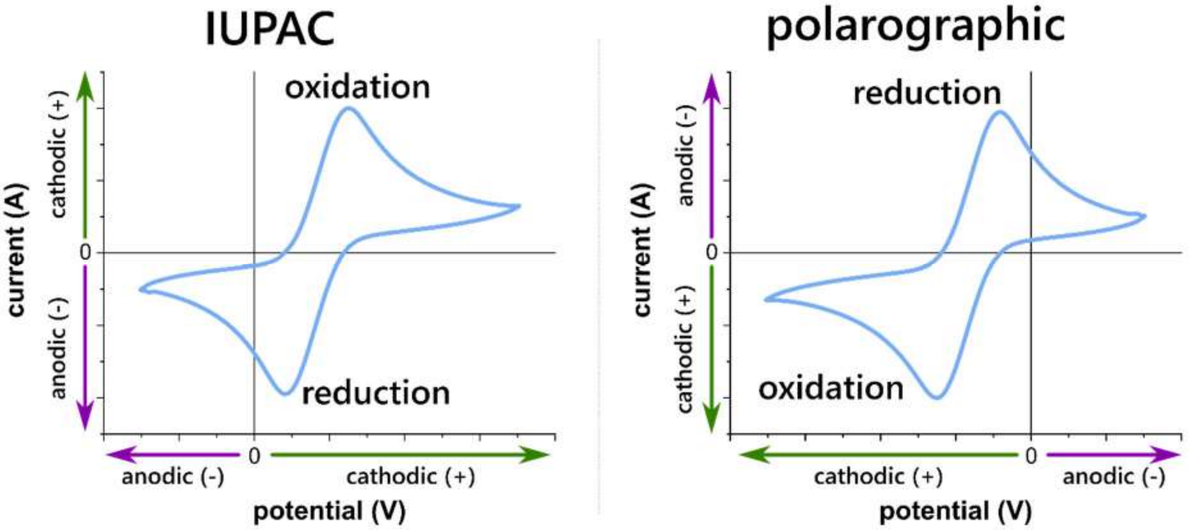

Figure 6.2 Scheme of electrochemical plotting conventions used in literature.

6.1.3 Photochronoamperometry

Chronoamperometry is an electrochemical method of measurement of current over time while keeping applied potential steady (or changed in slow steps). Photochronoamperometry adds light irradiating onto the sample, which can be switched on or off at chosen times (Figure 6.3).[35,39] It is widely used to determine photocurrent values of electrodes for different light and potential conditions. Moreover, the shape of the photocurrent response after both turning on and off the light gives information about processes occurring during and after illumination.[43,60,61]

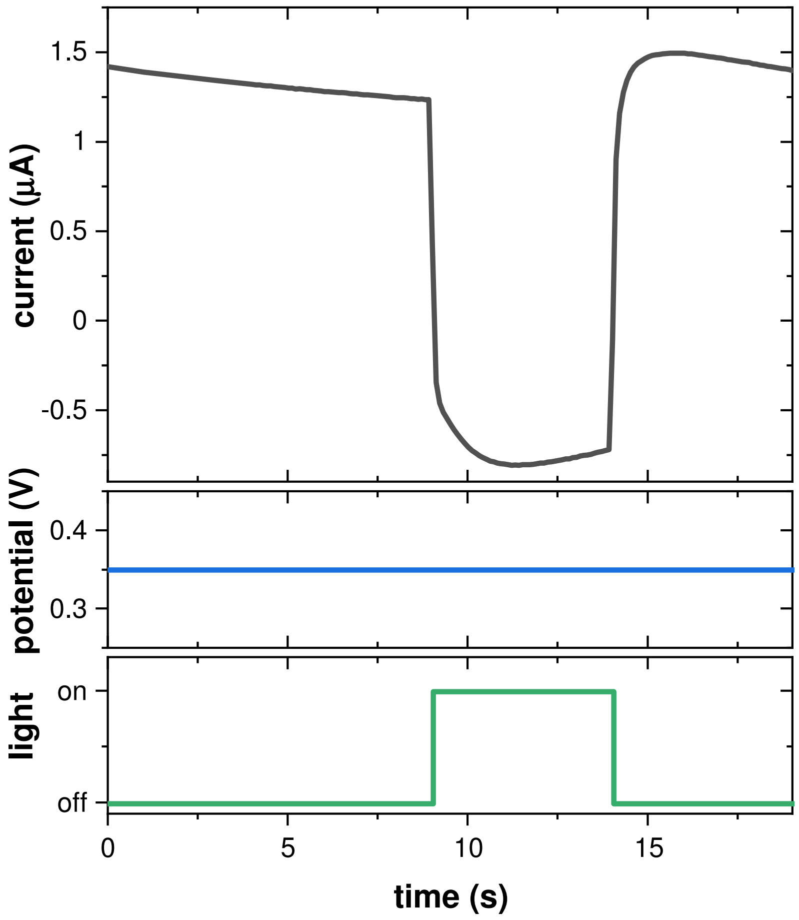

Figure 6.3 Exemplary plots of a simple photochronoamperometric result (top) along with the applied potential trace (middle) and a light switching trace (bottom).

In the case of all photochronoamperometric measurements described in this thesis[RB2-3] an automated setup, designed by me was used. The light source was an LED powered with a laboratory DC (direct current) power supply with regulated current. The light was turned on and off by chopping the current using a relay which was controlled via an electronic circuit with Arduino nano board as a main component. All instructions for Arduino board and electrochemical part of the experiment were operated by the NOVA 1.11 software by Autolab.[69]

6.1.4 Photocurrent action spectra

One of the possible expansions of photochronoamperometry experiments is measurement of photocurrent action spectra.[35,39] Sometimes, they are scaled in external quantum efficiency (6.7) and called Incident Photon to Current Efficiency (IPCE) spectra.

$$EQE(\lambda) = \frac{\Phi_{generated\ electrons}(\lambda)}{\Phi_{absorbed\ photons}(\lambda)} \tag{6.7}$$

Where: EQE – external quantum efficiency, λ – wavelength of absorbed photons, $\Phi_{generated\ electrons/absorbed\ photons}$ – flux of subscripted species.

Experiment is a typical photochronoamperometry with constant applied potential, but the wavelength of light is changed in steps between switching on the light. Resulting values of photocurrent at each wavelength are then corrected with the photon flux at the corresponding wavelengths. Such spectra should resemble in shape the absorptance (6.8) spectra of the element of the system generating photocurrent, as the flux of absorbed photons is proportional to it.

$$\alpha(\lambda) = \frac{\Phi_{absorbed}(\lambda)}{\Phi_{incident}(\lambda)} = 1 - 10^{-A(\lambda)} \tag{6.8}$$

Where: α – absorptance, $\Phi_{absorbed/incident}$ – flux of subscripted photons, A – absorbance.

This technique allows determination which element of the system is responsible for photocurrent generation and whether it behaves natively in the electrode configuration.

6.1.5 Cyclic Voltammetry

One of the most commonly used methods in a modern electrochemistry is a cyclic voltammetry (CV). It is widely used for acquiring information about electrochemical reactions such as redox potentials or kinetics of heterogenous electron transfer reactions.[68,70–72] It is one of the potential sweep methods, meaning that during experiment, the potential is constantly changed while the current response is measured. The potential sweep takes shape of the triangular wave (Figure 6.4B).

Sample result of CV of a single-electron reversible redox pair is presented in Figure 6.4A. There are two characteristic peaks: positive during sweep towards more positive (oxidating) potentials and negative during sweep towards more negative (reducing) potentials. The former one comes from oxidation, while the latter one – from reduction of the reacting species. Peaks are visible is CV scans instead of just steady-state oxidation/reduction currents due to depletion of reduced/oxidized form of the redox pair in the proximity of the electrode surface. After passing the peak, the current approaches steady-state current which is limited by a mass transport of substrate towards the electrode. Potential in the middle of these peaks is a redox potential of the studied species under applied conditions (orange line in Figure 6.4A).

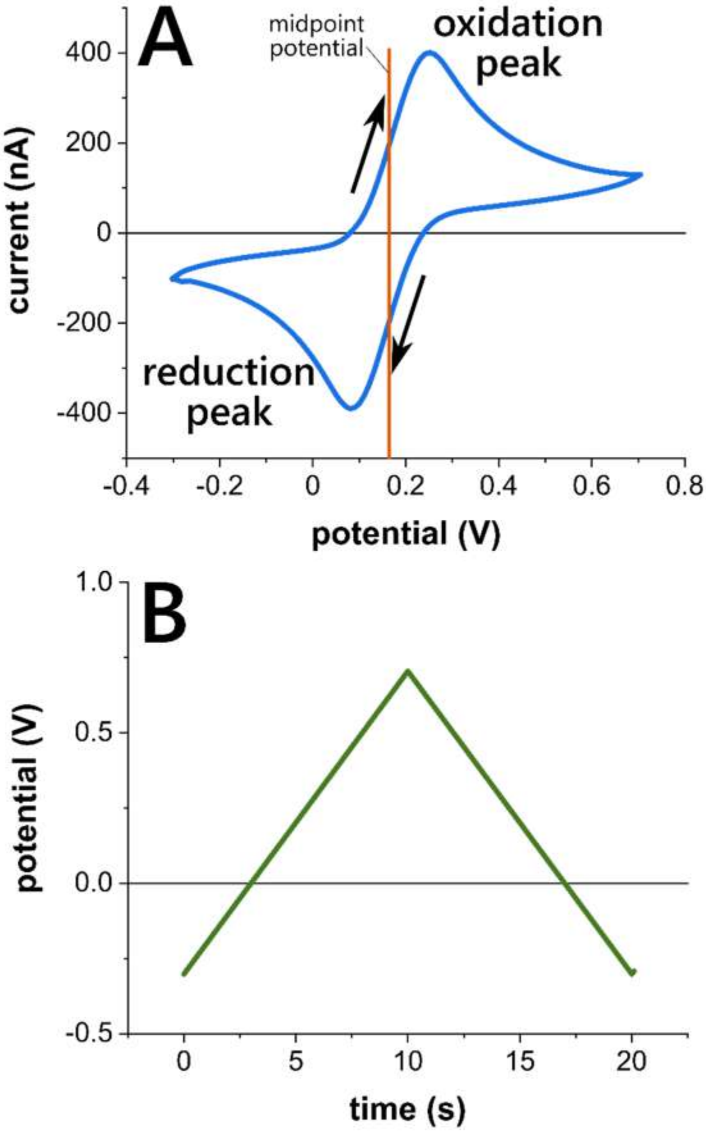

Figure 6.4 Sample result of cyclic voltammetry experiment for a single-electron reversible redox pair (A) and a potential time trace during conducting of this experiment (B).

CV is a very powerful tool in hand of an experienced electrochemist and can answer questions such as:[68,71,73,74]

- What is the redox potential of the studied species?
- What is the concentration of the studied species?
- Is the studied reaction reversible?
- How many electrons are involved in the reaction?
- Are the species freely diffusing or attached to the electrode surface?
- What is the kinetics of an electrode reaction?
- Are there any homogenous reactions following heterogenous electron transfer?

In the presented thesis, CV was used for characterization of both freely diffusing mediator (TMPD) and redox center immobilized in the hydrogel. It allowed determination of redox potentials and stability of the species.

6.1.6 Modelling

In complex systems, results of abovementioned methods may not be straight-forward to draw conclusions from about the mechanism of operation. In such case, creation of a mathematical model may be helpful. Such model allows recreation of all experimental results using a set of kinetic and thermodynamic parameters. In electrochemical systems there are a few processes, which have to be taken into account:

a) heterogenous reaction on the electrode surface,
b) homogenous reactions in the volume of the electrolyte,
c) mass transport (usually diffusion in stationary system).

Each of these processes can be described with a set of equations depending of the exact system studied and demanded level of accuracy. For heterogenous reaction kinetics, the Butler-Volmer equation is usually used (6.9), for homogenous reactions, one needs to write down kinetic equations, and for mass transport – a diffusion equation (6.10).[68]

$$j = j_0 \cdot \left\{ \exp\left[\frac{\alpha_a z F \eta}{RT}\right] - \exp\left[-\frac{\alpha_c z F \eta}{RT}\right] \right\} \tag{6.9}$$

Where: j – electrode current density, j_0 – exchange current density, $\alpha_{a/c}$ – anodic/cathodic charge transfer coefficient, z – number of electrons involved in reaction, F – Faraday constant, η – overpotential (difference between applied electrode potential and a redox potential of reacting species), R – universal gas constant, T – temperature in kelvins.

$$\frac{\partial c(x,y,z,t)}{\partial t} = D\nabla^2 c(x,y,z,t) \tag{6.10}$$

Where: $c(x,t)$ – molar concentration at position (x,y,z) and time t, D – diffusion coefficient.

Such set of differential equations can be solved numerically and fitted to a set of experimental results. However, in the [RB2] paper the system of equations was simplified in terms of diffusion due to the complex geometry of the electrode. It was assumed that there are two pools of freely diffused mediator: near electrode and bulk, which were in constant exchange of oxidized and reduced species. Further improvement of the model proposed in this paper should involve incorporation of equation 6.10 with proper model for electrode geometry, to deal with the diffusion.

6.2 UV-VIS-NIR SPECTROSCOPY

Spectroscopy in the UV, visible and near IR region allows scientists to analyze processes at energy levels characteristic for transitions between different electron states of atoms and molecules. Thus, it is very useful in monitoring (photo)chemical redox reactions, which are in principle electron transfer processes within or between molecules. Example of such reactions are electron transfer reactions within the RC or between RC and other molecules.

6.2.1 Jabłoński diagram[75]

The variety of electron transitions within organic molecules is often presented in the form of the Jabłoński diagram (Figure 6.5). For each molecule the exact form of this diagram is different (*e.g.* due to forbidden transitions), but here its most general version is discussed. In most cases, the ground, stable state of molecule is a singlet state (*i.e.* all electrons are paired) and is depicted as S_0. In order to change its electronic state from ground to any excited one, the molecule needs external energy, which can be provided by either absorption of photon or transfer from other molecule. Excitation can lead to formation of states with different energy and stability. There are two possible classifications of relaxation processes: (1) related to light emission properties – radiative (fluorescence and phosphorescence) and non-radiative (internal conversion, inter-system crossing and quenching) or (2) related to multiplicity – preserving multiplicity (fluorescence, internal conversion and some versions of quenching) and changing multiplicity (phosphorescence, inter-system crossing and some versions of quenching). Moreover, excited states can undergo further promotion to higher excited state, which is called transient absorption and is utilized in the experimental method called transient absorption spectroscopy.

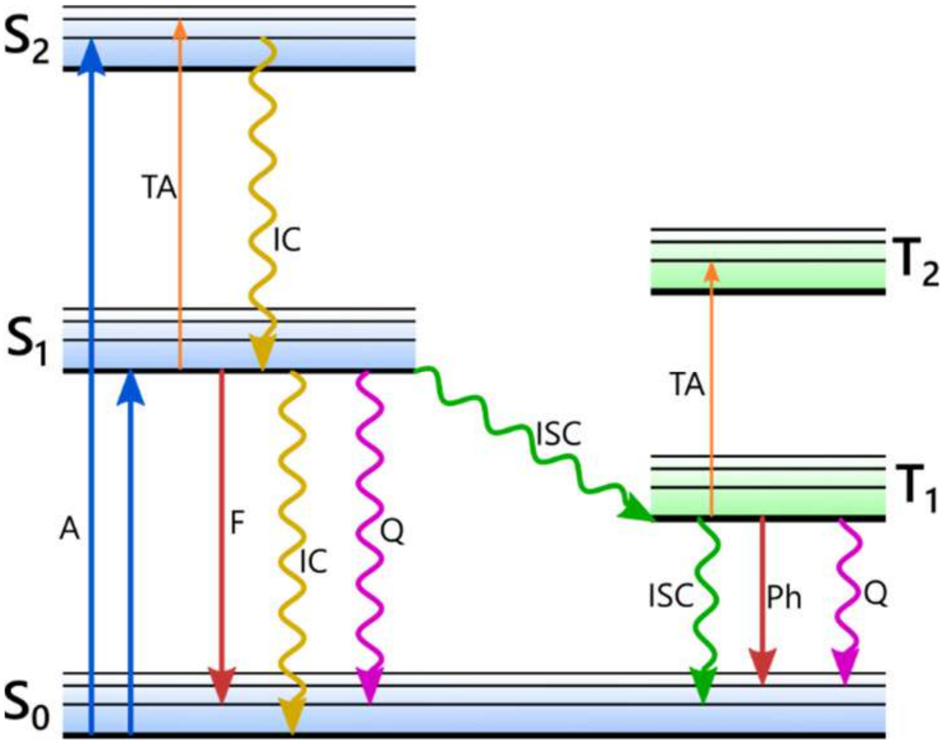

Figure 6.5 General Jabłoński diagram – scheme of possible electron transitions within the organic molecule. Thick horizontal lines represent vibrational ground state of electronic states, while thin lines – higher vibrational states. Wavy arrows represent non-radiative processes, while straight ones those involving photon. S_n – n^{th} singlet state, T_n – n^{th} triplet state, A – absorption, TA – transient absorption, F – fluorescence, IC – internal conversion, ISC – inter-system crossing, Ph – phosphorescence, Q – quenching.

6.2.2 Steady-state absorption spectroscopy

Physics

Light absorption is a process within which a photon is absorbed by a studied species (*e.g.* molecule) and converted into a form of internal energy. Steady-state absorption is a process within which the sample changes its state from the stable (ground) state to the one with higher energy (see Figure 6.5). To quantify the ability of the sample to absorb light, a quantity called absorbance is defined (equation 6.11).

$$A(\lambda) = \log \frac{I_0(\lambda)}{I(\lambda)} \tag{6.11}$$

Where: A – absorbance, λ – wavelength of probing light, I_0 – intensity of light before passing the sample, I – intensity of light after passing the sample.

Absorbance subjects to two important laws: Lambert-Beer law and law of absorbance additivity. Lambert-Beer law says that absorbance depends linearly on concentration of species and thickness of the sample layer (equation 6.12). The proportionality factor called extinction coefficient is a characteristic parameter of the material in studied conditions. This law allows utilization of absorption measurements for determination of concentration of species.

$$A = \varepsilon\, c\, l \tag{6.12}$$

Where: A – absorbance, ε – extinction coefficient (usually in $M^{-1}cm^{-1}$), c – concentration of species (usually in M), l – thickness of an absorbing layer (usually in cm).

The law of absorbance additivity says that the absorbance of mixture of substances is a sum of absorbances of all individual elements, assuming that the elements are not interacting with each other (equation 6.13).

$$A_{mixture} = \sum_i A_i \tag{6.13}$$

Where: $A_{mixture}$ – absorbance of a mixture, A_i – absorbance of i-th element of a mixture.

Experimental setup

Absorbance is usually defined for a single wavelength (equation 6.11) and thus a measurement of an absorption spectrum (plot of absorbance vs wavelength) is possible. A setup used for this kind of measurement is called spectrophotometer. There are two basic concepts of absorption spectra measurements: single- and multi-wavelength. In a single-wavelength concept the white light is transferred through a monochromator with moving dispersive element (*e.g.* diffraction grating) and the resulting monochromatic light is then guided through a sample to a photodetector (*e.g.* photodiode; Figure 6.6A). Spectrum is obtained by separate measurements of absorbance for each wavelength (by scanning with grating movements). In a multi-wavelength approach the white light is led directly through the sample and then is guided on the dispersive element *(e.g.* diffraction grating), and then the split light falls on the linear detector (photodiode array or CCD (charge-coupled device)/CMOS(complementary metal-oxide semiconductor) camera), at which intensity of each wavelength is measured simultaneously by different channels (Figure 6.6B).

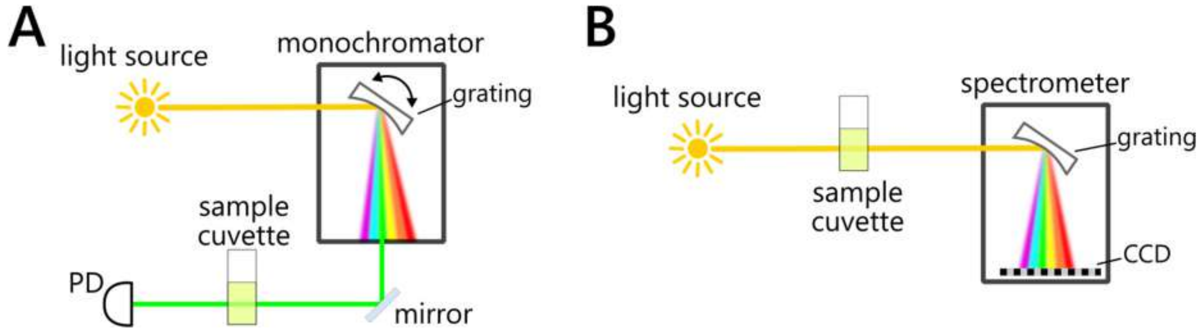

Figure 6.6 Simplified schematics of steady-state absorption measurements in single- (A) and multi-wavelength (B) approach. PD – photodetector, CCD – charge-coupled device.

6.2.3 Transient absorption spectroscopy

Physics

Transient absorption spectroscopy (TAS) is a technique which allows investigation of interaction of light with excited molecules (or their product) by probing their absorbance changes after short system perturbation (*e.g.* laser pulse). There are three basic phenomena which can be observed during measurement: transient absorption, ground state photobleaching and stimulated emission (Figure 6.7). Transient absorption is a process of light absorption by transient states of the molecule (*e.g.* excited state or unstable product). It is observable as a positive signal in a difference spectrum (additional absorbance). Other two processes are characterized by negative signals in a difference spectrum, however the source of this signal is different. Photobleaching of a ground state is caused by depopulation of the ground state of the molecule by the pump pulse, which simply results in lack of absorbance for wavelengths, at which molecule absorbs in steady-state spectrum. Stimulated emission, on the other hand, occurs at the same wavelength as a spontaneous emission, however the generated photon is coherent to the incident one. Generated light falls on the detector causing the apparent drop of absorbance. Observation of these phenomena over time gives information about kinetic processes within the sample.

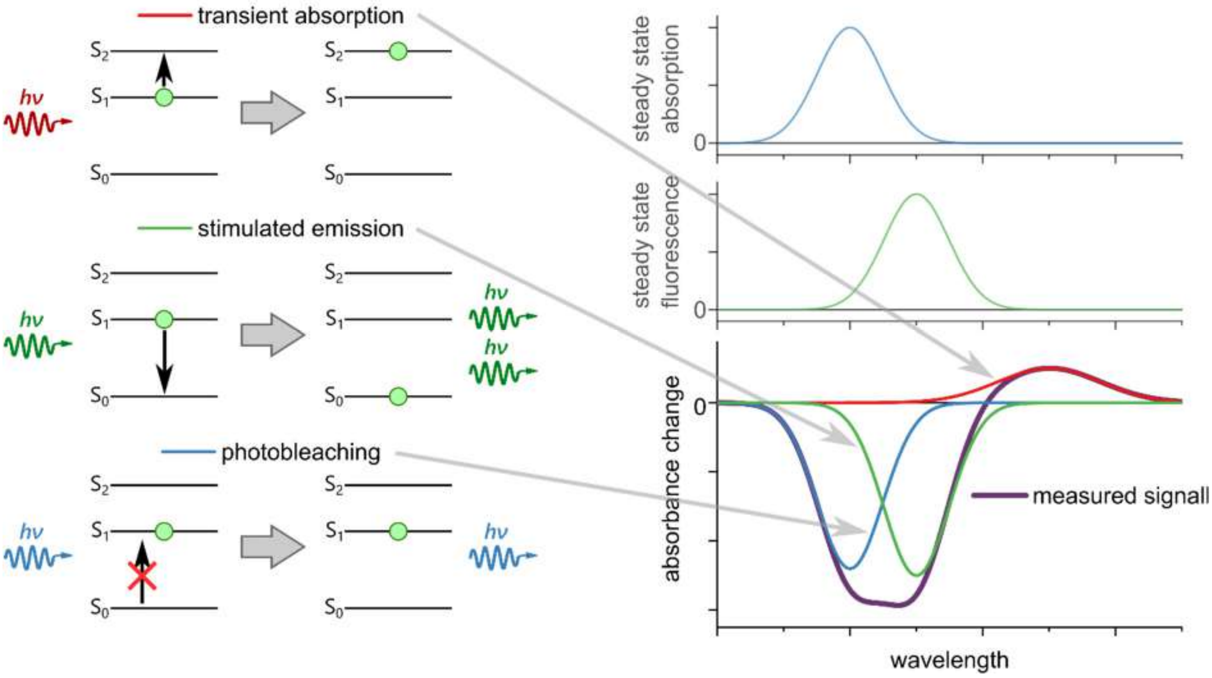

Figure 6.7 Summary of possible processes observed during transient absorption experiment. Left: energy schemes of interaction of excited molecules with light of different wavelengths. Right: comparison of the contributions to the resulting transient absorption spectrum with the steady-state absorption and emission spectra

Measurement

The TAS measurement is realized in a pump-probe setup. Short laser (or flash lamp) pulse is used as a pump to excite the analyzed species, and the probe light (either monochromatic or broadband with much lower intensity than the pump) is used to monitor absorbance changes. The probe light can be either continuous or pulsed with delay to the pump. Here I will focus on the setups with laser pulse used as a pump and a pulsed probe.

First, let us discuss the operation of the pump-probe setup with femtosecond Ti-sapphire laser and optical delay line. Ti-sapphire oscillator pumped by the continuous wave laser generates high-energy short pulses in the near IR region (~800 nm; exact wavelength can be tuned). Beam is then split into two separate lines: pump and probe. In the pump line there are usually additional devices used for increasing the power of the pulse (regenerative amplifier) and tuning its wavelength (*e.g.* OPO – optical parametric oscillator). Afterwards, the pump beam is guided towards the sample compartment through a set of mirrors and lenses. Simultaneously, the probe beam from the laser is guided through an optical delay line, which consists of a set of motorized mirrors, which can increase or decrease the path of light, thus change the travel time (light needs ~1 ns to travel ~30 cm in air). Afterwards, the probe light falls on the nonlinear crystal (such as CaF_2 or sapphire) in order to create white light continuum (WLC). Such generated white light is then led to the sample compartment usually almost parallel to the pump light. One of the challenges during experiment is an alignment of pump and probe beams so that they overlap within the volume of the sample and the probe light probes an excited volume. Afterwards, the probe light falls on the spectral detecting system, which usually consists of a diffraction grating and a linear detector (such as CCD camera; see chapter 6.2.2). Measurement of spectra at different delay times (both before and after pump pulse) allow construction of the 2D array of changes of absorbance versus time and wavelength. Use of optical delay lines allows obtaining high accuracy of setting the delay time (down to sub-femtosecond resolution), however, the main drawback is the maximal possible delay, usually no more than several nanoseconds due to the natural divergence of the laser light, causing enlarging of the beam diameter over longer distances as well as confined space and mechanical precision difficulties in bigger systems.

When longer time range is needed, an electronic delay may be used. Then the white probing light pulse can be generated by a separate laser and nonlinear crystal set triggered by an electronic system. In such case, the accuracy of the delay time setting is defined by the electronics speed and the shortest times available are down to sub-nanosecond. With this kind of setup one can measure at as long time-scale as needed.

In one of the papers constituting the thesis,[RB4] TAS measurements where conducted in a setup, which combined two of above approaches, with HELIOS Fire (time scale < 8 ns with optical delay line) and EOS Fire (time scale > 1 ns with electronic delay) probing and detection systems from Ultrafast Systems. This setup is arranged in such way, that the pump line and sample compartment are shared between HELIOS and EOS. This approach is helpful as one can perform TAS measurements in the time range from femtoseconds to even seconds at the same sample resting in one place. However, there is an important drawback: size of the excited volume. In the femtosecond pump-probe experiment (such as HELIOS Fire setup) the overlap between pump and probe beams (and thus an excited and probed volume) is defined by the focus of both beams and is of the order of a few hundreds of micrometers. In such case, stirring of the solution or even simple diffusion might shorten the apparent lifetimes due to escaping of the excited sample from the probed volume within the longer time scale (such as milliseconds).

Data treatment

Data obtained directly from TASF measurements usually needs additional work or information prior to modelling of the observed reactions. Figure 6.8 shows sample raw data directly from TAS measurements for an experiment at solution of *Rba. sphaeroides* RCs pumped at 800 nm and probed with visible and NIR light. At first glance, one can see significant signal around 800 nm. It is a scattering of a pump, which is an artifact and needs to be cut out. Moreover, data for lowest wavelengths has significant noise and also needs to be cut out. Afterwards, the baseline is corrected by subtraction of an average of several spectra at the beginning (before laser pump flash) from the whole surface. Resulting map is presented in Figure 6.9.

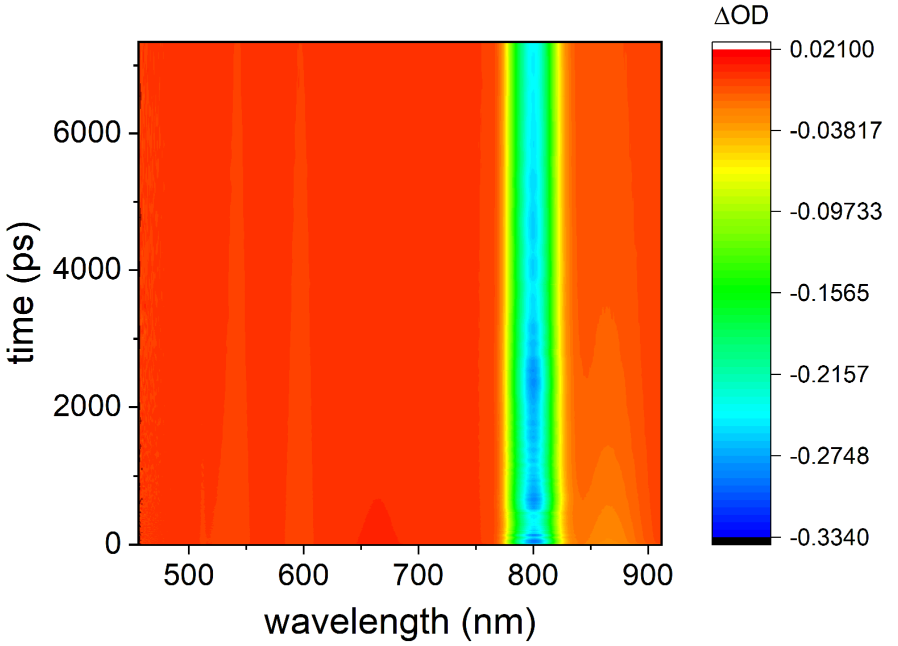

Figure 6.8 Result of TAS experiment without any corrections. Measurement was conducted on a solution of Rba. sphaeroides reaction centers using HELIOS Fire pump-probe setup with 800 nm pump and white light continuum probe.

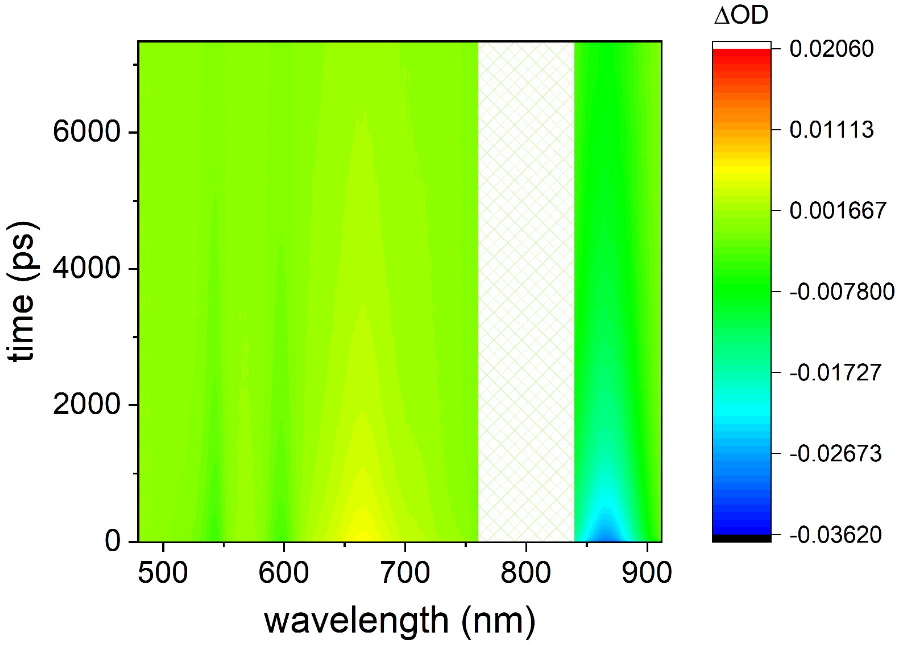

Figure 6.9 Data from Figure 6.8 after first corrections: background correction and cutting out the laser scattering and areas with high noise.

The overall map looks as there are no more artifacts that need correction, however, if one looks at the map zoomed in at first few picoseconds (Figure 6.10), they can see that the signal begins at different time for different wavelength. This effect is called chirp and derives from the group velocity (of light) dispersion (GVD) in various materials.[76] When white probe light passes through for example glass of lenses or cuvette, GVD causes the red light to go ahead of the blue one, thus light of the different wavelengths in the probe arrives at different times to the sample. To mitigate this problem, the data is corrected manually by shifting the time axis for each kinetics so that the signal begins at $t = 0$. Such corrected data is shown in Figure 6.11.

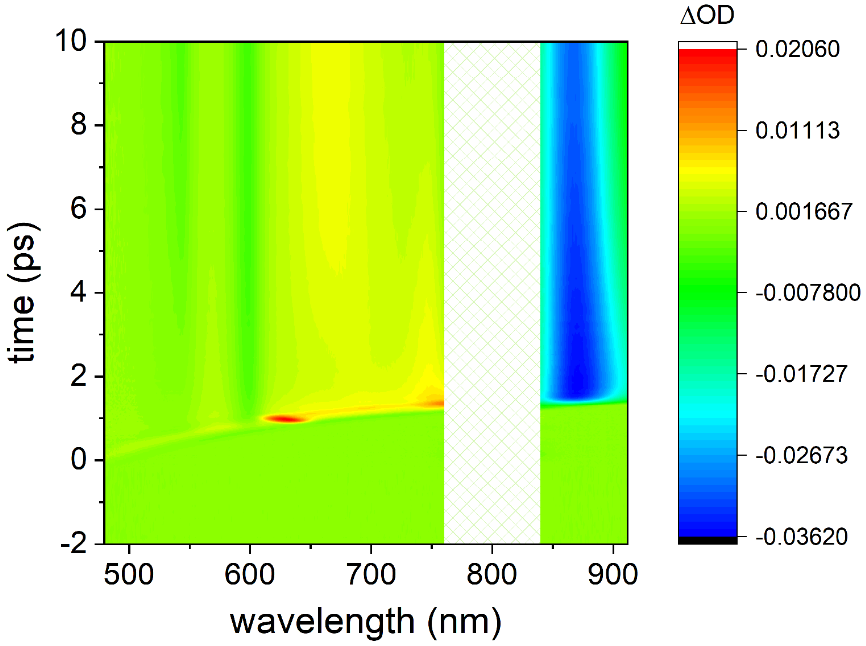

Figure 6.10 First few picoseconds of the signal from Figure 6.9 revealing the chirp effect.

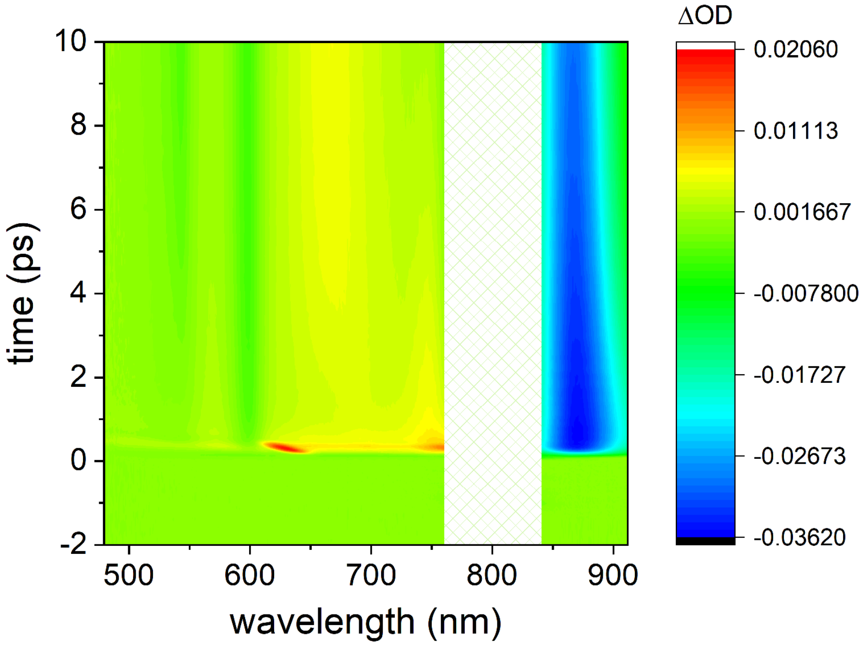

Figure 6.11 Chirp correction for data from Figure 6.10.

These corrections are typical for all TAS experiments within this time scale, however there might be more steps needed, but those are specific for the setup and method of further analysis and thus will not be described here.

Another issue worth mentioning before modelling of the data is the instrument response function (IRF) of the setup. It is by definition a response of the system to a delta function event. It defines the shortest event able to be measured using such setup. In pump-probe TAS, the time resolution is defined mainly by duration of pump and probe pulses. Therefore, it is defined by the type of the laser used (*e.g.* ~50 fs for Ti-sapphire lasers). IRF summarizes also other effects causing reduction of the time resolutions, such as precision of the delay line. Most importantly for further analysis: all the kinetics obtained during measurements are fitted with convolution of the IRF and the model decay (Figure 6.12). In TAS data analysis, IRF is usually simulated during fitting with a gaussian function.

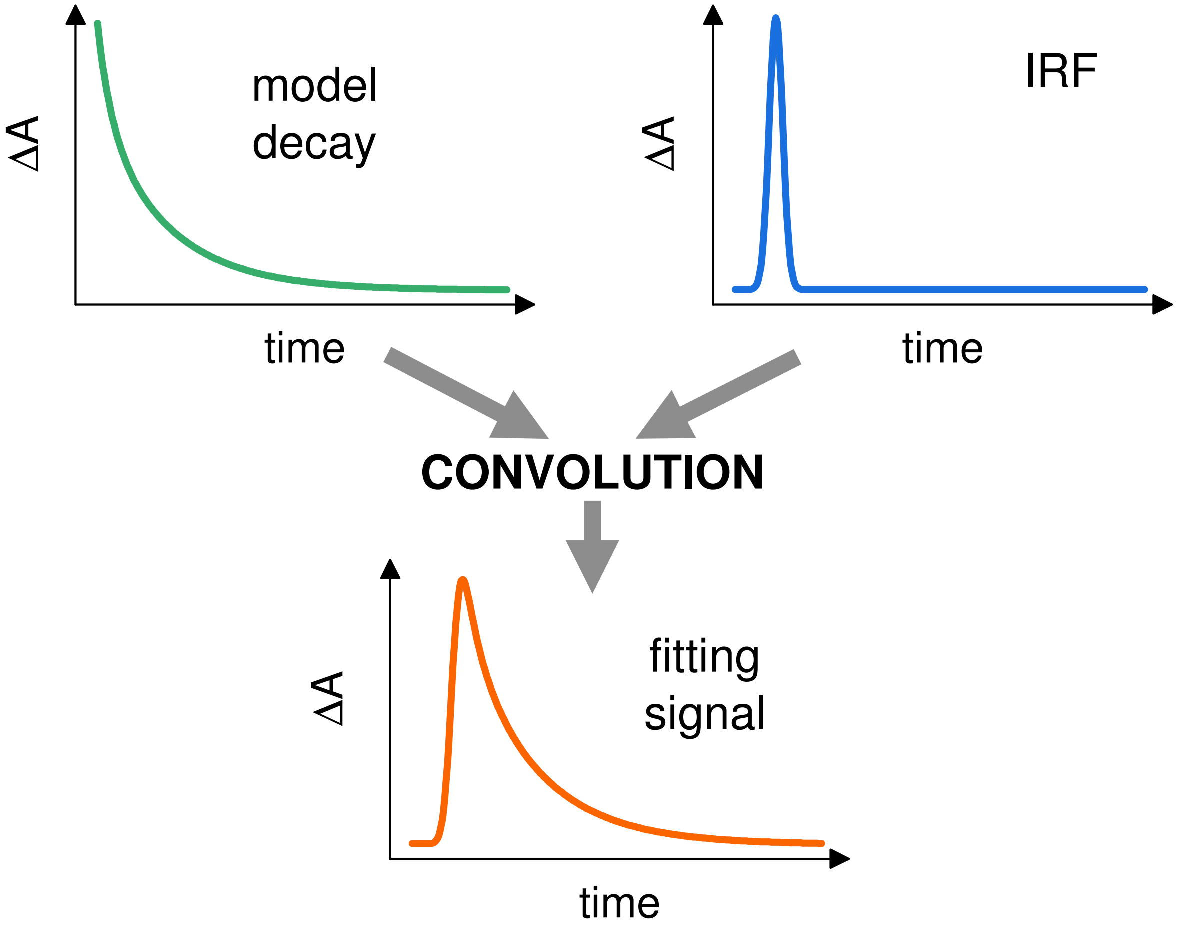

Figure 6.12 Scheme of the IRF convolution with the modelled signal decay.

When the data is already clean and IRF is known, one can approach modelling. The most common reactions observable using transient absorption spectroscopy are of the first (or pseudo-first) order, thus can be represented by an equation 6.14 with its kinetic equation and solution in 6.15 and 6.16 respectively.

$$X \rightarrow Y \tag{6.14}$$

$$\frac{d[X](t)}{dt} = -k[X](t) \tag{6.15}$$

$$[X](t) = X_0 \exp(-k\ t) \tag{6.16}$$

Where: $[X]$ – concentration of species X, t – time, k – reaction rate constant, X_0 – initial concentration of species X.

According to the Lambert-Beer law (equation 6.12), concentration of species is directly proportional to the absorbance of solution. Thus, observation of absorbance changes is a direct observation of concentration changes and one can write an equation 6.17.

$$\Delta A(\lambda, t) = A_0(\lambda) \exp(-k\ t) \tag{6.17}$$

Where: ΔA – absorbance difference, λ – wavelength, A_0 – initial absorbance difference.

However, in a real experiment, situation is hardly anytime as simple as in equation 6.17. Usually, there are multiple processes occurring simultaneously or one after another. In such situation the signal is often modelled with a sum of exponential functions (equation 6.18).

$$\Delta A(\lambda, t) = \sum_i A_i(\lambda) \exp(-k_i\ t) \tag{6.18}$$

The most straight-forward approach of modelling of TAS data is fitting of separate kinetics or integrals of kinetics over certain range of wavelengths (so-called band integrals) with equation 6.18. However, it can usually be enough only for very simple systems or for primary estimation of number of processes. More complex experimental systems need more comprehensive analysis such as *global* or *target analysis*.

Fitting of the signal with equation 6.18 for each wavelength simultaneously with shared rate constants is called *global analysis*. The exact mathematical procedure of fitting might be different in different software implementations (Glotaran,[77,78] Asufit,[79] Surface Xplorer[80]), however the resulting information is always the same: set of rate constants (or their reciprocals – lifetimes) and Decay Associated Difference Spectra (DADS; spectra of pre-exponential factors, $A_i(\lambda)$). Advantage of this fitting procedure is that one does not assume any particular model prior to fitting, however assignment of DADS and lifetimes to certain processes can be sometimes challenging.

Other approach is the *target analysis*. It is a method, which needs a *priori* assumption of the scheme of processes going on as a set of possible states (compartments/species) and transitions between them (Figure 6.13). The resulting information is a set of values of transition rate constants and Species Associated Difference Spectra (SADS), which are difference spectra of each of the species (states). Interpretation of these results is more straightforward than that of *global analysis*, however, there is a risk of making too many or wrong assumptions at the model building step. Moreover, the target analysis takes more time to perform than the global one.

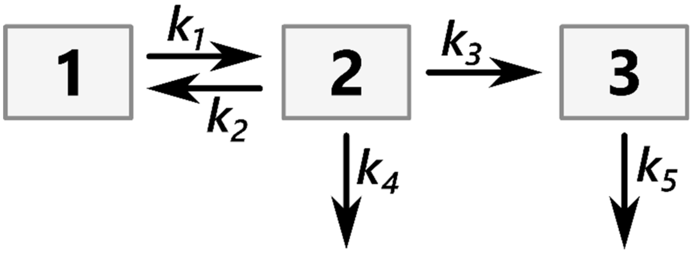

Figure 6.13 Sample compartmental model for target analysis. Arrows between compartments mean reactions of one state into another one while arrows pointing out of compartments mean decay of the state without forming another one.

However, as mentioned above, the signal from the TAS measurement includes not only kinetic data on the occurring processes, but also is convolved with the IRF. Thus, no matter which approach is used in modelling, the IRF (either measured or simulated with gaussian function) has to be convolved with the theoretical kinetics in the fitting procedure (equation 6.19).

$$\Delta A_{fit}(\lambda, t) = IRF(\lambda, t) \otimes \Delta A_{theoretical}(\lambda, t) \tag{6.19}$$

All in all, modelling of TAS data is a challenging task, which sometimes needs some external information from other types of experiments or literature, but is a powerful tool in understanding kinetics of processes within the studied system.

6.2.4 Spectroelectrochemistry

As described above, UV-vis absorption can be used to follow changes of concentration of different species in studied media. Thus, it can be also used to follow oxidation and reduction reactions at electrode surfaces. This combination of spectroscopic and electrochemical methods is called spectroelectrochemistry. In this work, spectroelectrochemistry was used for determination of the redox potentials of species immobilized on the electrode, *i.e.* redox hydrogel and primary donor in RCs.

Experimental setup

The setup, which was used for these studies was built by the author of the thesis. Its scheme is presented in Figure 6.14. The electrochemical part of the experiment was conducted using an Autolab PGSTAT204 potentiostat coupled with a specially designed 3D-printed cell (see chapter 6.3.1 for details) in a 3-electrode configuration. Spectra were measured using an Avantes halogen and deuterium combined lamp (AvaLight-DH-S-BAL) as a light source and an Avantes Hero (AvaSpec-HSC1024x58TEC-EVO) spectrometer as a detector. Light was conducted to and from the sample using multi-modal optical fibers of 200 µm diameter. The whole experiment was controlled via a PC with Autolab NOVA[69] and LabVIEW[81] communicating with each other via a virtual serial port. The whole experimental procedure was automated and a resulting data file contained absorbance difference spectra at different times with a baseline set at a first applied potential.

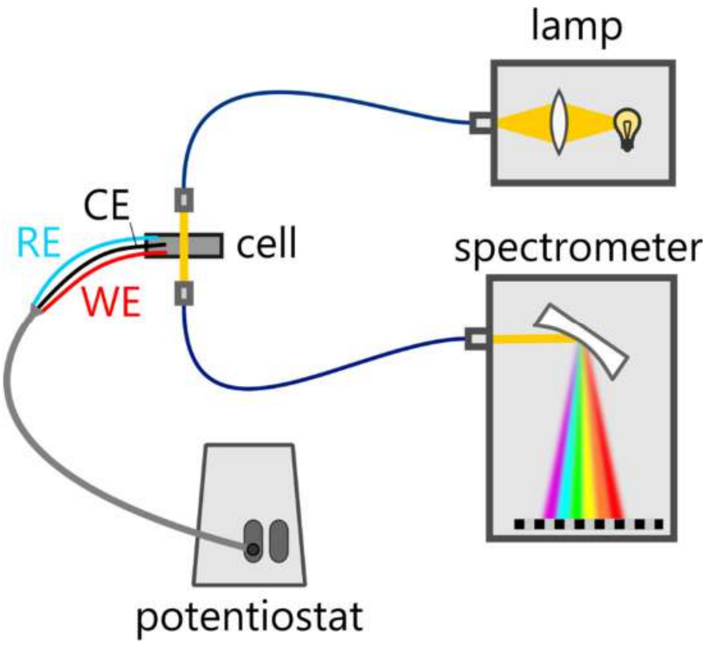

Figure 6.14 Scheme of the main idea of the steady-state UV-vis absorption spectroelectrochemical experiment. For details on the spectroscopic part of the experiment see Figure 6.6. Dark blue wires – optical fibers, grey, light blue, black and red wires – electrical cables.

There were a few main issues encountered along the preparation of the setup for measurements:

Long stabilization of the system after changing the potential

After changing the potential applied to the electrode the whole system reacts to it and it takes time to build new stationary state by *e.g.* oxidation/reduction of species in the proximity of the electrode and building the new electrical double-layer. Only after the new stationary state is achieved, the measured spectra can be taken for further analysis. In order to reduce this time, ionic strength of solution was increased by addition of 200 mM KCl. Higher ionic strength decreases the Debye length in the electrolyte, reducing also the electrical double-layer thickness, which makes it faster to form. Even after this modification, the stabilization time at each potential could not be less than 60 s.

Possible sample degradation due to the long illumination

Long illumination with high-intensity white light can cause damage to the sample, thus the light intensity passing the sample was kept low using the attenuator. In order to compensate for this, integration time for the detector was set to 200 ms and 20 spectra were averaged for each final spectrum.

Stability of the baseline

The baseline for spectral measurements was set at the first applied potential for the whole experiment. There are a few factors, which can cause the baseline to drift over the time of the experiment:

1. reduction of tensions and other small movements of optical fibers and other parts within the optical path, (it changes the speckle pattern in a multi-modal optical fiber and thus other speckles shine on the slit of the spectrometer)[82]
2. drift of the light source spectrum,
3. detachment of studied species from the electrode.

The first factor can be mitigated by usage of smaller diameter optical fibers (decreasing the light power) and/or bigger slit (reducing the spectral resolution), so that the size of the slit is not much smaller than diameter of the optical fiber, and most of the speckles get into the slit.[82] Moreover, it is important that the setup is not touched and there are no strong air flows around it during experiment. Second factor is addressed via turning on the light source at least half an hour before the start of the experiment, which is advised in the operation manual, so that it can reach its operational temperature and efficiency. Third factor can be reduced by leaving the sample immersed in solution for some time prior to experiment so that all loosely bound parts would detach then and move out of the probed area. In principle, all the changes of the baseline over time can be accounted for by additional measurements of a baseline in the middle of experiment, however it would increase the duration time significantly, thus it is done only if there are no other options.

Synchronization of spectral and electrochemical measurements

Electrochemical part of the experiment was controlled via an Autolab NOVA software[69], while the spectroscopic part with an interface prepared in LabVIEW[81]. However, both of these parts share parameters such as duration time. In order to allow communication between them, to avoid human errors in setting same parameters in both software, a virtual serial (COM) ports were set. Synchronization of time of start of experiment for spectrometer and potentiostat was achieved via TTL communication directly between them.

Data analysis

Results of the experiment are put in a 2-D array of changes of absorbance vs potential and wavelength. In general, there might be more than one species changing the redox state during experiment and might do this at different redox potential. To find the spectra of the species reacting at different applied potentials, a global analysis was performed, *i.e.* relationship at each wavelength was fitted with equation 6.20 with midpoint potentials kept constant for all wavelengths, while amplitudes were allowed to change between wavelengths (for full derivation see the supporting information of the publication[54]).

$$\Delta A(E,\lambda) = A_0(\lambda) + \sum_i \frac{A_i(\lambda)}{1+\exp\left(\frac{E_{0\_i}-E}{dE_i}\right)} \tag{6.20}$$

Where: $\Delta A(E,\lambda)$ *– absorbance difference at potential* E *and wavelength* λ, A_i *– amplitude of the* i*-th component,* E_{0_i} *– redox midpoint potential of the* i*-th component,* dE_i *– parameter describing width of the* i*-th component curve.*

6.3 3D-PRINTING

3D-printing is a kind of an additive manufacturing process which has recently gained much attention due to the high availability of cheap and high-quality printers along with a wide selection of different printing materials. Due to this, 3D-printing found its place in industry for fast prototyping and low-scale production, as well as in the hobbyists area of interest for making figurines or functional parts for personal projects. The power of 3D-printing lays also in the community around it, as the designs can be easily shared among users using dedicated platforms, such as MakerBot Thingiverse[83] or PrusaPrinters.[84]

Scientific equipment is often very expensive and not always fits the specific needs of the researcher. This is the perfect field in which 3D-printing might come in handy. The simplest parts, which could be printed for use in the laboratory are all sort of holders and mounting adapters, but the community has already shown that even so complicated and precise device as an automatic pipette[85] or a syringe pump[86] can be designed and 3D-printed.

One thing is designing and printing equipment for their own use and the other is sharing the projects. Recently, in the age of inequalities and high costs of access to the scientific results and equipment, there are different movements arising, trying to open source the science.[87,88] One of them is open source hardware, represented among others in the book *Open-Source Lab*.[89] Its aim is to create designs of hardware to be used in scientific laboratories, which can be created anywhere using relatively unexpensive or widely available technologies (such as 3D-printing). It allows scientists from developing countries or even students and hobbyists to access equipment to do research. There are even scientific journals, which focus on the open source hardware designs, such as HardwareX[90] and Journal of Open Hardware.[91] Although the commercially available equipment can be more precise and reliable, sometimes there is no other option but to build it yourself.

During work on preparation of the publications being part of this thesis multiple parts of laboratory equipment were designed and manufactured, most important of which are described in the following paragraphs.

6.3.1 Electrochemical cells

The most important parts, which I have designed and printed are the (spectro)electrochemical cells for spectro- and photoelectrochemical experiments. There are very few of these available on the market and none of them was able to meet our needs. Thus, two designs were made and are described in details below.

Big electrochemical cell

The first cell (Figure 6.15) was mainly designed to be used for photoelectrochemical measurements of electrodes based on an FTO glass with an LED illumination. The main body and the lid (black in Figure 6.15) were 3D-printed and additional acrylic glass windows were attached to the sides using bolts and nuts. For the vessel for the electrolyte, a 50x10 mm optical glass cuvette (Gallab G 21050) is used. For the counter and reference electrode any kind can be used, but cannot exceed 9.5 mm in diameter in order to fit in the cuvette. Working electrode is held in place by the alligator clip. LED is held in place between 4 threaded rods. This design main advantage is that it can use working electrodes of various size and almost any commercially available counter and reference electrodes. Moreover, if the side windows are covered with black material, the whole cell is shielded from the external light which might interfere with the experiment. However, the whole cell is bulky, which makes it difficult to put it in other experimental setups (such as spectrometers) and big volume of (sometimes precious) electrolyte is needed for experiment (>10 ml).

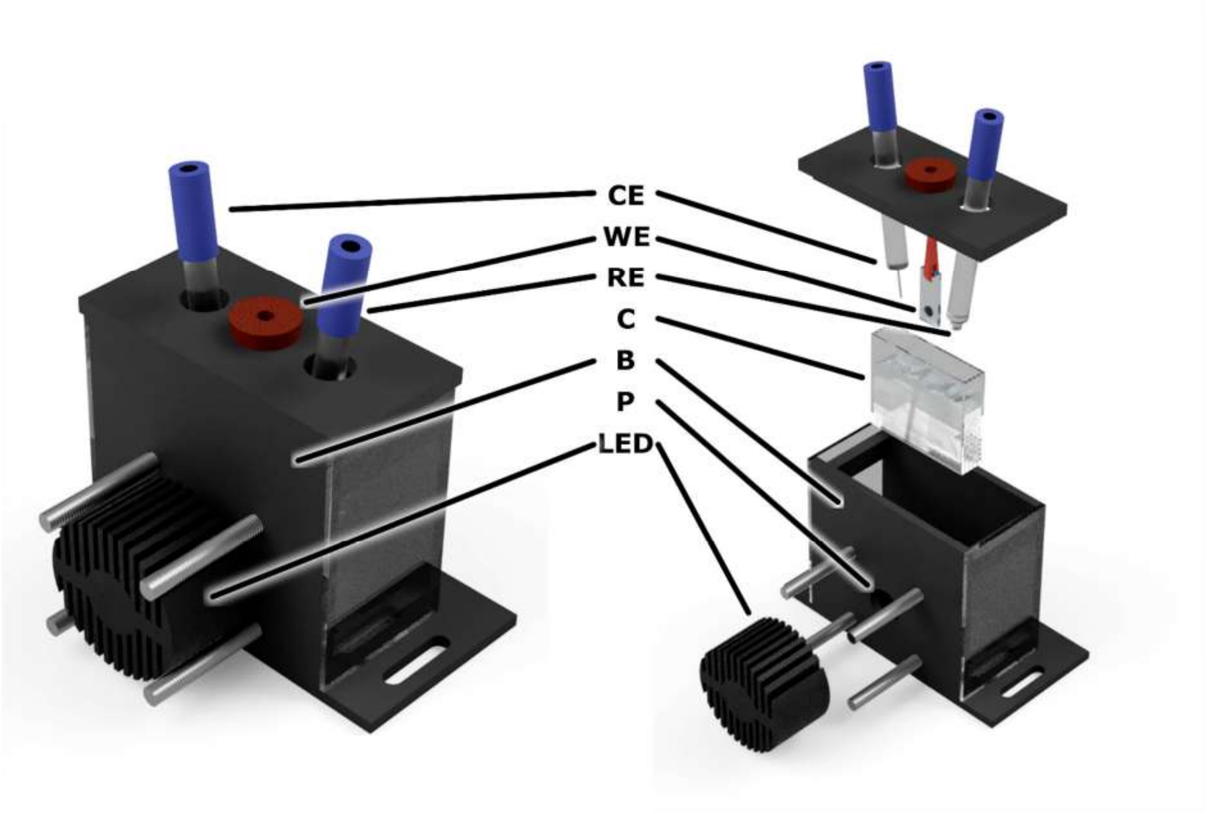

Figure 6.15 Home-build three-electrode electrochemical cell for photocurrent measurements: assembled (left) and exploded (right). WE – working electrode composed of FTO conducting glass covered with PSI multilayer; CE – Pt counter electrode; RE – Ag/AgCl reference electrode; C – cuvette filled with electrolyte; B – black-walled box; P – port for the LED illuminating the WE; LED – Light Emitting Diode with a radiator, used as an illumination source. Reproduced unchanged from ref. 92 under Creative Commons Attribution 4.0 International License.[§]

[§] http://creativecommons.org/licenses/by/4.0/

Small electrochemical cell

To perform spectroelectrochemical experiments on FTO based electrodes a smaller electrochemical cell have been designed (Figure 6.16). Most of its parts were 3D-printed, except for the gaskets, glass and bolts with nuts for assembly. It has a sandwich-like structure with main central element, where the electrolyte is placed. The electrolyte is poured from the top of the assembled cell through the holes at the bottom of the white element so that it has contact with working electrode (FTO) as well as counter and reference ones sticked from the top. This design needs the usage of a small Pt wire as a counter electrode and special, smaller reference electrode such as Ag/AgCl by ALS (012167 RE-1B). Moreover, the working electrode needs to be a square of 17x17 mm. Working electrode is connected to the proper wire of a potentiostat using a copper tape. This design allowed usage of this cell in both steady-state and time-resolved spectroelectrochemical experiments.[54,93]

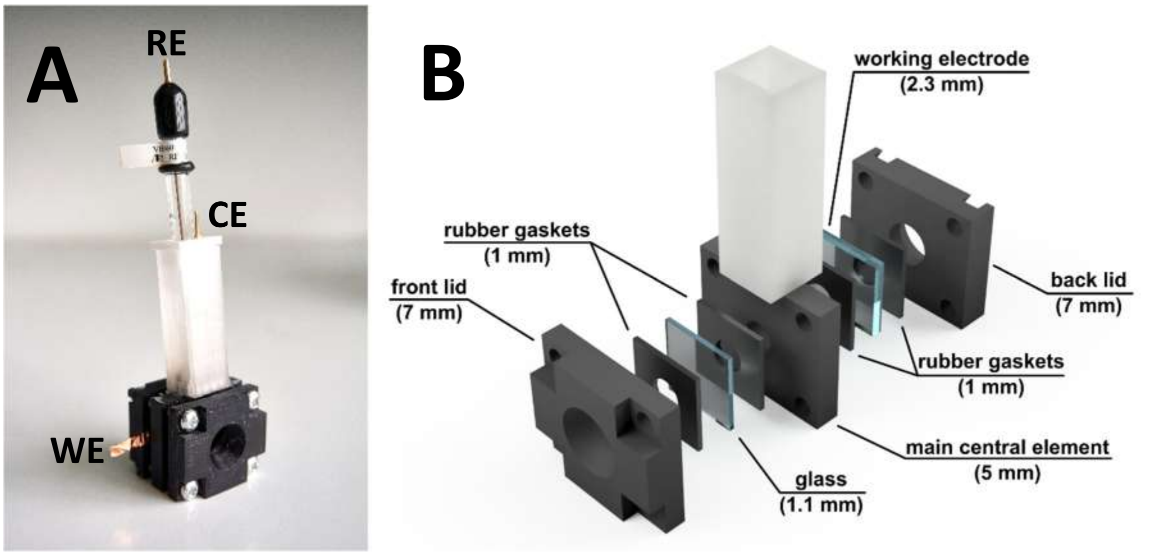

Figure 6.16 Assembled (A) and exploded (B) view of the spectroelectrochemical cell for absorption and photocurrent measurements. Dimensions in brackets in B are the thicknesses of the components. Reproduced unchanged from ref. [RB3] under Attribution-NonCommercial-NoDerivatives 4.0 International License.[**]

6.3.2 Spectroelectrochemical setup

Another big project that needed 3D-printing of certain parts was adaptation of the fiber optics Avantes spectrometer for absorption and fluorescence spectroscopy as well as spectroelectrochemistry (see Chapter 6.2.4). For this a set of adapters was needed.

First thing was a holder for cuvette with 4 ports for mounting optical fibers with collimating lenses for both absorption and florescence experiments (Figure 6.17). Thanks to the wide collar at the bottom it can be firmly attached to the optical table using a clamp.

[**] https://creativecommons.org/licenses/by-nc-nd/4.0/

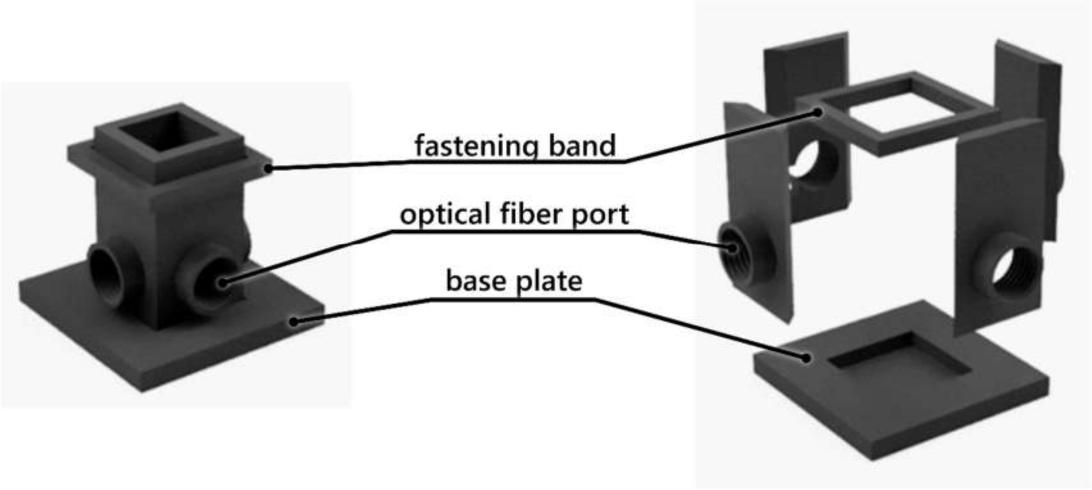

Figure 6.17 Assembled (left) and exploded (right) view of the holder for cuvette for fluorescence and absorption measurements using Avantes Hero fiber optics spectrometer.

Other part was a rail for absorption measurements (Figure 6.18), which can also be clamped to the optical table. It has two ports for optical fibers with collimating lenses creating a beam between them for the sample to be placed. The whole setup is shaped so that the small electrochemical cell from the previous chapter fits inside. It can be easily adapted to *e.g.* measure absorption of solid samples or cuvettes by designing additional holder fitting between the fiber ports. All elements can be slid along the rail keeping the light path straight.

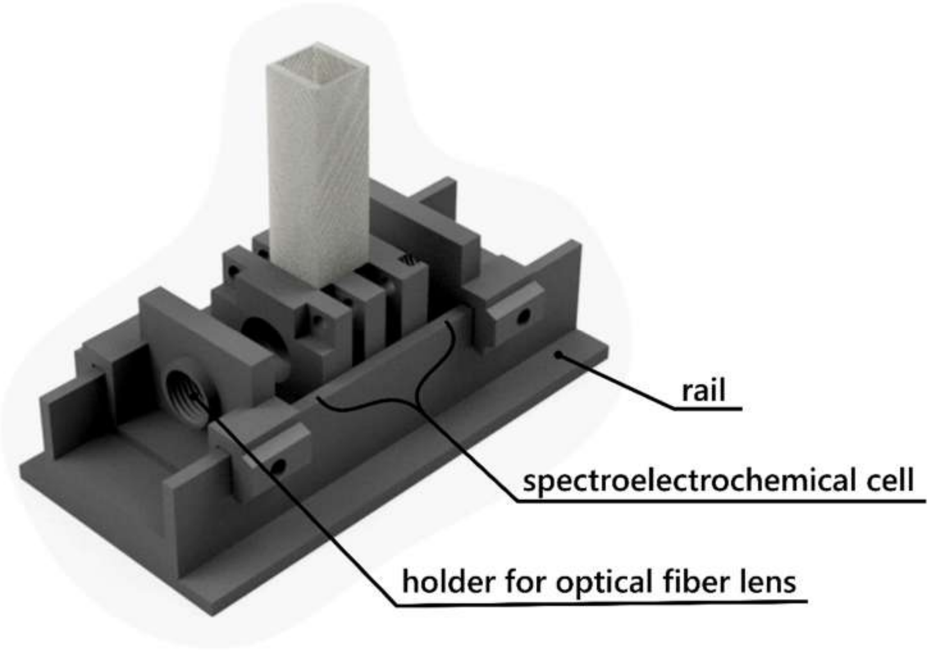

Figure 6.18 Assembled view of the full holder setup for measuring steady-state absorption spectroelectrochemistry. Note that all parts are mounted on the rail, which can also be used for mounting e.g. holder for cuvette or plates for absorption measurements.

6.3.3 3D-printing – is it valuable for science?

3D-prining is a powerful technology, but, as any, has its advantages and disadvantages. The main strong points of it are:

1. The printer and material are relatively cheap.
2. The whole process from idea to the final part is very fast (even under an hour for small parts) and does not need any sophisticated training.
3. The part produced exactly fit the needs.
4. The designs can be shared easily within the Open Hardware movement.

And the main drawbacks are:

1. There is a limited range of materials, which usually are not resistant to high temperature, chemical solvents and possess low thermal conductivity.
2. The precision is lower than for precisely machined metal opto-mechanics.
3. It usually needs self-designing of parts.
4. The prints are usually porous due to the layer-by-layer manufacturing procedure, thus the prints are not fully sealed and some residue can rest in the pores of the part after contact with liquid.

All in all, 3D-printing is a fast and reliable method of manufacturing of various scientific equipment. It can be used *ad-hoc* for creation of even one-time use holders or adapters, which for sure could be made using different methods, but probably in longer time. As shown in previous paragraphs, it has proven its usefulness in many projects. Hopefully, it will encourage scientists to open not only their results but also the unique equipment they design.

7 COMMENTS ON THE PUBLICATIONS

The proper design of biohybrid devices needs a comprehensive knowledge of structural and functional features of all the components. Thus, the topics of the publications included in this thesis span from the fundamental studies on the recombination processes within RCs,[RB1] through modelling of operation of cells based on TiO_2,[RB2] to spectroelectrochemical characterization of interaction between RCs and redox active hydrogel.[RB3-4] The full text of publications along with their supplementary information is placed after the reference list.

[RB1] WEAK TEMPERATURE DEPENDENCE OF $P^+H_A^-$ RECOMBINATION IN MUTANT *RHODOBACTER SPHAEROIDES* REACTION CENTERS

Recombination processes (both intra- and extraprotein) are known to be one of the factors limiting efficiency of the biohybrid devices.[10] As described in the 3.2.2 chapter, there are multiple of those occurring inside *Rba. sphaeroides* RCs. In this publication the focus is on the recombination of the $P^+H_A^-$ state, which was modelled with a multiexponential decay. There were proteins from three different genetically engineered strains with single-point mutations measured (ELL, YLH and GML). This complexity of the recombination is explained by the influence of the protein dynamics.

The main observations and conclusions of the publication include:

1. The $P^+H_A^-$ recombination dynamics in investigated genetically engineered RCs was only weakly dependent on temperature.
2. The protein dynamics model proposed in earlier work[31] was successfully applied to a new set of genetically engineered RCs.
3. There are three factors influencing the $P^+H_A^-$ recombination dynamics:
    a. the initial free energy gap between $P^+B_A^-$ and $P^+H_A^-$ states,
    b. the intrinsic rate of $P^+B_A^- \rightarrow PB_A$ charge recombination
    c. the dynamics of the protein relaxation in response to the charge separated states.
4. The RCs of the ELL mutant are characterized with the relatively fast charge recombination, which is caused mainly by the small initial free energy gap between $P^+B_A^-$ and $P^+H_A^-$ states, while in the RCs of the GML mutant the relatively slow charge recombination is caused by large value of this energy gap.
5. The RCs of the YLH mutant are characterized by similar average decay lifetime to that of wild-type RCs, though the $(P^+B_A^-/P^+H_A^-) \rightarrow PB_A$ charge recombination is relatively fast, as it is compensated for by an increased efficiency of protein relaxation.

[RB2] MODELLING OF THE CATHODIC AND ANODIC PHOTOCURRENTS FROM *RHODOBACTER SPHAEROIDES* REACTION CENTRES IMMOBILIZED ON TITANIUM DIOXIDE

Complexity of the biohybrid devices makes it difficult to understand all the processes underlying the experimental results. Thus, there is a need for preparation of mathematical models. In this publication the focus is on explanation of the shape of the photocurrent traces in the system with RCs immobilized on a mesoporous TiO_2 layer. Work on this publication allowed realization that there are multiple thermodynamic and kinetic parameters, needed for modelling, which were not reported in literature yet and even those reported were not measured *in situ* but rather in separated RCs or TiO_2. Moreover, system with TiO_2 seems to be complicated for modelling due to different formalisms needed for strict description of TiO_2 (semiconductor, solid state physics) and RCs (physical chemistry, electrochemistry).

The main observations and conclusions of the publication include:

1. Proposed construction yielded photocurrents of up to 300 nA cm^{-2} and Internal Quantum Efficiencies of up to 1.5×10^{-3} %.
2. The proposed model assumed three parallel sources of photocurrent:
   a. injection of electrons to the electrode from the triplet state of the primary donor P_{870} (anodic current)
   b. reduction of the oxidized primary donor by TiO_2 (cathodic current)
   c. oxidation/reduction of TMPD/$TMPD^+$ by the FTO glass substrate (cathodic and anodic peaks).
3. Relatively low net photocurrent arises from similar values of anodic and cathodic contributions.
4. There were two alternative versions of the model proposed:
   a. RMIL (RC-mediator interface limited), in which the electron transfer between protein and TMPD is inefficient, and thus a limiting step,
   b. IP (inactive pool), in which only 10% of RCs achieve charge separation between TiO_2 and 90 % only dissipate absorbed energy.
5. There is no one distinct parameter, whose change could improve the photocurrent in the studied design. To do so, one would need to suppress one of the sources of the current (anodic or cathodic) and improve the other.

[RB3] *IN SITU* SPECTROELECTROCHEMICAL INVESTIGATION OF A BIOPHOTOELECTRODE BASED ON PHOTOREACTION CENTERS EMBEDDED IN A REDOX HYDROGEL

After problems with working with TiO_2 the focus was put on the system with Os-complex based polymers, which promised higher efficiencies and easier understanding due to the same formalism used for description of RCs and polymers. One of the important thermodynamic parameters of the electrochemical system is redox potential of a species, which defines its ability to either give or accept electrons. It is important as all the components should be properly paired in terms of redox potentials to maintain an efficient electron transfer chain. In this publication a novel, *in situ*, steady-state spectroelectrochemical method for redox potential determination was described.

The main observations and conclusions of the publication include:

1. Internal quantum efficiency of the hydrogel-RCs biohybrid electrode is equal to $50 \pm 12\ \%$.
2. RCs remain functionally intact in the hydrogel matrix.
3. Application of potential to the studied electrode causes changes of absorbance, which can be attributed to change of the redox state of both redox centers in the hydrogel and the primary donor of RCs.
4. Midpoint redox potential of the primary donor in RCs is shifted towards more positive potential than that measured in solution and reported in literature. It shows an importance of *in situ* measurements for determination of system parameters.

[RB4] INSIGHT IN THE ELECTRON TRANSFER FROM REDOX POLYMERS TO A PHOTOACTIVE PROTEIN

After successful steady-state *in situ* spectroelectrochemical experiment on RCs-hydrogel hybrid,[RB3] there was a temptation to try it with time-resolved spectroscopy. Unfortunately, the attempts to perform *in situ* TAS experiments were unsuccessful, but experiments carried out in solutions with elements of the system (RCs, polymer and quinone) allowed determination of rate constants of electron transfer between them after excitation. These results explain partially why this biohybrid system is characterized by relatively high Internal Quantum Efficiency.

The main observations and conclusions of the publication include:

1. Os-complex-based polymer is able to efficiently reduce the primary donor of RCs.
2. The observed electron transfer is described by a three-exponential model and the lifetimes of electron transfer lay within the range between a few microseconds to millisecond.
3. Microsecond lifetime is comparable to that occurring in nature between the primary donor and cyt c_2.
4. All lifetimes are much shorter than the intrinsic recombination lifetime of $P_{870}^{+}Q_{A/B}^{-}$ by at least 2 orders of magnitude, which is one of the reasons of high internal quantum efficiency of the biohybrid electrode presented in the previous publication.[RB3]
5. Dependence of electron transfer lifetimes on concentration of both polymer and RCs suggests formation of aggregates based on electrostatic interaction.

8 SUMMARY

It was shown, that the dynamics of protein scaffold response to the charge being transported through it is important for the back electron transfer kinetics. This reminds that biological systems are not rigid structures and undergo many internal movements, which need to be taken under consideration during designing of biohybrid devices. Moreover, all extraprotein interactions (such as immobilization on the electrode surface) may lead to change of protein scaffold structure, effectively changing the kinetics of the electron transfer chain inside.

Each of biohybrid designs needs specific approach in theoretical analysis. In this thesis a model for RCs immobilized within TiO_2 mesoporous layer was proposed. It showed, that there are competing processes occurring and the way to improve efficiency of this design would be to suppress processes responsible for one direction of current while optimizing the other direction. It also showed that there is a lack of literature information on many important thermodynamic and kinetic parameters of elements of the system.

High internal quantum efficiency (50 ± 12 %) of the system with RCs embedded in the redox-active hydrogel matrix encouraged more comprehensive spectroscopic analysis of it. Steady-state spectroelectrochemical experiments allowed determination of a value of a redox potential of the primary donor P_{870} in RCs and showed that it is shifted towards more positive potential in operational electrode than the values reported for isolated RCs in solution. Subsequently, time-resolved experiments provided information about interaction of proteins with redox centers in polymer. It showed that polymer is able to reduce primary donor of RCs even in solubilized form and it occurs at a time scale between a few microseconds and a millisecond. The fastest lifetimes of this process are similar to that of natural reduction of the primary donor by cyt c_2.

To summarize, biohybrid devices are very complex systems with many factors influencing their photocurrent generation. It is very important to fully understand their operational principles in order to properly optimize their design and find inspirations for other types of devices. To do so, meticulous work has to be carried out on determination of structural, thermodynamic and kinetic parameters of the system. Publications presented in this thesis along with those presented by various research groups contribute to the general picture which is still getting clearer.

LIST OF REFERENCES

1 BP p.l.c. *bp Statistical Review of World Energy 2020*. London; 2020. URL: https://www.bp.com/content/dam/bp/business-sites/en/global/corporate/pdfs/energy-economics/statistical-review/bp-stats-review-2020-full-report.pdf.

2 Departmenf of Economic and Social Affairs United Nations. *2019 Revision of World Population Prospects*. 2019. URL: https://population.un.org/wpp/ (Accessed 8 November 2020).

3 Wraight CA, Clayton RK. The absolute quantum efficiency of bacteriochlorophyll photooxidation in reaction centres of Rhodopseudomonas spheroides. *Biochim Biophys Acta - Bioenerg* 1974;**333**:246–60. https://doi.org/10.1016/0005-2728(74)90009-7.

4 Janzen AF, Seibert M. Photoelectrochemical conversion using reaction-centre electrodes. *Nature* 1980;**286**:584–5. https://doi.org/10.1038/286584a0.

5 Drachev LA, Kondrashin AA, Samuilov VD, Skulachev VP. Generation of electric potential by reaction center complexes from Rhodospirillum rubrum. *FEBS Lett* 1975;**50**:219–22. https://doi.org/10.1016/0014-5793(75)80492-3.

6 Gross EL, Youngman DR, Winemiller SL. An FMN-Photosystem I Potovoltaic Cell. *Photochem Photobiol* 1978;**28**:249–56. https://doi.org/10.1111/j.1751-1097.1978.tb07703.x.

7 Kornienko N, Zhang JZ, Sakimoto KK, Yang P, Reisner E. Interfacing nature's catalytic machinery with synthetic materials for semi-artificial photosynthesis. *Nat Nanotechnol* 2018;**13**:890–9. https://doi.org/10.1038/s41565-018-0251-7.

8 Ravi SK, Tan SC. Progress and perspectives in exploiting photosynthetic biomolecules for solar energy harnessing. *Energy Environ Sci* 2015;**8**:2551–73. https://doi.org/10.1039/C5EE01361E.

9 Friebe VM, Frese RN. Photosynthetic reaction center-based biophotovoltaics. *Curr Opin Electrochem* 2017;**5**:126–34. https://doi.org/10.1016/j.coelec.2017.08.001.

10 Musazade E, Voloshin R, Brady N, Mondal J, Atashova S, Zharmukhamedov SK, *et al.* Biohybrid solar cells: Fundamentals, progress, and challenges. *J Photochem Photobiol C Photochem Rev* 2018;**35**:134–56. https://doi.org/10.1016/j.jphotochemrev.2018.04.001.

11 Blankenship RE, Madigan MT, Bauer CE, editors. *Anoxygenic Photosynthetic Bacteria*. Dordrecht: Kluwer Academic Publishers; 1995.

12 Blankenship RE. *Molecular Mechanisms of Photosynthesis*. Oxford, UK: Blackwell Science Ltd; 2002.

13 Hunter CN, Daldal F, Thurnauer MC, Beatty JT, editors. *The Purple Phototrophic Bacteria*. vol. 28. Dordrecht: Springer Netherlands; 2009.

14 Woodbury NW, Allen JP. The Pathway, Kinetics and Thermodynamics of Electron Transfer in Wild Type and Mutant Reaction Centers of Purple Nonsulfur Bacteria. In: Blankenship RE, Madigan M, Bauer CE, editors. *Anoxygenic Photosynth. Bact.* Dordrecht: Kluwer Academic Publishers; 1995. p. 527–57.

15 Lukashev EP, Nadtochenko VA, Permenova EP, Sarkisov OM, Rubin AB. Electron phototransfer between photosynthetic reaction centers of the bacteria Rhodobacter sphaeroides and semiconductor mesoporous TiO_2 films. *Dokl Biochem Biophys* 2007;**415**:211–6. https://doi.org/10.1134/S1607672907040138.

16 Mershin A, Matsumoto K, Kaiser L, Yu D, Vaughn M, Nazeeruddin MK, *et al.* Self-assembled

photosystem-I biophotovoltaics on nanostructured TiO_2 and ZnO. *Sci Rep* 2012;**2**:234. https://doi.org/10.1038/srep00234.

17 Kothe T, Pöller S, Zhao F, Fortgang P, Rögner M, Schuhmann W, *et al.* Engineered Electron-Transfer Chain in Photosystem 1 Based Photocathodes Outperforms Electron-Transfer Rates in Natural Photosynthesis. *Chem - A Eur J* 2014;**20**:11029–34. https://doi.org/10.1002/chem.201402585.

18 Badura A, Guschin D, Esper B, Kothe T, Neugebauer S, Schuhmann W, *et al.* Photo-Induced Electron Transfer Between Photosystem 2 via Cross-linked Redox Hydrogels. *Electroanalysis* 2008;**20**:1043–7. https://doi.org/10.1002/elan.200804191.

19 Sokol KP, Robinson WE, Warnan J, Kornienko N, Nowaczyk MM, Ruff A, *et al.* Bias-free photoelectrochemical water splitting with photosystem II on a dye-sensitized photoanode wired to hydrogenase. *Nat Energy* 2018;**3**:944–51. https://doi.org/10.1038/s41560-018-0232-y.

20 Sokol KP, Mersch D, Hartmann V, Zhang JZ, Nowaczyk MM, Rögner M, *et al.* Rational wiring of photosystem II to hierarchical indium tin oxide electrodes using redox polymers. *Energy Environ Sci* 2016;**9**:3698–709. https://doi.org/10.1039/C6EE01363E.

21 Verméglio A, Joliot P. The photosynthetic apparatus of Rhodobacter sphaeroides. *Trends Microbiol* 1999;**7**:435–40. https://doi.org/10.1016/S0966-842X(99)01625-X.

22 Ermler U, Fritzsch G, Buchanan SK, Michel H. Structure of the photosynthetic reaction centre from Rhodobacter sphaeroides at 2.65 å resolution: cofactors and protein-cofactor interactions. *Structure* 1994;**2**:925–36. https://doi.org/10.1016/S0969-2126(94)00094-8.

23 Mandal S, Carey A-M, Locsin J, Gao B-R, Williams JC, Allen JP, *et al.* Mechanism of Triplet Energy Transfer in Photosynthetic Bacterial Reaction Centers. *J Phys Chem B* 2017:acs.jpcb.7b03373. https://doi.org/10.1021/acs.jpcb.7b03373.

24 Angerhofer A. Electron Magnetic Resonance of Carotenoids. In: Frank HA, Young AJ, Britton G, Cogdell RJ, editors. *Photochem. Carotenoids*. Dordrecht: Kluwer Academic Publishers; 1999. p. 203–22.

25 Angerhofer A, Bornhäuser F, Aust V, Hartwich G, Scheer H. Triplet energy transfer in bacterial photosynthetic reaction centres. *Biochim Biophys Acta - Bioenerg* 1998;**1365**:404–20. https://doi.org/10.1016/S0005-2728(98)00093-0.

26 Volk M, Ogrodnik A, Michel-Beyerle M-E. The Recombination Dynamics of the Radical Pair P+H− in External Magnetic and Electric Fields. In: Blankenship RE, Madigan M, Bauer C, editors. *Anoxygenic Photosynth. Bact.* Dordrecht: Kluwer Academic Publishers; 1995. p. 595–626.

27 Uchoa AF, Knox PP, Turchielle R, Seifullina NK, Baptista MS. Singlet oxygen generation in the reaction centers of Rhodobacter sphaeroides. *Eur Biophys J* 2008;**37**:843–50. https://doi.org/10.1007/s00249-008-0287-y.

28 Woodbury NWT, Allen JP. Electron transfer in purple non-sulfur bacteria. In: Blankenship RE, Madigan MT, Bauer CE, editors. *Anoxygenic Photosynth. Bact.* Dordrecht: Kluwer Academic Publishers; 1995. p. 527–57.

29 Okamura MY, Feher G. Proton-Coupled Electron Transfer Reactions of QB in Reaction Centers from Photosynthetic Bacteria. In: Blankenship RE, Madigan M, Bauer C, editors. *Anoxygenic Photosynth. Bact.* Dordrecht: Kluwer Academic Publishers; 1995. p. 577–93.

30 Jones MR. Structural Plasticity of Reaction Centers from Purple Bacteria. In: Hunter CN, Daldal F, Thurnauer MC, Beatty JT, editors. *Purple Phototrophic Bact.* Springer Netherlands; 2009. p. 295–321.

31 Gibasiewicz K, Pajzderska M, Dobek A, Karolczak J, Burdziński G, Brettel K, *et al.* Analysis of the temperature-dependence of P+HA− charge recombination in the Rhodobacter sphaeroides reaction center suggests nanosecond temperature-independent protein relaxation. *Phys Chem Chem Phys* 2013;**15**:16321. https://doi.org/10.1039/c3cp44187c.

32 Shukla AK, Sudhakar K, Baredar P. A comprehensive review on design of building integrated photovoltaic system. *Energy Build* 2016;**128**:99–110. https://doi.org/10.1016/j.enbuild.2016.06.077.

33 National Renewable Energy Laboratory. *Best Research-Cell Efficiency Chart*. 2020. URL: https://www.nrel.gov/pv/cell-efficiency.html (Accessed 10 September 2020).

34 Haehnel W, Heupel A, Hengstermann D. Investigations on a Galvanic Cell Driven by Photosynthetic Electron Transport. *Zeitschrift Für Naturforsch C* 1978;**33**:392–401. https://doi.org/10.1515/znc-1978-5-614.

35 Plumeré N, Nowaczyk MM. Biophotoelectrochemistry of Photosynthetic Proteins. *Adv. Biochem. Eng. Biotechnol.*, vol. 123. 2016. p. 127–41.

36 Milano F, Punzi A, Ragni R, Trotta M, Farinola GM. Photonics and Optoelectronics with Bacteria: Making Materials from Photosynthetic Microorganisms. *Adv Funct Mater* 2019;**29**:1–17. https://doi.org/10.1002/adfm.201805521.

37 Ravi SK, Udayagiri VS, Suresh L, Tan SC. Emerging Role of the Band-Structure Approach in Biohybrid Photovoltaics: A Path Beyond Bioelectrochemistry. *Adv Funct Mater* 2018;**28**:1–18. https://doi.org/10.1002/adfm.201705305.

38 Nagy LL, Hajdu K, Fisher B, Hernadi K, Nagy K, Vincze J. Photosynthetic reaction centres-from basic research to application possibilities. *Not Sci Biol* 2010;**2**:7–13.

39 Jeuken LJC, editor. *Biophotoelectrochemistry: From Bioelectrochemistry to Biophotovoltaics*. vol. 158. Cham: Springer International Publishing; 2016.

40 Tan SC, Crouch LI, Jones MR, Welland M. Generation of Alternating Current in Response to Discontinuous Illumination by Photoelectrochemical Cells Based on Photosynthetic Proteins. *Angew Chemie Int Ed* 2012;**51**:6667–71. https://doi.org/10.1002/anie.201200466.

41 Tan SC, Crouch LI, Mahajan S, Jones MR, Welland ME. Increasing the Open-Circuit Voltage of Photoprotein-Based Photoelectrochemical Cells by Manipulation of the Vacuum Potential of the Electrolytes. *ACS Nano* 2012;**6**:9103–9. https://doi.org/10.1021/nn303333e.

42 Ravi SK, Yu Z, Swainsbury DJKK, Ouyang J, Jones MR, Tan SC. Enhanced Output from Biohybrid Photoelectrochemical Transparent Tandem Cells Integrating Photosynthetic Proteins Genetically Modified for Expanded Solar Energy Harvesting. *Adv Energy Mater* 2017;**7**:1601821. https://doi.org/10.1002/aenm.201601821.

43 Milano F, Ciriaco F, Trotta M, Chirizzi D, De Leo V, Agostiano A, *et al.* Design and modelling of a photo-electrochemical transduction system based on solubilized photosynthetic reaction centres. *Electrochim Acta* 2019;**293**:105–15. https://doi.org/10.1016/j.electacta.2018.09.198.

44 Hagfeldt A, Boschloo G, Sun L, Kloo L, Pettersson H. Dye-Sensitized Solar Cells. *Chem Rev* 2010;**110**:6595–663. https://doi.org/10.1021/cr900356p.

45 Grätzel M. Dye-sensitized solar cells. *J Photochem Photobiol C Photochem Rev* 2003;**4**:145–53.

https://doi.org/10.1016/S1389-5567(03)00026-1.

46 O'Regan B, Grätzel M. A low-cost, high-efficiency solar cell based on dye-sensitized colloidal TiO_2 films. *Nature* 1991;**353**:737–40. https://doi.org/10.1038/353737a0.

47 Lu Y, Liu Y, Xu J, Xu C, Liu B, Kong J. Bio-nanocomposite Photoelectrode Composed of the Bacteria Photosynthetic Reaction Center Entrapped on a Nanocrystalline TiO_2 Matrix. *Sensors* 2005;**5**:258–65. https://doi.org/10.3390/s5040258.

48 Simmerman RF, Zhu T, Baker DR, Wang L, Mishra SR, Lundgren CA, *et al.* Engineering Photosystem I Complexes with Metal Oxide Binding Peptides for Bioelectronic Applications. *Bioconjug Chem* 2015;**26**:2097–105. https://doi.org/10.1021/acs.bioconjchem.5b00374.

49 Yu D, Wang M, Zhu G, Ge B, Liu S, Huang F. Enhanced photocurrent production by bio-dyes of photosynthetic macromolecules on designed TiO_2 film. *Sci Rep* 2015;**5**:9375. https://doi.org/10.1038/srep09375.

50 Mersch D, Lee CY, Zhang JZ, Brinkert K, Fontecilla-Camps JC, Rutherford AW, *et al.* Wiring of Photosystem II to Hydrogenase for Photoelectrochemical Water Splitting. *J Am Chem Soc* 2015;**137**:8541–9. https://doi.org/10.1021/jacs.5b03737.

51 Hartmann V, Kothe T, Pöller S, El-Mohsnawy E, Nowaczyk MM, Plumeré N, *et al.* Redox hydrogels with adjusted redox potential for improved efficiency in Z-scheme inspired biophotovoltaic cells. *Phys Chem Chem Phys* 2014;**16**:11936–41. https://doi.org/10.1039/C4CP00380B.

52 Badura A, Guschin D, Kothe T, Kopczak MJ, Schuhmann W, Rögner M. Photocurrent generation by photosystem 1 integrated in crosslinked redox hydrogels. *Energy Environ Sci* 2011;**4**:2435. https://doi.org/10.1039/c1ee01126j.

53 Kothe T, Plumeré N, Badura A, Nowaczyk MM, Guschin DA, Rögner M, *et al.* Combination of A Photosystem 1-Based Photocathode and a Photosystem 2-Based Photoanode to a Z-Scheme Mimic for Biophotovoltaic Applications. *Angew Chemie Int Ed* 2013;**52**:14233–6. https://doi.org/10.1002/anie.201303671.

54 Białek R, Friebe V, Ruff A, Jones MR, Frese R, Gibasiewicz K. In situ spectroelectrochemical investigation of a biophotoelectrode based on photoreaction centers embedded in a redox hydrogel. *Electrochim Acta* 2020;**330**:135190. https://doi.org/10.1016/j.electacta.2019.135190.

55 Gizzie E a., Scott Niezgoda J, Robinson MT, Harris AG, Kane Jennings G, Rosenthal SJ, *et al.* Photosystem I-polyaniline/TiO_2 solid-state solar cells: simple devices for biohybrid solar energy conversion. *Energy Environ Sci* 2015;**8**:3572–6. https://doi.org/10.1039/C5EE03008K.

56 Gordiichuk PI, Wetzelaer GJAH, Rimmerman D, Gruszka A, De Vries JW, Saller M, *et al.* Solid-state biophotovoltaic cells containing photosystem i. *Adv Mater* 2014;**26**:4863–9. https://doi.org/10.1002/adma.201401135.

57 Ravi SK, Swainsbury DJK, Singh VK, Ngeow YK, Jones MR, Tan SC. A Mechanoresponsive Phase-Changing Electrolyte Enables Fabrication of High-Output Solid-State Photobioelectrochemical Devices from Pigment-Protein Multilayers. *Adv Mater* 2017;**1704073**:1704073. https://doi.org/10.1002/adma.201704073.

58 Kornienko N, Ly KH, Robinson WE, Heidary N, Zhang JZ, Reisner E. Advancing Techniques for Investigating the Enzyme–Electrode Interface. *Acc Chem Res* 2019;**52**:1439–48. https://doi.org/10.1021/acs.accounts.9b00087.

59 Zhang JZ, Reisner E. Advancing photosystem II photoelectrochemistry for semi-artificial photosynthesis. *Nat Rev Chem* 2020;**4**:6–21. https://doi.org/10.1038/s41570-019-0149-4.

60 Buesen D, Hoefer T, Zhang H, Plumeré N. A kinetic model for redox-active film based biophotoelectrodes. *Faraday Discuss* 2019;**215**:39–53. https://doi.org/10.1039/c8fd00168e.

61 Białek R, Swainsbury DJK, Wiesner M, Jones MR, Gibasiewicz K. Modelling of the cathodic and anodic photocurrents from Rhodobacter sphaeroides reaction centres immobilized on titanium dioxide. *Photosynth Res* 2018;**138**:103–14. https://doi.org/10.1007/s11120-018-0550-8.

62 Woronowicz K, Ahmed S, Biradar AA, Biradar A V, Birnie DP, Asefa T, *et al.* Near-IR absorbing solar cell sensitized with bacterial photosynthetic membranes. *Photochem Photobiol* 2012;**88**:1467–72. https://doi.org/10.1111/j.1751-1097.2012.01190.x.

63 Ito S, Chen P, Comte P, Nazeeruddin MK, Liska P, Péchy P, *et al.* Fabrication of screen-printing pastes from TiO_2 powders for dye-sensitised solar cells. *Prog Photovoltaics Res Appl* 2007;**15**:603–12. https://doi.org/10.1002/pip.768.

64 Ahmadi S, Asim N, Alghoul MA, Hammadi FY, Saeedfar K, Ludin NA, *et al.* The role of physical techniques on the preparation of photoanodes for dye sensitized solar cells. *Int J Photoenergy* 2014;**2014**:. https://doi.org/10.1155/2014/198734.

65 Sommeling PM, O'Regan BC, Haswell RR, Smit HJP, Bakker NJ, Smits JJT, *et al.* Influence of a $TiCl_4$ Post-Treatment on Nanocrystalline TiO_2 Films in Dye-Sensitized Solar Cells. *J Phys Chem B* 2006;**110**:19191–7. https://doi.org/10.1021/jp061346k.

66 Yates NDJ, Fascione MA, Parkin A. Methodologies for “Wiring” Redox Proteins/Enzymes to Electrode Surfaces. *Chem - A Eur J* 2018;**24**:12164–82. https://doi.org/10.1002/chem.201800750.

67 Atkins PW, de Paula J. *Chemia fizyczna*. 2nd ed. Warszawa; 2015.

68 Bard AJ, Faulkner LR. *Electrochemical Methods: Fundamentals and Applications*. 2nd editio. Wiley; 2001.

69 Autolab. *NOVA Software*. n.d. URL: https://metrohm-autolab.com/Products/Echem/Software/Nova.html (Accessed 10 November 2020).

70 Brownson DAC, Banks CE. Interpreting Electrochemistry. *Handb. Graphene Electrochem.* London: Springer London; 2014. p. 23–77.

71 Zoski CG, editor. *Handbook of Electrochemistry*. Elsevier; 2007.

72 Compton RG, Banks CE. *Understanding Voltammetry*. IMPERIAL COLLEGE PRESS; 2010.

73 Holze R. *Experimental Electrochemistry: A Laboratory Textbook*. 2nd editio. Wiley-VCH Verlag GmbH & Co. KGaA; 2019.

74 Elgrishi N, Rountree KJ, McCarthy BD, Rountree ES, Eisenhart TT, Dempsey JL. A Practical Beginner's Guide to Cyclic Voltammetry. *J Chem Educ* 2018;**95**:197–206. https://doi.org/10.1021/acs.jchemed.7b00361.

75 Lakowicz JR. *Principles of Fluorescence Spectroscopy*. 3rd ed. Boston, MA: Springer US; 2006.

76 Ruckebusch C, Sliwa M, Pernot P, de Juan A, Tauler R. Comprehensive data analysis of femtosecond transient absorption spectra: A review. *J Photochem Photobiol C Photochem Rev* 2012;**13**:1–27. https://doi.org/10.1016/j.jphotochemrev.2011.10.002.

77 Snellenburg JJ, Laptenok S, Seger R, Mullen KM, van Stokkum IHM. *Glotaran*. 2015. URL: https://glotaran.org (Accessed 8 November 2020).

78 Snellenburg JJ, Laptenok SP, Seger R, Mullen KM, van Stokkum IHM. Glotaran : A Java-based graphical user interface for the R package TIMP. *J Stat Softw* 2012;**49**:1–2. https://doi.org/10.18637/jss.v049.i03.

79 Katilius E, Arizona State University. *Asufit*. 2002. URL: http://www.public.asu.edu/~laserweb/asufit/asufit.html (Accessed 8 November 2020).

80 Ultrafast Systems. *Surface Xplorer. Data Analysis Software*. 2019. URL: https://ultrafastsystems.com/surface-xplorer-data-analysis-software/ (Accessed 8 November 2020).

81 National Instruments. *LabVIEW*. n.d. URL: https://www.ni.com/pl-pl/shop/labview.html (Accessed 10 November 2020).

82 Corbett JCW, Allington-Smith J. Fibre modal noise issues in astronomical spectrophotometry. *Ground-Based Airborne Instrum Astron* 2006;**6269**:62693N. https://doi.org/10.1117/12.669799.

83 MakerBot. *Thingiverse*. n.d. URL: https://www.thingiverse.com/ (Accessed 10 November 2020).

84 Prusa Research a.s. *PrusaPrinters*. n.d. URL: https://www.prusaprinters.org/ (Accessed 10 November 2020).

85 Brennan MD, Bokhari FF, Eddington DT. Open Design 3D-Printable Adjustable Micropipette that Meets the ISO Standard for Accuracy. *Micromachines* 2018;**9**:191. https://doi.org/10.3390/mi9040191.

86 Wijnen B, Hunt EJ, Anzalone GC, Pearce JM. Open-Source Syringe Pump Library. *PLoS One* 2014;**9**:e107216. https://doi.org/10.1371/journal.pone.0107216.

87 Woelfle M, Olliaro P, Todd MH. Open science is a research accelerator. *Nat Chem* 2011;**3**:745–8. https://doi.org/10.1038/nchem.1149.

88 Vicente-Saez R, Martinez-Fuentes C. Open Science now: A systematic literature review for an integrated definition. *J Bus Res* 2018;**88**:428–36. https://doi.org/10.1016/j.jbusres.2017.12.043.

89 Pearce JM. *Open-Source Lab*. Elsevier; 2014.

90 Elsevier. *HardwareX*. n.d. URL: https://www.journals.elsevier.com/hardwarex (Accessed 10 November 2020).

91 Ubiquity Press. *Journal of Open Hardware*. n.d. URL: https://openhardware.metajnl.com/ (Accessed 10 November 2020).

92 Szewczyk S, Białek R, Burdziński G, Gibasiewicz K. Photovoltaic activity of electrodes based on intact photosystem I electrodeposited on bare conducting glass. *Photosynth Res* 2020;**144**:1–12. https://doi.org/10.1007/s11120-020-00722-1.

93 Szewczyk S, Białek R, Giera W, Burdziński G, van Grondelle R, Gibasiewicz K. Excitation dynamics in Photosystem I trapped in TiO2 mesopores. *Photosynth Res* 2020;**144**:235–45. https://doi.org/10.1007/s11120-020-00730-1.

FULL TEXT OF PUBLICATIONS CONSTITUTING THE THESIS

Photosynth Res (2016) 128:243–258
DOI 10.1007/s11120-016-0239-9

ORIGINAL ARTICLE

Weak temperature dependence of $P^+H_{\mathrm{A}}^-$ recombination in mutant *Rhodobacter sphaeroides* reaction centers

Krzysztof Gibasiewicz[1] · Rafał Białek[1] · Maria Pajzderska[1] · Jerzy Karolczak[1,2] ·
Gotard Burdziński[1] · Michael R. Jones[3] · Klaus Brettel[4]

Received: 7 August 2015 / Accepted: 24 February 2016 / Published online: 4 March 2016

Abstract In contrast with findings on the wild-type *Rhodobacter sphaeroides* reaction center, biexponential $P^+H_{\mathrm{A}}^- \rightarrow PH_{\mathrm{A}}$ charge recombination is shown to be weakly dependent on temperature between 78 and 298 K in three variants with single amino acids exchanged in the vicinity of primary electron acceptors. These mutated reaction centers have diverse overall kinetics of charge recombination, spanning an average lifetime from ~2 to ~20 ns. Despite these differences a protein relaxation model applied previously to wild-type reaction centers was successfully used to relate the observed kinetics to the temporal evolution of the free energy level of the state $P^+H_A^-$ relative to $P^+B_{\mathrm{A}}^-$. We conclude that the observed variety in the kinetics of charge recombination, together with their weak temperature dependence, is caused by a combination of factors that are each affected to a different extent by the point mutations in a particular mutant complex. These are as follows: (1) the initial free energy gap between the states $P^+B_{\mathrm{A}}^-$ and $P^+H_{\mathrm{A}}^-$, (2) the intrinsic rate of $P^+B_{\mathrm{A}}^- \rightarrow PB_{\mathrm{A}}$ charge recombination, and (3) the rate of protein relaxation in response to the appearance of the charge separated states. In the case of a mutant which displays rapid $P^+H_{\mathrm{A}}^-$ recombination (ELL), most of this recombination occurs in an unrelaxed protein in which $P^+B_{\mathrm{A}}^-$ and $P^+H_{\mathrm{A}}^-$ are almost isoenergetic. In contrast, in a mutant in which $P^+H_{\mathrm{A}}^-$ recombination is relatively slow (GML), most of the recombination occurs in a relaxed protein in which $P^+H_{\mathrm{A}}^-$ is much lower in energy than $P^+H_{\mathrm{A}}^-$. The weak temperature dependence in the ELL reaction center and a YLH mutant was modeled in two ways: (1) by assuming that the initial $P^+B_{\mathrm{A}}^-$ and $P^+H_{\mathrm{A}}^-$ states in an unrelaxed protein are isoenergetic, whereas the final free energy gap between these states following the protein relaxation is large (~250 meV or more), independent of temperature and (2) by assuming that the initial and final free energy gaps between $P^+B_{\mathrm{A}}^-$ and $P^+H_{\mathrm{A}}^-$ are moderate and temperature dependent. In the case of the GML mutant, it was concluded that the free energy gap between $P^+B_{\mathrm{A}}^-$ and $P^+H_{\mathrm{A}}^-$ is large at all times.

Keywords *Rhodobacter sphaeroides* · Reaction centers · Charge recombination · Electron transfer · Transient absorption · Protein dynamics

Introduction

The contributions of protein dynamics to electron transfer occurring inside proteins are poorly understood. Photosynthetic reaction centers (RCs) are convenient model systems that allow systematic studies of this issue; they can be synchronously excited by ultrashort laser pulses, and the electron transfer may be observed by optical time-resolved techniques on time scales comparable with the duration of

---

Electronic supplementary material The online version of this article (doi:10.1007/s11120-016-0239-9) contains supplementary material, which is available to authorized users.

✉ Krzysztof Gibasiewicz
krzyszgi@amu.edu.pl

[1] Department of Physics, Adam Mickiewicz University, ul. Umultowska 85, 61-614 Poznań, Poland

[2] Center for Ultrafast Laser Spectroscopy, A. Mickiewicz University, ul. Umultowska 85, 61-614 Poznań, Poland

[3] School of Biochemistry, Medical Sciences Building, University of Bristol, University Walk, Bristol BS8 1TD, UK

[4] Laboratoire Mécanismes Fondamentaux de la Bioénergétique, UMR 8221, CEA - iBiTec-S, CNRS, Université Paris Sud, 91191 Gif-Sur-Yvette, France

the excitation pulse and longer. Experimental data relating to the influence of protein dynamics on light-induced electron transfer in RCs have been interpreted either in terms of an active contribution of the protein, the spontaneous diffusion of which in the conformational space is a factor that largely determines the rate of electron transfer (Wang et al. 2007, 2009, 2012; Torchała and Kurzyński 2008; Pieper and Renger 2009; Kurzyński and Chełminiak 2013) or in terms of passive conformational reorganization of the protein in response to the appearance of a strong electrical field caused by the light-induced charge separated states (Woodbury and Parson 1984; Peloquin et al. 1994; Gibasiewicz et al. 2013a).

Among the photosynthetic RCs, one of the most widely studied is that from the purple bacterium *Rhodobacter* (*Rba.*) *sphaeroides* (Woodbury and Allen 1995; Zinth and Wachtveitl 2005; Hunter et al. 2009; Jones 2009). Light-induced charge separation inside this protein occurs along a chain of electron transfer cofactors that engage in non-covalent interactions with the neighboring amino acids. The electron transfer starts at the primary electron donor, a dimer of bacteriochlorophyll *a* (BChl *a*) molecules, labeled traditionally as P870 or P (Fig. 1). Within ~3–7 ps, the electron is transferred from the first excited singlet state of P (P*) to H_A, a bacteriopheophytin (Fig. 1), forming the first spectroscopically easily observed charge separated state $P^+H_A^-$. Then, the electron is transferred within ~200–250 ps from H_A^- to the secondary electron acceptor, a quinone named Q_A (Fig. 1), forming the charge separated state, $P^+Q_A^-$. From Q_A, the electron is transferred on microsecond time scale to a dissociable quinone, Q_B. The forward electron transfer from H_A^- to Q_A can be artificially blocked by chemical or genetic removal of Q_A (Shuvalov and Parson 1981; Schenck et al. 1982; Chidsey et al. 1984; Ogrodnik et al. 1988; Tang et al. 1999; Ridge et al. 1999; McAuley et al. 2000), or by pre-reduction of Q_A to Q_A^- using a strong reductant, or through a combination of weak background illumination (forming the long-lived state $P^+Q_A^-$) and a relatively weak reductant (reducing P^+ to leave PQ_A^-) (Shuvalov and Parson 1981; Schenck et al. 1982; Gibasiewicz and Pajzderska 2008; Gibasiewicz et al. 2009). It cannot be excluded that in nature, under certain conditions, the state PQ_A^- may also be formed. When the electron transfer from H_A^- to Q_A is blocked, a charge recombination occurs in which the electron is transferred back to P^+ (Volk et al. 1995), and this charge recombination may be measured directly.

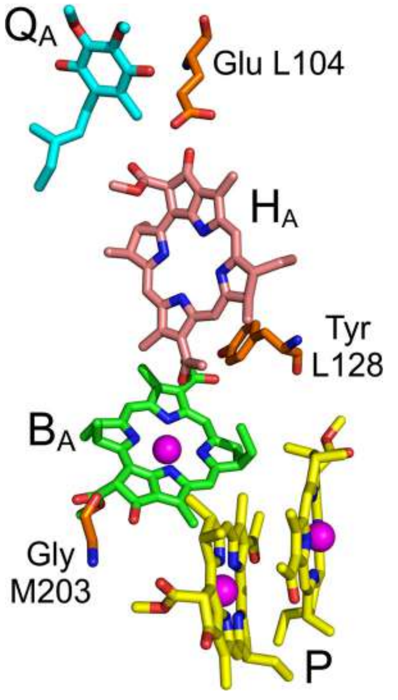

Fig. 1 Electron transfer cofactors of *Rba. sphaeroides* RC. The primary electron donor P BChls are shown with yellow carbons, B_A acceptor BChl–with green carbons, H_A acceptor BPhe–with pink carbons and Q_A acceptor ubiquinone–with cyan carbons. Amino acids replaced by mutation are shown with orange carbons. For other atoms, *red* = oxygen, *blue* = nitrogen, and *magenta* sphere = magnesium

The B_A BChl located between P and H_A (Fig. 1) acts as either a real or virtual intermediate electron carrier for both forward electron transfer from P* to H_A (Kirmaier and Holten 1988, 1991; Lockhart et al. 1990; Rodriguez et al. 1991; Chan et al. 1991; Arlt et al. 1993) and backward transfer from H_A^- to P^+ (Shuvalov and Parson 1981; Shkuropatov and Shuvalov 1993; Schmidt et al. 1994; Kirmaier et al. 1995; Gibasiewicz and Pajzderska 2008; Wang et al. 2012). Possible pathways for $P^+H_A^-$ recombination are summarized in Fig. 2. Involvement of B_A as a real carrier in charge recombination means that a discrete $P^+B_A^-$ state is formed before the electron arrives at P^+. Experimental data have shown that the energy level of $P^+B_A^-$ is higher than that of $P^+H_A^-$ (Shuvalov and Parson 1981; Arlt et al. 1993; Heller et al. 1996) and therefore the efficiency of this charge recombination pathway is temperature dependent (Gibasiewicz et al. 2013a). In contrast, the virtual involvement of B_A in charge recombination through superexchange provides an alternative pathway for this reaction that is temperature independent. Irrespective of mechanism, the charge recombination reaction leads with the highest probability to energy dissipation and immediate recovery of the singlet ground state of P. However, in Q_A-reduced wild-type (WT) RCs at room temperature there is a ~15 % probability that the spin of one of the radical pair electrons will change in the state $P^+H_A^-$ leading to a triplet configuration of the charge separated state, $^3(P^+H_A^-)$, followed by charge recombination yielding the triplet state of the primary donor ^3P (Volk et al. 1995). Triplet states decay on microsecond time scale (Shuvalov and Parson

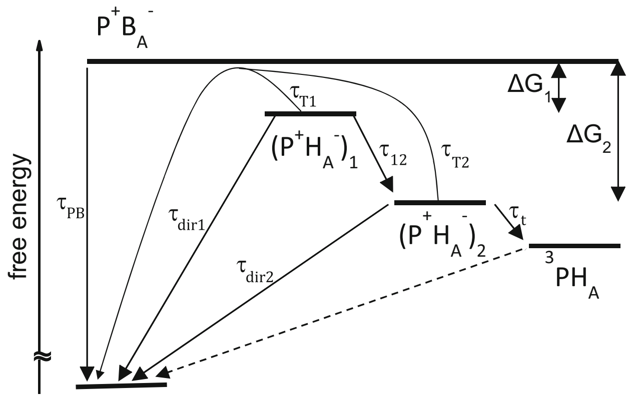

Fig. 2 Model scheme of $P^+H_A^-$ recombination in the case of one-step protein relaxation. Lifetimes τ_{T1} and τ_{T2} are temperature dependent and depict thermally activated charge recombination with real formation of the intermediate state $P^+B_A^-$, whereas lifetimes τ_{dir1} and τ_{dir2} are temperature independent and depict direct $P^+H_A^-$ recombination with virtual involvement of B_A. The free energy gap between $P^+H_A^-$ and $P^+B_A^-$ increases in time from ΔG_1 to ΔG_2, with a lifetime τ_{12}, due to protein reorganization (solvation) dynamics in response to the appearance of the charge separated states (Gibasiewicz et al. 2013a). Thus, $(P^+H_A^-)_1$ is the initial or unrelaxed form and $(P^+H_A^-)_2$ is the final or relaxed form of the charge separated state, and both are assumed to be in equilibrium with $P^+B_A^-$. Relaxation of $P^+H_A^-$ underlies the non-mono-exponential character of $P^+H_A^-$ recombination. The values of τ_{T1} and τ_{T2} depend on ΔG_1, ΔG_2, and τ_{PB}: $\tau_{Ti} = \tau_{PB}[1 + \exp(\Delta G_i/kT)]$, $i = 1, 2$ (compare Appendix in the Supporting Information). Formation of the triplet state ^3PH_A competes with recombination to the singlet states of P. Recombination to the singlet excited state P^* is not shown, since it was assumed that depopulation of the state $P^+H_A^-$ via fluorescence channel is much less efficient than those depicted in the scheme

1981; Woodbury et al. 1986; Volk et al. 1995; Gibasiewicz et al. 2011). Finally, there is a small probability that the electron on H_A^- will come back to the excited orbital of the primary donor regenerating the singlet excited state P^* (Woodbury and Parson 1984; Woodbury et al. 1986; Ogrodnik et al. 1994; Hartwich et al. 1998).

It has been hypothesized that $P^+H_A^-$ recombination is strongly influenced by protein dynamics (Gibasiewicz et al. 2011, 2013a; Wang et al. 2012), the main experimental evidence being the multiexponential character of this reaction. In the model shown in Fig. 2, the transition indicated by the arrow and label τ_{12} depicts a downshift of the energy level of $P^+H_A^-$ relative to $P^+B_A^-$ ascribed previously to protein conformational adaptation to the appearance of the new charges on P^+ and H_A^- (Gibasiewicz et al. 2013a). In membrane-bound WT *Rba. sphaeroides* RCs, the overall characteristic lifetime of this process was estimated to be $\tau_{12} = 3.7 \pm 0.4$ ns with no evident temperature dependence between 78 K and room temperature (RT) (Gibasiewicz et al. 2013b). For isolated *Rba. sphaeroides* RCs, it was possible to resolve as many as three exponential components in transient absorption measurements due to a better signal-to-noise ratio. Those results were treated with a similar model to that one shown in Fig. 2, but with two consecutive steps of protein relaxation that lower the free energy of $P^+H_A^-$ with lifetimes of $\tau_{12} = 0.6 \pm 0.1$ ns and $\tau_{23} = 10.5 \pm 1.5$ ns (not shown in Fig. 2). Again, no clear temperature dependence of these parameters was observed between 77 K and RT (Gibasiewicz et al. 2013a). The single value of $\tau_{12} = 3.7$ ns obtained for membrane-bound RCs falls in between the $\tau_{12} = 0.6$ ns and $\tau_{23} = 10.5$ ns obtained for isolated RCs and could be regarded as an average value.

Population of the state $P^+B_A^-$ in the WT RC is very low compared to that of $P^+H_A^-$, and thus B_A^- is very difficult to detect (Arlt et al. 1993; Woodbury and Allen 1995; Parson and Warshel 2009). However, manipulation of the free energy gap between $P^+B_A^-$ and $P^+H_A^-$ through genetic modification increased the amount of $P^+B_A^-$ to detectable levels (Kirmaier et al. 1991, 1995; Shkuropatov and Shuvalov 1993; Laporte et al. 1995; Heller et al. 1995, 1996; Schmidt et al. 1994, 1995; Huber et al. 1995; Arlt et al. 1996; Kennis et al. 1997). Interestingly, a $P^+B_A^-$ state in equilibrium with $P^+H_A^-$ was reported also for WT RCs both on the time scale of primary charge separation (a few picoseconds) and $P^+H_A^- \rightarrow PH_A$ charge recombination (~1 ns) (Arlt et al. 1993; Gibasiewicz et al. 2009; Zhu et al. 2013). Using femtosecond transient absorption measurements in the visible region, it was shown that contribution of the absorption increased at ~544 nm (due to $P^+H_A^- \rightarrow PH_A$ charge recombination; at ~544 nm only the signal from H_A^-/H_A contributes) relative to that at ~600 nm (due to $P^+B_A^- \rightarrow PB_A$ charge recombination; at ~600 nm both signals from P/P^+ and B_A^-/B_A contribute) was dependent on the presence/absence of the negative charge on Q_A and on the time delay between excitation and measurement (Gibasiewicz et al. 2009). At shorter times after excitation (below 1 ns) and/or with a negative charge on Q_A, the charge recombination was more pronounced at ~600 nm, whereas at later times and/or without negative charge on Q_A (in practice—without Q_A), the charge recombination was more pronounced at ~544 nm. It was therefore concluded that the bigger the charge recombination signal at ~600 nm relative to that at ~544 nm, the more the equilibrium between the states $P^+H_A^-$ and $P^+B_A^-$ shifts toward the latter and the smaller is the free energy gap between these states. Therefore, the relative amplitudes of the charge recombination signals at these two wavelengths may be treated as a fingerprint of this free energy gap (see also Heller et al. 1996). This finding will be particularly useful in interpretation of the femtosecond data for the mutants presented in the Results and Discussion.

Recently, it was proposed that charge separation may occur via two parallel pathways characterized by somewhat different electron transfer rates from P^* to B_A and from B_A^- to H_A, possibly due to different conformational states of the protein (Zhu et al. 2013) in line with older work reporting on heterogeneity of the charge separation reaction (Kirmaier and Holten 1990). Although we cannot rule out the possibility that similar heterogeneity underlies multiexponential charge recombination, in this contribution we limit our modeling to homogenous situation. Obviously, postulated structural heterogeneity occurring on the time scale of charge separation does not need to be sustained to the nanosecond time scale on which charge recombination occurs. A longer discussion on the issue of heterogeneity of charge recombination can be found in a previous report (Gibasiewicz et al. 2013a).

In this contribution, we compared the temperature dependence of the kinetics of $P^+H_A^-$ charge recombination in membrane-bound WT and three single point mutant RCs with identically blocked electron transfer from H_A^- to Q_A achieved by pre-reduction of the latter using background illumination and a weak reductant, sodium ascorbate. It is proposed that these mutations, which are known to reorganize hydrogen bond interactions either with H_A or with B_A (Bylina et al. 1988; Potter et al. 2005; Gibasiewicz et al. 2011), modulate not only the free energy levels of the state $P^+H_A^-$ relative to that of $P^+B_A^-$, as was proposed previously, but also the responsive protein dynamics. Consequently, both of these factors, as well as the intrinsic $P^+B_A^- \rightarrow PB_A$ charge recombination rate constant, are responsible for the observed variety of charge recombination kinetics and the weak temperature dependence of $P^+H_A^-$ charge recombination.

Materials and methods

Biological material

Strains of *Rba. sphaeroides* lacking both types of light-harvesting complex and containing either WT or mutated RCs were grown under dark/semiaerobic conditions as described previously (Jones et al. 1992). Cells were harvested and intracytoplasmic membranes isolated by breakage of cells in a French pressure cell, followed by sucrose gradient purification (Jones et al. 1994).

Nanosecond transient absorption measurements

Preparation of samples and instrumentation for nanosecond transient absorption measurements were described previously (Byrdin et al. 2009; Gibasiewicz et al. 2013b). In brief, RC-only membranes were diluted to $OD_{800nm,1.5mm} \approx 0.5$ in Tris–HCl buffer (pH 8.2) containing ~0.0001 % β-dodecyl maltoside (β-DM), ~50 % glycerol (v/v), 20 mM sodium ascorbate, and 12 mM *o*-phenanthroline. During the experiments, the samples were continuously illuminated with a white halogen light (~1 mW/cm^2). Under these conditions, RCs are in the closed state with Q_A permanently reduced (Shuvalov and Parson 1981; Schenck et al. 1982; Gibasiewicz and Pajzderska 2008). *O*-phenanthroline is known to replace quinone Q_B thus preventing reoxidation of Q_A^- by Q_B (Okamura et al. 1975; Michel et al. 1986). The samples were placed in a flat cuvette formed by two transparent round plastic plates separated by 1.5-mm rubber o-ring, and the cuvette was placed in a liquid nitrogen cryostat (Janis VPF-100) controlled by a temperature controller (LakeShore 331S-T2). The samples were excited at 532 nm (Nd:-YAG laser, Continuum Leopard SS-10), at a repetition rate of ~2 Hz, with light pulses of ~2 mJ energy and 100 ps duration. Monitoring light, directed orthogonally to the excitation beam, was generated at 690 nm by a laser diode (EOSI 2010) and detected by a fast photodiode (rise time 200 ps; model UPD-200-UP from Alphalas) connected to a digitizing oscilloscope (Agilent Infinium 81004B; 10 GHz; sampling rate, 40 G samples/s). The transient absorption signals were collected in a 6 μs temporal window and averaged over 1024 laser shots for each temperature. Experiments were performed at a range of temperatures between 77 and 298 K.

Kinetic traces were fitted with the sum of one or two exponential functions and a constant using Origin (OriginLab). The fitting was performed in a 100 and/or 200 ns window, and the starting point of the fits was at the maximum of the experimental kinetics.

Femtosecond transient absorption measurements

Transient absorption measurements on the femtosecond time scale were performed at RT essentially as described earlier (Gibasiewicz et al. 2009) using the 1 kHz femtosecond laser system (Ti:sapphire, Spectra Physics) and a grating polychromator (Spectra Pro 150, Acton Research Corp.) with a thermoelectrically cooled CCD camera (Back Illumin., Princeton Instruments) described in detail previously (Maciejewski et al. 2000). The data were collected over a 2 ns temporal window and over a ~330–700 nm spectral window using ~300 fs excitation at 800 nm. RC-only membranes were diluted in either 15 mM Tris–HCl (pH 8.2) containing 0.025 % LDAO and 1 mM EDTA, or 50 mM glycine-NaOH (pH 10.5) containing 0.025 % β-DM. In order to keep the RCs in the open state (all electron transfer cofactors in their neutral state), fresh 10 mM sodium ascorbate was added to the sample before each experiment. In order to keep the RCs in the closed state (Q_A permanently reduced), 20 mM sodium ascorbate and 12 mM *o*-phenanthroline were added to the samples and continuous background illumination of the sample was applied during the measurement. Samples (~2.0 ml) were placed in a flat rotating quartz cuvette, allowing relaxation between each laser flash. The optical path of the probe laser beam in the sample was approximately 1.5 mm. White light probe pulses were generated in a calcium fluoride plate. Typically, absorption changes were measured at 70 different temporal points distributed unevenly between a few picoseconds before to two nanoseconds after the excitation pulse, with the pump-probe delay ranging from 100 fs around time zero to 200 ps at delays above 1000 ps. In the case of closed RCs, a part of measurements were performed for only 26 temporal points with lower resolution around time zero (pump-probe delays differences of 1 ps). This way, the experiments took less time that was essential for maintaining RCs in fully closed state all the time during the measurements.

The temporal evolution of the transient absorption spectra was subjected to global and target analysis (Holzwarth 1996; van Stokkum et al. 2004) using the software package Asufit developed at Arizona State University (available at http://www.public.asu.edu/~laserweb/asufit/asufit.html) as well as Glotaran software (Snellenburg et al. 2012). This evolution was fitted using sum of typically four exponential lifetimes convoluted with an instrumental response function modeled by a Gaussian of ~400 fs width.

Results and discussion

Nanosecond transient absorption measurements at 690 nm

Nanosecond transient absorption spectroscopy was applied to antenna-deficient membranes containing either WT RCs or RCs with one of three single residue replacements near $\mathrm{H_A}$ or $\mathrm{B_A}$ that bring about known changes to the structure of the protein. Replacement of Glu L104 by Leu (ELL—Fig. 3a) and Gly M203 by Leu (GML—Fig. 3c) removed a hydrogen bond donor to H_A and B_A, respectively (Bylina et al. 1988; Potter et al. 2005). Oppositely, replacement of Tyr L128 by His (YLH—Fig. 3b) provided a new hydrogen bond donor to B_A (Gibasiewicz et al. 2011). Figure 3d shows the expected effect of each mutation from the phenomenological rule that the removal of the hydrogen bond from a cofactor destabilizes (shifts up) the energy of the charge separated state involving this cofactor, whereas introducing a new hydrogen bond to a cofactor has the opposite effect (Lin et al. 1994). These mutant RCs, although widely characterized in many aspects, have not been studied with respect to the temperature dependence of charge recombination.

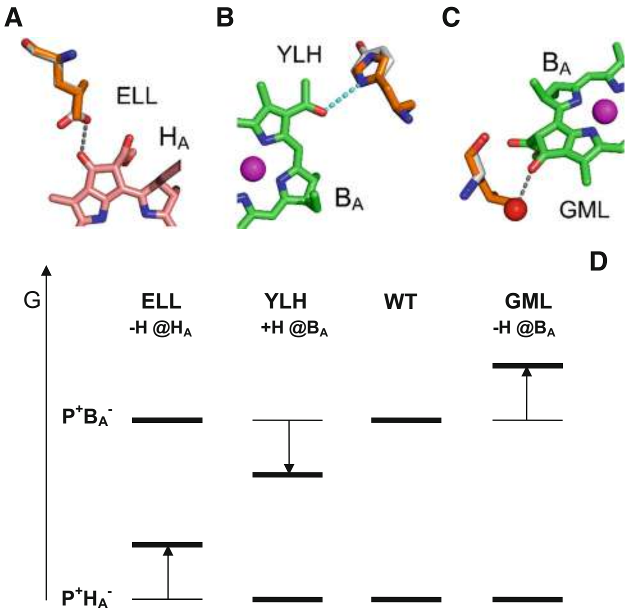

Fig. 3 Single point mutations introduced to the mutant RC (**a**, **b**, **c**) and expected effects of these mutations on the free energy levels of the charge separated states caused by removal (labeled "−H") or introduction ("+H") of a hydrogen bond to either H_A or B_A (**d**). For *panels* (**a**–**c**), atom *colors* are as for Fig. 1. Carbons of the replaced amino acid are in white and carbons of the introduced amino acid are in orange. Lost hydrogen bonds are indicated with *gray dashed lines*, introduced hydrogen bonds with *cyan dashed line*. In (**c**) the *red sphere* is a hydrogen bond donor water molecule that is sterically excluded on replacing Gly with Leu

Figure 4 shows the kinetics of $P^+H_A^-$ recombination measured as absorption changes at 690 nm for membrane-bound WT and mutant RCs. As was shown previously (Fajer et al. 1975; Heller et al. 1995; Huber et al. 1995; Gibasiewicz et al. 2009), changes in absorbance at this wavelength originate mostly from rapid (a few picoseconds) formation and slow (nanosecond) decay of the BPhe anion, H_A^-, as well as of the BChl anion, B_A^-. The relative contribution of the latter depends on the free energy gap between the states $P^+H_A^-$ and $P^+B_A^-$ (Kirmaier et al. 1991, 1995; Shkuropatov and Shuvalov 1993; Laporte et al. 1995; Heller et al. 1995, 1996; Schmidt et al. 1994, 1995; Huber et al. 1995; Arlt et al. 1996; Kennis et al. 1997) and may be negligible if the equilibrium is strongly shifted toward $P^+H_A^-$. Any non-decaying signal on the 100 ns time scale is due to the formation of triplet states. As concluded previously (Gibasiewicz et al. 2013a), the relatively small amplitude of the non-decaying signal was due to a significantly smaller differential extinction coefficient of the triplet state relative to that of the $P^+H_A^-/PH_A$ transition at 690 nm (Volk et al. 1995). The transient absorption signal at 690 nm was fitted by a two-exponential function in each case except for the GML mutant for which a mono-

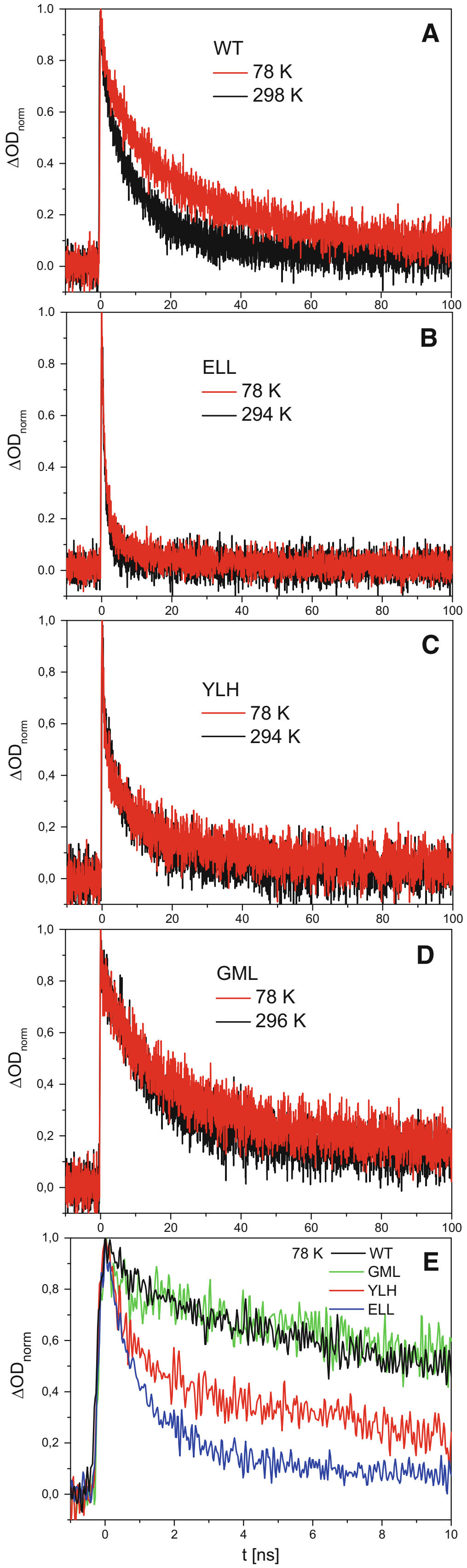

◀**Fig. 4** Comparison of absorption changes kinetics at 690 nm measured at RT and 78 K after picosecond excitation at 532 nm, revealing $P^+H_A^-$ recombination

exponential fit was performed. Parameters of the best fits are presented in Table 1.

Each of the mutations affected the overall kinetics (τ_{ave}, Table 1), charge recombination being most rapid in the ELL mutant, least rapid in the GML mutant and with the YLH mutant being intermediate and closest to the WT. The differences were reflected by different lifetimes and relative amplitudes for the kinetic components (τ_1, τ_2, A_1, and A_2; Table 1). In addition, unlike for the WT RC where $P^+H_A^-$ charge recombination was clearly temperature dependent, recombination in the mutant RCs was only weakly temperature dependent (Figs. 4b–d compared with Fig. 4a).

The kinetics of charge recombination in the WT, ELL, and YLH RCs (Fig. 4a–c) were well fitted by the two-exponential function predicted by the model shown in Fig. 2. In general, the model predicts a temperature-dependent overall decay of the $P^+H_A^-$ state via the temperature-dependent lifetimes τ_{T1} and τ_{T2} (see Appendix in Supporting Information for the formulae). However, the weak temperature dependence of charge recombination for the two mutant RCs would still be consistent with this model if the initial $(P^+H_A^-)_1$ state was quasi-isoenergetic with $P^+B_A^-$, whereas the relaxed state $(P^+H_A^-)_2$ was separated by a large free energy gap from $P^+B_A^-$. It was estimated that for a τ_{PB} as short as 0.2 ns (Heller et al. 1996; Katilius et al. 1999), the energy gap of ~250 meV is large enough to make charge recombination from the relaxed state practically temperature independent (the recombination pathway via $P^+B_A^-$ is inefficient, with $\tau_{T2} > 1000$ ns both at RT and 77 K, and almost all recombination must occur via the direct, temperature-independent singlet or triplet pathway).

An alternative explanation for the weak temperature dependence of the $P^+H_A^-$ charge recombination in the ELL and YLH RCs could be that the free energy gap between the states $P^+H_A^-$ and $P^+B_A^-$ is roughly proportional to the temperature. Thus, the lifetimes τ_{T1} and τ_{T2} remain almost temperature independent (Eqs. A21–A22 and A7–A8 in Supporting Information). This issue is treated in a quantitative way below (section: *Model-based estimation of the molecular parameters*) and in an extended way in Supporting Information.

In the case of the GML RCs, no clear fast phase of the order of 1–3 ns could be resolved in the nanosecond experiment (Fig. 4d). Instead, a mono-exponential fit yielded a lifetime of 16.5 ns at RT which increased to 23.7 ns at

Table 1 Fit parameters of charge recombination kinetics

	Sample	T (K)	Fit parameters[a]									
			Nanosecond experiment @ 690 nm						Femtosecond experiment @ 400–700 nm			
			τ_1 (ns)	A_1	τ_2 (ns)	A_2	A_0	τ_{av}^{c} (ns)	τ_1 (ns)	A_1	τ_2 (ns) (fixed)	A_2
2-exp	WT[b]	298	2.4	0.34	13	0.61	0.048	9.2	1.6	0.54	20	0.46
		78	3.8	0.29	26	0.62	0.093	18.9	–		–	
	ELL	294	1.0	0.92	20	0.07	0.007	2.3	0.68	0.77	20	0.23
		78	1.2	0.88	20	0.11	0.015	3.3	–		–	
	YLH	294	1.5	0.57	15	0.41	0.021	7.1	0.49	0.60	20	0.40
		78	1.2	0.59	20	0.35	0.053	8.1	–		–	
	GML	296	–	–	–	–	–	–	1.6	0.24	20	0.76
1-exp	GML	296	16.5	0.84	–	–	0.16	16.5	–	–	–	–
		78	23.7	0.80	–	–	0.20	23.7	–	–	–	–

[a] In the case of the nanosecond experiments, two- and one-exponential fits were performed according to the formula $\Delta A = \sum_{i=1}^{N} A_i \exp(-t/\tau_i) + A_0$ ($N = 1$ or 2) in a 200-ns temporal window (100-ns in the case of the WT RC) and the fitted kinetics are shown in Fig. 4. In the case of the femtosecond experiments, the lifetimes τ_1 and τ_2 come from the global analysis (Fig. 5), whereas the amplitudes A_1 and A_2 were taken from the target analysis (see Fig. 6) and are consistent with the relative amplitudes of the two phases of charge recombination shown in Fig. 5e–h

[b] Data taken from Gibasiewicz et al. (2013b)

[c] For two-exponential fits $\tau_{av} = (\tau_1 A_1 + \tau_2 A_2)/(A_1 + A_2)$. The estimated experimental error of the fit parameters obtained for the nanosecond experiment is ±20 %

78 K (Table 1). This increase suggests a possible minor contribution from a thermally activated pathway at RT or a temperature-dependent direct charge recombination.

The average decay lifetimes (τ_{av}) both at RT and at 78 K for all four samples were well correlated with the amplitude (A_0) of the non-decaying component assigned to triplet states. Across the four RCs, the slower the charge recombination the larger was the amount of triplet state.

Model-based calculations of the molecular parameters

An extended description of the model-based calculations of molecular parameters shown in Fig. 2 can be found in Supporting Information. A summary of the main results is presented in Table 2. For WT, ELL, and YLH RCs, representative sets of molecular parameters estimated on the basis of the model parameters from single wavelength experiments (Table 1) are shown for the two cases introduced above. In case "*a*," the free energy gaps ΔG_1 and ΔG_2 were fixed either at the values estimated on the basis of previous studies on WT RCs (Gibasiewicz et al. 2013b) or it was assumed that $\Delta G_1 = 0$ meV and $\Delta G_2 =$ 250 meV (ELL and YLH RCs), the values for the mutants ensuring temperature independence of charge recombination as discussed above. In case "*b*," ΔG_1 and ΔG_2 were free parameters. One can see that in the case *b*, the weak temperature dependence of charge recombination for the mutant RCs is ensured by decreased free energy gap between $P^+H_A^-$ and $P^+B_A^-$ at low temperatures (see the values of ΔG_1 and ΔG_2 at 78 K and at room temperature in Table 2). In this case, we assumed the same values of τ_{PB} as those estimated from the femtosecond experiment for WT, ELL, and YLH RCs (see below). Options *a* and *b* for the ELL RC are illustrated in Fig. S1 in the Supporting Information. The decay of GML mutant was not treated with the model shown in Fig. 2, since it was fitted by a single exponential component.

Femtosecond transient absorption measurements from 400 to 700 nm

In order to verify the above considerations on the different sizes of the initial free energy gap between $P^+B_A^-$ and the unrelaxed $(P^+H_A^-)_1$ state, RT femtosecond transient absorption measurements were performed over 2 ns and in a wide 400–700 nm spectral window allowing more precise identification of RC states and transitions between these states than is possible from single wavelength measurements. In addition, the better temporal resolution of femtosecond measurements enabled a more exact estimation of the fastest, subnanosecond phase of charge recombination (Gibasiewicz et al. 2009; Wang et al. 2012).

Figure 5 compares the results of global fits of RT femtosecond data for the WT and mutant RCs in the form of decay-associated difference spectra (DADS) (Holzwarth 1996; van Stokkum et al. 2004). For each sample, DADS are shown for the open RCs in which there was free

Table 2 Selected model molecular parameters for charge recombination kinetics

Sample	Nanosecond experiments						Femtosecond experiments		
	T (K)	Model parameters[a]					Model parameters (room temperature only)		
		Option	τ_{12} (ns)	ΔG_1 (meV)	ΔG_2 (meV)	τ_{PB} (ns)	τ_{12} (ns)	ΔG_1 (meV)	τ_{PB} (ns)
WT	298	*a*	4.3 ± 1.1	*90 ± 18*	*128 ± 26*	*0.2*	–	–	–
		b	4.2 ± 1.1	77 ± 17	119 ± 14	*0.26 ± 0.15*	3.1 ± 0.2	60 ± 17	0.26 ± 0.15
	78	*a*	6.1 ± 1.5	*90 ± 18*	*128 ± 26*	*0.2*	–	–	–
		b	6.0 ± 1.5	25 ± 4	48 ± 16	*0.26 ± 0.15*			
ELL	296	*a*	6.5 ± 2.1	*0*	*250*	0.54 ± 0.05	–	–	–
		b	9.1 ± 3.7	22 ± 14	131 ± 14	*0.32 ± 0.10*	1.9 ± 0.4 (2.0 ± 0.3)	15 ± 15 (30 ± 15)	0.32 ± 0.10 (0.22 ± 0.10)
	78	*a*	5.0 ± 1.6	*0*	*250*	0.68 ± 0.13	–	–	–
		b	7.7 ± 2.8	7.9 ± 3.3	42 ± 10	*0.32 ± 0.10*			
YLH	296	*a*	1.9 ± 0.5	*0*	*250*	1.30 ± 0.29	–	–	–
		b	3.7 ± 1.0	79 ± 16	140 ± 16	*0.11 ± 0.07*	1.0 ± 0.1	49 ± 15	0.11 ± 0.07
	78	*a*	1.5 ± 0.4	*0*	*250*	0.97 ± 0.22	–	–	–
		b	2.9 ± 0.8	19 ± 4	50 ± 11	*0.11 ± 0.07*			
GML	RT	–	–	–	–	–	2.1	90	0.2

[a] Model parameters for the nanosecond experiments were estimated from the fit parameters of the nanosecond kinetics shown in Table 1 and the formulae shown in the Appendix (Supporting Information). Assumed values are shown in italics (in most cases, ranges of assumed values were considered). Uncertainties of the model parameters were estimated using the formula: $u(y) = \sqrt{\sum_i \left(u(x_i)\frac{\partial y}{\partial x_i}\right)^2}$, where y is any of the model parameters, x_i is i-th independent variable (fit parameter), and $u(x_i)$ is the uncertainty of i-th independent variable (assumed to be ±20 %). Prior to uncertainty estimations, formulas for model parameters were transformed as a function of independent variables obtained directly from the fit, which were $A_1, A_2, A_0, \tau_1, \tau_2$. Options *a*—$\Delta G_1$ and ΔG_2 values were assumed. Options *b*—ΔG_1 and ΔG_2 were free parameters. The two sets of model parameters for femtosecond experiments (ELL mutant) correspond to ways of estimation of ΔG_1 depicted in Fig. 7 (the parameters in brackets correspond to Fig. 7a)

electron transfer from H_A^- to Q_A (panels a–d), and for closed RCs in which the electron transfer from H_A^- to Q_A was blocked (panels e–h). Where a DADS is positive, the absorption decreased in that spectral region within the specified lifetime, and where a DADS is negative the absorption increased with the respective lifetime.

Charge separation in open RCs

Temporal evolution of transient absorption spectra for all four RCs was analyzed using three lifetimes and a non-decaying component. The fastest ~0.4 ps component was assigned to excitation energy transfer from the directly excited monomeric BChls at 800 nm to P (not shown). The remaining DADS for the WT membrane-bound RC (Fig. 5a) were similar to spectra published for isolated WT RCs (Gibasiewicz et al. 2009). The spectra obtained for the three mutant RCs (Fig. 5b–d) were generally very similar to those of the WT RC (Fig. 5A), as were the associated lifetimes (except for the GML RC, see below). The following does not describe precisely all details of the spectra, since this has been done previously (Gibasiewicz et al. 2009). Instead, we indicate minor differences between the DADS for the WT and mutant RCs and we focus on the spectral features that are most important for the further interpretation.

In each case (Fig. 5a–d), the black thick solid line is the amplitude spectrum of the charge separation reaction: $P^* \rightarrow P^+H_A^-$. This reaction involves transient formation of the state $P^+B_A^-$ but, due to its relatively slow formation and fast decay (~1 ps; see for example Arlt et al. 1993 and Parson and Warshel 2009 for reviews) its contribution is expected to be low and difficult to resolve. With the exception of the GML RC, charge separation was not strongly affected by the mutations and occurred within ~5–7 ps, a lifetime similar to that in the WT RC (Fig. 5a–c). The slower charge separation in the GML RC, ~21 ps, is consistent with a previous report (Potter et al. 2005). The charge separation DADS for all RCs showed a significant positive band at ~545 nm due to loss of H_A ground state absorption on formation of H_A^-. With the same lifetime, a new absorption band appeared as revealed by a negative band centered at ~670 nm, except for the ELL mutant for which this maximum was blue-shifted to ~640 nm. This band is assigned to H_A^- but especially in the case of the ELL RC, it may also contain a

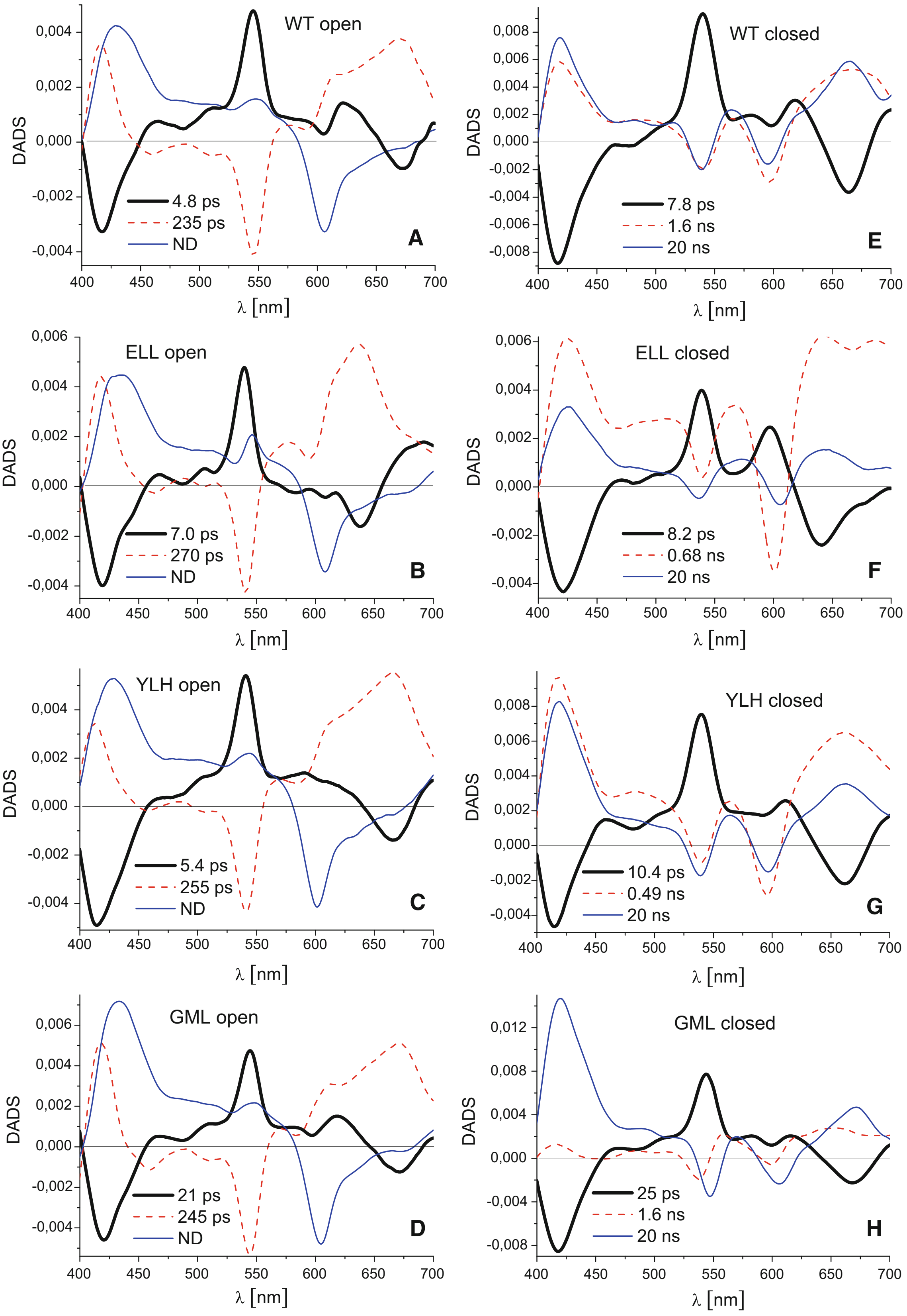

Fig. 5 Decay-associated difference spectra for RCs in *open* and *closed* states. The spectra were estimated from femtosecond transient absorption difference spectra recorded following excitation at 800 nm with ~300 fs light pulses

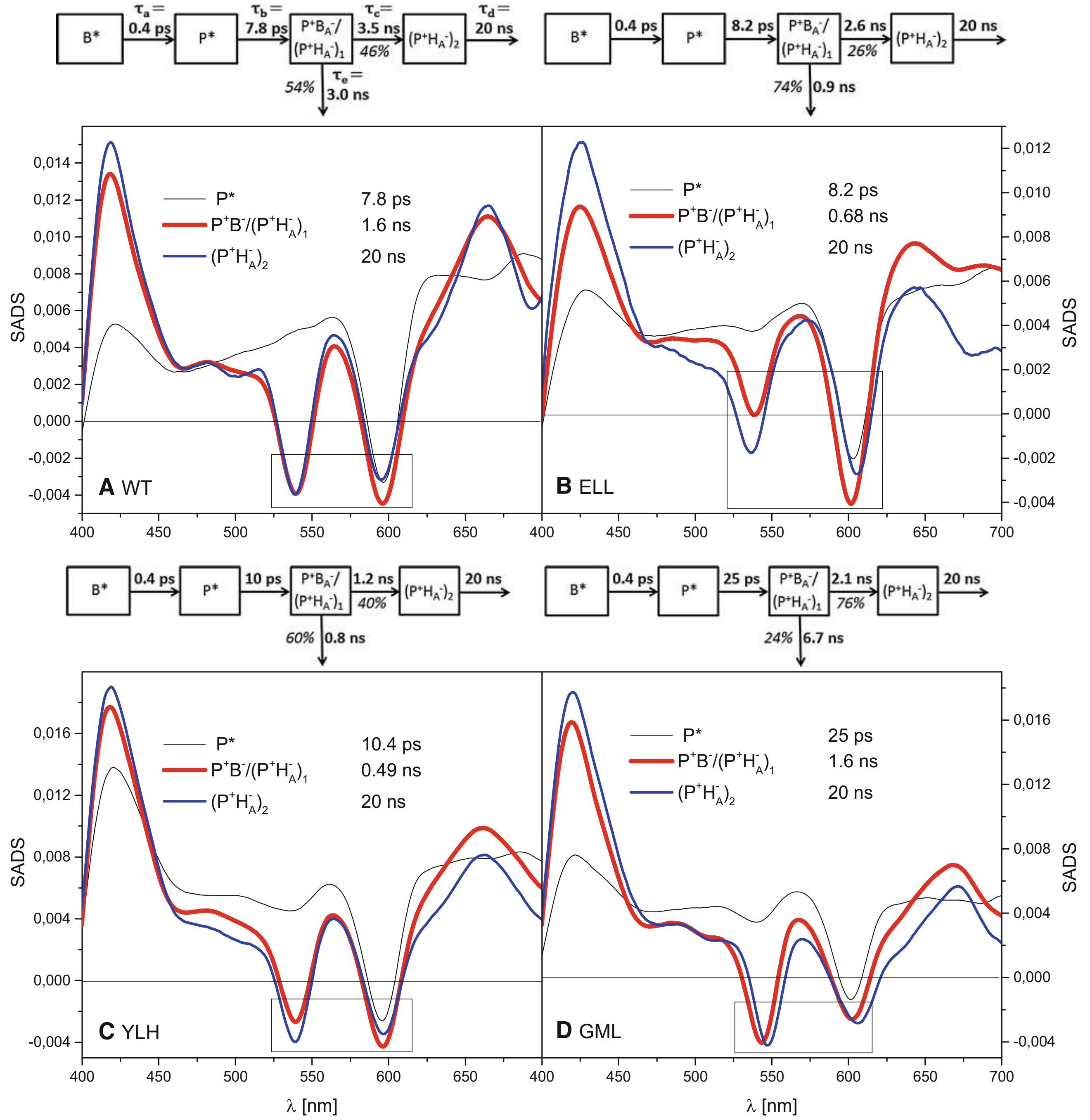

Fig. 6 Species-associated difference spectra and compartmental model schemes for RCs in closed state. The spectra were estimated from femtosecond transient absorption difference spectra recorded following excitation at 800 nm with ~300 fs light pulses. Reversibility of the reaction $P^+B_A^-/(P^+H_A^-)_1 \rightarrow (P^+H_A^-)_2$ was ignored in the modeling due to large free energy gap between the states $P^+B_A^-/(P^+H_A^-)_1$ and $(P^+H_A^-)_2$. The five lifetimes obtained from the target analysis yields the four apparent lifetimes obtained from the global analysis

contribution from the formation of B_A^- (see below). The reason for the blue shift of this band in ELL RC is the removal of a hydrogen bond to H_A in this RC (Fig. 3a) (Bylina et al. 1988).

The main bands of the next DADS (red thin dashed line in Fig. 5a–d) were largely mirror reflections of the respective bands in the charge separation DADS. This was particularly the case for the bands at ~545 nm and at ~640/670 nm, assigned to electron transfer from H_A^- to Q_A. This is to be expected since charge separation populates H_A^-, whereas electron transfer from H_A^- to Q_A recovers H_A. The lifetime of the latter reaction was not significantly

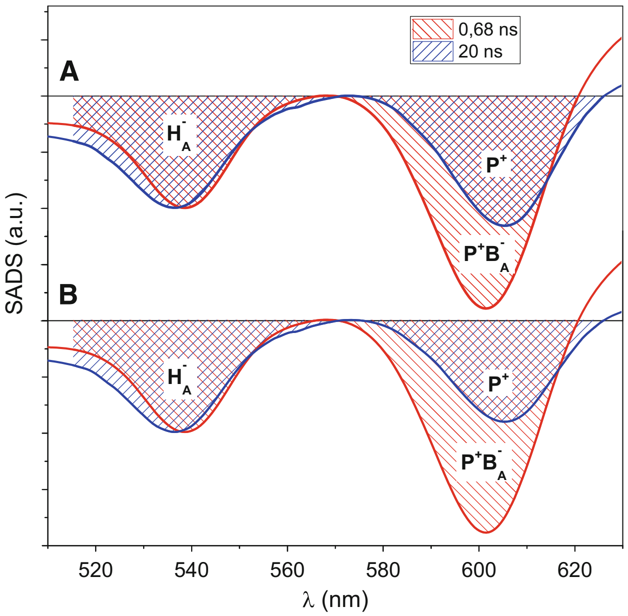

Fig. 7 Comparison of the "fast" and "slow" charge recombination SADS of ELL RCs in the spectral region of Q_x bands at ~545 and ~600 nm. The original SADS (from Fig. 6b) were vertically shifted relative to one another and normalized in order to have the same amplitudes at ~565–570 and ~540 nm. This way, the area above the ~600 nm band of the "slow" SADS represents the contribution of P^+ from the state $P^+H_A^-$ in the ~600 nm band of the "fast" SADS, whereas the remaining area of the latter band represents the contributions of P^+ and B_A^- from the state $P^+B_A^-$. The respective areas labeled "P^+" and "$P^+B_A^-$" allows estimation of the free energy gap between unrelaxed $P^+H_A^-$ and $P^+B_A^-$ from the equation: $\Delta G = kT \ln \frac{\text{“}P^+\text{”}}{\text{“}P^+B_A^-\text{”}} \frac{\Delta\varepsilon(P^+ - P)}{\Delta\varepsilon(P^+ - P) + \Delta\varepsilon\left(B_A^- - B_A\right)}$, where k is the Boltzmann constant, T—absolute temperature, $\Delta\varepsilon(P^+ - P)$, and $\Delta\varepsilon(B_A^-\ B_A)$—-$B_A$)—mean differential absorption coefficients of the respective species within the 600-nm band. **a**—the "slow" charge recombination SADS was taken directly from the target analysis shown in Fig. 6b. **b**–the "slow" charge recombination SADS was corrected in the following way. It was assumed that a part of the ~600-nm band was due to a contribution from open RCs; in order to reject this contribution, the amplitude of the original ~600-nm band was vertically shrunk in such a way that the resulting amplitude ratio of the bands at ~545 and ~600 nm was the same as for WT RCs (compare to the "slow" charge recombination SADS in Fig. 6b)

affected by the mutations (235 ps in the WT vs. ~250–270 ps in the mutant RCs). The non-decaying component (blue) originating from the long-lived state $P^+Q_A^-$ was essentially identical for all RCs. DADS estimated for experimental data obtained at pH 10.5 (data not shown) were similar to those for data obtained at pH 8 (Fig. 5a–d).

Charge separation in closed RCs

Standard experimental conditions commonly used to permanently reduce Q_A in isolated RCs were not fully effective in the case of membrane-bound RCs. The experiments performed under these conditions revealed the presence of mixed populations of open and closed RCs in the samples. It was established that increasing the buffer pH from 8 to 10.5 and shortening the time for the collection of each set of data at the expense of a decreased number of time points (thus leading to somewhat worse signal-to-noise ratio and lower temporal resolution) allowed the collection of data for fully or almost fully closed RCs (see below).

Charge separation DADS obtained for closed RCs at pH 10.5 were generally similar in lineshape to the respective DADS for open RCs except for the region around 600 nm in which, especially in the case of the ELL RCs, some differences were observed (compare panels a–d and e–h in Fig. 5). The lifetimes of charge separation were somewhat increased from ~5 to 7 ps in open RCs (Fig. 5a–c) to ~8–10 ps in closed RCs (Fig. 5e-g), and from 21 to 25 ps for the GML RC (Fig. 5h). This effect of pre-reduction of Q_A has been reported previously (Woodbury et al. 1985; Wang et al. 1994; Gibasiewicz et al. 2009). Changes in the spectral shape of the DADS for charge separation around 600 nm (wavelength of the Q_x absorption band of B_A) may be rationalized by an increased contribution from $P^+B_A^-$ admixing with $P^+H_A^-$ (black spectrum) (Heller et al. 1996). In previous work on isolated WT RCs, an increase of the positive signal at ~600 nm after RC closure was shown and explained by a repulsive electrostatic interaction between Q_A^- and H_A^- that pushes the free energy of $P^+H_A^-$ up toward that of $P^+B_A^-$ (Gibasiewicz et al. 2009). Although in the present work, the spectral shape of the charge separation DADS at around 600 nm in open membrane-bound RCs is more complex than was reported previously for isolated RCs, careful comparison of the DADS for open and closed RCs reveals that the signal at around 600 nm is generally more positive for all the RCs after closing them except for the GML mutant (Fig. 5h). Therefore, we conclude that pre-reduction of Q_A leads in all the membrane-bound RCs under study (except for GML RC, see below) to a similar increase of the $P^+H_A^-$ free energy level as reported for isolated RCs.

The effect of RC closure on the 600 nm region of the charge separation DADS was particularly prominent for the ELL RC (compare Fig. 5b and h). A prominent positive band appeared at this wavelength which was more than half as large as the H_A/H_A^- band at ~545 nm. We interpret this as a manifestation of substantial formation of $P^+B_A^-$ in this RC due to a particularly large shift of the free energy of $P^+H_A^-$ toward that of $P^+B_A^-$ upon pre-reduction of Q_A. In contrast, closure of the GML RC exerted almost no effect on the shape of the charge separation DADS in the ~600 nm region (Fig. 5d, h). This observation may mean that the interaction between Q_A^- and H_A^- does not result in an observable change in the initial free energy gap between the $P^+B_A^-$ and $P^+H_A^-$ in this RC.

Charge recombination in closed RCs

Pre-reduction of Q_A causes back electron transfer from H_A^- to P^+ to be observed during the 2 ns measuring window. Therefore, the lineshapes of the two "slowest" DADS for closed RCs were markedly different from their equivalents for open RCs. Importantly, these closed RC DADS showed significant differences between RCs.

The two processes described by the two "slowest" DADS were, except for the GML RC, attributable to two phases of charge recombination (Fig. 5e–g; compare to data for isolated WT RCs in (Gibasiewicz et al. 2009)). In the case of GML RC, only the slowest phase could confidently be assigned to charge recombination (Fig. 5f). In principle, the phases of charge recombination should be the same as those observed in nanosecond measurements at 690 nm. However, given the different temporal resolutions, temporal windows and signal-to-noise ratios in these two types of experiment, the lifetimes resolved were somewhat different. As expected, the lifetimes of the fast phase of charge recombination, τ_1, were found to be smaller in the femtosecond experiments (see comparison of τ_1 values in nanosecond and femtosecond experiments in Table 1). Importantly, however, results from both techniques showed that the fast phase of charge recombination was slower in WT RCs than in the ELL and YLH mutants, suggesting a larger energetic barrier for this recombination in the former. The 1.6-ns component resolved in the femtosecond experiment for the GML RC had no counterpart in the nanosecond experiment, probably due to its small amplitude at 690 nm and the poorer signal-to-noise ratio in the nanosecond experiment.

The temporal window of 2 ns in the femtosecond experiment was insufficient for a proper estimation of the lifetimes of the slow charge recombination phase. Therefore, in analyzing the data from the femtosecond experiment, the lifetime of the slow phase was fixed for all RCs at 20 ns. As expected and checked, the exact value of this parameter was not essential for the results of fitting procedure.

It is interesting to note the differences between the relative amplitudes of the "slow" and "fast" charge recombination DADS. Focusing on the spectral region covering the bands at ~545 and ~600 nm, it can easily be seen that in the case of WT and YLH RCs (Fig. 5e, g), the contributions of both phases were roughly equal, whereas in the case of ELL RC, the contribution of the 0.68 ns component was much larger than that of the 20 ns component (Fig. 5f). These observations correlate very well with the relative amplitudes from the nanosecond fits (Table 1).

The shape and relative amplitude of the bands in the fast nanosecond DADS found for the GML RC (1.6 ns; Fig. 5h) were markedly different from those obtained for the remaining RCs. The main features of this DADS was "differential-like" structures at ~545 and ~600 nm suggesting that the process underlying this 1.6 ns DADS is not primarily the fast phase of charge recombination as it is in the remaining RCs but rather an electrochromic shift of BPhe absorbance at ~545 nm and BChl absorbance at ~600 nm. This hypothesis was confirmed through a target analysis of the femtosecond data.

Target analysis

Figure 6 presents results of target analysis performed for the femtosecond data collected for closed RCs. A common model of considered states was used for all samples consisting of the following four compartments or species: a BChl excited state (B^*), the excited state of P (P^*), a charge separated state equilibrated over $P^+B_A^-$ and an unrelaxed $(P^+H_A^-)_1$ state, and a relaxed $(P^+H_A^-)_2$ charge separated state (see the schemes above the spectra in Fig. 6). The lifetimes of 0.4 ps ($B^* \rightarrow P^*$) and 20 ns (depicting $(P^+H_A^-)_2$ charge recombination) were fixed. Moreover, a constraint was applied that the sum of amplitudes of the bands at ~545 and ~600 nm for the fast charge recombination spectrum should be the same as the sum of the amplitudes of the respective bands for the slow charge recombination spectrum. (The amplitudes of these bands were measured relative to the local maximum at ~565 nm). This constraint was justified by an assumption that the differential molar extinction coefficients related to photobleaching signals from H_A^- at ~545 nm are the same as those from P^+ and B_A^- at ~600 nm (see below). The resulting spectra of the excited state P^* (black thin lines in Fig. 6) are rather similar to each other for the four samples. In the analysis, one should focus on the differences in the relative amplitudes of the bands at ~545 and ~600 nm in fast (thick red lines) and slow (blue lines) charge recombination spectra.

As mentioned in the Introduction, the relative amplitudes of the Q_x photobleaching bands at ~545 and ~600 nm in the two charge recombination phases are good indicators of the free energy gap between $P^+B_A^-$ and $P^+H_A^-$ on the respective time scales. The bigger the signal at ~600 nm relative to that at ~545 nm, the smaller this gap and the more the $P^+B_A^- \longleftrightarrow P^+H_A^-$ equilibrium is shifted toward the left. Comparison of these two negative bands in the fast recombination species-associated difference spectra (SADS; Fig. 6a–c, red; 1.6 ns for WT, 0.68 ns for ELL, and 0.49 ns for YLH) clearly shows that for WT and YLH RCs, the band at ~600 nm is only slightly deeper than that at ~545 nm, whereas in ELL RC the difference between these bands is much bigger. This difference is consistent with the postulate formulated above that the free energy gap between $P^+B_A^-$ and unrelaxed state $(P^+H_A^-)_1$, is smaller for ELL than for the WT and YLH RCs.

The relative amplitudes of the bands at ~545 and ~600 nm in the "slow" charge recombination spectrum were shown in a previous publication on isolated WT RCs to be similar to each other, with the band at ~545 nm being slightly deeper (Gibasiewicz et al. 2009). A similar pattern is observed for WT, YLH, and GML membrane-bound RCs (Figs. 6a,c,d, blue). An opposite observation that the band at ~600 nm was somewhat deeper than that at ~545 nm in the case of the ELL RC (Fig. 6b, blue) may be explained by a minor admixture of RCs in the open state. This explanation seems to be very likely since we found that full closing of RCs was difficult for all samples—it was necessary to increase pH of the RCs solution to 10.5 in order to close RCs efficiently. However, we also considered an alternative possibility that the band at 545 nm is intrinsically smaller than that at 600 nm in the case of the ELL RC, due to the mutation which may affect Q_x band of H_A. Apparently, the mutation affects also the absorption band of H_A^- above 625 nm which is clearly blue-shifted compared to the remaining samples (compare "fast" and "slow" charge recombination SADS in this region for all samples (Fig. 6)). The two approaches result in somewhat different estimations of the free energy gap between $P^+B_A^-$ and unrelaxed $P^+H_A^-$ (see Fig. 7 and below). For all samples, the "slow" charge recombination SADS is believed to originate from the relaxed state of $P^+H_A^-$ $(P^+H_A^-)_2$, with a negligible contribution from $P^+B_A^-$ in analogy to the slow phase obtained in the nanosecond experiments.

The relative amplitudes or areas of the photobleaching bands at ~545 and ~600 nm in the charge recombination SADS (Fig. 6a–c) may serve to estimate the relative populations of the equilibrated states $P^+B_A^-$ and $(P^+H_A^-)_1$ as well as the free energy gap between these states in a quantitative way described previously (Gibasiewicz et al. 2009) and presented in Fig. 7 for the case of the ELL RCs. In brief, assuming that the 20 ns SADS is contributed to exclusively by relaxed state $(P^+H_A^-)_2$ (with the band at ~545 nm assigned to H_A^- and the band at ~600 nm assigned to P^+), the "excess" of the photobleaching signal of the ~600 nm band in the fast charge recombination SADS (0.49–1.6 ns) relative to the 20 ns SADS in each dataset (except for GML RCs) is a measure of the population of $P^+B_A^-$ that is in equilibrium with $(P^+H_A^-)_1$. Assuming further similar differential extinction coefficients of the photobleaching signals, Δε, for P^+/P and B_A^-/B_A at ~600 nm$(0.5\Delta\varepsilon(P^+ - P) < \Delta\varepsilon(B_A^-\ \ B_A) < 2\Delta\varepsilon(P^+ - P))$-$B_A) < 2\Delta\varepsilon(P^+ - P))$ and testing somewhat different ways of estimation of the photobleaching bands' areas at ~545 and ~600 nm (one of them is illustrated in Fig. 7; in another, we limited the integration of the band to the region of the band minimum (~545 or ~600 nm) ± 20 nm), a set ΔG_1 of ranges was obtained (Table 2).

For the GML RC, unlike for the remaining complexes, the relative amplitudes of the bands at ~545 and ~600 nm in the fast charge recombination SADS were very similar to the corresponding amplitudes in the slow charge recombination SADS (Fig. 6d, red and blue). This observation indicates that the contribution of the state $P^+B_A^-$ being in equilibrium with $(P^+H_A^-)_1$ is negligible and that the initial free energy gap between these states (ΔG_1) is large, which is confirmed by calculations (Table 2, $\Delta G_1 = 90$ meV for the assumed τ_{PB} value of 0.2 ns). On the other hand, the two negative bands at ~545 and ~600 nm in the slow charge recombination SADS are red shifted relative to those in the fast charge recombination SADS. This spectral shift explains the "differential-like" shape of the 1.6-ns DADS (Fig. 5h).

The lifetimes estimated from the target analysis ($\tau_a - \tau_e$) are presented in Fig. 6 in the compartmental model schemes. They allow direct estimation of the branching ratio that determines what percentage of the RCs in equilibrated state $P^+B_A^-/(P^+H_A^-)_1$ recombine (with lifetime τ_e) and what percentage evolve to the relaxed state $(P^+H_A^-)_2$ (with lifetime τ_c)—values are given in the schemes (Fig. 6). Moreover, together with the values of ΔG_1 estimated from the same femtosecond experiment (Table 2), the lifetimes obtained from the target analysis (τ_c and τ_e) allow independent estimation of the molecular lifetimes τ_{12} and τ_{PB} (Fig. 2) from the following formulae:

$$\tau_{12} = P_1\tau_c = \frac{e^{\Delta G_1/kT}}{1 + e^{\Delta G_1/kT}}\tau_c,$$

$$\tau_{PB} = (1 - P_1)\tau_e = \frac{1}{1 + e^{\Delta G_1/kT}}\tau_d,$$

where $(1 - P_1)$ and P_1 are the probabilities of occupation of the states $P^+B_A^-$ and $(P^+H_A^-)_1$, respectively, in the $P^+B_A^-/(P^+H_A^-)_1$ equilibrium, k is the Boltzmann constant, and T is the absolute temperature.

Comparative analysis of the results obtained from the nanosecond and femtosecond experiments

The nanosecond and femtosecond measurements gave consistent raw results, although both the relative amplitudes A_1–A_2 and lifetimes τ_1–τ_2 of the two charge recombination phases obtained from the two techniques were somewhat different (Table 1). In the case of the femtosecond measurements, the amplitudes of the two phases were similar to one another for the WT RC, with the fast phase dominating over the slow phase to a moderate extent for the YLH RC or to a large extent for the ELL RC. The slow phase largely dominated over the fast phase for the GML RC (see also Fig. 5e–h). Similar tendency in A_1/A_2 proportions were observed in the nanosecond experiments (Table 1). Some differences may be explained by different temporal resolution and temporal windows in these two techniques, as well as a worse signal-to-noise ratio in the nanosecond experiment. Probably for the same reasons, no fast component was resolved for GML RC in the nanosecond experiment.

Analysis of the model molecular parameters obtained from the nanosecond and femtosecond data (Table 2) leads to the following observations. Treating the free energy gaps as free parameters (case *b* in the nanosecond experiment), both techniques indicate similar initial free energy gaps (ΔG_1) between the states $P^+B_A^-$ and $(P^+H_A^-)_1$ for WT (77 and 60 meV), ELL (22 and 15 meV), and YLH RCs (79 and 49 meV). The significant value of ΔG_1 for the YLH RC estimated from the femtosecond experiment seems to exclude the possibility that the weak temperature dependence of charge recombination is caused by isoenergeticity of $P^+B_A^-$ and $(P^+H_A^-)_1$ in this case (option *a*). Oppositely, the small value of ΔG_1 for the ELL RC makes both options (*a* and *b*) likely. According to both femtosecond and nanosecond results, all three molecular parameters shown in Table 2, τ_{12}, ΔG_1, and τ_{PB}, co-determine the overall charge recombination kinetics. The femtosecond results, characterized by better temporal resolution, indicate that the protein relaxation is accelerated in all three mutants relative to WT RC, with this relaxation being particularly fast for YLH RC, 1 ns versus 3.1 ns for WT. Ranges of the τ_{PB} values extracted from the femtosecond experiments (from 0.11 ns for YLH to 0.32 ns for ELL) agree well with those published before (Heller et al. 1996; Katilius et al. 1999).

Conclusions

The observed variety of charge recombination dynamics in the mutant RCs is caused by three factors undergoing modulation by the introduced mutations: (1) the initial free energy gap between the states $P^+B_A^-$ and $P^+H_A^-$, (2) the intrinsic rate of $P^+B_A^- \rightarrow PB_A$ charge recombination, and (3) the dynamics of protein relaxation in response to the appearance of the charge separated states. The main factor responsible for the particularly fast charge recombination in the ELL RC is small initial free energy gap between $P^+B_A^-$ and $P^+H_A^-$, whereas large initial free energy gap between these two states is responsible for particularly slow charge recombination in the GML mutant. The YLH RC showed a similar average decay of the charge separated states to that of WT RCs, despite a particularly fast $P^{+-}B_A^- \rightarrow PB_A$ charge recombination which was compensated for by an increased efficiency of protein relaxation. In all the mutant RCs, no significant temperature dependence of the protein relaxation could be concluded from the model calculations, in line with a previous report on WT RCs. The question of whether the free energy gap between $P^+B_A^-$ and $P^+H_A^-$ states is temperature dependent or not was not definitely answered for the WT, ELL, and GML RCs. Model calculations for YLH RCs indicate that this free energy gap decreases at low temperature but still undergoes the temporal evolution. An identification of the structural rearrangements underlying the mutation-specific variations in protein dynamics is a real challenge and will be the subject of future work.

Acknowledgements K.G. acknowledges financial support from the National Science Center, Poland (project entitled "Bio-semiconductor hybrids for photovoltaic cells" No. 2012/07/B/NZ1/02639. MRJ acknowledges funding from the Biotechnology and Biological Sciences Research Council of the UK (Project BB/I022570/1).

References

Arlt T, Schmidt S, Kaiser W, Lauterwasser C, Meyer M, Scheer H, Zinth W (1993) The accessory bacteriochlorophyll: a real electron carrier in primary photosynthesis. Proc Natl Acad Sci USA 90:11757–11761

Arlt T, Dohse B, Schmidt S, Wachtveitl J, Laussermair E, Zinth W, Oesterhelt D (1996) Electron transfer dynamics of *Rhodopseudomonas viridis* reaction centers with a modified binding site for the accessory bacteriochlorophyll. Biochemistry 35:9235–9244

Bylina EJ, Kirmaier C, McDowell L, Holten D, Youvan DC (1988) Influence of an amino-acid residue on the optical properties and electron transfer dynamics of a photosynthetic reaction centre complex. Nature 336:182–184

Byrdin M, Thiagarajan V, Villette S, Espagne A, Brettel K (2009) Use of ruthenium dyes for subnanosecond detector fidelity testing in real time transient absorption. Rev Sci Instrum 80:043102

Chan CK, DiMagno TJ, Chen LX, Norris JR, Fleming GR (1991) Mechanism of the initial charge separation in bacterial photosynthetic reaction centers. Proc Natl Acad Sci USA 88:11202–11206

Chidsey CED, Kirmaier C, Holten D, Boxer SG (1984) Magnetic field dependence of radical-pair decay kinetics and molecular triplet quantum yield in quinone-depleted reaction centers. Biochim Biophys Acta 766:424

Fajer J, Brune DC, Davis MS, Forman M, Spaulding LD (1975) Primary charge separation in bacterial photosynthesis: oxidized chlorophylls and reduced pheophytin. Proc Natl Acad Sci USA 72:4956–4960

Gibasiewicz K, Pajzderska M (2008) Primary radical pair P^+H^- lifetime in *Rhodobacter sphaeroides* with blocked electron transfer to QA. effect of o-phenanthroline. J Phys Chem B 112:1858–1865

Gibasiewicz K, Pajzderska M, Ziółek M, Karolczak J, Dobek A (2009) Internal electrostatic control of the primary charge separation and recombination in reaction centers from *Rhodobacter sphaeroides* revealed by femtosecond transient absorption. J Phys Chem B 113:11023–11031

Gibasiewicz K, Pajzderska M, Potter JA, Fyfe PK, Dobek A, Brettel K, Jones MR (2011) Mechanism of recombination of the $P^+H_A^-$ radical pair in mutant *Rhodobacter sphaeroides* reaction centers with modified free energy gaps between $P^+B_A^-$ and $P^+H_A^-$. J Phys Chem B 115:13037–13050

Gibasiewicz K, Pajzderska M, Dobek A, Karolczak J, Burdziński G, Brettel K, Jones MR (2013a) Analysis of the temperature-dependence of $P^+H_A^-$ charge recombination in the *Rhodobacter sphaeroides* reaction center suggests nanosecond temperature-independent protein relaxation. Phys Chem Chem Phys 15:16321–16333

Gibasiewicz K, Dobek A, Brettel K, Jones MR (2013b) Analysis of the kinetics of $P^+H_A^-$ recombination in membrane-embedded wild-type and mutant *Rhodobacter sphaeroides* reaction centers between 298 and 77 K indicates that the adjacent negatively charged Q_A ubiquinone modulates the free energy of $P^+H_A^-$ and may influence the rate of the protein dielectric response. J Phys Chem B 117:11112–11123

Hartwich G, Lossau H, Michel-Beyerle ME, Ogrodnik A (1998) Nonexponential fluorescence decay in reaction centers of *Rhodobacter sphaeroides* reflecting dispersive charge separation up to 1 ns. J Phys Chem B 102:3815–3820

Heller BA, Holten D, Kirmaier C (1995) Control of electron transfer between the L- and M-sides of photosynthetic reaction. Biochemistry 34:5294

Heller BA, Holten D, Kirmaier C (1996) Effects of Asp residues near the L-side pigments in bacterial reaction centers. Biochemistry 35:15418–15427

Holzwarth AR (1996) Data analysis of time-resolved measurements. In: Amesz J, Hoff AJ (eds) Biophysical techniques in photosynthesis advances in photosynthesis research. Kluwer Academic Publishers, Dordrecht, pp 75–92

Huber H, Meyer M, Nägele T, Hartl I, Scheer H, Zinth W, Wachtveitl J (1995) Primary photosynthesis in reaction centers containing four different types of electron acceptors at site HA. Chem Phys 197:297–305

Hunter CN, Daldal F, Thurnauer MC, Beatty JT (2009) The purple phototropic bacteria, advances in photosynthesis and respiration, vol 28. Springer, Dordrecht

Jones MR (2009) The petite purple photosynthetic powerpack. Biochem Soc Trans 37:400–407

Jones MR, Fowler GJS, Gibson LCD, Grief GG, Olsen JD, Crielaard W, Hunter CN (1992) Construction of mutants of *Rhodobacter sphaeroides* lacking one or more pigment-protein complexes and complementation with reaction centre, LH1 and LH2 genes. Mol Microbiol 6:1173–1184

Jones MR, Heer-Dawson M, Mattioli TA, Hunter CN, Robert B (1994) Site-specific mutagenesis of the reaction centre from *Rhodobacter sphaeroides* studied by Fourier-transform Raman spectroscopy: mutations at tyrosine M210 do not affect the electronic structure of the primary donor. FEBS Lett 339:18–24

Katilius E, Turanchik T, Lin S, Taguchi AKW, Woodbury NW (1999) B-side electron transfer in a *Rhodobacter sphaeroides* reaction center mutant in which the B-side monomer bacteriochlorophyll is replaced with bacteriopheophytin. J Phys Chem B 103:7386–7389

Kennis TM, Shkuropatov AY, van Stokkum IHM, Gast P, Hoff AJ, Shuvalov VA, Aartsma TJ (1997) Formation of a long-lived $P^+B(\mathrm{A})^-$ state in plant pheophytin-exchanged reaction centers of *Rhodobacter sphaeroides* R26 at low temperature. Biochemistry 36:16231–16238

Kirmaier C, Holten D (1988) Subpicosecond characterization of the optical properties of the primary electron donor and the mechanism of the initial electron transfer in *Rhodobacter capsulatus* reaction centers. FEBS Lett 239:211–218

Kirmaier C, Holten D (1990) Evidence that a distribution of bacterial reaction centers underlies the temperature detection-wavelength dependence of the rates of the primary electron-transfer reactions. Proc Natl Acad Sci USA 87:3552–3556

Kirmaier C, Holten D (1991) An assessment of the mechanism of initial electron transfer in bacterial reaction centers. Biochemistry 30:609–613

Kirmaier C, Gaul D, DeBey R, Holten D, Schenck CC (1991) Charge separation in a reaction center incorporating bacteriochlorophyll for photoactive bacteriopheophytin. Science 251:922–927

Kirmaier C, Laporte L, Schenck CC, Holten D (1995) Nature and dynamics of the charge-separated intermediate in reaction centers in which bacterichlorophyll replaces the photoactive bacteriopheophytin. 2: The rates and yields of charge separation and recombination. J Phys Chem 99:8910–8917

Kurzynski M, Chelminiak P (2013) Temperature and detection-wavelength dependence of the electron transfer rates in initial stages of photosynthesis. J Phys Chem B 117:12339–12346

Laporte L, Kirmaier C, Schenck CC, Holten D (1995) Free-energy dependence of the rate of electron transfer to the primary quinone in beta-type reaction centers. Chem Phys 197:225–237

Lin X, Murchison HA, Nagarajan V, Parson WW, Allen JP, Williams JC (1994) Specific alteration of the oxidation potential of the electron donor in reaction centers from *Rhodobacter sphaeroides*. Proc Natl Acad Sci USA 91:10265–10269

Lockhart DJ, Kirmaier C, Holten D, Boxer SG (1990) Electric field effects on the initial electron-transfer kinetics in bacterial photosynthetic reaction centers. J Phys Chem 94:6987–6995

Maciejewski A, Naskrecki R, Lorenc M, Ziolek M, Karolczak J, Kubicki J, Matysiak M, Szymanski M (2000) Transient absorption experimental set-up with femtosecond time resolution. Femto- and picosecond study of DCM molecule in cyclohexane and methanol solution. J Mol Struct 555:1–13

McAuley KE, Fyfe PK, Ridge JP, Cogdell RJ, Isaacs NW, Jones MR (2000) Ubiquinone binding, ubiquinone exclusion, and detailed cofactor conformation in a mutant bacterial reaction center. Biochemistry 39:15032–15043

Michel H, Epp O, Deisenhofer J (1986) Pigment—protein interactions in the photosynthetic reaction centre from *Rhodopseudomonas viridis*. EMBO J 5:2445

Ogrodnik A, Volk M, Letterer R, Feick R, Michel-Beyerle ME (1988) Determination of free energies in reaction centers of *Rb. sphaeroides*. Biochim Biophys Acta 936:361–371

Ogrodnik A, Keupp W, Volk M, Aumeier G, Michel-Beyerle ME (1994) Inhomogeneity of radical pair energies in photosynthetic reaction centers revealed by differences in recombination dynamics of P^+HA^- when detected in delayed emission and in absorption. J Phys Chem 98:3432–3439

Okamura MY, Isaacson RA, Feher G (1975) Primary acceptor in bacterial photosynthesis: obligatory role of ubiquinone in photoactive reaction centers of *Rhodopseudomonas spheroids*. Proc Natl Acad Sci USA 79:3491–3495

Parson WW, Warshel A (2009) Mechanism of charge separation in purple bacterial reaction centers. In: Hunter CN, Daldal F, Thurnauer MC, Beatty JT (eds) The purple phototropic bacteria, advances in photosynthesis, respiration, vol 28. Springer, Dordrecht, pp 355–377

Peloquin JM, Williams JAC, Lin X, Alden RG, Taguchi AKW, Allen JP, Woodbury NW (1994) Time-dependent thermodynamics during early electron transfer in reaction centers from *Rhodobacter sphaeroides*. Biochemistry 33:8089–8100

Pieper J, Renger G (2009) Protein dynamics investigated by neutron scattering. Photosynth Res 102:281–293

Potter JA, Fyfe PK, Frolov D, Wakeham MC, van Grondelle R, Robert B, Jones MR (2005) Strong effects of an individual water molecule on the rate of light-driven charge separation in the *Rhodobacter sphaeroides* reaction center. J Biol Chem 280:27155–27164

Ridge JP, van Brederode ME, Goodwin MG, van Grondelle R, Jones MR (1999) Mutations that modify or exclude binding of the Q(A) ubiquinone and carotenoid in the reaction center from *Rhodobacter sphaeroides*. Photosynth Res 59:9–26

Rodriguez J, Kirmaier C, Johnson MR, Friesner RA, Holten D, Sessler JL (1991) Picosecond studies of quinone-substituted monometalated porphyrin dimers: evidence for superexchange-mediated electron transfer in a photosynthetic model system. J Am Chem Soc 113:1652–1659

Schenck CC, Blankenship RE, Parson WW (1982) Radical-pair decay kinetics, triplet yields and delayed fluorescence from bacterial reaction centers. Biochim Biophys Acta 680:44–59

Schmidt S, Arlt T, Hamm P, Huber H, Nägele T, Wachtveitl J, Meyer M, Scheer H, Zinth W (1994) Energetics of the primary electron transfer reaction revealed by ultrafast spectroscopy on modified bacterial reaction centers. Chem Phys Lett 223:116–120

Schmidt S, Arlt T, Hamm P, Huber H, Nägele T, Wachtveitl J, Meyer M, Scheer H, Zinth W (1995) Electron-transfer dynamics in modified bacterial reaction centers containing pheophytin-a instead of bacteriopheophytin-a. Spectrochim Acta Part A 51:1565–1578

Shkuropatov AY, Shuvalov VA (1993) Electron transfer in pheophytin a-modified reaction centers from *Rhodobacter sphaeroides* (R-26). FEBS Lett 322:168–172

Shuvalov VA, Parson WW (1981) Energies and kinetics of radical pairs involving bacteriochlorophyll and bacteriopheophytin in bacterial reaction centers. Proc Natl Acad Sci USA 78:957–961

Snellenburg JJ, Laptenok S, Seger R, Mullen KM, van Stokkum IHM (2012) Glotaran: a java-based graphical user interface for the R package TIMP. J Stat Softw 49:1–22

Tang CK, Williams JC, Taguchi AKW, Allen JP, Woodbury NW (1999) $P^{+}H(\mathrm{A})^{-}$ charge recombination reaction rate constant in *Rhodobacter sphaeroides* reaction centers is independent of the P/P^{+} midpoint potential. Biochemistry 38:8794–8799

Torchala M, Kurzynski M (2008) Underdamped vibrations control the primary electron transfer in photosynthesis at low temperatures. J Phys Chem B 112:6508–6512

van Stokkum IHM, Larsen DS, van Grondelle R (2004) Global and target analysis of time-resolved spectra. Biochim Biophys Acta 1657:82–104

Volk M, Ogrodnik A, Michel-Beyerle ME (1995) The recombination dynamics of the radical pair $P^{+}H^{-}$ in external magnetic and electric fields. In: Blankenship RE, Madigan MT, Bauer CE (eds) Anoxygenic photosynthetic bacteria. Kluwer Academic Publishers, Dordrecht/Boston/London, p 595

Wang S, Lin S, Lin X, Woodbury NW, Allen JP (1994) Comparative study of reaction centers from purple photosynthetic bacteria: isolation and optical spectroscopy. Photosynth Res 42:203–2015

Wang H, Lin S, Allen JP, Williams JAC, Blankert S, Laser C, Woodbury NW (2007) Protein dynamics control the kinetics of initial electron transfer in photosynthesis. Science 316:747–750

Wang H, Lin S, Katilius E, Laser C, Allen JP, Williams JAC, Woodbury NW (2009) Unusual temperature dependence of photosynthetic electron transfer due to protein dynamics. J Phys Chem B 113:818–824

Wang H, Hao Y, Jiang Y, Lin S, Woodbury NW (2012) Role of protein dynamics in guiding electron-transfer pathways in reaction centers from rhodobacter sphaeroides. J Phys Chem B 116:711–717

Woodbury NWT, Allen JP (1995) The pathway, kinetics and thermodynamics of electron transfer in wild type and mutant reaction centers of purple nonsulfur bacteria. In: Blankenship RE, Madigan MT, Bauer CE (eds) Anoxygenic photosynthetic bacteria. Kluwer Academic Publishers, Dordrecht/Boston/London, p 527

Woodbury NWT, Parson WW (1984) Nanosecond fluorescence from isolated photosynthetic reaction centers of Rhodopseudomonas sphaeroides. Biochim Biophys Acta 767:345–361

Woodbury NW, Becker M, Middendorf D, Parson WW (1985) Picosecond kinetics of the initial photochemical electron-transfer reaction in bacterial photosynthetic reaction centers. Biochemistry 24:7516–7521

Woodbury NWT, Parson WW, Gunner MR, Prince RC, Dutton PL (1986) Radical-pair energetics and decay mechanisms in reaction centers containing anthraquinones, naphthoquinones or benzoquinones in place of ubiquinone. Biochim Biophys Acta 851:6–22

Zhu JY, van Stokkum IHM, Paparelli L, Jones MR, Groot ML (2013) Early bacteriopheophytin reduction in charge separation in reaction centers of *Rhodobacter sphaeroides*. Biophys J 104(11):2493–2502

Zinth W, Wachtveitl J (2005) The first picoseconds in bacterial photosynthesis—ultrafast electron transfer for the efficient conversion of light energy. ChemPhysChem 6:871–880

Supporting Information

Extended description of the model-based calculations of the molecular parameters

The observed weak temperature dependence of the charge recombination reaction in the ELL and YLH RCs may be explained in two ways using the model shown in Fig. 2 and data from the nanosecond measurements. The first assumes that the initial charge separated state $(P^+H_A^-)_1$ is quasi-isoenergetic with $P^+B_A^-$ and the relaxed charge separated state $(P^+H_A^-)_2$ is energetically far below $P^+B_A^-$ (option "*a*"). The second assumes that the free energy gaps between $P^+B_A^-$ and $(P^+H_A^-)_1$ and between $(P^+H_A^-)_1$ and $(P^+H_A^-)_2$ may decrease with decreasing temperature, which causes a similar efficiency of thermally activated charge recombination, via $P^+B_A^-$, at different temperatures (option "*b*"; see below). Other words, lowering the thermal energy is compensated by lowering the energetic barrier of the charge recombination reaction. Both of these options are discussed separately below. For WT RCs two subcases with fixed ΔG_i were considered – one with τ_{PB} fixed at the level of 0.2 ns (option *a*) and another one with τ_{PB} =1 ns (option *a'*).

Option a: Constraints on values of ΔG_i. On the basis of the parameters from the fits of the nanosecond kinetic data (Table 1 and Fig. 4) the molecular parameters shown in the model in Fig. 2 can be estimated. In the following, instead of the lifetimes shown in Fig. 2 their reciprocals, rate constants (k) are used. In the Appendix, formulae relating the fit and molecular parameters are presented. Unfortunately, the number of four linearly independent equations, A5, A6, A15, and A16 (see Appendix), resulting from solution of the proper set of differential equations (Eqs. A1) is lower than the number of seven molecular parameters $(\mathrm{k_{12}, k_t, k_{dir1}, k_{dir2}, k_{PB}, \Delta G_1, \Delta G_2})$, resulting from the model (Fig. 2). Therefore, it is necessary to make assumptions as to the values of some of these parameters in order to estimate the remaining ones. Obviously, this may be done in a multiple ways. However, given the qualitative considerations presented above, it seems justifiable to assume first that for the ELL and YLH RCs, ΔG_1 = 0 meV and ΔG_2 = 250 meV. As mentioned above, the precise value of ΔG_2 is not essential for the estimations, the essential factor being that it is sufficiently large that thermally activated charge recombination from the relaxed $P^+H_A^-$ state is not effective and thus may be neglected. The above assumptions regarding the values of ΔG_1 and ΔG_2 are sufficient to yield the weak or absent temperature dependence of charge recombination in the mutant RCs. An additional assumption for the ELL and YLH RCs is that $k_{dir1} = k_{dir2}$.

As can be seen from the formulae in the Appendix (Eqs. A20-A21), the relaxation and triplet parameters, k_{12} and k_t, may be estimated directly from the fit parameters (Table 1) with the only assumption made on the values of ΔG_1 and ΔG_2 via the population factors P_1 and P_2 (Eqs. A7-A8) describing the probability that the state $P^+H_A^-$, being in equilibrium with $P^+B_A^-$, is populated. It should be noted that $P_1 = 1/2$ for $\Delta G_1 = 0$ meV and $P_2 \approx 1$ for $\Delta G_2 = 250$ meV, independent of temperature.

Values of τ_{12} and τ_t estimated for the mutant RCs using the above constraints on ΔG_i are collected in Table S1 (option *a*). In the case of the WT RC the values of ΔG_1 and ΔG_2 were fixed on temperature-independent levels of 90 and 128 meV (±20%), respectively. These ΔG_i values were obtained previously (Gibasiewicz et al. 2013b) from the temperature dependence of the fit parameters τ_1 and τ_2 (defined as those shown in Table 1), under the assumption that the sole source of their temperature dependence is decreasing accessibility of the state $P^+B_A^-$ when lowering the temperature. In the present model, the values of ΔG_i for the WT RC depend strongly on τ_{PB} and in option *a* they were estimated assuming $\tau_{PB} = 0.2$ ns (Heller et al. 1996; Katilius et al. 1999). The only major effect of increasing τ_{PB} to 1 ns (Schmidt et al. 1994; Kirmaier et al. 1995) was, as expected, decreasing the values of ΔG_1 and ΔG_2 to 44 and 85 meV, respectively (Table S1; option *a'*).

It can be seen that the relaxation lifetime τ_{12} for the ELL RC is 5 ns at 78 K and 6.5 ns at 296 K, not very different from equivalent values estimated for WT RCs 6.1 ns at 78 K and ~4 ns at 298 K). Under the above constraints, the much faster overall charge recombination in the case of the ELL RC is caused by the isoenergetic character of the states $P^+B_A^-$ and $(P^+H_A^-)_1$ and, consequently, by particularly efficient charge recombination via $P^+B_A^-$ and not by particularly slow relaxation, which in principle could also contribute to acceleration of charge recombination.

RCs of the YLH mutant are characterized by an approximately three times faster protein relaxation ($\tau_{12} = 1.5$ ns at 78 K and 1.9 ns at 294 K; Table S1; option *a*) than in ELL RCs despite the fact that $(P^+H_A^-)_1$ was assumed to be isoenergetic with $P^+B_A^-$ in both RCs. The fast relaxation is one of the reasons why the relative amplitude of the slower phase is significantly larger in the YLH RC than in the ELL RC; simply relaxation to the state $(P^+H_A^-)_2$ is a more competitive pathway in the YLH RC (Fig. 2). Another reason could in principle be the slower intrinsic charge recombination lifetime, τ_{PB}, from $P^+B_A^-$ in the YLH RC (Table S1), although this is not confirmed by the femtosecond experiment (see the main text).

Formation of a triplet state in all the RCs undergoing the modelling was characterized by a lifetime τ_t ranging from ~30 to ~60 ns which was somewhat temperature-dependent, but not sensitive to different constraints put on the model parameters (Table S1; options *a* and *b*).

Table S1 also shows lifetimes τ_{dir1}, τ_{dir2}, and τ_{PB} calculated from Eqs. A5 and A6 under additional constraints ($\tau_{dir1} = \tau_{dir2}$ for the ELL and YLH RCs, as described above). However, it should be noted that the constraint $\tau_{dir1} = \tau_{dir2}$ is not necessarily valid. We have also assumed one single value for τ_{PB} which is also not necessarily valid. The value of τ_{PB} may be different in unrelaxed and relaxed states of the RC, and therefore the values of the parameters τ_{dir1}, τ_{dir2}, and τ_{PB} shown in Table S1 should be treated as very approximate.

Option b: Constraints on values of τ_{diri} and τ_{PB}. Leaving ΔG_1 and ΔG_2 as free parameters and fixing τ_{diri} and τ_{PB} led to an alternative interpretation of the weak temperature dependence of charge recombination observed in the ELL and YLH RCs. Under such conditions the energy levels of the states $(P^+H_A^-)_1$ and $(P^+H_A^-)_2$ become temperature dependent. Table S1 shows results of estimations performed for values of τ_{PB} taken from the modelling of the femtosecond data (see the main text). It was further assumed that $\tau_{dir1} = \tau_{dir2} = 100$ ns (smaller values of $\tau_{dir1} = \tau_{dir2}$ led to non-physical solutions). With these assumptions, for ELL RC the free energy of $(P^+H_A^-)_1$ remained almost isoenergetic with $P^+B_A^-$, independent of temperature, whereas the energy of $(P^+H_A^-)_2$ strongly depended on temperature (ΔG_2 equals 131 meV at RT and only 42 meV at 78 K). For the YLH RC both ΔG_1 and ΔG_2 significantly changes with temperature. The free energy levels estimated for the ELL RC (options *a* and *b*) are presented in Fig. S1. Interestingly, in option *b* the estimated relaxation lifetimes, τ_{12}, are not significantly different from those estimated in option *a*.

The assumed constraints under option *b* were also applied to WT RCs (Table S1). It turned out that the strong temperature dependence of charge recombination in WT RCs may be modeled not only under the assumption of temperature-independence of ΔG_1 and ΔG_2 as was done previously (Gibasiewicz et al. 2013b) but also when treating these gaps as free parameters. The results presented in Table S1 show that similar to the case for the YLH RCs, the free energy gaps ΔG_1 and ΔG_2 in the WT RC decrease with decreasing temperature, although the effect is less pronounced as expected from stronger temperature dependence of charge recombination in WT RCs.

Appendix

In order to relate molecular parameters shown in Fig. 2 with the fit parameters obtained experimentally in the nanosecond experiment and presented in Table 1 one needs to solve the following set of differential equations (with lifetimes replaced by their reciprocals – rate constants; compare very similar models used before (Gibasiewicz et al. 2013a, 2013b)):

$$\begin{cases} \frac{dA(t)}{dt} = -k_{PH1}A(t) \\ \frac{dB(t)}{dt} = k_{12}P_1A(t) - k_{PH2}B(t) \\ \frac{dC(t)}{dt} = k_tP_2B(t) \end{cases} \quad (A1)$$

where *t* stands for time,

$$A(t) = [(P^+H_A^-)_1](t) + [(P^+B_A^-)_1](t) \quad (A2)$$

$$B(t) = [(P^+H_A^-)_2](t) + [(P^+B_A^-)_2](t) \quad (A3)$$

$$C(t) = [{}^3P](t) \quad (A4)$$

and $[(P^+H_A^-)_i](t)$ and $[(P^+B_A^-)_i](t)$ (i = 1, 2) are transient concentrations of the respective states shown in Fig. 2. $(P^+B_A^-)_1$ and $(P^+B_A^-)_2$ are the states being in equilibrium with the states $(P^+H_A^-)_1$ and $(P^+H_A^-)_2$, respectively; in the energetic scheme, the states $(P^+B_A^-)_1$ and $(P^+B_A^-)_2$ are drawn as having identical energy levels and are labeled $P^+B_A^-$. This is because the aim of the Fig. 2 is to show energetic relaxation of the state $P^+H_A^-$ relative to that of the state $P^+B_A^-$. However, it is likely that the state $P^+B_A^-$ relaxes in parallel with the state $(P^+H_A^-)$ but to a different extent.

Furthermore,

$$k_{PH1} = k_{PB}(1 - P_1) + (k_{12} + k_{dir1})P_1 \quad (A5)$$

$$k_{PH2} = k_{PB}(1 - P_2) + (k_t + k_{dir2})P_2 \quad (A6)$$

where P_1 and P_2 are probabilities of population of the states $(P^+H_A^-)_1$ and $(P^+H_A^-)_2$, respectively, being in equilibrium with the respective states of $P^+B_A^-$ (the total probability of population of the $(P^+H_A^-)_1$ and $(P^+B_A^-)_1$ states is normalized to one; similarly for the $(P^+H_A^-)_2$ and $(P^+B_A^-)_2$ states):

$$P_1 = \left(1 + \exp\left(-\frac{\Delta G_1}{kT}\right)\right)^{-1} \quad (A7)$$

$$P_2 = \left(1 + \exp\left(-\frac{\Delta G_2}{kT}\right)\right)^{-1} \quad (A8)$$

Solution of the set of differential equations leads to the following formulae:

$$A(t) = e^{-k_{PH1}t} \quad (A9)$$

$$B(t) = -\frac{(e^{-k_{PH1}t} - e^{-k_{PH2}t})k_{12}P_1}{k_{PH1} - k_{PH2}} \quad (A10)$$

$$C(t) = \frac{k_{12}(k_{PH1} - e^{-k_{PH2}t}k_{PH1} + (-1 + e^{-k_{PH1}t})k_{PH2})k_tP_1P_2}{k_{PH1}(k_{PH1} - k_{PH2})k_{PH2}} \quad (A11)$$

These equations describe concentrations of different states in the system. In order to get a formula for change of absorbance one has to use differential extinction coefficients for different states. In general:

$$\Delta\mathrm{OD}(t) = A(t)\cdot\Delta\varepsilon(P^{+}H_{A}^{-}/PH_{A}) + B(t)\cdot\Delta\varepsilon(P^{+}H_{A}^{-}/PH_{A}) + C(t)\cdot\Delta\varepsilon({}^{3}P/P) \qquad \text{(A12)}$$

Assuming, as before (Gibasiewicz et al. 2013a, 2013b), that at 690 nm $\Delta\varepsilon(P^{+}H_{A}^{-}/PH_{A}) = \Delta\varepsilon(P^{+}B_{A}^{-}/PB_{A}) = 5\Delta\varepsilon({}^{3}P/P)$ the formula for normalized differential absorbance is given by:

$$\Delta\mathrm{OD}(t) = A(t) + B(t) + \frac{1}{5}C(t) \qquad \text{(A13)}$$

After substitution of A9-A11 to A13 one obtains an equation identical to that one used in two-exponential fitting of the nanosecond kinetics:

$$\Delta\mathrm{OD}(t) = A_1 \exp\left(-\frac{t}{\tau_1}\right) + A_2 \exp\left(-\frac{t}{\tau_2}\right) + A_0 \qquad \text{(A14)}$$

where:

$$A_1 = \frac{5k_{PH1}^2 - 5k_{PH1}k_{PH2} - 5k_{12}k_{PH1}P_1 + k_{12}k_tP_1P_2}{5k_{PH1}^2 - 5k_{PH1}k_{PH2}} \qquad \text{(A15)}$$

$$A_2 = \frac{5k_{12}k_{PH2}P_1 - k_{12}k_tP_1P_2}{5k_{PH1}k_{PH2} - 5k_{PH2}^2} \qquad \text{(A16)}$$

$$A_0 = \frac{k_{12}k_tP_1P_2}{5k_{PH1}k_{PH2}} \qquad \text{(A17)}$$

and experimental lifetimes are the same as model ones:

$$\tau_1 = \frac{1}{k_{PH1}}, \qquad \text{(A18)}$$

$$\tau_2 = \frac{1}{k_{PH2}}. \qquad \text{(A19)}$$

Out of the three equations A15-A17, only two are linearly independent since the third one may be calculated from the normalization condition: $A_1 + A_2 + A_0 = 1$. These amplitudes are identical to normalized experimental amplitudes.

Eq. A13 allow more precise correction for extinction coefficients than formulas used previously (Gibasiewicz et al. 2013a, 2013b).

Thus, four linearly independent equations A5, A6, A15, A16 interrelate seven model-based parameters, $k_{12}, k_t, k_{dir1}, k_{dir2}, k_{PB}, \Delta G_1, \Delta G_2$ (Fig. 2), with five parameters obtained from the two-exponential fitting, τ_1, τ_2, A_0-A_2 (Table 1).

In particular, from eqs. A15-A17, the following useful formulae for the $k_{12}P_1$ and k_tP_2 products may be derived:

$$k_{12}P_1 = k_{PH1} - A_1k_{PH1} - A_2k_{PH2} \qquad \text{(A20)}$$

$$k_tP_2 = \frac{5(1-A_1-A_2)k_{PH1}k_{PH2}}{((1-A_1)k_{PH1} + A_2k_{PH2})} \qquad \text{(A21)}$$

Finally, it is important to notice that the temperature-dependent lifetimes, τ_{T1} and τ_{T2}, in Fig. 2 may be calculated from the formulae (compare to formulae A5 and A6):

$$\mathrm{k_{T1} = k_{PB}(1 - P_1)}, \tag{A22}$$

$$\mathrm{k_{T2} = k_{PB}(1 - P_2)}. \tag{A23}$$

Table S1. Model parameters for charge recombination kinetics.

Sample	T [K]	**Model parameters**(1)							
		Op-tion	**τ_{12} [ns]**	τ_t [ns]	ΔG_1 [meV]	ΔG_2 [meV]	τ_{dir1} [ns]	τ_{dir2} [ns]	τ_{PB} [ns]
WT	298	*a*	**4.3±1.1**	29±10	*90±18*	*128±26*	23±55	110±430	*0.2*
		a'	**3.7±1.0**	29±10	*44±9*	*85±17*	23±36	120±390	*1.0*
		b	**4.2±1.1**	29±10	77±17	119±14	*150±30*		*0.26±0.15*
	78	*a*	**6.1±1.5**	35±12	*90±18*	*128±26*	10±2	103±75	*0.2*
		a'	**6.1±1.5**	35±12	*44±9*	*85±17*	10±2	103±75	*1.0*
		b	**6.0±1.5**	35±12	25±4	48±16	*150±30*		*0.26±0.15*
ELL	296	*a*	**6.5±2.1**	46±15	*0*	*250*	35±10		0.54±0.10
		b	**9.1±3.7**	46±15	22±14	131±14	*100±20*		*0.32±0.10*
	78	*a*	**5.0±1.6**	30±10	*0*	*250*	62±33		0.68±0.13
		b	**7.7±2.8**	30±10	7.9±3.3	42±10	*100±20*		*0.32±0.10*
YLH	296	*a*	**1.9±0.5**	56±19	*0*	*250*	21±5		1.30±0.29
		b	**3.7±1.0**	56±19	79±16	140±16	*100±20*		*0.11±0.07*
	78	*a*	**1.5±0.4**	30±10	*0*	*250*	65±36		0.97±0.22
		b	**2.9±0.8**	30±10	19±4	50±11	*100±20*		*0.11±0.07*

(1)Model parameters were estimated from the fit parameters of the nanosecond kinetics shown in Table 1 and the formulae shown in the Appendix. Assumed values are shown in italics (in most cases, ranges of assumed values were considered). Uncertainties of the model parameters were estimated using the formula: $u(y) = \sqrt{\sum_i \left(u(x_i)\ \frac{\partial y}{\partial x_i}\right)^2}$, where y is any of the model parameters, x_i is i-th independent variable (fit parameter), $u(x_i)$ is uncertainty of i-th independent variable (assumed to be ±20%). Prior to uncertainty estimations, formulas for model parameters were transformed as a function of independent variables obtained directly from the fit, which were $\mathrm{A}_1, \mathrm{A}_2, \mathrm{A}_0, \tau_1, \tau_2$.

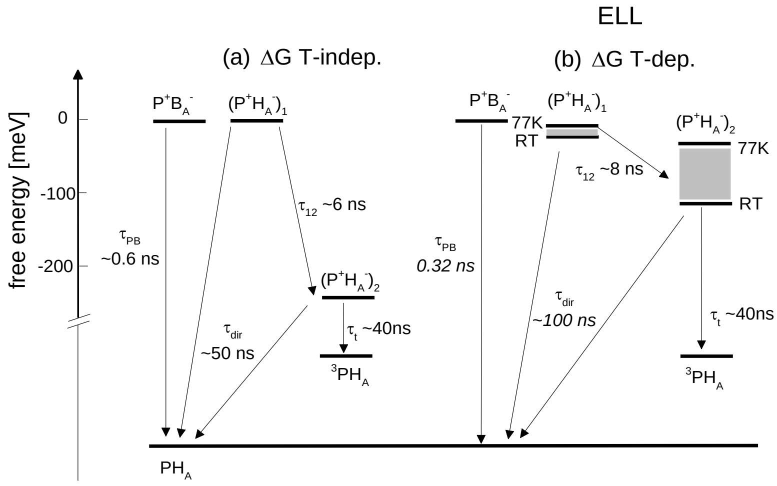

Fig. S1. Comparison of two possible energetic diagrams describing charge recombination in the ELL RC. Diagrams (a)and (b) correspond to the two sets of model parameters estimated from the nanosecond experiment and presented for the ELL RC in Table 2 (options *a* and *b*, respectively; see also Tab. S1 for the remaining parameters). (a) The free energy gaps between (P$^+$H$_A^-$)$_1$ or (P$^+$H$_A^-$)$_2$ and P$^+$B$_A^-$ were assumed to be temperature-independent and fixed at 0 and 250 meV, respectively. (b) The free energy gaps between (P$^+$H$_A^-$)$_1$ or (P$^+$H$_A^-$)$_2$ and of P$^+$B$_A^-$ were free parameters, and it was assumed that τ_{PB} = 0.32 ns and τ_{dir} = ~100 ns. In all cases $\tau_{dir} = \tau_{dir1} = \tau_{dir2}$. Assumed lifetimes are shown in italics.

Photosynthesis Research
https://doi.org/10.1007/s11120-018-0550-8

ORIGINAL ARTICLE

Modelling of the cathodic and anodic photocurrents from *Rhodobacter sphaeroides* reaction centres immobilized on titanium dioxide

Rafał Białek[1] · David J. K. Swainsbury[2,4] · Maciej Wiesner[1,3] · Michael R. Jones[2] · Krzysztof Gibasiewicz[1]

Received: 14 February 2018 / Accepted: 21 June 2018

Abstract

As one of a number of new technologies for the harnessing of solar energy, there is interest in the development of photoelectrochemical cells based on reaction centres (RCs) from photosynthetic organisms such as the bacterium *Rhodobacter* (*Rba.*) *sphaeroides*. The cell architecture explored in this report is similar to that of a dye-sensitized solar cell but with delivery of electrons to a mesoporous layer of TiO_2 by natural pigment-protein complexes rather than an artificial dye. *Rba. sphaeroides* RCs were bound to the deposited TiO_2 via an engineered extramembrane peptide tag. Using TMPD (*N,N,N′,N′*-tetramethyl-*p*-phenylenediamine) as an electrolyte, these biohybrid photoactive electrodes produced an output that was the net product of cathodic and anodic photocurrents. To explain the observed photocurrents, a kinetic model is proposed that includes (1) an anodic current attributed to injection of electrons from the triplet state of the RC primary electron donor (P^T) to the TiO_2 conduction band, (2) a cathodic current attributed to reduction of the photooxidized RC primary electron donor (P^+) by surface states of the TiO_2 and (3) transient cathodic and anodic current spikes due to oxidation/reduction of TMPD/$TMPD^+$ at the conductive glass (FTO) substrate. This model explains the origin of the photocurrent spikes that appear in this system after turning illumination on or off, the reason for the appearance of net positive or negative stable photocurrents depending on experimental conditions, and the overall efficiency of the constructed cell. The model may be a used as a guide for improvement of the photocurrent efficiency of the presented system as well as, after appropriate adjustments, other biohybrid photoelectrodes.

Keywords Photovoltaics · Purple bacteria · Bioelectronics · Titanium dioxide · Photosynthesis

Introduction

Sunlight is arguably the most sustainable source of energy for mankind. Nature has evolved very efficient molecular processes for the conversion of solar energy that have provided inspiration for the design of man-made photovoltaic materials and provide natural components that can be exploited directly in biohybrid devices. One of the best characterized of these is the reaction centre (RC) from the purple photosynthetic bacterium *Rhodobacter* (*Rba.*) *sphaeroides*, a complex of protein and cofactors in which photon absorption powers charge separation (Zinth and Wachtveitl 2005). The protein provides a matrix that holds in place two primary electron donor (P) bacteriochlorophylls (BChls), two accessory BChls (B_A and B_B), two bacteriopheophytins (BPhe - H_A and H_B), two ubiquinones (Q_A and Q_B) and a carotenoid (Car) (see inset in Fig. 1) (D'Haene et al. 2014). The initial charge separation occurs between the P BChls and one of the two BPhes, forming the state $P^+H_A^-$. Subsequently,

---

Electronic supplementary material The online version of this article (https://doi.org/10.1007/s11120-018-0550-8) contains supplementary material, which is available to authorized users.

✉ Rafał Białek
rafal.bialek@amu.edu.pl

✉ Krzysztof Gibasiewicz
krzyszgi@amu.edu.pl

[1] Faculty of Physics, Adam Mickiewicz University in Poznań, ul. Umultowska 85, 61-614 Poznan, Poland

[2] School of Biochemistry, Biomedical Sciences Building, University of Bristol, University Walk, Bristol BS8 1TD, UK

[3] NanoBioMedical Center, Adam Mickiewicz University in Poznań, ul. Umultowska 85, 61-614 Poznan, Poland

[4] Present Address: Department of Molecular Biology and Biotechnology, University of Sheffield, Sheffield S10 2TN, UK

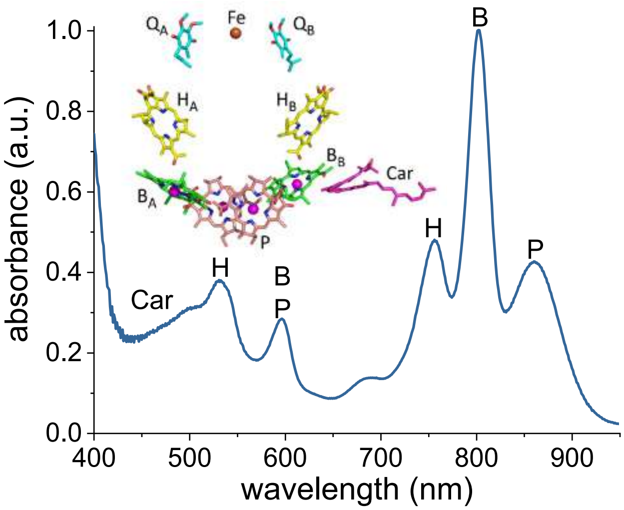

Fig. 1 Cofactor structure and absorbance spectrum of the *Rba. sphaeroides* RCs. For the cofactor structure, color coding is cyan, yellow, green, pink or magenta—carbon; red—oxygen; blue—nitrogen; purple spheres—magnesium; brown sphere—iron. Bands in the absorption spectrum of RCs in 20 mM Tris–HCl (pH 8.0)/0.1% LDAO are labelled with the names of the contributing cofactors

there are three ways electron transfer can proceed. In "open" RCs, with all of the electron transfer cofactors initially in their neutral ground state, the electron is transferred to the first of the ubiquinones, Q_A, and then on to the second, Q_B, completing photochemical charge separation. In "closed" RCs, where Q_A is already reduced, the most probable event is recombination of $P^+H_A^-$ to the ground state. In a smaller percentage of RCs, recombination occurs to a long-lived triplet excited state of P, termed P^T (Woodbury and Allen 1995), which is usually efficiently quenched either by the carotenoid or by the BPhes (Arellano et al. 2004; Białek et al. 2016). The quantum yield of primary charge separation in open RCs is near 100% (Wraight and Clayton 1974), while the yield of P^T triplet formation in closed RCs is approximately 15% (Blankenship et al. 1995).

One of the most promising alternatives to silicon cells for solar energy conversion is the dye-sensitized solar cell (DSSC) (O'Regan and Grätzel 1991). This consists of a working electrode made of a material such as fluorine-doped tin oxide (FTO) conductive glass coated with a mesoporous TiO_2 film that is covered with a layer of dye molecules, and a counter electrode also made of conductive glass. Between the electrodes there is a solution containing an electrolyte, originally iodide/triiodide (O'Regan and Grätzel 1991), which closes the electrical circuit inside the cell by allowing electrons to be transported between the two electrodes. The TiO_2 film provides a three-dimensional semi-conducting matrix which improves light harvesting efficiency by increasing the surface area onto which the sensitizing dye can bind. Photoexcitation of the dye causes charge injection into the conduction band of the TiO_2, followed by re-reduction of the dye by the electrolyte.

A feature of the ruthenium dyes commonly used in DSSCs is their limited ability to absorb light beyond 700 nm, with many having no significant absorbance beyond 800 nm, regions which are photon-rich in natural sunlight (Nazeeruddin et al. 2011). In contrast, as illustrated in Fig. 1, pigment-proteins from organisms containing BChl *a* have very strong absorbance in the near infrared between 700 and 900 nm, and up to 1100 nm in organisms that contain BChl *b* (Mikhailyuk et al. 2006). Thus, a possible modification of the design of the DSSC is to replace the synthetic dye with a photoactive pigment-protein such as a RC. An additional benefit is that, unlike many synthetic dyes, natural pigment-proteins are not harmful to the environment. Bacterial RCs and other photosynthetic proteins such as Photosystem I (PSI) have been tested in a variety of prototype photovoltaic devices (Lu et al. 2007; Nagy et al. 2010). Substrates employed have typically been flat metal surfaces (Ciesielski et al. 2010; den Hollander et al. 2011; Chen et al. 2013; Swainsbury et al. 2014), or alternatively flat (Tan et al. 2012a, b; Caterino et al. 2015) or porous (Lu et al. 2005b, a; Lukashev et al. 2007; Nadtochenko et al. 2008; Woronowicz et al. 2012; Mershin et al. 2012; Nikandrov et al. 2012; Gizzie et al. 2015b; Shah et al. 2015; Yu et al. 2015; Kavadiya et al. 2016) semiconductor layers. A porous semiconductor film provides an up to 2000-fold higher surface area than that can be achieved with a planar electrode of the same 2-D area (O'Regan and Grätzel 1991) and materials such as TiO_2 are much cheaper than the precious metals such as gold and platinum commonly used for planar electrodes. In previous work, both PSI (Mershin et al. 2012; Nikandrov et al. 2012; Gizzie et al. 2015b; Shah et al. 2015; Yu et al. 2015; Kavadiya et al. 2016) and the purple bacterial RC (Lu et al. 2005a, b; Lukashev et al. 2007; Nadtochenko et al. 2008; Woronowicz et al. 2012) have been deposited on TiO_2 porous substrates for the study of photocurrent generation. The highest photocurrents obtained so far for a photosynthetic protein-TiO_2 composite cell were presented by Shah et al., who achieved current densities of a few hundreds of $\mu A\ cm^{-2}$ using PSI and a nanostructured leaf-like TiO_2 (Shah et al. 2015). A variety of protein deposition methods, electron mediators and formulations of TiO_2 layer have been explored. However, none of these studies have attempted a full model of electron transport within the cell, with only schematic diagrams of the selected processes that underlie the photocurrent.

In this study, a photoelectrochemical cell based on *Rba. sphaeroides* RCs, TiO_2, conducting glass and a redox mediator is investigated through a combination of experiment and modelling. To obtain oriented, self-directed binding to the working electrode, the RC was engineered with a TiO_2-binding peptide exposed at the electron donor side (P-side) of the protein. The usage of these particular materials for working electrode was a way to have mixed anodic and cathodic photocurrents, despite the tag. The net photocurrents obtained from the engineered RCs were either cathodic or anodic, depending on how the TiO_2 electrode was prepared. To explain the mechanism of photocurrent generation in detail, a series of electrochemical and spectroscopic measurements were conducted and a kinetic model was prepared. This model, which includes electron transfer from the P^T state to the TiO_2, electron transfer from surface states of the TiO_2 to P^+, and interactions of the redox mediator with RCs and the conductive electrode surface, explains the principal features of the observed photocurrent transients and reveals the factors that limit the photocurrent outputs of the cells.

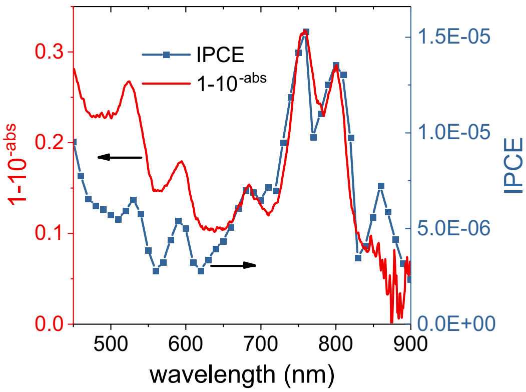

Fig. 3 Source of photocurrents. The IPCE action spectrum (blue) and absorptance spectrum (red) for an I-50 RC electrode are compared. Each point of the IPCE spectrum was constructed from the magnitude of the cathodic photocurrent after 10 s of illumination (see "Experimental section" for details)

Results and discussion

Photocurrents from RC working electrodes

Protein-coated electrodes submerged in an electrolyte solution comprising 250 µM TMPD in 20 mM tris (pH 8.0) produced photocurrents, an example of which is shown in Fig. 2a for RCs adhered to a W-50 TiO_2 film (see "Experimental section"). Turning on the light produced a negative (cathodic) peak of current density that decayed non-exponentially to a constant level. Turning off the light produced a positive (anodic) peak followed by a nonexponential decay to around zero current. No photocurrents were obtained when TiO_2 electrodes without RCs were immersed in the TMPD electrolyte, showing that the photocurrent was dependent on the photochemical activity of the RC. In agreement, an action spectrum of incident photon to current efficiency (IPCE) as a function of excitation wavelength matched the absorbance spectrum of the TiO_2-bound RCs (Fig. 3) but did not contain contributions from TMPD/$TMPD^+$ between 450 and 650 nm (Figure S3), confirming that the photocurrent was being driven by the RC. The absorbance and IPCE action spectra of RCs bound to TiO_2 (Fig. 3) showed an increase in the absorbance band at 760 nm relative to that at 802 nm which we attribute to partial pheophytinization of RC BChls caused by binding of the protein to TiO_2 (compare Figs. 1, 3; see also Figure S4 and Sect. 4 and 5 in Supporting Information). The absorption spectra of working electrodes before and after (photo) electrochemical experiments showed no significant differences in line shape (data not shown). This confirmed that no further pheophytinization took place during measurements, and that the protein was stable on the electrode surface when submerged in buffer solution. The maximum measured value of IPCE was 1.5×10^{-5} (Fig. 3), which is much lower than efficiencies reported in the literature for systems containing photosynthetic proteins immobilized on nanostructured TiO_2 (Mershin et al. 2012).

Photocurrents recorded for working electrodes that had been treated using $TiCl_4$ (see "Experimental section") showed a different behaviour in which the initial spike

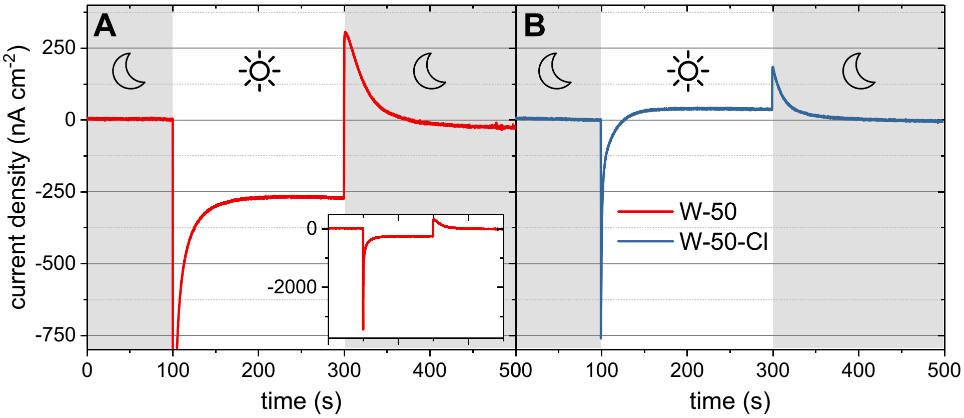

Fig. 2 Photocurrent generation by RC/TiO_2 electrodes in response to illumination at ~860 nm. Typical photochronoamperometric data are shown for W-50 electrodes (**a**) without and (**b**) with $TiCl_4$ treatment prior to protein adherence. The inset in panel A shows same data over their full amplitude range. Positive currents mean an anodic process. Grey background indicates periods without illumination

of cathodic current decayed to a steady anodic current (Fig. 2b). The size of the light-on and light-off spikes of cathodic and anodic current, respectively, were also strongly affected by $TiCl_4$ treatment.

Mechanism of anodic and cathodic photocurrents

Such photocurrent transients with opposing current spikes on light-on/off have been presented previously in the literature for RC cells not involving TiO_2 (Tan et al. 2012a; Caterino et al. 2015; Friebe et al. 2016) and explained in different ways. Friebe et al. (2016) attributed this effect to the diffusion-limited transfer of mediator to and from the working electrode and showed that this could be overcome by use of a rotating disc electrode to achieve mixing. A similar explanation was presented by Tan et al. (2012a), who proposed that the bottleneck reaction is reduction of $TMPD^+$ by quinone in the RC. This leads to a capacitor-like behaviour, where absorption of light causes accumulation of electrons on cofactors of RC and positive charges in $TMPD^+$, with discharge of the system after turning off the light observable as an anodic photocurrent. This explanation may be sufficient for a situation in Fig. 2a, where both the initial light-on spike and steady-state current are cathodic, but does not explain the anodic stable photocurrent illustrated in Fig. 2b.

An alternative explanation for photocurrent transients of this type has been presented by Caterino et al. (2015), based on the concept that both cathodic and anodic photocurrents coexist, but with different kinetics. The source of these two currents was proposed to be interactions of either the P (oxidizing) or Q (reducing) sides of the RC with the electrode. The peak current after light-on arises mostly from the cathodic contribution while the peak after light-off arises mostly from the anodic contribution. The sign of the stable current is determined by the relative magnitudes of the stable cathodic and anodic components.

Taking into account all the abovementioned hypotheses, we build a kinetic model with different sources of anodic and cathodic photocurrents being presented in the following paragraphs.

Regarding the observed anodic steady-state current (Fig. 2b), it has previously been proposed that electrons can be injected into the conduction band of TiO_2 from the P^T triplet excited state of the primary donor BChls (Fig. 4, blue arrows) (Lukashev et al. 2007). P^T is usually short-lived in *Rba. sphaeroides* RCs due to transfer of energy to the RC carotenoid (Car) via the intervening B_B BChl in around 40 ns (Angerhofer et al. 1998). However, as described in Sect. 4 of Supporting Information, it is likely that a significant fraction of this B_B BChl undergoes pheophytinization after deposition of RCs on the TiO_2 porous layer. It has been shown previously in the literature that genetic replacement of the native B_B BChl by a BPhe leads to an increase of the lifetime for triplet energy transfer from P^T to the Car to around 1.6 µs (Mandal et al. 2017). This raises the possibility that, in the present work, P^T may also have an extended lifetime in a large majority of RCs. Given this, in our proposed model the anodic photocurrent is attributed to electron transfer from P^T to the conduction band of TiO_2 (Fig. 4, blue arrows), with re-reduction of the resulting P^+ by TMPD. Although it has a suitable reduction potential, electron injection from H_A^- into the conduction band of TiO_2 is unlikely as this cofactor is deeply buried within the RC and the lifetime of H_A is short (~ 200 ps if Q_A is neutral and may accept the electron from H_A^- (Woodbury and Allen 1995), and a few ns if Q_A is reduced to Q_A^- (Woodbury and Parson 1984; Gibasiewicz and Pajzderska 2008; Gibasiewicz et al. 2011)). The higher energy P* singlet excited state has an even shorter lifetime of ~ 3 ps and decays to $P^+H_A^-$ with a close to 100% quantum yield. Electron injection from Q_A^- into the conduction band of TiO_2 is unlikely due to too positive redox midpoint potential of Q_A^-/Q_A (Fig. 4).

Regarding the cathodic current, TiO_2 electrodes have surface states that lie between the conduction and valence bands, at around + 550 mV versus SHE (Fig. 4), the value obtained for a set of redox mediators in acetonitrile solution (Frank and Bard 1975). This is slightly above the P/P^+ redox midpoint potential of the RC primary donor (+ 500 mV versus SHE) (Maróti and Wraight 2008). As it is known that in aqueous basic solutions the conduction band is shifted towards less positive potentials than in organic solvents (Fitzmaurice 1994), there is a possibility that the potential of the TiO_2 surface states in our system was also shifted toward less positive potentials, making electron transfer from these states to the oxidized RC primary donor (P^+) more favourable. Thus, we propose that the source of the cathodic photocurrent is the transfer of electrons from the FTO electrode through the surface states of TiO_2 to P^+ (Fig. 4, yellow arrows), with TMPD carrying electrons from the RC quinones to the counter electrode. The injection of electrons from any state of the RC into the surface states of TiO_2 is unlikely due to occupation of these surface states with electrons at the applied potential of + 225 mV versus SHE (Frank and Bard 1975). As with an anodic current dependent on P^T, this mechanism for the cathodic current would be expected to be facilitated by attachment of the RC to the TiO_2 by a protein tag that positions the P BChls close to the TiO_2 surface. However, in both cases, productive electron exchange with the TiO_2 is expected to be in competition with energy losses through its dissipation within RCs, such that at any given time the photocurrent is supported by only a sub-set of RC proteins where P^T oxidation or P^+ reduction by the adjacent TiO_2 is possible. There is a possibility that some of the RCs are not properly attached to TiO_2 (e.g. freely diffusing in pores) which favours inner energy

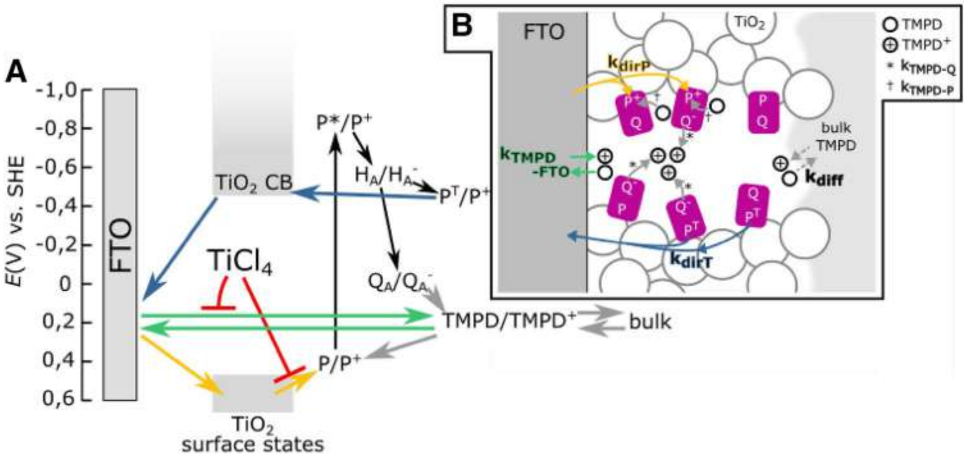

Fig. 4 Modelling to account for the mechanism of photocurrent generation and shapes of photocurrent transients. **a** Scheme of energy levels and processes in the system. Green, blue and yellow arrows correspond to three different processes that contribute to the net current. Black arrows—processes occurring inside RCs, red lines—suppression of electron transfer by $TiCl_4$ treatment, grey arrows—other electron transfer processes including recombination mediated by TMPD/$TMPD^+$. CB signifies conduction band, TMPD/$TMPD^+$ signifies the mediator redox pair inside pores, bulk signifies redox mediator within the bulk volume of the electrochemical cell. **b** Scheme of the same processes as in panel A but depicting the architecture of the electrode and charge transfer reactions occurring between FTO, TiO_2, RCs and mediator inside a TiO_2 pore. Six RC states are considered: PQ_A, $P^+Q_A^-$, P^+Q_A, PQ_A^-, $P^TQ_A^-$ and P^TQ_A. Four of these states may exchange electrons with TMPD/$TMPD^+$: $P^+Q_A^-$, P^+Q_A, PQ_A^- and $P^TQ_A^-$. Two of the states may inject the electron to TiO_2: $P^TQ_A^-$ and P^TQ_A. Two of the states may take the electron from TiO_2: $P^+Q_A^-$ and P^+Q_A. Two of the states may be photoexcited: PQ_A and PQ_A^-

dissipation, thus these RCs could be treated as a source of parasitic absorption.

Regarding the interaction of the mediator with RCs it has been reported that the TMPD/$TMPD^+$ redox pair can either reduce P^+ or oxidize Q^- (Fig. 4), with the rate constant for reduction of P^+ being around 200-fold faster than for the oxidation of Q (Agalidis and Velthuys 1986). However, these results were obtained for RCs and TMPD freely diffusing in solution. In the case of RCs immobilized in the porous TiO_2 matrix, the two reaction rate constants could be significantly different from solution values. Thus, in one of the models (RMIL—see "Simulation of photocurrents using a kinetic model") these rate constants were left as free parameters in optimization. In addition to redox interactions with RC cofactors there is the possibility that the TMPD/$TMPD^+$ electrolyte can interact with the FTO glass electrode either directly at any locations where the FTO is not fully covered by the TiO_2 layer, or via tunnelling in any areas where the FTO is covered by only a very thin layer of TiO_2 from $TiCl_4$ treatment (see "Experimental section"). However, the redox potential of TMPD/$TMPD^+$ is unsuited to an exchange of electrons with TiO_2 itself (Fig. 4). As the potential applied to working electrode (+ 225 mV SHE) was close to the midpoint potential of the TMPD/$TMPD^+$ couple, in darkness, the [TMPD]/[$TMPD^+$] ratio in the vicinity of the working electrode should be around one, similarly as in the bulk solution (see Fig S5 and Sect. 6 and 7 of Supporting Information). However, our modelling shows that under illumination, the local value of this ratio in the immediate vicinity of the mesoporous surface may be transiently or even permanently significantly different from one (see Figs. S7 and S8). Therefore, diffusion of the oxidized and reduced forms of the mediator between the mesoporous region near the electrode surface (pores) and the bulk solution also has to be taken into account.

Simulation of photocurrents using a kinetic model

A set of differential equations was used to model the experimental data demonstrating a net cathodic stable photocurrent from the W-50 electrodes and a net anodic stable photocurrent from the W-50-Cl electrodes (Fig. 2). A simplified schematic of this model is shown in Fig. 4B, a detailed account of the physical and mathematical basis for the model is given in Fig. S6 and Sect. 8 of Supporting Information. Two sets of conditions were considered (1) only $1-x=10\%$ of RCs achieve electron transfer between TiO_2 and the mediator, while 90% of RCs dissipate the energy (a so-called "inactive pool" (IP) model) and (2) all RCs achieve such electron transfer but the rate constants of electron transfer reactions between RC and TMPD/$TMPD^+$ are smaller than those cited in the literature [a so-called "RC-mediator interface limited" (RMIL) model]. For both conditions, some parameters were taken from the literature, while others were optimized to achieve the best fit to the experimental photocurrent transients (see Table 1 and Sect. 8 of Supporting Information).

The resulting simulated photocurrent transients are shown in Fig. 5, overlaid with the experimental data. Accounting for the difference in the data with and without $TiCl_4$ (Fig. 5B versus 5A) required variation of only three parameters, the rate constant for electron transfer from TiO_2 surface states to P^+ (k_{dirP}), the rate constant for electron transfer between FTO and TMPD/$TMPD^+$ ($k_{TMPD-FTO}$), which was the same in both directions and the rate constant for TMPD/$TMPD^+$ diffusion (k_{diff}) (Fig. 4b). Table 1 contains resulting values of all the parameters. As it is presented in literature (O'Regan et al. 2007), the $TiCl_4$ treatment decreases the number of surface states thus electron transfer from TiO_2 surface states to P^+ is suppressed (k_{dirP} is decreased). This effect is depicted by the red lines in Fig. 4a. On the other hand, the expected suppression of electron transfer between FTO and TMPD/$TMPD^+$ by $TiCl_4$ treatment was rather limited ($k_{TMPD-FTO}$), and the value of this parameter was strongly dependent on the value of the third parameter, the rate constant for TMPD/$TMPD^+$ diffusion (k_{diff}; these two parameters were compensatory). The values used for these two latter rate constants were chosen to properly model the shape of the spike of positive current obtained after turning off the light. Proper interpretation of these two rate constants will require additional independent experiments to obtain the value of at least one of them.

The simulated photocurrent transients resulting from the two models are composites of the three component currents depicted by the blue, yellow and green arrows in Fig. 4. These three component transients are presented in Fig. 6. In the RMIL model, all three contribute to the decay of the initial cathodic current after turning on the light (Fig. 6a, b), whereas the spike of anodic current after turning off the light comes mostly from TMPD oxidation by the FTO. Simulation of the shapes of both spikes was achieved by

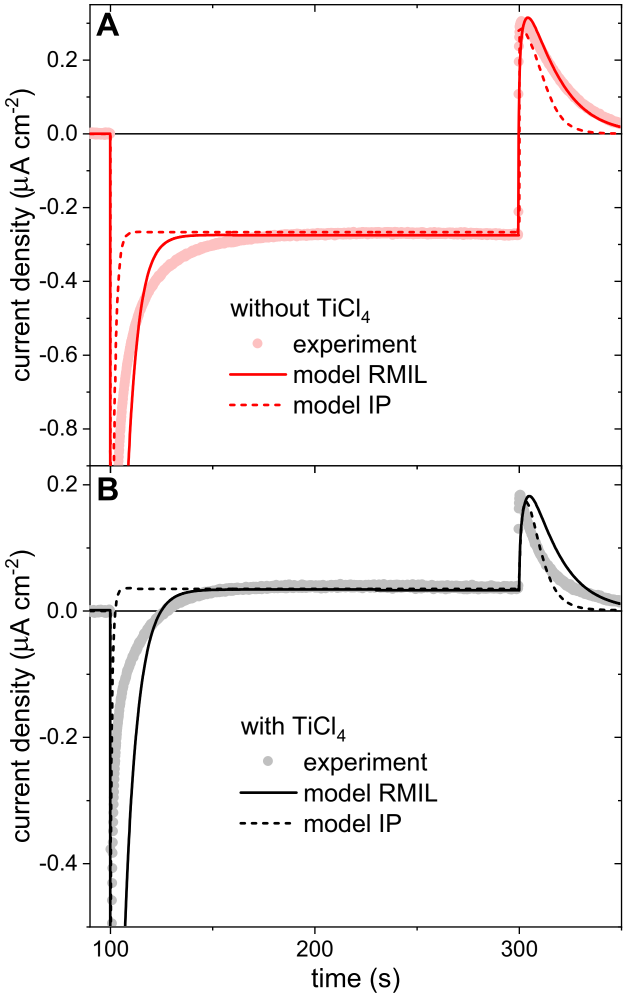

Fig. 5 Simulations of photocurrent transients. Simulations based on two models (lines) for electrodes **a** without and **b** with $TiCl_4$ treatment are compared with experimental data from Fig. 2 (circles)

Table 1 Simulation parameters for the IP and RMIL models

Parameter	Unit	Value			
		RMIL model no $TiCl_4$	RMIL model with $TiCl_4$	IP model no $TiCl_4$	IP model with $TiCl_4$
k_{TMPD-P}	$mol^{-1}\ m^3\ s^{-1}$	2		800*	
k_{TMPD-Q}	$mol^{-1}\ m^3\ s^{-1}$	0.6		4*	
χ	–	0.0		0.9	
k_{dirT}	s^{-1}	5×10^1		8×10^3	
k_{dirP}	s^{-1}	9.7×10^{-2}	4.5×10^{-2}	8.0×10^3	3.5×10^2
$k_{TMPD-FTO}$	$m\ s^{-1}$	8×10^{-7}	7×10^{-7}	1.7×10^{-7}	1.7×10^{-7}
k_{diff}	$mol^{-1}\ m^3\ s^{-1}$	5.5	8	3.3×10^{-1}	3.3×10^{-1}
$k_{h\nu}$**	$mol\ m^{-3}\ s^{-1}$	2.3	2.7	2.0×10^{-2}	7.2×10^{-2}
$k_{h\nu T}$**	$mol\ m^{-3}\ s^{-1}$	6.9	6.4	9.1×10^{-1}	9.0×10^{-1}

For the meaning of the parameters see main text, Fig. 4, and Fig. S6 in Supporting information

*values taken from the literature and fixed (Agalidis and Velthuys 1986)

**values after 299 s (end of the steady photocurrent phase)

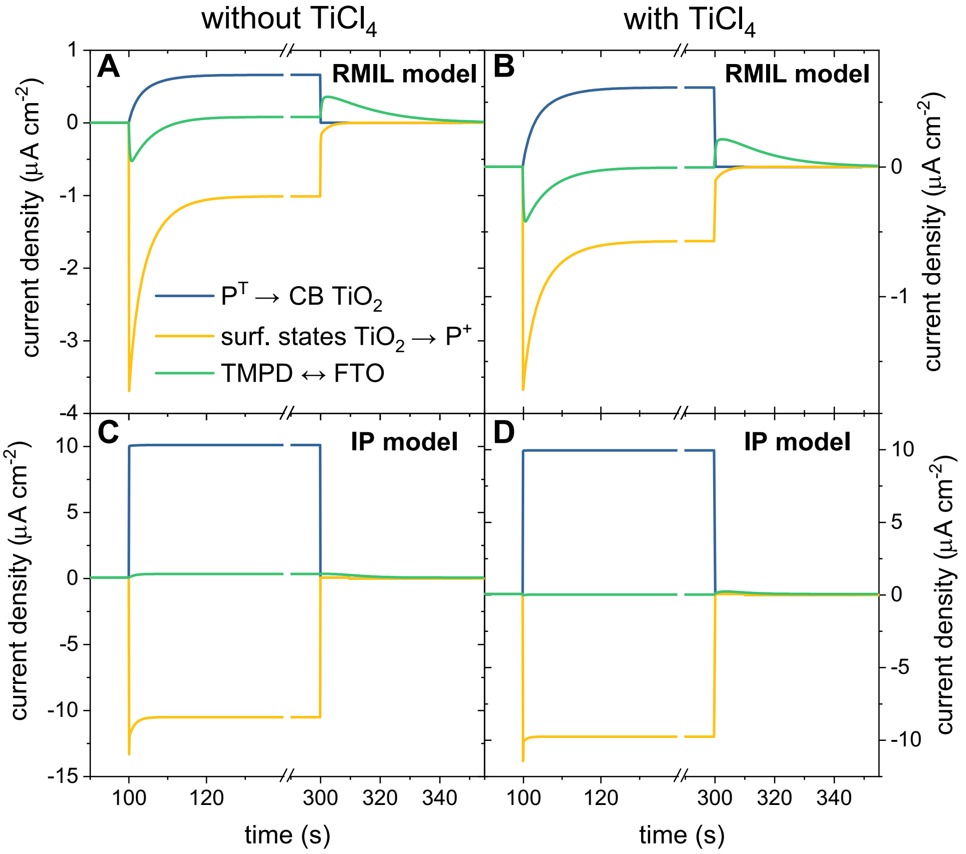

Fig. 6 Photocurrent components. Plots present time traces of the three component photocurrents derived from the **a, b** RMIL model with all RCs active and **c, d** IP model with a 90% pool of inactive RCs

optimization of the rate constants of P^+ reduction by TMPD and Q_B^- oxidation by TMPD$^+$ (k_{TMPD-P} and k_{TMPD-Q} in Fig. 4b) and simulation of their amplitudes by optimization of the rate constants of the TMPD/TPMD$^+$–FTO interaction ($k_{TMPD-FTO}$) and TMPD/TMPD$^+$ diffusion (k_{diff}). The region of steady photocurrent is dominated by opposing contributions from the primary donor P^+ and P^T states interaction with TiO$_2$ (yellow and blue in Fig. 6a, b), and the correct sign and amplitude of the current in this region was obtained by optimizing the corresponding rate constants k_{dirP} and k_{dirT}.

In the IP model, the cathodic spike after turning on the light comes mostly from reduction of P^+ by the TiO$_2$ (Fig. 4a, yellow arrows and Fig. 6c, d yellow line), whereas the anodic peak after turning off the light comes, as in RMIL model, from TMPD oxidation by the FTO. In this case, the rate constants for diffusion and the reaction between TMPD/TMPD$^+$ and FTO were again optimized to simulate the shape of the current spikes. Furthermore, in the IP model for electrodes without TiCl$_4$ treatment, the current from the TMPD–FTO interaction made a small contribution to the steady current (Fig. 6c), and thus had to be taken into account during the fitting procedure.

Irrespective of the model, the data in Fig. 6 demonstrate that competition between cathodic and anodic currents produces a low net output, the sign of which is sensitive to the relative amplitudes of the two currents.

From the values of parameters summarized in Table 1, one can calculate lifetimes of respective reactions as the reciprocals of rates for first-order reactions or the reciprocals of the product of rate constants and TMPD or TMPD$^+$ concentration in the steady photocurrent phase (for second-order reactions) (Table 2). One can see that, for the RMIL model, direct electron transfer from P^T to TiO$_2$ ($\tau_{dirT} = 20$ ms) is three orders of magnitude slower than the lifetime for P^T recombination ($\tau_{recT} = 50\ \mu$s). A similar situation is found for electron transfer from TiO$_2$ to P^+ ($\tau_{dirP} = 10/22$ s) and recombination of the P^+Q^- state ($\tau_{recPQ} = 100$ ms), with the former reaction being two orders of magnitude slower than the latter one. Hence, recombination processes that are much faster than direct electron transfer reactions between RCs and TiO$_2$ are the most important factors underlying the overall low photocurrent efficiency (IPCE $\approx 10^{-5}$; Fig. 3) in the RMIL model. Other factors are a low efficiency of light capture (up to ~ 10%), and compensation between opposing cathodic and anodic currents. Artificially increasing the yield of triplet formation from 15 to 100% in the model increased both the cathodic and anodic current contributions, but did not significantly change the net current (data not shown). An additional factor responsible for the low IPCE

Table 2 Modelled lifetimes of the electron transfer reactions to and from RCs and the lifetimes of recombination reactions inside RCs in the two models

Parameter	Unit	Value			
		RMIL model no TiCl4 ($\chi = 0$)	RMIL model with TiCl4	IP model no TiCl4 ($\chi = 0.9$)	IP model with TiCl4
$\tau_{\text{TMPD-P0}}$	s	3.8	4.0	6.0×10^{-3}	1.1×10^{-2}
$\tau_{\text{TMPD-Q0}}$	s	13.9	13.3	6.1	1.8
τ_{dirT}	s	2×10^{-2}		1.3×10^{-4}	
τ_{dirP}	s	10.3	22.2	1.3×10^{-4}	2.9×10^{-3}
τ_{recT}	s	5×10^{-5}			
τ_{recPQ}	s	1×10^{-1}			

The first two lifetimes were calculated as $\tau_{TMPD-P0}=1/(k_{TMPD-P}$ [TMPD]) and $\tau_{TMPD-Q0}=1/(k_{TMPD-Q}$ [TMPD$^+$]), where values for rate constants were taken from Table 1, whereas [TMPD] and [TMPD$^+$] values were taken from 299 s of simulation (end of photocurrent, see Figs. S7 and S8), hence these values are reliable only for the stable photocurrent region. The remaining lifetimes were simply calculated as reciprocals of corresponding rate constants shown in Table 1 (τ_{dirT}, τ_{dirP}) or taken from literature (τ_{recT}, τ_{recPQ}) (Blankenship et al. 1995; Frank et al. 1996)

of the cathodic current is donation of electrons by TMPD to P$^+$ in the steady photocurrent region ($\tau_{\text{TMPD-P0}} = 3.8/4.0$ s) which is ~ 3–5 times faster than electron transfer from TiO$_2$ to P$^+$ ($\tau_{\text{dirP}} = 10/22$ s) and so short circuits the RC.

In the IP model, the lifetimes for direct electron transfer between the TiO$_2$ and P$^+$ are much shorter than those in the RMIL model (6/11 ms c.f. 3.8/4.0 s), and either comparable with wasteful recombination reactions (compare with the values of τ_{dirT} and τ_{recT}) or even shorter than that (compare with the values of τ_{dirP} and τ_{recPQ}). Thus, in the IP model, the main factors responsible for the low overall current are no longer the competing recombination reactions, but instead, the compensating effect of the cathodic and anodic currents which diminishes the net current (of the order of ~ 100 nA) by about two orders of magnitude relative to the individual cathodic and anodic components (~ 10 µA each; compare Figs. 5, 6). This compensation is a consequence of a short circuit in electron transfer that can be summarized as $P^T \rightarrow TiO_2 \rightarrow P^+$. The other factors responsible for the low IPCE in the scenario are a small pool of active RCs (10%) and, as in the RMIL model, a low efficiency of capturing the light (up to ~ 10%). Also as in the RMIL model, an increase of yield of triplet formation up to 100% would not lead to significant change of the net current due to compensation between the current contributions.

To sum up, the models reveal four possible reasons, other than low absorbance, for the relatively low photocurrent output of the cell. They are (1) electron transfer rates between RCs and TiO$_2$ lower than the rate of charge recombination within RCs (dominates in the RMIL model); (2) competition between anodic and cathodic photocurrents (dominates in the IP model); (3) a pool of photoelectrochemically inactive RCs (IP model only); (4) short-circuiting of the RCs by TMPD acting as both oxidant and reductant (especially in RMIL model).

For efficient DSSCs, typical lifetimes for electron injection into TiO$_2$ by the photoexcited dye are of the order of 10^{-10} s (Martín et al. 2016) which is several orders of magnitude faster than the values obtained in this work for electron donation from P^T. The most probable reason for this is the lack of an excess of energy for the state injecting the electron relative to the conduction band edge of the TiO$_2$; as can be seen from Fig. 4, the triplet state of the RC primary donor is almost isoenergetic with the edge of the conduction band of TiO$_2$. A possible way of improving this pathway would be to change the energy of the TiO$_2$ conduction band through the addition of lithium ions (Yu et al. 2010) or the use of an alternative semiconductor such as ZnO with different energy levels. On the other hand, surface states are known to be low efficiency in terms of electron transfer (Frank and Bard 1975) and this pathway would be hard to improve.

Each of the two models presented in Fig. 5 seemed to be able to fit the experimental data well only in some parts of the time range, and it is possible that combination of these into a single, more complex model could lead to a better agreement between the experimental data and the simulation in all respects. Furthermore, in the existing models, there are five or six parameters that are chosen arbitrarily and may compensate each other, and it would be very useful to measure at least some of these in independent experiments. Although at this stage it is hard to clearly say which assumptions are proper for the studied system, the results obtained show that the proposed approach for modelling can give useful information about the operation mechanism of such a biohybrid photochemical device. The proposed model could be used to simulate data obtained by laboratories that have reported higher efficiencies of systems in which proteins and TiO$_2$ have been combined (Lukashev et al. 2007; Mershin et al. 2012; Gizzie et al. 2015a; Kavadiya et al.

2016), to diagnose what could be improved to obtain even higher efficiencies.

Conclusions

Our measured electrochemical and photoelectrochemical data, and the associated kinetic model, have produced new insights into the photocurrent output of photovoltaic cells fabricated from photosynthetic RCs and TiO_2. The net observable photocurrent is proposed to consist of three parallel sources: (1) injection of electrons from the triplet state of P (anodic), (2) reduction of P^+ by TiO_2 (cathodic) and (3) oxidation/reduction of TMPD/$TMPD^+$ by the FTO glass substrate (producing cathodic and anodic peaks). These combine to yield a relatively modest stable photocurrent of up to 300 nA cm^{-2} with an IPCE of up to 1.5×10^{-3}%. The two models show two alternative main reasons for the low efficiency of the system, relatively fast inner recombination in the RMIL model and efficient recombination via TiO_2 in the IP model. Deconstruction of the net current using the kinetic model provides insight into how the photocurrent amplitude may be enhanced in either a cathodic or anodic direction through future manipulation of the system. The efficiency of the system could not be improved significantly by changing only one parameter in the system, as any change influences both cathodic and anodic contributions to the current, which then compensate each other. There is therefore a need to both suppress one of the current contributions and improve the efficiency of the other.

Experimental section

Biological material

The *Rba. sphaeroides* RC used in this work was modified at the C-terminus of the PufM polypeptide with the sequence LALVPRGSSA**AHKKPSKSA**SA*HHHHHHHHHH* (see Sect. 1 of Supporting Information), using the same approach as described previously for His tag modification (Swainsbury et al. 2014). The synthetic DNA sequence used to prepare this construct is included in the Supporting Information. This sequence comprised a thrombin cleavage site (underlined), followed by an LSTB1 tag (Chen et al. 2009) to target binding to TiO_2 (bold), followed by a deca-histidine tag to facilitate purification (italics). The addition of the histidine tag also ensured the whole population of purified RCs which contained the LSBT1 tag by selecting for proteins that had not had the tag cleaved during protein assembly or protein purification. The modified RC gene was expressed in *Rba. sphaeroides* strain DD13, producing an antenna-deficient transconjugant strain with the modified RC as the sole pigment-protein (Swainsbury et al. 2014). This strain was grown in the dark, and RCs purified by a combination of nickel affinity chromatography and size exclusion chromatography, as described elsewhere (Swainsbury et al. 2014).

Preparation of TiO_2 paste

TiO_2 paste for photocurrent measurements was prepared by applying a procedure based on the one described by Woronowicz et al. (2012) to 50 nm anatase nanoparticles (MKnano, 98% pure). Briefly, TiO_2 nanoparticles were mixed with double-distilled water with acetylacetone followed by slow addition of double-distilled water with Triton X-100. Electrodes prepared using this procedure were denoted W-50.

TiO_2 paste for absorption measurements and IPCE was prepared by a procedure based on the one described by Ito et al. (Ito et al. 2007), with the exception that a three-roller mill was not used. It was chosen for absorption measurements due to its lower light scattering and similar photocurrent results to W-50 (data not shown). Briefly, nanoparticles were mixed with water, acetic acid, ethanol, terpineol and ethyl cellulose by subsequent treatments with a mortar, magnetic stirrer and ultrasonic horn (Sonics Vibra-Cell VCX130). Excess ethanol was evaporated using a rotary evaporator. Ethanol and acetic acid were from Avantor, and all other chemicals were from Sigma-Aldrich. Electrodes prepared using this procedure were denoted I-50.

Assembly of working electrodes

Glass slides covered with FTO (Sigma-Aldrich, TEC 15) were washed in an ultrasonic bath (CT-Brand CT-432H1) sequentially in water with dish soap, double-distilled water and ethanol for 10 min each. TiO_2 paste was then deposited on the cleaned FTO glass using a doctor-blading technique (for paste formulation see above) using Scotch 3M Magic Tape as a mask and to define layer thickness. This was followed by sintering in a Nabertherm 5/11 – P330 oven that was warmed up to 570 °C over 25 min and held at that temperature for a further 30 min. The active area of the TiO_2 film was 0.25 cm^2. After cooling to room temperature, 1 µL of a stock solution of ~ 230 µM RC protein in 20 mM Tris–HCl (pH 8.0)/0.1% LDAO (*N,N*-dimethyldodecylamine *N*-oxide) was drop casted onto the sintered substrate and left to dry at 4 °C in the dark overnight (the RC concentration was determined using an extinction coefficient of 288 mM^{-1} cm^{-1} for the RC absorbance band at 803 nm) (Straley et al. 1973). Coated films were then rinsed with 20 mM Tris–HCl (pH 8.0) to remove any loosely bound RCs, and dried under a flow of compressed air for around 10 s. Uncoated areas of the FTO glass were covered with Scotch 3M Magic Tape to prevent direct contact of mediator with the conductive surface and to reduce the dark current.

For some working electrodes (those denoted W-50-Cl), an additional treatment with $TiCl_4$ was applied before deposition of the RCs on the TiO_2 layer, as described previously (Sommeling et al. 2006). Briefly, after sintering as described above, the electrodes were immersed in a 50 mM $TiCl_4$ (Sigma-Aldrich) aqueous solution for 30 min at 70 °C, followed by rinsing with double-distilled water and sintering again at 570 °C for 30 min. The aim of the $TiCl_4$ treatment was to cover the mesoporous TiO_2 structure, and any bare areas of FTO glass, with an additional thin layer of TiO_2 (Sommeling et al. 2006).

Characterization of working electrodes

Photochronoamperometry was conducted using PGSTAT204 Autolab potentiostat and an 861 nm LED (LED870-66-60, Roithner LaserTechnik GmbH – for spectrum see Figure S9). The intensity of light used was 29.3 ± 1.5 mW cm^{-2}, unless indicated differently. A home-made 3-D printed electrochemical cell (with a $1 \times 5 \times 4.5$ cm (L × W × H) glass cuvette for the electrolyte compartment) was used for all electrochemical experiments in a three-electrode configuration. The reference electrode was Ag/AgCl with 3 M KCl (+ 210 mV vs. SHE—standard hydrogen electrode) and the counter electrode was a Pt wire. The electrolyte solution was 250 µM TMPD (*N,N,N′,N′*-tetramethyl-*p*-phenylenediamine; Sigma-Aldrich) in 20 mM Tris–HCl (pH 8.0). All constant-potential electrochemical measurements were conducted at + 225 mV versus SHE as this was the average open-circuit potential (OCP) in the dark.

Action spectra were recorded using a PGSTAT302N Autolab potentiostat coupled with a photoelectric spectrometer (Instytut Fotonowy). For each wavelength (in 10 nm steps), the light was turned on for 10 s and off for 10 s while recording the current at an applied potential of + 225 mV versus SHE. For the photocurrent amplitude, the average value over the last 2 s of dark current was subtracted from the average value of the last 2 s of light current for each wavelength. The photocurrent amplitudes were then corrected for the intensity of the incident light.

Absorption spectra of TiO_2 electrodes were measured using a Jasco V-770 spectrophotometer with an integrating sphere (ILN-925). Scanning electron microscopy (SEM) of TiO_2 electrodes was performed using a Jeol 7001TTLS microscope with an acceleration voltage of 13 kV and current on sample of 35 pA. Samples were coated with thin layer of gold prior to SEM measurements in order to reduce surface charging.

Acknowledgements DJKS and MRJ acknowledge support from the Biotechnology and Biological Sciences Research Council of the UK (Project BB/I022570/1). RB and KG acknowledge support from the National Science Center, Poland (Project entitled "Bio-semiconductor hybrids for photovoltaic cells" No. 2012/07/B/NZ1/02639).

References

Agalidis I, Velthuys BR (1986) Oxidation of Q_A^- and of Q_B^- of photosynthetic reaction centers by an artificial acceptor. FEBS Lett 197:263–266. https://doi.org/10.1016/0014-5793(86)80339-8

Angerhofer A, Bornhäuser F, Aust V et al (1998) Triplet energy transfer in bacterial photosynthetic reaction centres. Biochim Biophys Acta 1365:404–420. https://doi.org/10.1016/S0005-2728(98)00093-0

Arellano JB, Melø TB, Fyfe PK et al (2004) Multichannel flash spectroscopy of the reaction centers of wild-type and mutant *Rhodobacter sphaeroides*: bacteriochlorophyll$_B$-mediated interaction between the carotenoid triplet and the special pair. Photochem Photobiol 79:68–75. https://doi.org/10.1111/j.1751-1097.2004.tb09859.x

Białek R, Burdziński G, Jones MR, Gibasiewicz K (2016) Bacteriopheophytin triplet state in *Rhodobacter sphaeroides* reaction centers. Photosynth Res 129:205–216. https://doi.org/10.1007/s11120-016-0290-6

Blankenship RE, Madigan MT, Bauer CE (eds) (1995) Anoxygenic photosynthetic bacteria. Kluwer Academic Publishers, Dordrecht

Caterino R, Csiki R, Lyuleeva A et al (2015) Photocurrent generation in diamond electrodes modified with reaction centers. ACS Appl Mater Interfaces 7:8099–8107. https://doi.org/10.1021/acsami.5b00711

Chen H, Su X, Neoh K-G, Choe W-S (2009) Context-dependent behaviour of cyclic and linear peptides on metal oxide surfaces. Langmuir 25:1588–1593

Chen G, LeBlanc G, Jennings GK, Cliffel DE (2013) Effect of redox mediator on the photo-induced current of a photosystem I modified electrode. J Electrochem Soc 160:H315–H320. https://doi.org/10.1149/2.054306jes

Ciesielski PN, Faulkner CJ, Irwin MT et al (2010) Enhanced photocurrent production by photosystem I multilayer assemblies. Adv Funct Mater 20:4048–4054. https://doi.org/10.1002/adfm.201001193

D'Haene SE, Crouch LI, Jones MR, Frese RN (2014) Organization in photosynthetic membranes of purple bacteria in vivo: the role of carotenoids. Biochim Biophys Acta 1837:1665–1673. https://doi.org/10.1016/j.bbabio.2014.07.003

den Hollander M-J, Magis JG, Fuchsenberger P et al (2011) Enhanced photocurrent generation by photosynthetic bacterial reaction centers through molecular relays, light-harvesting complexes, and direct protein–gold interactions. Langmuir 27:10282–10294. https://doi.org/10.1021/la2013528

Fitzmaurice D (1994) Using spectroscopy to probe the band energetics of transparent nanocrystalline semiconductor films. Sol Energy Mater Sol Cells 32:289–305

Frank SN, Bard AJ (1975) Semiconductor electrodes. II. Electrochemistry at n-type titanium dioxide electrodes in acetonitrile solutions. J Am Chem Soc 97:7427–7433. https://doi.org/10.1021/ja00859a007

Frank HA, Chynwat V, Posteraro A et al (1996) Triplet state energy transfer between the primary donor and the carotenoid in *Rhodobacter sphaeroides* R-26.1 reaction centers exchanged with modified bacteriochlorophyll pigments and reconstituted with spheroidene. Photochem Photobiol 64:823–831. https://doi.org/10.1111/j.1751-1097.1996.tb01842.x

Friebe VM, Delgado JD, Swainsbury DJKK et al (2016) Plasmon-enhanced photocurrent of photosynthetic pigment proteins on nanoporous silver. Adv Funct Mater 26:285–292. https://doi.org/10.1002/adfm.201504020

Gibasiewicz K, Pajzderska M (2008) Primary radical pair P^+H^- lifetime in *Rhodobacter sphaeroides* with blocked electron transfer to Q_A. Effect of o-phenanthroline. J Phys Chem B 112:1858–1865. https://doi.org/10.1021/jp075184j

Gibasiewicz K, Pajzderska M, Potter JA et al (2011) Mechanism of recombination of the $P^+H_A{}^-$ radical pair in mutant *Rhodobacter sphaeroides* reaction centers with modified free energy gaps between $P^+B_A{}^-$ and $P^+H_A{}^-$. J Phys Chem B 115:13037–13050. https://doi.org/10.1021/jp206462g

Gizzie E, Scott Niezgoda J, Robinson MT et al (2015a) Photosystem I-polyaniline/TiO_2 solid-state solar cells: simple devices for biohybrid solar energy conversion. Energy Environ Sci 8:3572–3576. https://doi.org/10.1039/C5EE03008K

Gizzie EA, Leblanc G, Jennings GK, Cliffel DE (2015b) Electrochemical preparation of photosystem I-polyaniline composite films for biohybrid solar energy conversion. ACS Appl Mater Interfaces 7:9328–9335. https://doi.org/10.1021/acsami.5b01065

Ito S, Chen P, Comte P et al (2007) Fabrication of screen-printing pastes from TiO_2 powders for dye-sensitised solar cells. Prog Photovoltaics Res Appl 15:603–612. https://doi.org/10.1002/pip.768

Kavadiya S, Chadha TS, Liu H et al (2016) Directed assembly of the thylakoid membrane on nanostructured TiO_2 for a photo-electrochemical cell. Nanoscale 8:1868–1872. https://doi.org/10.1039/C5NR08178E

Lu Y, Liu Y, Xu J et al (2005a) Bio-nanocomposite photoelectrode composed of the bacteria photosynthetic reaction center entrapped on a nanocrystalline TiO_2 matrix. Sensors 5:258–265. https://doi.org/10.3390/s5040258

Lu Y, Yuan M, Liu Y et al (2005b) Photoelectric performance of bacteria photosynthetic proteins entrapped on tailored mesoporous WO_3-TiO_2 films. Langmuir 21:4071–4076. https://doi.org/10.1021/la0470129

Lu Y, Xu J, Liu B, Kong J (2007) Photosynthetic reaction center functionalized nano-composite films: effective strategies for probing and exploiting the photo-induced electron transfer of photosensitive membrane protein. Biosens Bioelectron 22:1173–1185. https://doi.org/10.1016/j.bios.2006.05.026

Lukashev EP, Nadtochenko VA, Permenova EP et al (2007) Electron phototransfer between photosynthetic reaction centers of the bacteria *Rhodobacter sphaeroides* and semiconductor mesoporous TiO2 films. Dokl Biochem Biophys 415:211–216. https://doi.org/10.1134/S1607672907040138

Mandal S, Carey A-M, Locsin J et al (2017) Mechanism of triplet energy transfer in photosynthetic bacterial reaction centers. J Phys Chem B https://doi.org/10.1021/acs.jpcb.7b03373

Maróti P, Wraight CA (2008) The redox midpoint potential of the primary quinone of reaction centers in chromatophores of *Rhodobacter sphaeroides* is pH independent. Eur Biophys J 37:1207–1217. https://doi.org/10.1007/s00249-008-0301-4

Martín C, Ziółek M, Douhal A (2016) Ultrafast and fast charge separation processes in real dye-sensitized solar cells. J Photochem Photobiol C Photochem Rev 26:1–30. https://doi.org/10.1016/j.jphotochemrev.2015.12.001

Mershin A, Matsumoto K, Kaiser L et al (2012) Self-assembled photosystem-I biophotovoltaics on nanostructured TiO_2 and ZnO. Sci Rep 2:234. https://doi.org/10.1038/srep00234

Mikhailyuk IK, Knox PP, Paschenko VZ et al (2006) Analysis of absorption spectra of purple bacterial reaction centers in the near infrared region by higher order derivative spectroscopy. Biophys Chem 122:16–26. https://doi.org/10.1016/j.bpc.2006.02.002

Nadtochenko V, Nikandrov VV, Gorenberg AA et al (2008) Nanophotobiocatalysts based on mesoporous titanium dioxide films conjugated with enzymes and photosynthetic reaction centers of bacteria. High Energy Chem 42:591–593. https://doi.org/10.1134/S0018143908070291

Nagy LL, Hajdu K, Fisher B et al (2010) Photosynthetic reaction centres-from basic research to application possibilities. Not Sci Biol 2:7–13

Nazeeruddin MK, Baranoff E, Grätzel M (2011) Dye-sensitized solar cells: a brief overview. Sol Energy 85:1172–1178. https://doi.org/10.1016/j.solener.2011.01.018

Nikandrov VV, Borisova YV, Bocharov E et al (2012) Photochemical properties of photosystem 1 immobilized in a mesoporous semiconductor matrix. High Energy Chem 46:200–205. https://doi.org/10.1134/S0018143912030095

O'Regan B, Grätzel M (1991) A low-cost, high-efficiency solar cell based on dye-sensitized colloidal TiO_2 films. Nature 353:737–740. https://doi.org/10.1038/353737a0

O'Regan BC, Durrant JR, Sommeling PM, Bakker NJ (2007) Influence of the $TiCl_4$ treatment on nanocrystalline TiO_2 films in dye-sensitized solar cells. 2. charge density, band edge shifts, and quantification of recombination losses at short circuit. J Phys Chem C 111:14001–14010. https://doi.org/10.1021/jp073056p

Shah VB, Henson WR, Chadha TS et al (2015) Linker-free deposition and adhesion of photosystem I onto nanostructured TiO_2 for biohybrid photoelectrochemical cells. Langmuir 31:1675–1682. https://doi.org/10.1021/la503776b

Sommeling PM, O'Regan BC, Haswell RR et al (2006) Influence of a $TiCl_4$ post-treatment on nanocrystalline TiO_2 films in dye-sensitized solar cells. J Phys Chem B 110:19191–19197. https://doi.org/10.1021/jp061346k

Straley SC, Parson WW, Mauzerall DC, Clayton RK (1973) Pigment content and molar extinction coefficients of photochemical reaction centers from *Rhodopseudomonas spheroides*. Biochim Biophys Acta 305:597–609. https://doi.org/10.1016/0005-2728(73)90079-0

Swainsbury DJK, Friebe VM, Frese RN, Jones MR (2014) Evaluation of a biohybrid photoelectrochemical cell employing the purple bacterial reaction centre as a biosensor for herbicides. Biosens Bioelectron 58:172–178. https://doi.org/10.1016/j.bios.2014.02.050

Tan SC, Crouch LI, Jones MR, Welland M (2012a) Generation of alternating current in response to discontinuous illumination by photoelectrochemical cells based on photosynthetic proteins. Angew Chemie Int Ed 51:6667–6671. https://doi.org/10.1002/anie.201200466

Tan SC, Crouch LI, Mahajan S et al (2012b) Increasing the open-circuit voltage of photoprotein-based photoelectrochemical cells by manipulation of the vacuum potential of the electrolytes. ACS Nano 6:9103–9109. https://doi.org/10.1021/nn303333e

Woodbury NWT, Allen JP (1995) Electron transfer in purple non-sulfur bacteria. In: Blankenship RE, Madigan MT, Bauer CE (eds) Anoxygenic photosynthetic bacteria. Kluwer Academic Publishers, Dordrecht, pp 527–557

Woodbury NWT, Parson WW (1984) Nanosecond fluorescence from isolated photosynthetic reaction centers of Rhodopseudomonas sphaeroides. Biochim Biophys Acta 767:345–361. https://doi.org/10.1016/0005-2728(84)90205-6

Woronowicz K, Ahmed S, Biradar AA et al (2012) Near-IR absorbing solar cell sensitized with bacterial photosynthetic membranes. Photochem Photobiol 88:1467–1472. https://doi.org/10.1111/j.1751-1097.2012.01190.x

Wraight CA, Clayton RK (1974) The absolute quantum efficiency of bacteriochlorophyll photooxidation in reaction centres of *Rhodopseudomonas spheroides*. Biochim Biophys Acta 333:246–260. https://doi.org/10.1016/0005-2728(74)90009-7

Yu Q, Wang Y, Yi Z et al (2010) High-efficiency dye-sensitized solar cells: the influence of lithium ions on exciton dissociation, charge recombination, and surface states. ACS Nano 4:6032–6038. https://doi.org/10.1021/nn101384e

Yu D, Wang M, Zhu G et al (2015) Enhanced photocurrent production by bio-dyes of photosynthetic macromolecules on designed TiO_2 film. Sci Rep 5:9375. https://doi.org/10.1038/srep09375

Zinth W, Wachtveitl J (2005) The first picoseconds in bacterial photosynthesis-ultrafast electron transfer for the efficient conversion of light energy. ChemPhysChem 6:871–880. https://doi.org/10.1002/cphc.200400458

Supporting Information

Modelling of the Cathodic and Anodic Photocurrents from *Rhodobacter sphaeroides* Reaction Centers Immobilized on Titanium Dioxide

Rafał Białek[1*], David J.K. Swainsbury[2†], Maciej Wiesner[1,3], Michael R. Jones[2]
and Krzysztof Gibasiewicz[1*]

[1] Faculty of Physics, Adam Mickiewicz University in Poznań, ul. Umultowska 85,
61-614 Poznań, Poland
[2] School of Biochemistry, Biomedical Sciences Building, University of Bristol,
University Walk, Bristol, BS8 1TD, United Kingdom
[3] NanoBioMedical Center, Adam Mickiewicz University in Poznań, ul. Umultowska 85,
61-614 Poznań, Poland
[†] Present address: Department of Molecular Biology and Biotechnology, University of Sheffield,
Sheffield S10 2TN, United Kingdom
* e-mail: rafal.bialek@amu.edu.pl, krzyszgi@amu.edu.pl

SECTION 1 – DETAILS OF THROMBIN CLEAVABLE LSTB1-HIS10 TAG

Protein
LALVPRGSSA**AHKKPSKSA**SA*HHHHHHHHHH**

DNA
CTGGTGCCGCGCGGGAGCAGCGCC**GCCCACAAGAAGCCGTCGAAGTCGGCC**AGCGCC*CATCACCACCATCATCACCATCACCACCAC*TGA

SECTION 2 – CHARACTERIZATION OF TiO_2 LAYERS

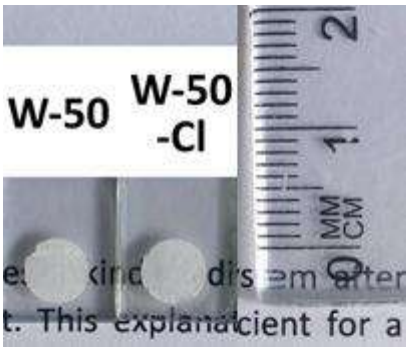

Figure S1. Images of TiO_2 layers before addition of RCs. The ruler is added for scale and text background to illustrate opacity.

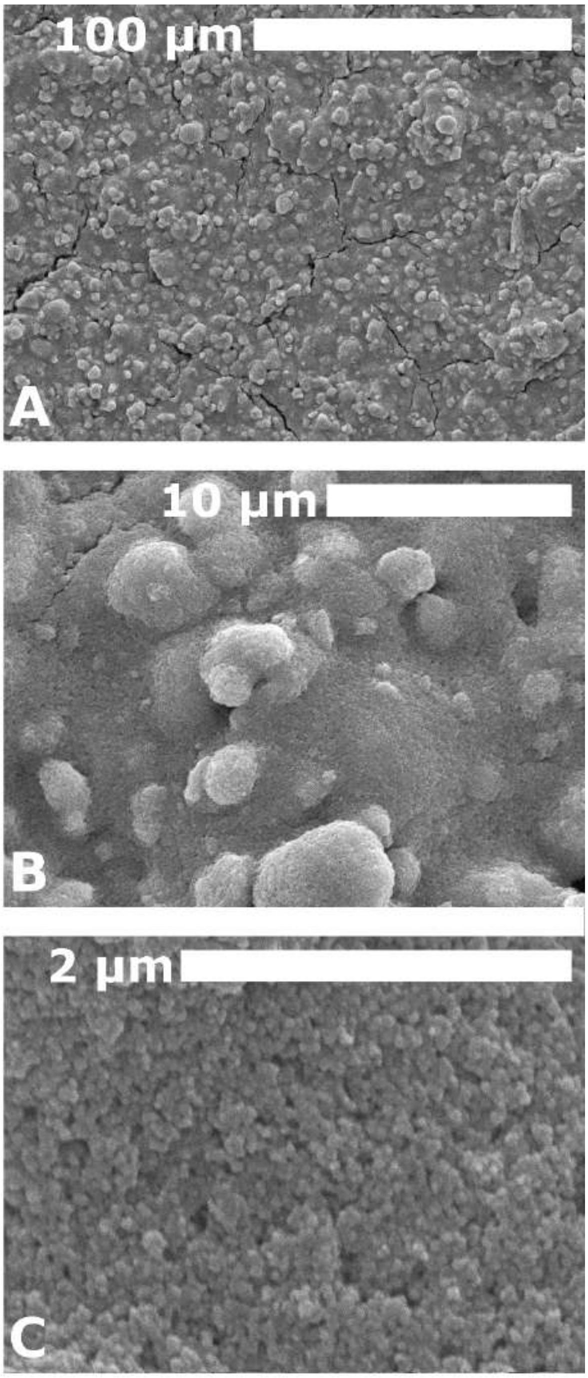

Figure S2. SEM micrographs of TiO_2 nanoparticle layers on FTO-glass after sintering and prior to protein deposition (no $TiCl_4$ treatment). Images show W-50 layers at different magnifications. All surfaces were covered with a thin layer of gold via sputtering to decrease surface charge and increase resolution.

SECTION 3 – TMPD ABSORPTION SPECTRUM

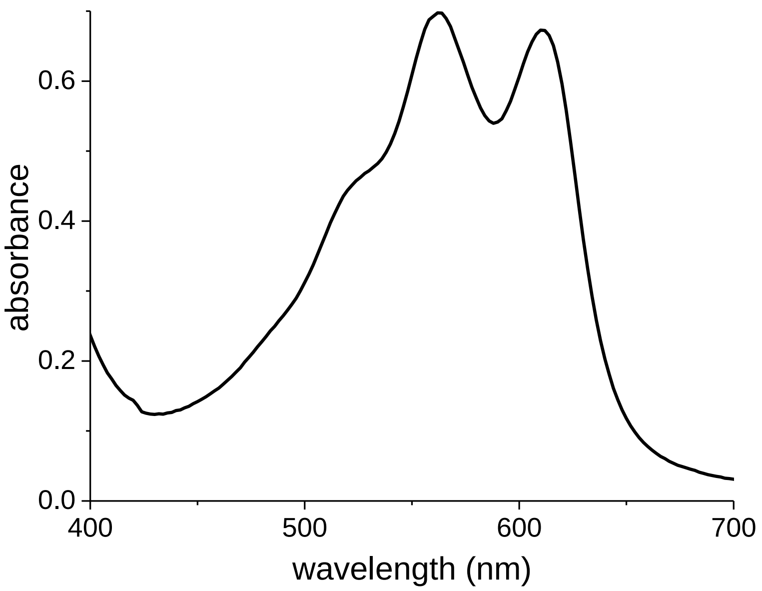

Figure S3. Absorption spectrum of 500 µM TMPD in 20 mM Tris-HCl (pH 8.0). The absorption bands originate from the oxidized form $TMPD^+$.

SECTION 4 – ABSORBANCE PROPERTIES OF BOUND RCS

Binding of RCs to the surface of deposited TiO_2 pastes caused some changes to the native absorbance spectrum of the bacteriochlorin cofactors (Figure S4A). The band around 865 nm attributable to the primary donor BChls was missing, an often-observed effect that can be attributed to oxidation of P in the air-dried sample (Moss et al. 1991). In addition, the 800-nm band attributable to the two accessory BChls was reduced in intensity relative to the 760-nm band attributable to the two RC BPhes. There are two possible reasons for such a change. The first one is a damage to the RC protein such that a BChl is detached from its native binding pocket – such a change would be expected to cause a reduction in the absorbance bands at 865 and/or 800 nm and an increase in absorbance around 760 nm due to the appearance of "free" BChl. The second is pheophytinization of a proportion of the RC BChls such that their central Mg^{2+} metal is replaced by two protons but they are retained in the protein scaffold in their binding pocket(s).

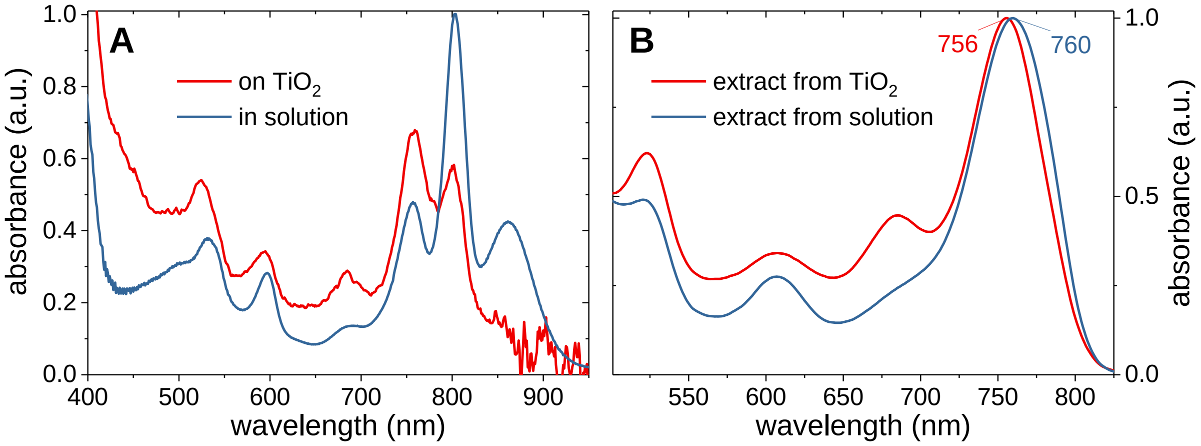

Figure S4. Absorbance properties revealing cofactor composition of RCs in solution and adhered to TiO_2. (A) Absorption spectrum of RCs immobilized on I-50 film partially corrected for TiO_2 scattering compared with the absorption spectrum of RCs in 20 mM Tris-HCl (pH 8.0)/0.1 % LDAO. The spectra were normalized to the same sum of concentrations of bacteriopheophytins and bacteriochlorophylls. (B) Comparison of absorption spectra of methanolic extracts of RCs in solution and immobilized on TiO_2. Absorbance maxima are indicated.

To investigate this change, bacteriochlorin pigments were extracted using methanol from RCs in solution and immobilized on TiO_2. For extraction of pigments with methanol (Avantor) a 2 µL aliquot of RC stock solution or a RC-coated TiO2 slide was immersed in 500 µL methanol and vigorously mixed for 1 min. The resulting solution was centrifuged at 12,100 g and the absorbance spectrum of the supernatant recorded using a Hitachi U-2800A spectrophotometer. The absorbance spectrum of pigments extracted from RCs immobilized on TiO_2 showed a blue-shift of the longest-wavelength absorbance band relative to that of pigments extracted from RCs in solution (Figure 2B). This spectral change is characteristic of a higher amount of BPhe relative to BChl, as the absorption maximum of BPhe in methanol is blue-shifted relative to that of BChl (Straley and Clayton 1973). This indicated that pheophytinization and not dissociation of BChl was responsible for the spectral changes shown in Figure 2A. In addition a band appeared at 680 nm in the spectrum of the TiO_2 RC extract that was probably attributable to a small amount of BChl decomposition products other than BPhe, such as 3-acetyl chlorophyll (Clayton 1966; Makhneva et al. 2016). With the assumption that a BPhe in a binding pocket normally occupied by a monomeric BChl has the same absorption spectrum as a BPhe in its native binding pocket, the spectrum of RCs deposited on TiO_2 in Figure 2A was normalized to the same total number of four BPhe and monomeric BChl molecules as for native RCs in solution.

This approach allowed estimation of a ratio of BPhe:monomeric-BChl of 2.8:1.2 in the TiO_2-bound RCs, which means that an average of 0.8 monomeric BChls per RC had undergone pheophytinization (see next section for a full account of the derivation of these values and the normalization method).

Further evidence that the spectral change undergone by RCs on binding to the TiO_2 electrode was due to *in situ* pheophytinization came from the similarity the ratio of amplitudes of the bands at 760 nm and 800 nm between the IPCE action spectrum for an I-50 electrode and the absorbance spectrum of the electrode. As free BChl pigments released from their binding pockets due to photodamage would not be expected to contribute to a cathodic photocurrent (Tsui et al. 2014), this matching supports the conclusion that RCs on the electrode surface had undergone some conversion of monomeric BChls to BPhe, producing the observed absorbance change. Furthermore, it suggested that the BChl being pheophytinized was B_B (see inset in Figure 1), as it does not take part in the electron transfer process (Kamran et al. 2015). A pheophytinization of B_A would be expected to suppress electron transfer in RC. The vulnerability of B_B to pheophytinization could be related to the fact that it takes part in photoprotection against triplet states, so there is a bigger risk for it to be damaged (Frank et al. 1996). A final point to note is that the IPCE action spectrum had a band at 865 nm attributable to the P BChls, supporting the conclusion that this band is bleached due to P oxidation when RCs are adhered to the TiO_2 electrode in air, but this bleaching is reversible after immersion in a solution of suitable redox potential.

SECTION 5 – ANALYSIS OF PHEOPHYTINIZATION

For normalization of absorption spectra of RCs bound to the surface of TiO_2 the following assumptions were made: (1) absorbance at 800 nm comes only from the accessory BChls, while that at 760 nm comes only from BPhe; (2) the only change in spectrum comes from transformation of BChl into BPhe; (3) the extinction coefficient of BPhe is the same for both natural positions of BPhe in the RC (i.e. H_A and H_B) and for BPhe at a location normally occupied by a monomeric BChl (i.e. BPhe formed after pheophytinization of B_A or B_B). These assumptions lead to the following set of equations:

$$\frac{A_{760(sol)}}{\varepsilon_{BPhe}} + \frac{A_{800(sol)}}{\varepsilon_{BChl}} = \frac{A_{760(TiO_2)-normalized}}{\varepsilon_{BPhe}} + \frac{a \cdot A_{760(TiO_2)-normalized}}{\varepsilon_{BChl}} \tag{S1}$$

$$a = \frac{A_{800(TiO_2)-measured}}{A_{760(TiO_2)-measured}} \tag{S2}$$

$$\varepsilon_{BPhe} = \frac{A_{760(sol)}}{2} \tag{S3}$$

$$\varepsilon_{BChl} = \frac{A_{800(sol)}}{2} \tag{S4}$$

Where: $A_{xxx(sol)}$ is the absorbance at *xxx* nm for RCs in solution, $A_{xxx(TiO_2)-normalized}$ is the absorbance at *xxx* nm for RCs on TiO_2 after normalization, $A_{xxx(TiO_2)-measured}$ is the absorbance at *xxx* nm for RCs on TiO_2 directly from measurements, ε_{yyy} is a dimensionless quantity proportional to the extinction coefficient for species *yyy*, and a is the experimental ratio of measured absorbances. Equations (S3) and (S4) take into account that there are normally two BPhes and two accessory BChls per RC molecule.

After solving equations S1 to S4, one obtains:

$$A_{760(TiO_2)-normalized} = \frac{2 \cdot A_{760(sol)} \cdot A_{800(sol)}}{a \cdot A_{760(sol)} + A_{800(sol)}} \tag{S5}$$

The absorbance spectrum of RCs on TiO_2 presented in Figure 2 was normalized to this value at the maximum around 760 nm. The normalized absorption spectrum was then used to calculate an average number (*n*) of BPhes and accessory BChls per RC molecule using the equations:

$$n_{BChl} = \frac{A_{800(TiO_2)-normalized}}{\varepsilon_{BChl}} \tag{S6}$$

$$n_{BPhe} = \frac{A_{760(TiO_2)-normalized}}{\varepsilon_{BPhe}} \tag{S7}$$

SECTION 6 – ELECTROCHEMICAL PROPERTIES OF THE ELECTROLYTE

The supporting electrolyte was 20 mM Tris-HCl (pH 8.0). TMPD, which has previously been used as a component of solar cells based on *Rba. sphaeroides* RCs (Tan et al. 2012; Ravi et al. 2017), has two steps of oxidation (Figure S5). However only the first occurring at a formal potential of +260 mV vs SHE is of use because the doubly oxidized form, present at potentials over 700 mV vs SHE, undergoes decomposition with displacement of dimethylamine (Brownson and Banks 2014). The contribution of particular redox states to the electroactive species can be calculated by analysis of the values of stable currents in cyclic voltammetry (CV) scans on the right and left side of the formal redox potential (Figure S5), as these currents depend on the bulk concentrations of either reduced or oxidized species (assuming similar diffusion coefficients for reduced and oxidized form) (Zoski 2007). In the 1.2 mM solution the TMPD (neutral) and TMPD$^+$ (monocationic) forms dominated in a ~1:1 ratio (see lengths of A and B line segments in Figure S5 and next section for the derivation of the method; the diffusion coefficients of TMPD and TMPD$^+$ do not differ by more than 15 %) (Wang et al. 1997). The OCP of a freshly prepared solution of TMPD oscillated around +225 mV vs SHE, and so this potential was applied in all subsequent photocurrent measurements in order to minimize the dark current. It is also visible as the potential near which the CV curve in Figure S5 crosses zero current line.

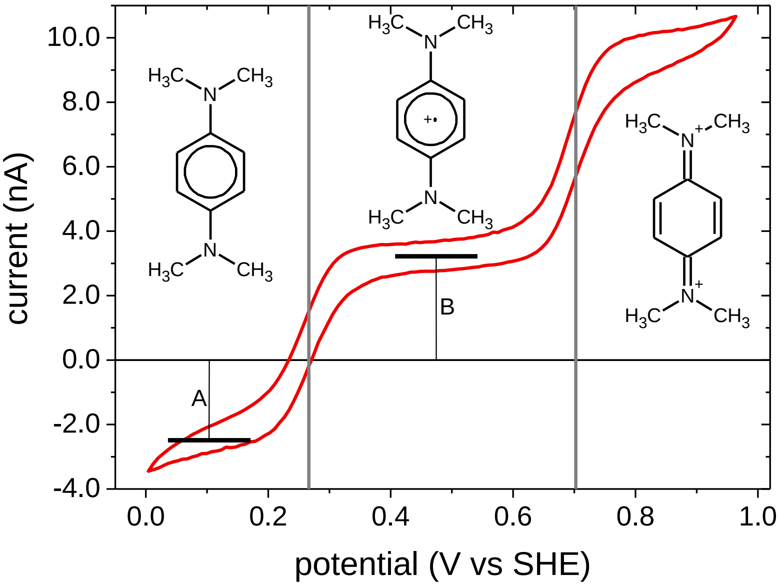

Figure S5. Electrochemical properties of the electrolyte. Cyclic voltammogram of 1.2 mM TMPD in 20 mM Tris-HCl (pH 8.0) on a 25 µm platinum disc microelectrode at a scan rate of 100 mV s^{-1}. The structures of the three redox forms of TMPD (neutral, mono- and bicathionic) are presented. In this and similar solution used for photocurrent measurements the bulk concentrations of the neutral and monocationic forms are similar, as estimated from similar positive and negative currents at ~+480 mV (B) and ~+110 mV (A) potentials (vs SHE), respectively (see text for details). The two long vertical lines indicate the formal redox potentials of neutral/monocationic and monocationic/bicationic TMPD pairs at +260 mV and +700 mV, respectively.

SECTION 7 – DETERMINATION OF THE TMPD/TMPD$^+$ RATIO

The steady-state current in cyclic voltammetry measurements on a microelectrode is given by (Bard and Faulkner 2001):

$$i_{ss} = 4nFDC^* \tag{S8}$$

Where: n is the number of electrons transferred within reaction, F is Faraday's constant, D is the diffusion coefficient of the reacting species (either the oxidized or reduced form), and C^* is the bulk concentration of the reacting species.

This equation is valid only for microelectrode, as it allows probing bulk concentration of species. It is because of the low current flow, which does not much affect the local concentration of species as well as diffusion around microelectrode is closer to the spherical one than that on the macroelectrode. Spherical diffusion ensures efficient mass transport of species to the surface of electrode from the bulk volume (Bard and Faulkner 2001).

Using values for the cathodic and anodic steady-state currents (lines A and B in Figure S5) one can determine the concentration ratio of the oxidized and reduced forms of the redox mediator from:

$$\frac{C_{ox}^*}{C_{red}^*} = \frac{i_{cath}}{i_{an}} \cdot \frac{D_{red}}{D_{ox}} \tag{S9}$$

SECTION 8 – DESCRIPTION OF KINETIC MODEL

Physical details

Figure S6 shows the processes and associated rate constants included in the model used to simulate experimental photocurrent data. For simplicity only the RC states involving the primary electron donor P and terminal quinone acceptor Q are considered due to the much shorter lifetimes of other RC states (Blankenship et al. 1995). It is assumed that only a fraction $(1-\chi)$ of RCs are fully functional meaning that they can efficiently conduct electron transfer between TiO_2 and the mediator. The remaining fraction (χ) can absorb light but undergo wasteful charge recombination and dissipate energy without contribution to the photocurrent, and therefore represent parasitic absorption. The number of photons absorbed per second per area unit is counted from the absorbance of the whole system (see Equations S19 and S20). The triplet state P^T can be formed only in RCs in a closed state (PQ^-) as a result of $P^+H_A^- \rightarrow P^TH_A$ charge recombination, with a quantum yield Φ_T that is used as a parameter.

Diffusion of TMPD is, for simplicity, simulated as the exchange of reduced and oxidized forms of the mediator near the working electrode (TMPD, $TMPD^+$) with the bulk volume ($TMPD_{bulk}$, $TMPD^+_{bulk}$) and is characterized by rate constant k_{diff}. Thus, the flux of diffusion is proportional to the concentration difference between bulk and the region in immediate proximity of the working electrode (see Equation S17), which in general doesn't have to be strictly correct, especially while the concentrations of species are changing rapidly. It is a place for future possible improvements of the model.

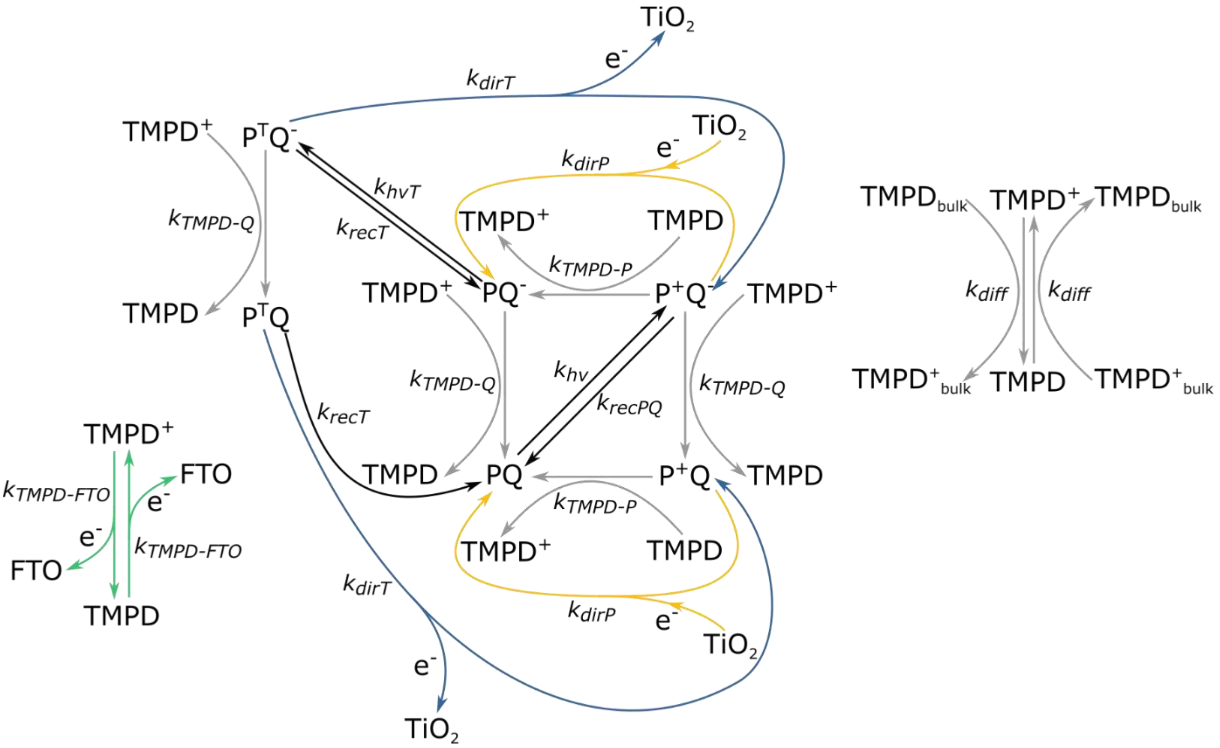

Figure S6. Schematic of the processes included in the kinetic model. The colors of arrows correspond to those indicating processes in Figure 5. Six RC states are considered: PQ, $P^+Q_A^-$, P^+Q_A, PQ_A^-, $P^TQ_A^-$, and P^TQ_A. Four of these states may exchange electrons with TMPD/$TMPD^+$: $P^+Q_A^-$, P^+Q_A, PQ_A^-, $P^TQ_A^-$. Two of the states may inject the electron to TiO_2: $P^TQ_A^-$ and P^TQ_A. Two of the states may accept an electron from TiO_2: $P^+Q_A^-$ and P^+Q_A. Two of the states may be excited by light: PQ_A and PQ_A^-.

Mathematical model

The differential equations presented below (S10 – S20) are the mathematical expression of the model presented in Figure S6. Most of the symbols are self-explanatory or are presented in Figure S6 (those with "n" at the beginning depict RCs inactive in photocurrent generation). The others are:

$[x]$ – concentration of state/species x,
$[TMPD_0]$ – initial concentration of TMPD (sum of reduced and oxidized species),
$[PQ_0]$ – total concentration of all RCs in the porous layer (equal to initial concentration of the RCs in state PQ assuming χ=0),
χ – fraction of RCs inactive in photocurrent generation,
l – thickness of the mesoporous TiO$_2$ layer,
ε – extinction coefficient of P at 861 nm,
P_0 – intensity of the incident light in units of power per unit area,
t – time,
t_{ON} – time of turning on the light,
t_{OFF} – time of turning off the light,
Φ_T – triplet formation quantum yield.

$$\begin{aligned}\frac{d[PQ]}{dt} = -k_{h\nu} + k_{recPQ}[P^+Q^-] + k_{TMPD-P}[P^+Q][TMPD] \\ + k_{TMPD-Q}[PQ^-][TMPD^+] + k_{recT}[P^TQ] + k_{dirP}[P^+Q]\end{aligned} \tag{S10}$$

$$\begin{aligned}\frac{d[P^+Q^-]}{dt} = k_{h\nu} - k_{recPQ}[P^+Q^-] - k_{TMPD-P}[P^+Q^-][TMPD] \\ - k_{TMPD-Q}[P^+Q^-][TMPD^+] + k_{dirT}[P^TQ^-] - k_{dirP}[P^+Q^-]\end{aligned} \tag{S11}$$

$$\begin{aligned}\frac{d[P^+Q]}{dt} = -k_{TMPD-P}[P^+Q][TMPD] + k_{TMPD-Q}[P^+Q^-][TMPD^+] + k_{dirT}[P^TQ] \\ - k_{dirP}[P^+Q]\end{aligned} \tag{S12}$$

$$\begin{aligned}\frac{d[PQ^-]}{dt} = k_{TMPD-P}[P^+Q^-][TMPD] - k_{TMPD-Q}[PQ^-][TMPD^+] - k_{h\nu T} \\ + k_{recT}[P^TQ^-] + k_{dirP}[P^+Q^-]\end{aligned} \tag{S13}$$

$$\frac{d[nPQ]}{dt} = 0 \tag{S14}$$

$$\frac{d[P^TQ]}{dt} = k_{TMPD-Q}[P^TQ^-][TMPD^+] - k_{recT}[P^TQ] - k_{dirT}[P^TQ] \tag{S15}$$

$$\frac{d[P^TQ^-]}{dt} = k_{h\nu T} - k_{TMPD-Q}[P^TQ^-][TMPD^+] - k_{recT}[P^TQ^-] - k_{dirT}[P^TQ^-] \tag{S16}$$

$$\begin{aligned}\frac{d[TMPD^+]}{dt} = \frac{k_{diff}[TMPD][TMPD_0]}{2} - \frac{k_{diff}[TMPD^+][TMPD_0]}{2} \\ + \frac{k_{TMPD-FTO}}{l}[TMPD] - \frac{k_{TMPD-FTO}}{l}[TMPD^+] \\ - k_{TMPD-Q}[P^TQ^-][TMPD^+] - k_{TMPD-Q}[PQ^-][TMPD^+] \\ - k_{TMPD-Q}[P^+Q^-][TMPD^+] + k_{TMPD-P}[P^+Q^-][TMPD] \\ + k_{TMPD-P}[P^+Q][TMPD]\end{aligned} \tag{S17}$$

$$\frac{d[TMPD]}{dt} = -\frac{d[TMPD^+]}{dt} \tag{S18}$$

$$k_{hv} = \\ = \begin{cases} 0 & t < t_{ON} \\ \frac{[PQ]}{[PQ]+[PQ^-]+[nPQ]}\left(1-10^{-l\,\varepsilon\,([PQ]+[PQ^-]+[nPQ])}\right)\frac{P_0\lambda}{chN_A l} & t \in \langle t_{ON}, t_{OFF}\rangle \\ 0 & t > t_{OFF} \end{cases} \tag{S19}$$

$$k_{hvT} = \\ = \begin{cases} 0 & t < t_{ON} \\ \Phi_T\frac{[PQ^-]}{[PQ]+[PQ^-]+[nPQ]}\left(1-10^{-l\,\varepsilon\,([PQ]+[PQ^-]+[nPQ])}\right)\frac{P_0\lambda}{chN_A l} & t \in \langle t_{ON}, t_{OFF}\rangle \\ 0 & t > t_{OFF} \end{cases} \tag{S20}$$

The equations described above together with boundary conditions (equations S21-S29) were solved using Wolfram Mathematica NDSolve function with parameters: $MaxStepSize = 0.1$, $MaxSteps = \infty$ and $WorkingPrecision = 25$.

$$[PQ](0) = (1-\chi)[PQ_0] \tag{S21}$$

$$[nPQ](0) = \chi[PQ_0] \tag{S22}$$

$$[P^+Q^-](0) = 0 \tag{S23}$$

$$[P^+Q](0) = 0 \tag{S24}$$

$$[PQ^-](0) = 0 \tag{S25}$$

$$[P^TQ](0) = 0 \tag{S26}$$

$$[P^TQ^-](0) = 0 \tag{S27}$$

$$[TMPD](0) = [TMPD_0]/2 \tag{S28}$$

$$[TMPD^+](0) = [TMPD_0]/2 \tag{S29}$$

The resulting current was calculated using Equation S30:

$$\begin{aligned} I(t) = I_{TMPD}(t) + I_{triplet}(t) + I_{surface\,states}(t) = \\ = F\,\{k_{TMPD-FTO}\,([TMPD]-[TMPD^+]) \\ + k_{dirT}\,l\,([P^TQ^-]+[P^TQ]) - k_{dirP}\,l\,([P^+Q]+[P^+Q^-])\} \end{aligned} \tag{S30}$$

Model Parameters

Simulations of photocurrent transients for electrodes both treated with $TiCl_4$ and not treated with $TiCl_4$ were performed with the parameters presented in S31. The extinction coefficient is taken from literature (Straley et al. 1973). The thickness of the TiO_2 layer is the value typical for DSSCs (Ito et al. 2007). Recombination rate constants are taken from literature (Blankenship et al. 1995; Frank et al. 1996). Values of k_{TMPD-P} and k_{TMPD-Q} were taken from the literature for freely diffusing RCs with TMPD (Agalidis and Velthuys 1986). The concentration of RCs was calculated using the Beer-Lambert law and the value of light absorption at the Q_y maximum. The concentration of TMPD and the light intensity were as used in experiments.

$$
\begin{aligned}
&F = 96485\, C\, mol^{-1} \\
&c = 3 \cdot 10^{8}\, m\, s^{-1} \\
&N_A = 6.02 \cdot 10^{23}\, mol^{-1} \\
&\varepsilon = 14400\, mol^{-1}\, m^{2} \\
&l = 4 \cdot 10^{-6}\, \mathrm{m} \\
&k_{recPQ} = 10\, s^{-1} \\
&k_{recT} = 20000\, s^{-1} \\
&k_{TMPD-P} = 800\, mol^{-1}\, m^{3}\, s^{-1} \\
&k_{TMPD-Q} = 4\, mol^{-1}\, m^{3}\, s^{-1} \\
&[TMPD_0] = 0.25\, mol\, m^{-3} \\
&[PQ_0] = 1.2\, mol\, m^{-3} \\
&P_0 = 300\, W\, m^{-2} \\
&\Phi_T = 0.15
\end{aligned}
\tag{S31}
$$

Two sets of values were used for the remaining parameters according to two models. The “inactive pool” (IP) model assumed that 90 % of RCs dissipate energy quickly and do not contribute to the photocurrent. The “RC-mediator interface limited” (RMIL) model assumed that 100 % of RCs undergo charge separation and do not dissipate energy, but the values of k_{TMPD-P} and k_{TMPD-Q} are different from those available in the literature due to immobilization of RCs on the TiO_2 surface which hinders access of the mediator to reduced and oxidized cofactors within protein. In the case of this second model the values of k_{TMPD-P} and k_{TMPD-Q} were optimized to obtain the best fit to the photocurrent traces. The values for these parameters are shown in Table 1 in the main text.

Time-dependence of species concentrations

The time-dependence of the concentrations of all species are shown in Figures S9 and S10. Interpretation of these plots is presented in the main text.

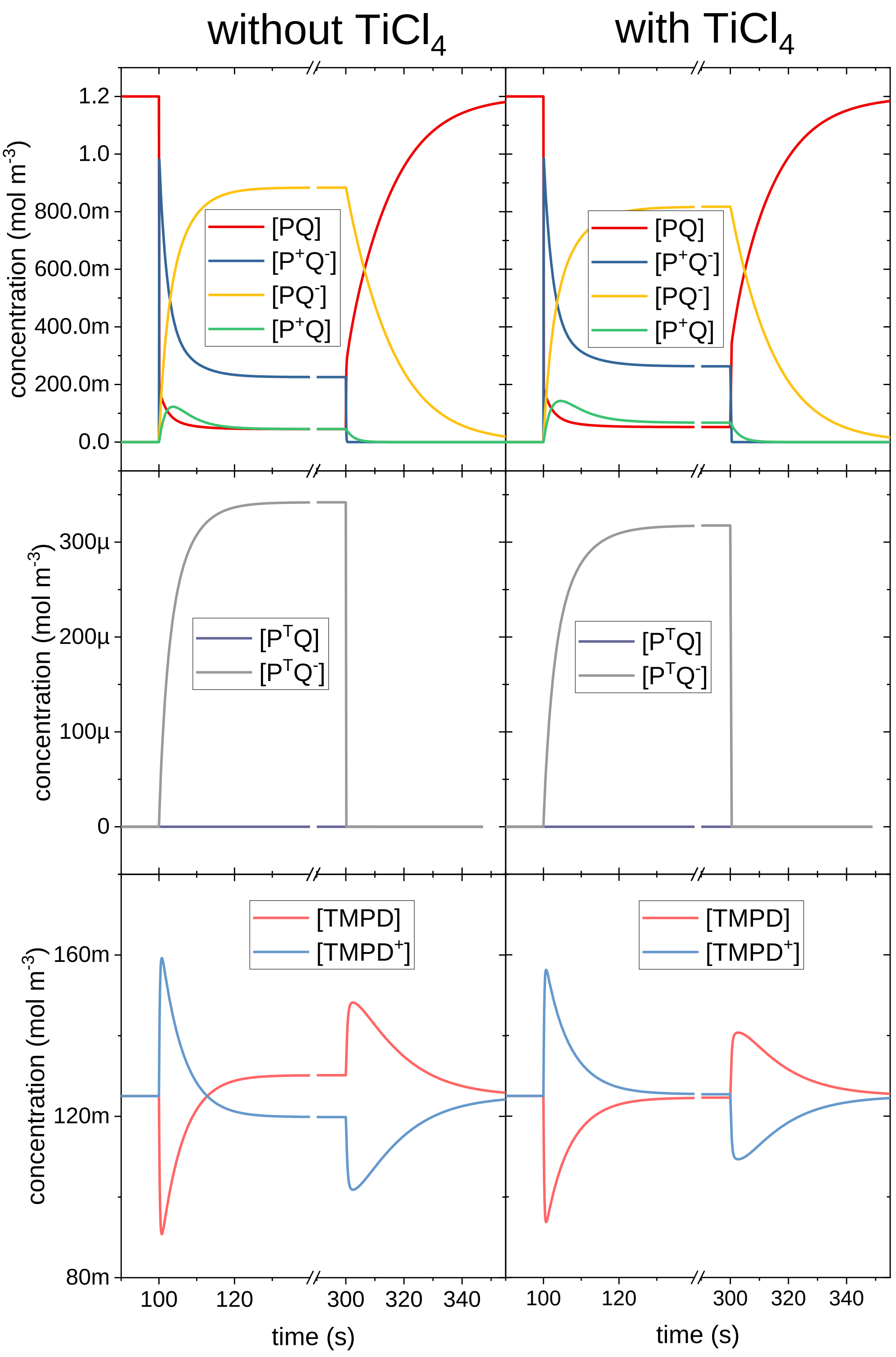

Figure S7. Species concentrations simulated using the RMIL model.

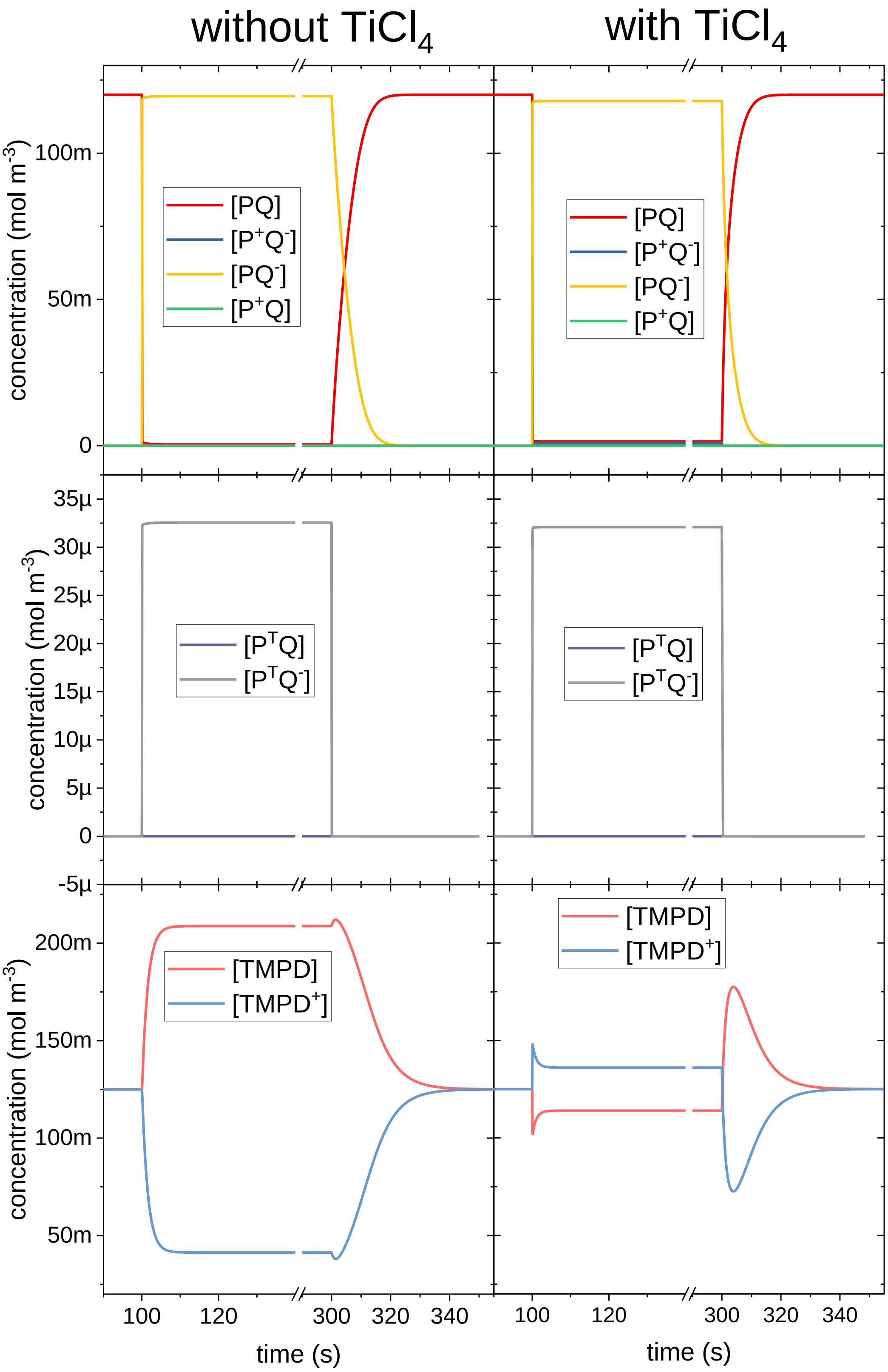

Figure S8. Species concentrations simulated using the IP model.

SECTION 9 – LED CHARACTERISTICS

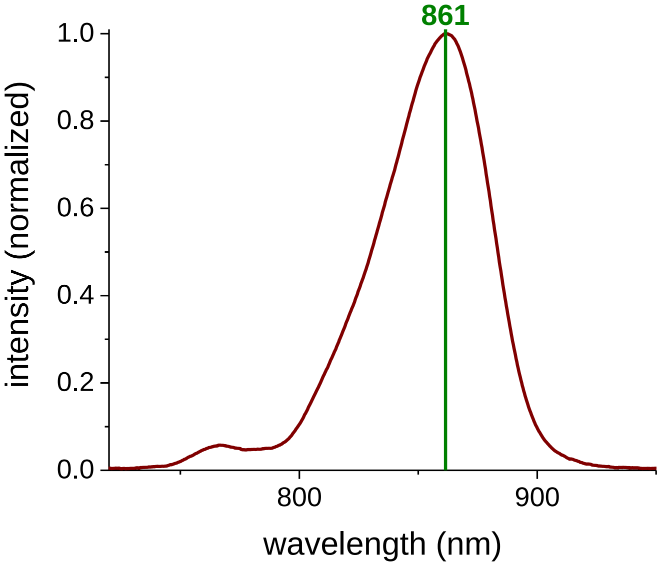

Figure S9. Spectrum of the LED used as the excitation light source for all experiments except action spectra. FWHM 53 nm, incident intensity 29.3 ± 1.5 mW cm^{-2}.

REFERENCES

Agalidis I, Velthuys BR (1986) Oxidation of Q_A^- and of Q_B^- of photosynthetic reaction centers by an artificial acceptor. FEBS Lett 197:263–266 . doi: 10.1016/0014-5793(86)80339-8

Bard AJ, Faulkner LR (2001) Electrochemical Methods: Fundamentals and Applications, 2nd editio. Wiley

Blankenship RE, Madigan MT, Bauer CE (eds) (1995) Anoxygenic Photosynthetic Bacteria. Kluwer Academic Publishers, Dordrecht

Brownson DAC, Banks CE (2014) Interpreting Electrochemistry. In: The Handbook of Graphene Electrochemistry. Springer London, London, pp 23–77

Clayton RK (1966) Spectroscopic Analysis of Bacteriochlorophylls in vitro and in vivo. Photochem Photobiol 5:669–677 . doi: 10.1111/j.1751-1097.1966.tb05813.x

Frank HA, Chynwat V, Posteraro A, et al (1996) Triplet state energy transfer between the primary donor and the carotenoid in *Rhodobacter sphaeroides* R-26.1 reaction centers exchanged with modified bacteriochlorophyll pigments and reconstituted with spheroidene. Photochem Photobiol 64:823–831 . doi: 10.1111/j.1751-1097.1996.tb01842.x

Ito S, Chen P, Comte P, et al (2007) Fabrication of screen-printing pastes from TiO_2 powders for dye-sensitised solar cells. Prog Photovoltaics Res Appl 15:603–612 . doi: 10.1002/pip.768

Kamran M, Friebe VM, Delgado JD, et al (2015) Demonstration of asymmetric electron conduction in pseudosymmetrical photosynthetic reaction centre proteins in an electrical circuit. Nat Commun 6:6530 . doi: 10.1038/ncomms7530

Makhneva ZK, Ashikhmin AA, Bolshakov MA, Moskalenko AA (2016) 3-Acetyl-chlorophyll formation in light-harvesting complexes of purple bacteria by chemical oxidation. Biochem 81:176–186 . doi: 10.1134/S0006297916020115

Moss DA, Leonhard M, Bauscher M, Mäntele W (1991) Electrochemical redox titration of cofactors in the reaction center from *Rhodobacter sphaeroides*. FEBS Lett 283:33–36 . doi: 10.1016/0014-5793(91)80547-G

Ravi SK, Yu Z, Swainsbury DJKK, et al (2017) Enhanced Output from Biohybrid Photoelectrochemical Transparent Tandem Cells Integrating Photosynthetic Proteins Genetically Modified for Expanded Solar Energy Harvesting. Adv Energy Mater 7:1601821 . doi: 10.1002/aenm.201601821

Straley SC, Clayton RK (1973) Extraction of oxidized bacteriochlorophyll from illuminated photosynthetic reaction center particles. Biochim Biophys Acta - Bioenerg 292:685–691 . doi: 10.1016/0005-2728(73)90016-9

Straley SC, Parson WW, Mauzerall DC, Clayton RK (1973) Pigment content and molar extinction coefficients of photochemical reaction centers from *Rhodopseudomonas spheroides*. Biochim Biophys Acta - Bioenerg 305:597–609 . doi: 10.1016/0005-2728(73)90079-0

Tan SC, Crouch LI, Jones MR, Welland M (2012) Generation of Alternating Current in Response to Discontinuous Illumination by Photoelectrochemical Cells Based on Photosynthetic Proteins. Angew Chemie Int Ed 51:6667–6671 . doi: 10.1002/anie.201200466

Tsui L, Huang J, Sabat M, Zangari G (2014) Visible Light Sensitization of TiO_2 Nanotubes by Bacteriochlorophyll-C Dyes for Photoelectrochemical Solar Cells. ACS Sustain Chem Eng 2:2097–2101 . doi: 10.1021/sc500386g

Wang RL, Tam KY, Compton RG (1997) Applications of the channel flow cell for UV-visible spectroelectrochemical studies Part 3. Do radical cations and anions have similar diffusion coefficients to their neutral parent molecules? J Electroanal Chem 434:105–114 . doi: 10.1016/S0022-0728(97)00114-9

Zoski CG (ed) (2007) Handbook of Electrochemistry. Elsevier, Amsterdam

Electrochimica Acta 330 (2020) 135190

Contents lists available at ScienceDirect

Electrochimica Acta

journal homepage: www.elsevier.com/locate/electacta

In situ spectroelectrochemical investigation of a biophotoelectrode based on photoreaction centers embedded in a redox hydrogel

Rafał Białek [a], [*], Vincent Friebe [b], [c], Adrian Ruff [d], Michael R. Jones [e], Raoul Frese [b], Krzysztof Gibasiewicz [a], [**]

[a] *Faculty of Physics, Adam Mickiewicz University in Poznań, Ul. Uniwersytetu Poznańskiego 2, 61-614, Poznań, Poland*
[b] *Department of Physics and Astronomy, LaserLaB Amsterdam, VU University Amsterdam, De Boelelaan 1081, Amsterdam, 1081 HV, the Netherlands*
[c] *Center for Electrochemical Sciences – Molecular Nanostructures, Faculty of Biochemistry and Chemistry, Ruhr-University Bochum, Universitätsstrasse 150, D-44780, Bochum, Germany*
[d] *Analytical Chemistry – Center for Electrochemical Sciences (CES), Faculty of Biochemistry and Chemistry, Ruhr-University Bochum, Universitätsstrasse 150, D-44780, Bochum, Germany*
[e] *School of Biochemistry, Biomedical Sciences Building, University of Bristol, University Walk, Bristol, BS8 1TD, UK*

ARTICLE INFO

Article history:
Received 17 June 2019
Received in revised form
31 October 2019
Accepted 31 October 2019
Available online 1 November 2019

Keywords:
Biophotovoltaics
Photobioelectrode
Rhodobacter sphaeroides
Redox hydrogel
Osmium complex
Reaction centers

ABSTRACT

The field of biophotoelectrochemistry and its application in biophotovoltaics and biosensors has gained more and more attention in recent years. Knowledge of the redox potentials of the catalytically active protein cofactors in biophotovoltaic devices is crucial for accurate modelling and in discerning the mechanisms of their operation. Here, for the first time, we used spectroelectrochemical methods to investigate thermodynamic parameters of a biophotoelectrode *in situ*. We determined redox potentials of two elements of the system: the primary electron donor in photosynthetic reaction centers (RCs) of the bacterium *Rhodobacter sphaeroides* and osmium-complex based redox mediators that are bound to a hydrogel matrix. We observe that the midpoint potential of the primary donor is shifted towards more positive potentials in comparison to literature data for RCs solubilized in buffered water solution, likely due to interaction with the polymer matrix. We also demonstrate that the osmium-complex modified redox polymer efficiently wires the RCs to the electrode, maintaining a high Internal Quantum Efficiency with approximately one electron per two photons generated ($IQE = 50\pm12\%$). Overall, this biophotoelectrode may be attractive for controlling the redox state of the protein when performing other types of experiments, e.g. time resolved absorption or fluorescence measurements, in order to gain insights into kinetic limitations and thereby help in the rational design of bioelectronic devices.

1. Introduction

With more and more biophotovoltaic device prototypes emerging, determination of the redox potentials of cofactors inside complex proteins is becoming an important topic in the field of bioelectrochemistry. For some small and accessible proteins it is possible to directly measure such potentials via cyclic voltammetry (CV) in solution without additional redox mediators, for example for cytochrome *c* [1]. However, for complex membrane photoproteins such as Photosystem I (PSI) or the *Rhodobacter (Rba.) sphaeroides* Reaction Center (RC) these measurements are challenging due to the typically deeply-embedded nature of the redox centers within the protein scaffold and the surrounding detergent micelle. A direct electron transfer (DET) between the electrode and the protein is thus difficult because of large tunneling distances, and generally necessitate the use of an electron mediator to ensure a mediated electron transfer (MET) regime [2,3]. Electrochemical titration of photosynthetic proteins coupled with spectral measurements has been widely reported in the literature but only for proteins solubilized in solution and in the presence of soluble redox mediators [4–8]. The redox potential of a cofactor buried inside such a protein depends on many factors including the species of organism from which the protein was sourced [6], the type of detergent used for solubilization [7], and the pH or ionic strength of the solution [9,10]. As accurate knowledge of cofactor redox

---

[*] Corresponding author.
[**] Corresponding author.
E-mail addresses: rafal.bialek@amu.edu.pl (R. Białek), krzyszgi@amu.edu.pl (K. Gibasiewicz).

https://doi.org/10.1016/j.electacta.2019.135190

potentials is crucial for the correct description of the mode of operation of bioelectronic devices and for modelling of their performance, there is a need for methodologies for the *in situ* determination of redox potentials in a device setting. At present, it is common practice to rely on literature values obtained for proteins in buffered solutions when discussing or modelling the mechanism of photocurrent or photovoltage generation in a photoelectrochemical device [11,12]. However, such values may not be relevant for a complex photoprotein in a device or on an electrode where the interaction of the protein with the surrounding medium is likely to be different to that in aqueous solution.

The model system we have used to explore solutions to this problem is the RC from the purple bacterium *Rba. Sphaeroides* incorporated in a well-known osmium-complex based redox hydrogel (HG) matrix [13] (Fig. 1A) that was used earlier for the wiring of other photoactive enzymes to the electrode surfaces [14–16]. The RC is a highly-characterized natural solar energy converter that has been used in a variety of both biophotovoltaic [17–19] and biosensing [20] systems, whilst polymer HG with redox active centers such as osmium complexes have been used extensively for the electrochemical wiring of enzymes [21] and other pigment-proteins to electrode surfaces [14,15]. Both systems display redox-dependent absorption change that make them good candidates for a spectroelectrochemical investigation, and have well understood absorbance spectra (Fig. 1C). On deposition of a RC/HG blend on an FTO-glass substrate the osmium-complex species have a potential (≈400 mV vs. SHE) suitable to wire the RC to the electrode for a cathodic current (Fig. 1B), whilst ubiquinone-0 (Q_0) acts as a soluble electron acceptor. The RC comprises of a set of cofactors buried in protein scaffold in two branches (A and B). There are four bacteriochlorophylls, two of which form a dimer that acts as the primary donor of electron (P_{860}) and the other two are accessory bacteriochlorophylls (B_A and B_B). There are also two bacteriopheophytins (H_A and H_B), two quinones (Q_A and Q_B) and one carotenoid (Fig. 1A) [22].

Typically, after light absorption by any of the chromophores in the RC, the energy is transferred to the primary donor forming the P_{860}* excited state (Fig. 1B). The vast majority of excitation leads to charge separation within 3 ps, forming the $P^{+}_{860}H^{-}_{A}$ state [23]. Later on, the electron is transferred to a quinone at the Q_B binding site, through Q_A, forming the relatively long-lived $P^{+}_{860}Q^{-}_{B}$ state [24]. A current will flow in the cell if wiring of P^{+}_{860} and Q^{-}_{B} to the electrodes by the osmium HG and Q_0 outcompetes ~1 s lifetime recombination of $P^{+}Q^{-}_{B}$ (Fig. 1B).

Here, we describe the use of a combination of spectroscopic and electrochemical methods for the *in situ* determination of cofactor redox potentials in an assembled biophotovoltaic system with high Internal Quantum Efficiency (50±12 %), characterizing cofactor absorbance and photocurrent as a function of applied potential.

2. Experimental

2.1. Biophotoelectrochemical electrodes

FTO-coated glass slides (TEC 15, Sigma-Aldrich) were cleaned in an ultrasonic bath (Ct-Brand CT-432H1) sequentially in water with 4% TRILUX dish soap solution (Analab), double-distilled water and ethanol for 10 min each. After air-drying a 2-μl drop of aqueous HG-RC blend was placed on the slide surface. Composition of the blend was 5 mg/ml HG, 1 mg/ml wild type RC solution, 0.02 mg/ml poly (ethylene glycol) diglycidyl ether (PEGDGE, acts as crosslinker), 50 mM KCl, 50 mM phosphate buffer pH 7.0. After drop casting, electrodes were incubated in the dark at room temperature overnight. Prior to measurement, electrodes were gently rinsed with double-distilled water to remove loosely bound RCs and HG.

Rba. Sphaeroides RCs were purified as described previously [20].

Osmium-complex based redox HG poly (1-vinylimidazole-*co*-allylamine)-[Os(bpy)$_2$Cl]Cl (with bpy = 2,2′-bipyridine) was synthesized as described previously [13]. Briefly the Os-complex precursor Os(II) (bpy)$_2$Cl$_2$ and the polymer backbone poly (1-vinylimidazole-*co*-allylamine) were refluxed in ethanol in a 1.6:1 mass -ratio for several days. The polymer was precipitated by adding diethyl ether. The crude polymer was purified by several precipitations from ethanol/chloroform solution by adding diethyl ether. The polymer was obtained as a water soluble dark red solid in good yields. The polymer bound Os-complex moieties act as electron relays for shuttling electrons between the electrode surface and the enzyme, while the amino groups in the allylamine co-monomer react with the diepoxy based crosslinker PEGDGE and ensure the formation of stable polymer-enzyme films.

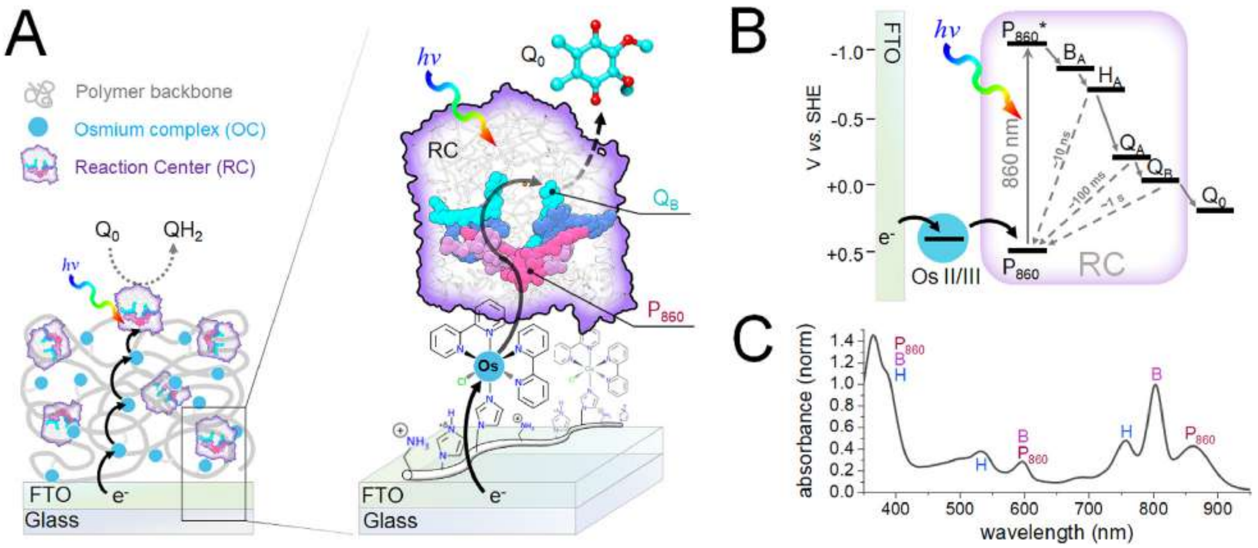

Fig. 1. (A) Scheme of the constructed optically active half-cell. Zoomed picture shows both the chemical structure of the HG and inner structure of RC's cofactors. (B) Energy diagram of the operating half-cell. Additionally, chosen recombination lifetimes inside the RC are presented. (C) Absorption spectrum of the RC solubilized in buffered (20 mM Tris-HCl pH 8.0) solution with detergent (0.1% LDAO).

2.2. Sample characterization

For both photoelectrochemical and absorbance measurements, an FTO-|HG|RC working electrode was employed in a three-electrode configuration in a specially-constructed spectroelectrochemical cell containing an electrolyte of 20 mM citrate buffer (pH 4.0) with 200 mM KCl (and 1.5 mM 2,3-dimethoxy-5-methyl-*p*-benzoquinone (Q_0; Sigma-Aldrich) for photocurrents). Details of the cell design and the experimental setup are given in Supporting Information, Figs. S1–S5. The FTO-|HG|RC working electrode was connected to the potentiostat by copper tape and ports gave access to the working electrode for absorbance measurements or photoexcitation and to the electrolyte for the reference and counter electrodes. For all electrochemical characterizations an Autolab PGSTAT204 potentiostat was used.

For measurements of absorbance change as a function of applied potential a custom setup was built. The measuring UV-VIS-NIR light source was an Avantes combined halogen and deuterium lamp (AvaLight-DH-S-BAL). Broadband detection was achieved using an Avantes HERO (AvaSpec-HSC1024x58TEC-EVO) spectrometer with range 285–1060 nm and 25-μm slit, equipped with a CCD. Light was guided by 600-μm-core optical fibers. The light after exiting the optical fiber before the sample was collimated through a lens (Avantes COL-UV/VIS) and after passing the sample was focused into a second optical fiber through a similar lens and then led to spectrometer. The spectrometer was set to a 200 ms integration time and 20 spectra were averaged for each final spectrum. The light intensity was kept low enough to prevent saturation of the detector in the chosen integration time. Potential was applied in steps lasting 60 s each, as this was enough to reach the plateau in current measurements. Spectra at the plateau of each of these steps were taken for further analysis.

For photocurrent measurements, an 860-nm LED was used whose characteristics are presented in Fig. S6. For each potential, the sample was equilibrated for 120 s prior to illumination, which lasted 30 s. At each potential the photocurrent was determined as the difference between the maximum cathodic current upon illumination and the dark current just before turning on the light.

Measurements of photocurrent External Quantum Efficiency (EQE) spectra were carried out with a photoelectric spectrometer (Instytut Fotonowy). Illumination was via a monochromator from a xenon arc lamp, and light intensity was constantly monitored for correction of the photon flux at the sample. The applied potential was +260 mV vs. SHE. At each wavelength the light was turned on for 10 s and then turned off for 10 s.

2.3. Internal Quantum Efficiency estimation

Internal Quantum Efficiency (IQE) estimation was based on the LED emission spectrum, the RC absorption spectrum in solution and the amplitude of P_{860} absorption band of RCs in HG from spectroelectrochemical measurements (see Supporting Information for details on the calculation). The LED emission spectrum was measured using an Avantes Hero fiber optics spectrometer calibrated for CCD sensitivity. The RC absorption spectrum was measured in buffered (20 mM Tris-HCl pH 8.0) solution with detergent (0.1% LDAO) using a Hitachi U-2800A spectrophotometer.

3. Results and discussion

3.1. Absorption

Absorption spectroscopy at applied potentials between +155 and + 805 mV vs. SHE (Fig. 2A) showed changes in absorbance relative to that at +155 mV vs. SHE attributable to the osmium-complex based redox HG, with maxima around 520 nm and 725 nm, and to the RC in the region between 750 nm and 950 nm. The latter included a highly characteristic bleach at 860 nm and an electrochromic band shift centered at 800 nm.

To confirm these assignments, global analysis with a Nernst curves model was performed on the absorbance data. Global analysis has already proven its utility in the field of time-resolved spectroscopy allowing accurate determination of lifetimes in exponential decay models [25]. The resulting Potential Associated Spectra (PAS) are shown in Fig. 2B (see SI section S3 for details of analysis and the derivation of equations). The PAS associated with a redox midpoint potential (E_m) of +531 ± 6 mV could be attributed to oxidation of the RC P_{860} primary donor, which is well known to cause a bleach at 860 nm and electrochromic blue- and red-shifts centered at 800 nm and 750 nm, respectively, due to the positive charge on P^{+}_{860} [7,8]. The PAS associated with an E_m of +425 ± 3 mV was attributable to the osmium complexes inside the HG matrix, and such shape of spectrum was also observable in a photoelectrode prepared without RCs (Fig. S7).

Fig. 3A shows a full electrochemical titration in which absorbance change (relative to the absorbance at +155 mV) at 520 nm or 860 nm was plotted as a function of time, with the applied potential changed at regular intervals. The data demonstrate that the absorbance changes reporting on the redox state of the RC and the Os-complex based HG were reversible. A plot of absorbance change

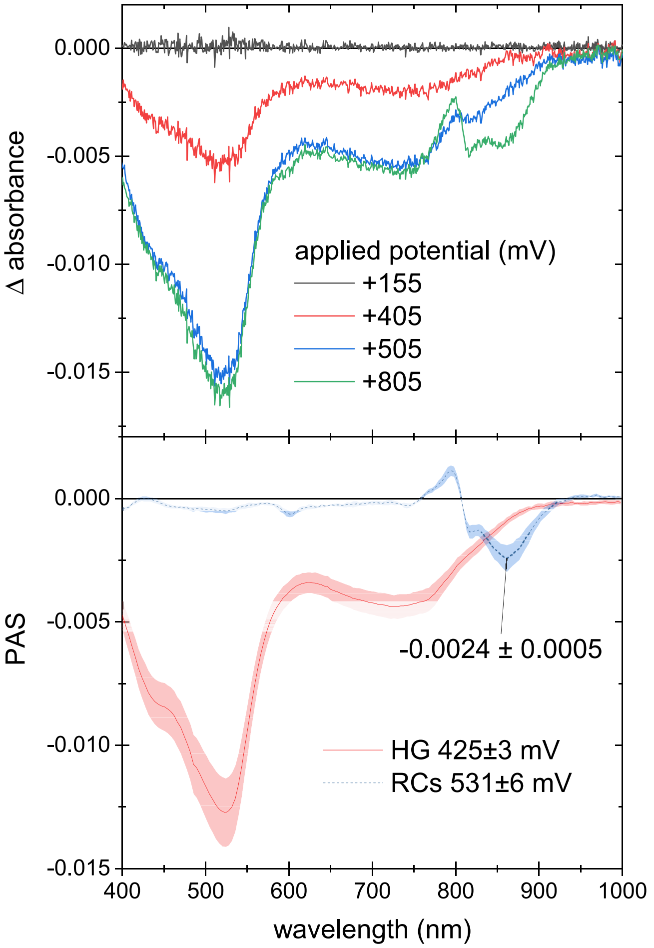

Fig. 2. (A) Absorbance change relative to that at +155 mV of a RC-HG modified FTO-electrode. (B) PAS obtained from global fitting of absorbance change vs. potential measurements. Spectra were averaged between samples (N = 5). Lighter shadow indicates standard deviation.

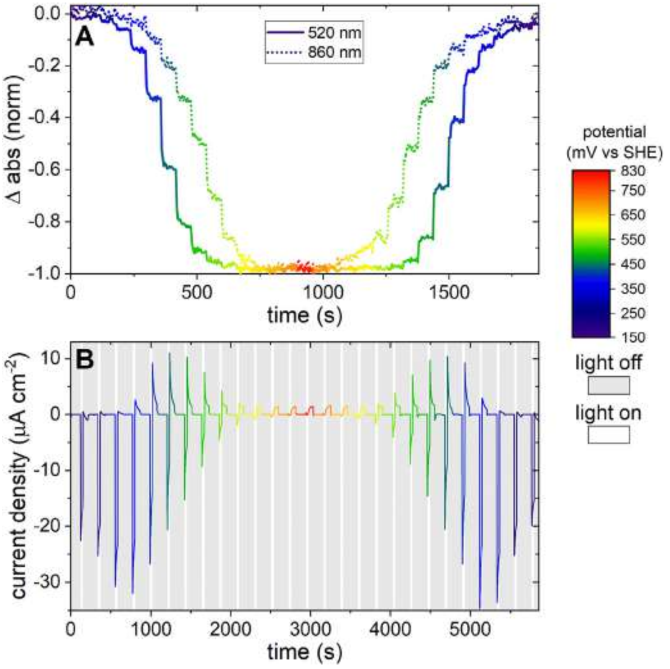

Fig. 3. Time traces for (A) absorbance difference and (B) photocurrent. Data in (A) are normalized for comparison. Data in (B) were corrected for the baseline dark current at each potential.

at 520 nm as a function of applied potential (Fig. 4A) could be fit with an n = 1 Nernst curve with an E_m at +425 ± 3 mV whilst a plot of the absorbance change at 860 nm was clearly biphasic (Fig. 4A), and could be fit as the sum of two n = 1 Nernst curves with E_m values of 425 ± 3 mV and 531 ± 6 mV.

The amplitude of the PAS attributed to RCs gives the opportunity to determine the amount of electrically connected RCs in the film. The amplitude of the photobleaching band around 860 nm (−0.0024 ± 0.0005) can be attributed to the absorbance of P_{860} in electrically connected RCs in the film in the fully reduced state (without P_{860}^{+} state; see Fig. 1C for comparison). The PAS does not look significantly different to the difference spectrum of P_{860}/P_{860}^{+} presented in literature [7], thus we can estimate the absorbance of the electrically connected RCs at the maximum around 800 nm to be equal to 0.0057 ± 0.0012 based on the absorption spectrum in aqueous solution (Fig. 1C). Using the literature value of the 800 nm extinction coefficient ($288\,000\ M^{-1}cm^{-1}$) [26] and Lambert-Beer law the surface concentration of the electrically connected RCs was estimated to be $\Gamma_{RCs} = 20{\pm}4\ pmol\ cm^{-2}$.

3.2. Photocurrents

Upon illumination by an 860-nm LED (Fig. S6), significant cathodic photocurrents were generated by the RC/osmium-complex polymer working electrode (see example in Fig. S8). The average photocurrent density among different samples (N = 5) at optimal potential and measured with freshly prepared electrode was 52±5 $\mu A cm^{-2}$.

A spectrum of photocurrent EQE as a function of excitation wavelength (Fig. 5) was in a good agreement with the absorptance spectrum of the RC confirming it as the source of the photocurrent. We used absorptance spectrum instead of absorption spectrum as the absorptance is proportional to the number of absorbed photons just as photocurrent density is. Variation of the photocurrent density with applied bias potential is shown in Fig. 3B; changes in photocurrent amplitude were again reversible, drop to zero

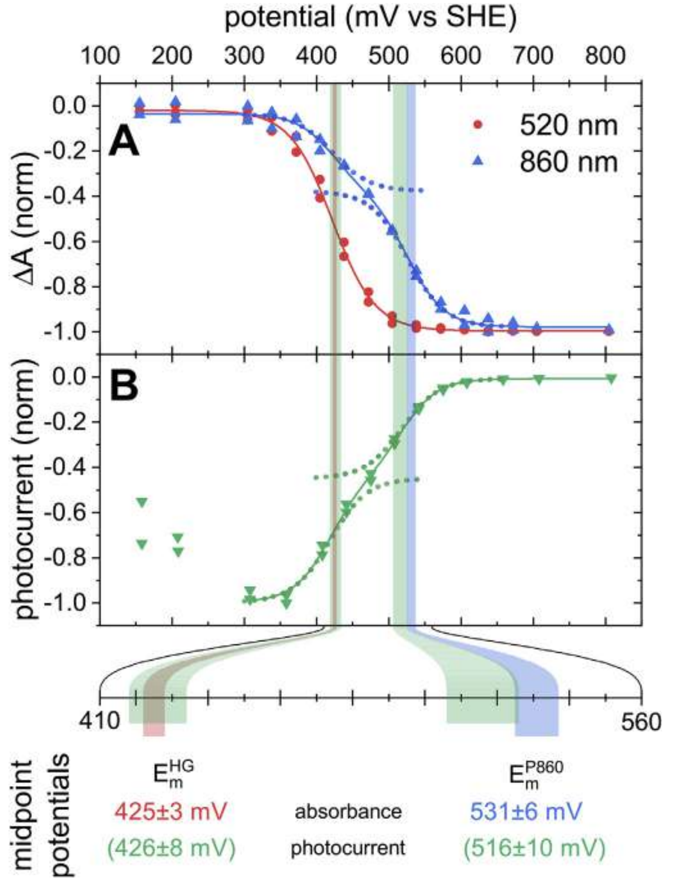

Fig. 4. Electrochemical titration plots for absorption and photocurrents. Vertical bars represent midpoint potentials obtained from color-matching curves with standard deviation. All plots were fitted with either one (red) or two Nernst curves (blue and green). For two-component fits the dotted lines show individual components and the solid line – the sum. (A) Normalized absorbance changes relative to the spectrum at +155 mV. (B) Normalized peak photocurrent. (For interpretation of the references to color in this figure legend, the reader is referred to the Web version of this article.)

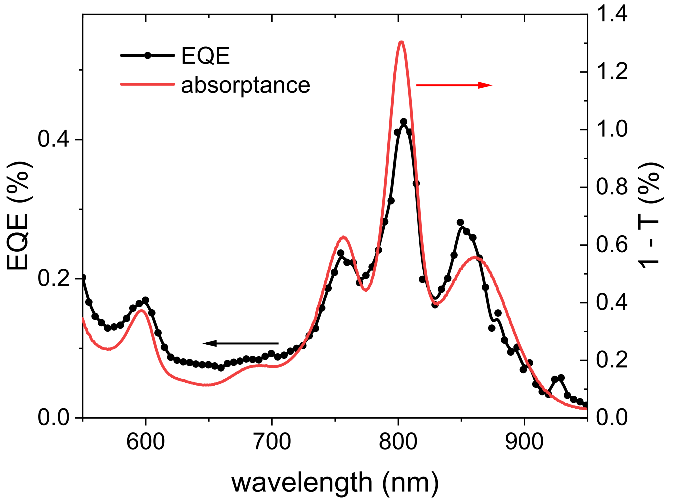

Fig. 5. Photocurrent External Quantum Efficiency (EQE) spectrum of the system compared with the absorptance (1 minus transmission) spectrum taken for RCs in buffered solution (same as in Fig. 1C, but scaled for the thin film absorption).

above +650 mV, and show a maximum around +300 mV. The maximum photocurrent value in Fig. 3B was lower than mentioned above for optimal potential, as the data in Fig. 3B were derived from the second potential sweeping cycle for this sample, thus the sample had undergone partial degradation. After this primary degradation within first potential sweeping cycle the photocurrent and absorbance changes were reversible. Plotting the maximum photocurrent (Fig. 4B), at potentials above +300 mV the decline had a compound sigmoidal shape and could be fitted with the sum of two one-electron Nernst curves with $E_m = 426 \pm 8$ mV and 516 ± 10 mV, in a good agreement with the results from absorbance measurements. Photocurrent vs. potential curve shape is by theory not a simple Nernst curve. However, within the obtained data the fit was sufficient. In general, this shape depends on relative rate constants of electron transfer between different elements of the system and the electrode as well as on electron diffusion constants. However, a full analysis of the latter lies outside the scope of this paper. The lower photocurrents seen at potentials below +300 mV (Figs. 3B and 4B) are likely due to reduction of freely diffusing quinone at the electrode surface, which decreases its ability to receive electrons from RCs (Q_0 is expected to have an E_m of around +230 mV in pH 4.0) [27].

3.3. *Internal Quantum Efficiency*

IQE of the cells was calculated based on the absorbance amplitude of electrically connected RCs (0.0024 ± 0.0005 at around 860 nm) and photocurrent density (52±5 μAcm^{-2}) to be equal to 50±12 %. It is only 2-fold lower than the quantum efficiency of the charge transfer within RCs in living cells [28]. The high IQE confirms that the investigated system is suitable for deeper characterization as the amount of loss is low. So far lower values of IQE were reported or even not calculated for some systems. One of the highest values so far was IQE of 39% reported for two system in two papers: Friebe et al. [29] for RC-LH1 complexes on rough silver electrodes with plasmon enhancement (white light, 1 sun illumination) and Stieger et al. [30] for PSI on mesoporous ITO (white light, around 1 mW cm^{-2}). Both of these systems consist of porous conductive electrodes and proteins are wired to the surface with cytochrome c. Other system worth mentioning are Langmuir-Blodget (LB) monolayers of RC-LH1 complexes on gold electrodes by Kamran et al. [31] with 32% IQE (880 nm LED, 23 mW cm^{-2}). It shows that even in LB films where the geometry and orientation of proteins is uniform, IQE is lower than in the system with electron mediator filling the space between protein and electrode, such as redox HG. In most of other papers, the IQE reported is below 10% (for example 1.3% for Singh et al. [32]).

3.4. *Midpoint potential shift*

The E_m^{HG} of redox HG has been reported to depend on pH, ionic strength of the solution and type of protein included in the matrix. In combination with various enzymes and operated under different conditions value for the redox potential of the here used polymer lay in the range from 395 to 463 mV [15,33,34]. Moreover, CV recorded with a HG modifed FTO electrode under the same conditions that are used for the spectroelectrochemical experiments reveal a redox potential for the polymer of 421 mV (see Fig. S9 for sample CV). The value obtained here by absorbance measurements (425 mV ± 3) is in a good agreement with these values, thus confirming the correctness of the method.

The E_m^{P860} of *Rba. Sphaeroides* RCs solubilized in solution has been extensively studied using absorbance measurements coupled with both chemical and electrochemical titration, with values of 450–505 mV reported [7–9,35–42]. The value of 531 mV obtained here by absorbance measurements was at least 25 mV higher than previous reports on RCs in solution, indicating an influence of the Os-complex based hyrogel matrix. It is known that the use of different detergents can cause changes in E_m^{P860} [7], likely due to electric charge and the polarity of surfactant head groups in the vicinity of P_{860}. In the present case the backbone of the redox polymer used to encapsulate the RC as well as the Os-complex based electron mediator are positively charged, which likely shifts E_m^{P860} to the observed higher value. This highlights the importance of the polymer backbone composition in terms of its interaction with the redox active protein.

The obtained difference between E_m^{HG} and E_m^{P860} of about 105 mV gives a driving force lower than that occurring in the natural system with cytochrome c_2 (+300 mV vs. SHE *in vivo*) [43] serving as the electron donor to P_{860}. It may be one of the reasons for lowering of IQE along with unknown spatial coupling of osmium-complex redox centers with RCs. Knowing the exact values of E_m^{HG} and E_m^{P860} *in situ* is a basis for improvement of future designs for example in terms of IQE. On the other hand, a further decrease of the driving force would decrease energy losses in the system, and the net effect of increased voltage of the device and decreased photocurrent (IQE) could be positive.

4. Conclusions

To conclude, although the *Rba. Sphaeroides* RC and related proteins have been used extensively as the basis for a wide variety of bio-photoelectrochemical cells, there has been relatively little attempt to use absorbance spectroscopy to interrogate their properties on an electrode or in a photoelectrochemical cell. In the present work a spectrophotoelectrochemical cell was constructed that enabled measurements of absorbance and photocurrent as a function of applied potential, producing information on the effect of potential on the redox state of key components and their impact on the measured photocurrent. From the EQE spectrum and the differential absorption spectra it was possible to conclude that the RCs remained functionally intact within the HG matrix, and that the midpoint potential of the primary electron donor was shifted towards a more positive potentials than those reported in the literature. Moreover, the IQE of the system was estimated in a relatively high value of 50 ± 12% presenting it as a good model system. This showed the importance of *in situ* measurements when an exact value is necessary for the modelling of mechanism of operation of a biophotovoltaic devices. Looking ahead, a major issue in the design of biophotovoltaic devices is understanding processes such as recombination, electron transfer bottlenecks and energy transfer inefficiencies that limit their photocurrents and photovoltages they can generate. Devices in which absorbance and photocurrent can be measured under controlled redox conditions open the door to the use of time-resolved optical spectroscopy for determination of kinetic rate constants for electron transfer between different parts of the system. Such techniques have unlocked the secrets of the high quantum efficiency of natural solar energy conversion, and there is the prospect of their use to inform iterative rational design of biophotovoltaic devices with improved performance.

Notes

The authors declare no competing financial interests.

Acknowledgment

We would like to thank Prof. Dr. Nicolas Plumeré from Ruhr-University Bochum for fruitful discussions and support in preparation of this work. RB acknowledges support from the Ministry of

Science and Higher Education, Poland (project entitled: “Construction of solar cells based on purple bacteria Reaction Centers and polymer hydrogels” no. 0129/DIA/2016/45). KG acknowledges support from the National Science Center, Poland (project entitled “Bio-semiconductor hybrids for photovoltaic cells” no. 2012/07/B/NZ1/02639). AR thanks the Deutsche Forschungsgemeinschaft (DFG) under Germany’s Excellence Strategy EXC-2033 (project number 390677874) for a PostDoc fellowship.

Appendix A. Supplementary data

Supplementary data to this article can be found online at https://doi.org/10.1016/j.electacta.2019.135190.

References

[1] C. Léger, P. Bertrand, Direct electrochemistry of redox enzymes as a tool for mechanistic studies, Chem. Rev. 108 (2008) 2379–2438, https://doi.org/10.1021/cr0680742.

[2] O. Kievit, G.W. Brudvig, Direct electrochemistry of photosystem I, J. Electroanal. Chem. 497 (2001) 139–149, https://doi.org/10.1016/S0022-0728(00)00467-8.

[3] M. Ciobanu, H.A. Kincaid, V. Lo, A.D. Dukes, G. Kane Jennings, D.E. Cliffel, Electrochemistry and photoelectrochemistry of photosystem I adsorbed on hydroxyl-terminated monolayers, J. Electroanal. Chem. 599 (2007) 72–78, https://doi.org/10.1016/j.jelechem.2006.09.019.

[4] A. Nakamura, T. Suzawa, Y. Kato, T. Watanabe, Significant species-dependence of P700 redox potential as verified by spectroelectrochemistry: comparison of spinach and Theromosynechococcus elongatus, FEBS Lett. 579 (2005) 2273–2276, https://doi.org/10.1016/j.febslet.2005.02.076.

[5] A. Nakamura, T. Suzawa, T. Watanabe, Spectroelectrochemical determination of the redox potential of P700 in spinach with an optically transparent thin-layer electrode, Chem. Lett. 33 (2004) 688–689, https://doi.org/10.1246/cl.2004.688.

[6] A. Nakamura, T. Suzawa, Y. Kato, T. Watanabe, Species dependence of the redox potential of the primary electron donor P700 in photosystem I of oxygenic photosynthetic organisms revealed by spectroelectrochemistry, Plant Cell Physiol. 52 (2011) 815–823, https://doi.org/10.1093/pcp/pcr034.

[7] S.S. Deshmukh, H. Akhavein, J.C. Williams, J.P. Allen, L. Kálmán, Light-induced conformational changes in photosynthetic reaction centers: impact of detergents and lipids on the electronic structure of the primary electron donor, Biochemistry 50 (2011) 5249–5262, https://doi.org/10.1021/bi200595z.

[8] S.S. Deshmukh, J.C. Williams, J.P. Allen, L. Kálmán, Light-induced conformational changes in photosynthetic reaction centers: redox-regulated proton pathway near the dimer, Biochemistry 50 (2011) 3321–3331, https://doi.org/10.1021/bi200169y.

[9] X. Lin, H. a Murchison, V. Nagarajan, W.W. Parson, J.P. Allen, J.C. Williams, Specific alteration of the oxidation potential of the electron donor in reaction centers from Rhodobacter sphaeroides, Proc. Natl. Acad. Sci. U. S. A 91 (1994) 10265–10269, https://doi.org/10.1073/pnas.91.22.10265.

[10] J. Petrović, R.A. Clark, H. Yue, D.H. Waldeck, E.F. Bowden, Impact of surface immobilization and solution ionic strength on the formal potential of immobilized cytochrome c, Langmuir 21 (2005) 6308–6316, https://doi.org/10.1021/la0500373.

[11] R. Białek, D.J.K. Swainsbury, M. Wiesner, M.R. Jones, K. Gibasiewicz, Modelling of the cathodic and anodic photocurrents from Rhodobacter sphaeroides reaction centres immobilized on titanium dioxide, Photosynth. Res. 138 (2018) 103–114, https://doi.org/10.1007/s11120-018-0550-8.

[12] M.T. Robinson, D.E. Cliffel, G.K. Jennings, An electrochemical reaction-diffusion model of the photocatalytic effect of photosystem i multilayer films, J. Phys. Chem. B 122 (2018) 117–125, https://doi.org/10.1021/acs.jpcb.7b10374.

[13] F. Conzuelo, N. Marković, A. Ruff, W. Schuhmann, The open circuit voltage in biofuel cells: nernstian shift in pseudocapacitive electrodes, Angew. Chem. Int. Ed. 57 (2018) 13681–13685, https://doi.org/10.1002/anie.201808450.

[14] T. Kothe, S. Pöller, F. Zhao, P. Fortgang, M. Rögner, W. Schuhmann, N. Plumeré, Engineered electron-transfer chain in photosystem 1 based photocathodes outperforms electron-transfer rates in natural photosynthesis, Chem. Eur J. 20 (2014) 11029–11034, https://doi.org/10.1002/chem.201402585.

[15] T. Kothe, N. Plumeré, A. Badura, M.M. Nowaczyk, D.A. Guschin, M. Rögner, W. Schuhmann, Combination of A Photosystem 1-based photocathode and a photosystem 2-based photoanode to a Z-scheme mimic for biophotovoltaic applications, Angew. Chem. Int. Ed. 52 (2013) 14233–14236, https://doi.org/10.1002/anie.201303671.

[16] K.P. Sokol, D. Mersch, V. Hartmann, J.Z. Zhang, M.M. Nowaczyk, M. Rögner, A. Ruff, W. Schuhmann, N. Plumeré, E. Reisner, Rational wiring of photosystem II to hierarchical indium tin oxide electrodes using redox polymers, Energy Environ. Sci. 9 (2016) 3698–3709, https://doi.org/10.1039/C6EE01363E.

[17] M.R. Jones, The petite purple photosynthetic powerpack, Biochem. Soc. Trans. 37 (2009) 400–407, https://doi.org/10.1042/bst0370400.

[18] V.M. Friebe, R.N. Frese, Photosynthetic reaction center-based biophotovoltaics, Curr. Opin. Electrochem. 5 (2017) 126–134, https://doi.org/10.1016/j.coelec.2017.08.001.

[19] S.K. Ravi, S.C. Tan, Progress and perspectives in exploiting photosynthetic biomolecules for solar energy harnessing, Energy Environ. Sci. 8 (2015) 2551–2573, https://doi.org/10.1039/C5EE01361E.

[20] D.J.K. Swainsbury, V.M. Friebe, R.N. Frese, M.R. Jones, Evaluation of a biohybrid photoelectrochemical cell employing the purple bacterial reaction centre as a biosensor for herbicides, Biosens. Bioelectron. 58 (2014) 172–178, https://doi.org/10.1016/j.bios.2014.02.050.

[21] A. Ruff, Redox polymers in bioelectrochemistry: common playgrounds and novel concepts, Curr. Opin. Electrochem. 5 (2017) 66–73, https://doi.org/10.1016/j.coelec.2017.06.007.

[22] S.E. D’Haene, L.I. Crouch, M.R. Jones, R.N. Frese, Organization in photosynthetic membranes of purple bacteria in vivo: the role of carotenoids, Biochim. Biophys. Acta Bioenerg. 1837 (2014) 1665–1673, https://doi.org/10.1016/j.bbabio.2014.07.003.

[23] P. Müller, G. Bieser, G. Hartwich, T. Langenbacher, H. Lossau, A. Ogrodnik, M.-E. Michel-Beyerle, The internal conversion rate of the primary donor in reaction centers of Rhodobacter sphaeroides, Berichte Der Bunsengesellschaft Für Phys. Chemie. 100 (1996) 1967–1973, https://doi.org/10.1002/bbpc.19961001207.

[24] J.P. Allen, J.C. Williams, M.S. Graige, M.L. Paddock, A. Labahn, G. Feher, M.Y. Okamura, Free energy dependence of the direct charge recombination from the primary and secondary quinones in reaction centers from Rhodobacter sphaeroides, Photosynth. Res. 55 (1998) 227–233.

[25] I.H.M. van Stokkum, D.S. Larsen, R. van Grondelle, Global and target analysis of time-resolved spectra, Biochim. Biophys. Acta Bioenerg. 1657 (2004) 82–104, https://doi.org/10.1016/j.bbabio.2004.04.011.

[26] S.C. Straley, W.W. Parson, D.C. Mauzerall, R.K. Clayton, Pigment content and molar extinction coefficients of photochemical reaction centers from *Rhodopseudomonas spheroides*, Biochim. Biophys. Acta Bioenerg. 305 (1973) 597–609, https://doi.org/10.1016/0005-2728(73)90079-0.

[27] P. Maróti, C.A. Wraight, The redox midpoint potential of the primary quinone of reaction centers in chromatophores of *Rhodobacter sphaeroides* is pH independent, Eur. Biophys. J. 37 (2008) 1207–1217, https://doi.org/10.1007/s00249-008-0301-4.

[28] C.A. Wraight, R.K. Clayton, The absolute quantum efficiency of bacteriochlorophyll photooxidation in reaction centres of Rhodopseudomonas spheroides, Biochim. Biophys. Acta Bioenerg. 333 (1974) 246–260, https://doi.org/10.1016/0005-2728(74)90009-7.

[29] V.M. Friebe, J.D. Delgado, D.J.K.K. Swainsbury, J.M. Gruber, A. Chanaewa, R. van Grondelle, E. Von Hauff, D. Millo, M.R. Jones, R.N. Frese, Plasmon-enhanced photocurrent of photosynthetic pigment proteins on nanoporous silver, Adv. Funct. Mater. 26 (2016) 285–292, https://doi.org/10.1002/adfm.201504020.

[30] K.R. Stieger, S.C. Feifel, H. Lokstein, M. Hejazi, A. Zouni, F. Lisdat, Biohybrid architectures for efficient light-to-current conversion based on photosystem i within scalable 3D mesoporous electrodes, J. Mater. Chem. A. 4 (2016) 17009–17017, https://doi.org/10.1039/c6ta07141d.

[31] M. Kamran, J.D. Delgado, V. Friebe, T.J. Aartsma, R.N. Frese, Photosynthetic protein complexes as bio-photovoltaic building blocks retaining a high internal quantum E ffi ciency, Biomacromolecules 15 (2014) 2833–2838, https://doi.org/10.1021/bm500585s.

[32] V.K. Singh, S.K. Ravi, J.W. Ho, J.K.C. Wong, M.R. Jones, S.C. Tan, Biohybrid photoprotein-semiconductor cells with deep-lying redox shuttles achieve a 0.7 V photovoltage, Adv. Funct. Mater. 1703689 (2017) 1–8, https://doi.org/10.1002/ADFM.201703689.

[33] A. Badura, D. Guschin, B. Esper, T. Kothe, S. Neugebauer, W. Schuhmann, M. Rögner, Photo-Induced electron transfer between photosystem 2 via cross-linked redox hydrogels, Electroanalysis 20 (2008) 1043–1047, https://doi.org/10.1002/elan.200804191.

[34] F. Zhao, K. Sliozberg, M. Rogner, N. Plumere, W. Schuhmann, The role of hydrophobicity of Os-Complex-Modified polymers for photosystem 1 based photocathodes, J. Electrochem. Soc. 161 (2014) H3035–H3041, https://doi.org/10.1149/2.0081413jes.

[35] D.A. Moss, M. Leonhard, M. Bauscher, W. Mäntele, Electrochemical redox titration of cofactors in the reaction center from Rhodobacter sphaeroides, FEBS Lett. 283 (1991) 33–36, https://doi.org/10.1016/0014-5793(91)80547-G.

[36] J.C. Williams, R.G. Alden, H.A. Murchison, J.M. Peloquin, N.W. Woodbury, J.P. Allen, Effects of mutations near the bacteriochlorophylls in reaction centers from rhodobacter sphaeroides, Biochemistry 31 (1992) 11029–11037, https://doi.org/10.1021/bi00160a012.

[37] H.A. Murchison, R.G. Alden, J.P. Allen, J.M. Peloquin, A.K.W. Taguchi, N.W. Woodbury, J.C. Williams, Mutations designed to modify the environment of the primary electron donor of the reaction center from rhodobacter sphaeroides: phenylalanine to leucine at L167 and histidine to phenylalanine at L168, Biochemistry 32 (1993) 3498–3505, https://doi.org/10.1021/bi00064a038.

[38] V. Nagarajan, W.W. Parson, D. Davis, C.C. Schenck, Kinetics and free energy gaps of electron-transfer reactions in Rhodobacter sphaeroides reaction centers, Biochemistry 32 (1993) 12324–12336, https://doi.org/10.1021/bi00097a008.

[39] K. Artz, J.C. Williams, J.P. Allen, F. Lendzian, J. Rautter, W. Lubitz, G. Feher, Relationship between the oxidation potential and electron spin density of the primary electron donor in reaction centers from Rhodobacter sphaeroides,

Biophys. Approv. 94 (1997) 13582–13587, https://doi.org/10.1073/pnas.94.25.13582.

[40] J.P. Ridge, P.K. Fyfe, K.E. McAuley, M.E. van Brederode, B. Robert, R. van Grondelle, N.W. Isaacs, R.J. Cogdell, M.R. Jones, An examination of how structural changes can affect the rate of electron transfer in a mutated bacterial photoreaction centre, Biochem. J. 351 Pt 3 (2000) 567–578, https://doi.org/10.1042/0264-6021:3510567.

[41] T.N. Kropacheva, A.J. Hoff, Electrochemical oxidation of bacteriochlorophyll a in reaction centers and antenna complexes of photosynthetic bacteria, J. Phys. Chem. B 105 (2001) 5536–5545, https://doi.org/10.1021/jp003381b.

[42] D. Spiedel, M.R. Jones, B. Robert, Tuning of the redox potential of the primary electron donor in reaction centres of purple bacteria: effects of amino acid polarity and position, FEBS Lett. 527 (2002) 171–175, doi:Pii S0014-5793(02)03203-9.

[43] R.C. Prince, P.L. Dutton, The pH dependence of the oxidation-reduction midpoint potential of cytochromes c2 in vivo, BBA - Bioenerg 459 (1977) 573–577, https://doi.org/10.1016/0005-2728(77)90055-X.

Supporting Information

In Situ Spectroelectrochemical Investigation of a Biophotoelectrode Based on Photoreaction Centers Embedded in a Redox Hydrogel

Rafał Białek[1]*, Vincent Friebe[2,3], Adrian Ruff[4], Michael R. Jones[5], Raoul Frese[2] and Krzysztof Gibasiewicz[1]*

[1] Faculty of Physics, Adam Mickiewicz University in Poznań, ul. Uniwersytetu Poznańskiego 2, 61-614 Poznań, Poland

[2] Department of Physics and Astronomy, LaserLaB Amsterdam, VU University Amsterdam, De Boelelaan 1081, Amsterdam 1081 HV, The Netherlands

[3] Center for Electrochemical Sciences – Molecular Nanostructures, Faculty of Biochemistry and Chemistry, Ruhr-University Bochum, Universitätsstrasse 150, D-44780 Bochum, Germany

[4] Analytical Chemistry – Center for Electrochemical Sciences (CES), Faculty of Biochemistry and Chemistry, Ruhr-University Bochum, Universitätsstrasse 150, D-44780 Bochum, Germany

[5] School of Biochemistry, Biomedical Sciences Building, University of Bristol, University Walk, Bristol BS8 1TD, UK

SECTION S1 SPECTROPHOTOELECTROCHEMICAL CELL

For absorbance and photocurrent measurements a specialist cell was designed and manufactured from polyethylene terephthalate glycol (PETG) filament using a 3D printer. Components of the cell were held together with M3 bolts and nuts. Figure S1 presents its appearance and Figures S2-S4 present technical drawings. Some of the dimensions (especially inner ones) were in practice somewhat smaller due to shrinkage of the material during 3D printing. The FTO-coated glass formed the working electrode (WE), an Ag/AgCl (3 M NaCl) electrode (012167 RE-1B from ALS) formed the reference (RE) and Pt wire formed the counter electrode (CE). The working electrode was connected to a potentiostat via a copper tape (3M).

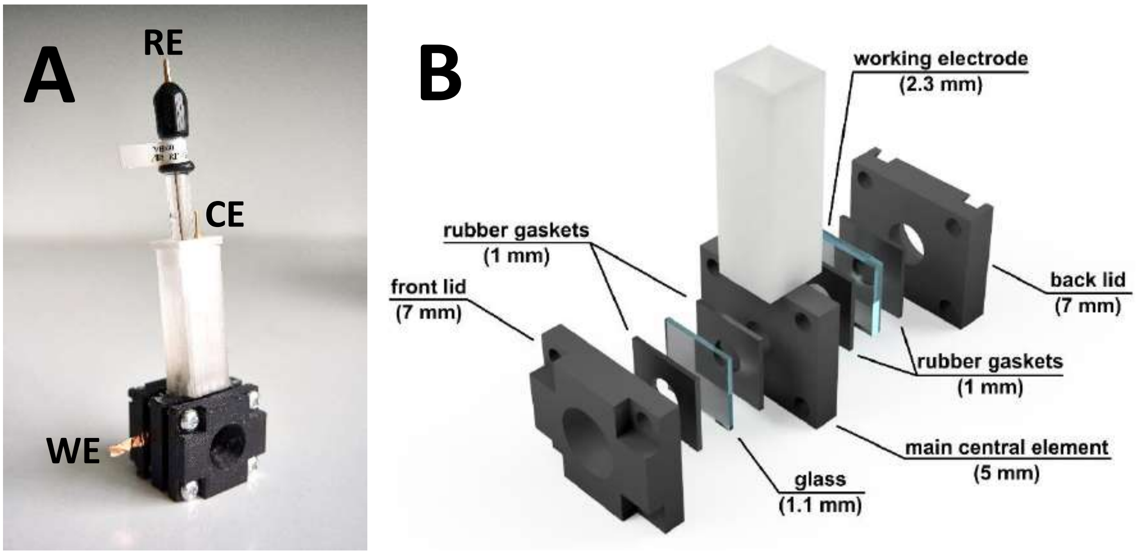

Figure S1 Assembled (A) and exploded (B) view of the spectroelectrochemical cell for absorption and photocurrent measurements. Dimensions in brackets in B are the thicknesses of the components.

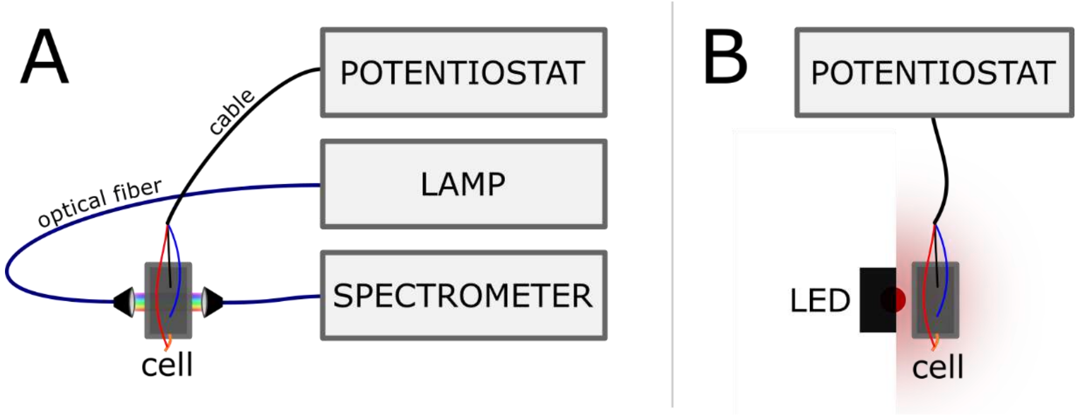

Figure S2 Experimental setup schemes for (A) absorption and (B) photocurrent measurements. Cell means the spectroelectrochemical cell from Figure S1.

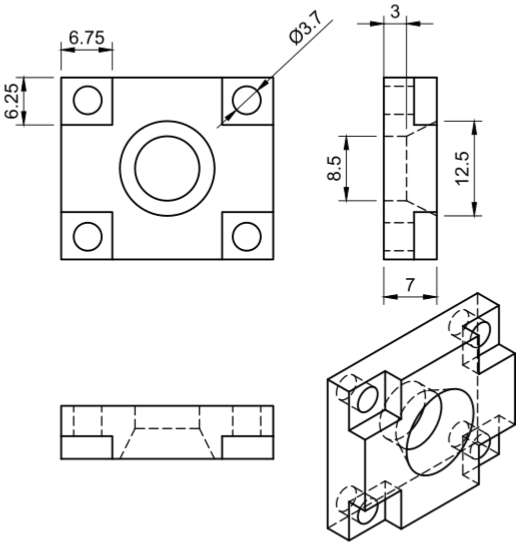

Figure S3 Technical drawing of the front lid of the spectroelectrochemical cell.

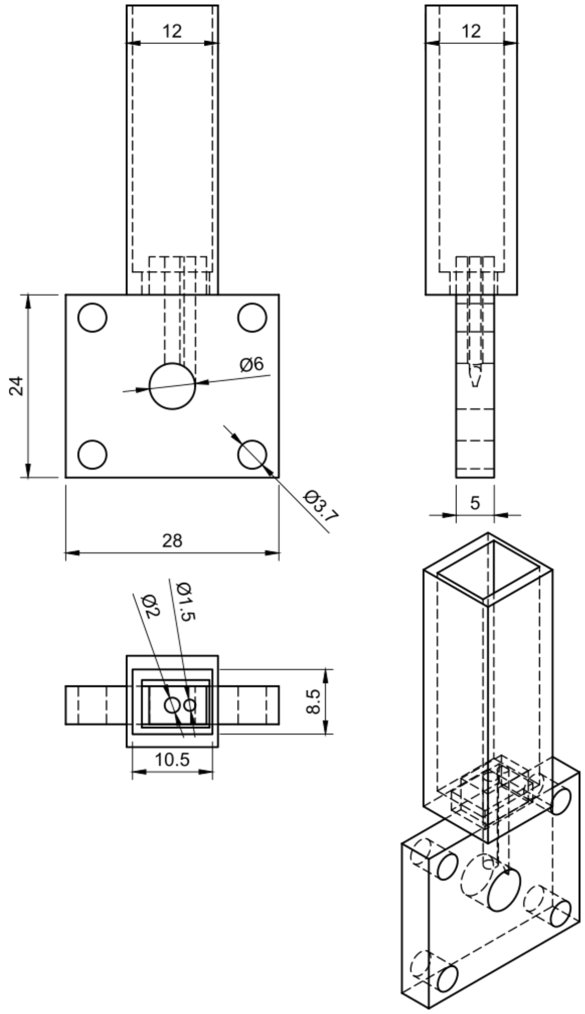

Figure S4 Technical drawing of the central element of the spectroelectrochemical cell. It was printed as two separate parts and glued together with silicon glue.

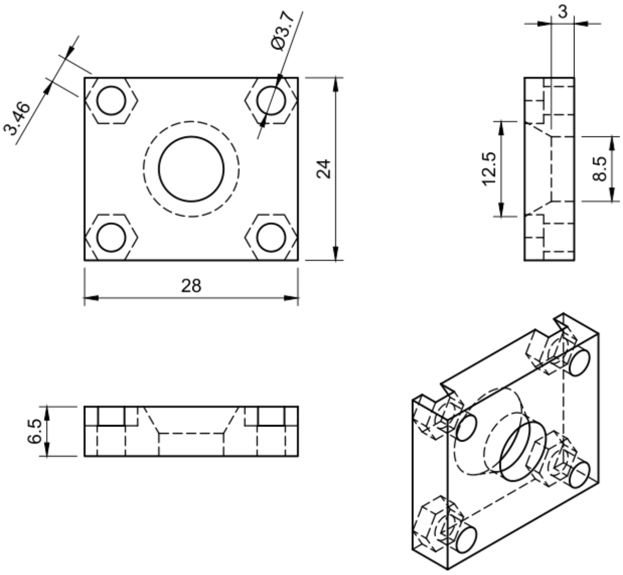

Figure S5 Technical drawing of the rear lid of the spectroelectrochemical cell.

SECTION S2 LED FOR PHOTOCURRENT MEASUREMENTS

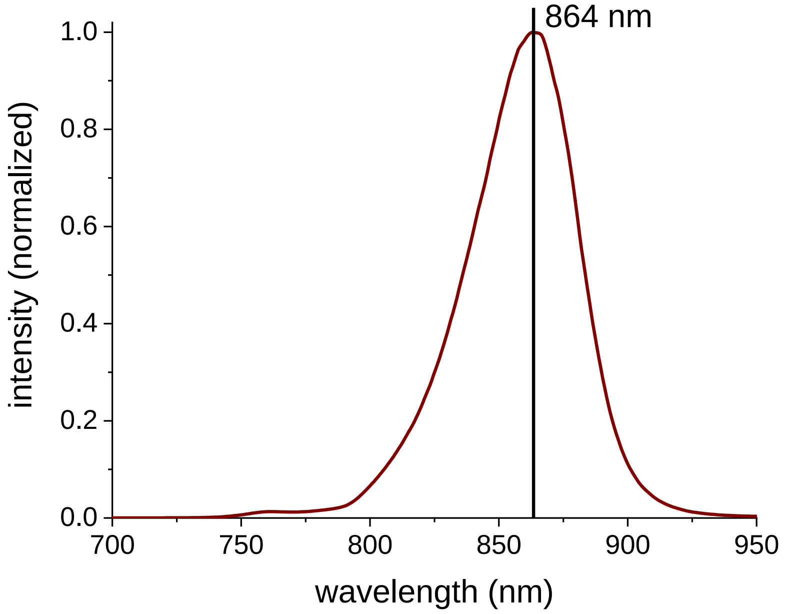

Figure S6 Spectrum of the LED used as the excitation light source for photocurrent measurements. FWHM 53 nm, incident intensity at sample position 29.3 ± 1.5 mW cm^{-2}.

SECTION S3 DATA ANALYSIS

S3.1 Fitting with the Nernst equation

For one-electron ($n = 1$) reversible reaction one can write a Nernst equation:

$$E = E_m - \frac{RT}{F}\ln\frac{[red]}{[ox]} \tag{S1}$$

Where:

E – electrochemical potential,

E_0 – electrochemical midpoint potential,

R – universal gas constant ($R = 8.314\, J\ K^{-1} mol^{-1}$),

T – temperature in kelvin,

F – Faraday constant ($F = 96485.34\ C\ mol^{-1}$),

$[red]/[ox]$ – molar concentration of reduced/oxidized species.

From equation S2 one can obtain mole fraction of the oxidized state of the species as a function of the electrochemical potential:

$$\frac{[ox]}{[ox] + [red]} = \frac{1}{1 + \exp\left((E_m - E) \cdot \frac{F}{R\,T}\right)} \tag{S2}$$

Thus, everywhere in the analysis, where Nernst curve is mentioned, following simplified and generalized fitting equations with additional offset correction, *A₀*, was used:

$$f(x) = A_0 + \sum_i \frac{A_i}{1 + \exp\left(\frac{x_{0\_i} - x}{dx_i}\right)} \tag{S3}$$

Where: A_i – amplitude of i-th component, x_{0_i} – inflection point position of i-th component, dx_i – parameter describing width of the i-th component curve, x – independent variable (applied potential in described case).

Additionally, dx_i was fixed at value determined by constants for one-electron reaction $dx_i = \frac{R\,T}{F} = = \frac{8.314\ J\ K^{-1} mol^{-1} \cdot 297\ K}{96485.34\ C\ mol^{-1}} = 25.6 mV$.

S3.2 Global analysis of data on absorbance vs potential

Spectra from measurements of absorbance as a function of applied potential were placed in a 2-D array of time versus wavelength. All data from each experiment were fitted simultaneously using a global analysis algorithm in which midpoint potentials were kept constant for all wavelengths, while amplitudes were allowed to change between wavelengths. The final fitting equation was:

$$f(x,\lambda) = A_0(\lambda) + \sum_i \frac{A_i(\lambda)}{1 + \exp\left(\frac{x_{0\_i} - x}{dx_i}\right)} \tag{S4}$$

Fitting function was implemented in Python using the scipy.optimize module.[1]

S3.3 IQE estimation

Internal Quantum Efficiency (IQE) for photoelectrochemical device is defined as:

$$IQE = \frac{N_{gen.el.}}{N_{abs.ph.}} \tag{S5}$$

Where: $N_{gen.el.}$ – number of generated electrons per unit time per unit area $[s^{-1}cm^{-2}]$, $N_{abs.ph.}$ – number of absorbed photons per unit time per unit area $[s^{-1}cm^{-2}]$.

$N_{gen.el.}$ can be calculated from the photocurrent density:

$$N_{gen.el.} = \frac{J}{e} \tag{S6}$$

Where: J – photocurrent density $[A\ cm^{-2}]$, e – elementary charge $(1.6 \cdot 10^{-19}\ C)$.

$N_{abs.ph.}$ can be calculated from the spectral distribution of photon flux shining on the device (LED emission spectrum) and absorption spectrum of RCs:

$$N_{abs.ph.} = \int \Phi(\lambda)\big(1 - T(\lambda)\big)d\lambda \tag{S7}$$

Where: $\Phi(\lambda)$ – photon flux spectral distribution $[cm^{-2}s^{-1}nm^{-1}]$, $T(\lambda)$ – transmission spectrum of RCs (known from measurements in aqueous solution, properly scaled for absorption of RCs in HG), λ – wavelength $[nm]$.

SECTION S4 ADDITIONAL RESULTS

S4.1 Absorption changes without RCs

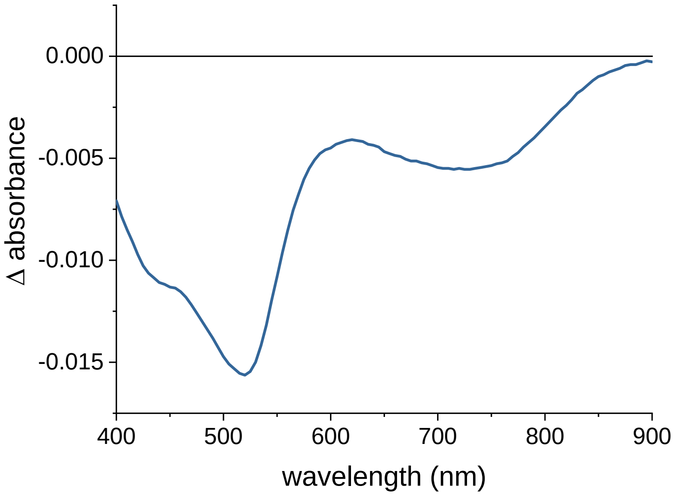

Figure S7 Absorption change at +505 mV applied potential relative to that at +155 mV of the FTO electrode modified with HG without RCs (buffer used in preparation instead of RCs in preparation).

S4.2 Sample photocurrent trace

The typical shape of the photocurrent trace at a reducing applied bias showed initial peak of cathodic photocurrent followed by a slow decrease (Figure S7), likely due to the consumption and diffusion limited mass transport of the Q_0 mediator, as well as recombination of its reduced form (quinol – Q_0H_2) with the working electrode. Charge recombination was clearly visible after turning off the light, whereby there was an anodic current overshoot due to the recombination of the quinol product with the working electrode. This was seen more strongly at more oxidizing potentials, where quinol oxidation is thermodynamically favorable – Figure 3C).

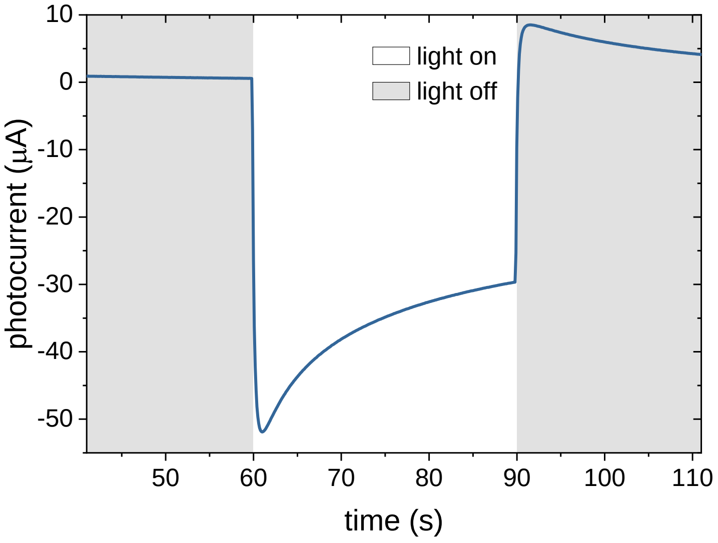

Figure S8 Sample photocurrent at +360 mV vs SHE applied potential.

S4.3 Cyclic Voltammetry

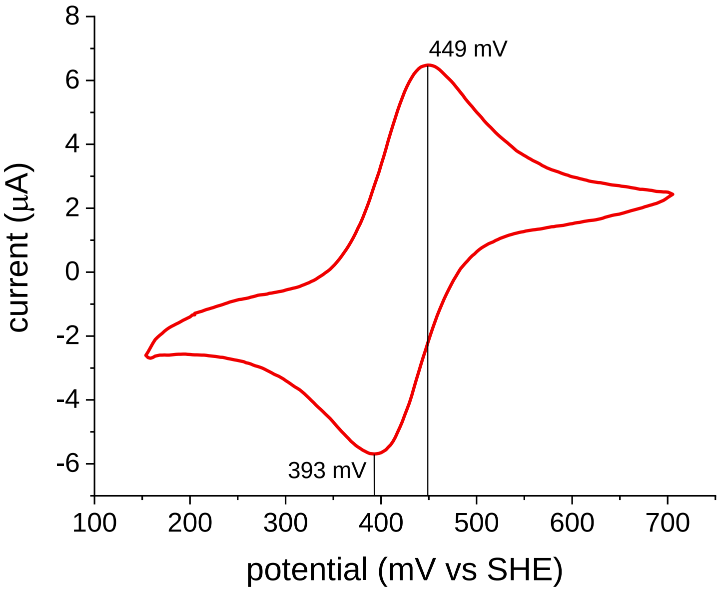

Figure S9 Sample cyclic voltammogram of HG-RCs-modified FTO electrode measured at 100 mV s^{-1} in pH 4.0 20 mM citrate buffer with addition of 200 mM KCl. The midpoint potential is equal to 421 mV.

SECTION S5 REFERENCES

[1] E. Jones, O. Travis, P. Peterson, SciPy: Open Source Scientific Tools for Python, (2001). http://www.scipy.org/ (accessed January 28, 2019).

Insight in the electron transfer from a redox polymer to a photoactive protein

Journal:	*The Journal of Physical Chemistry*
Manuscript ID	jp-2020-087149.R2
Manuscript Type:	Article
Date Submitted by the Author:	n/a
Complete List of Authors:	Białek, Rafał; Uniwersytet im Adama Mickiewicza w Poznaniu, Faculty of Physics Thakur, Kalyani; Max Planck Institute for Polymer Research, Molecular Electronics Ruff, Adrian; Ruhr-Universitat Bochum, Lehrstuhl für Analytische Chemie; PPG Deutschland Business Support GmbH, Packaging EMEA Jones, Michael; University of Bristol, School of Biochemistry Schuhmann, Wolfgang; Ruhr-Universitat Bochum, Lehrstuhl für Analytische Chemie Ramanan, Charusheela; Max-Planck-Institut fur Polymerforschung, Gibasiewicz, Krzysztof; Uniwersytet im Adama Mickiewicza w Poznaniu, Faculty of Physics

Insight in the electron transfer from a redox polymer to a photoactive protein

Rafał Białek[a]*, Kalyani Thakur[b], Adrian Ruff[c#], Michael R. Jones[d], Wolfgang Schuhmann[c], Charusheela Ramanan[b], and Krzysztof Gibasiewicz[a]*

[a] Faculty of Physics, Adam Mickiewicz University, Poznań, ul. Uniwersytetu Poznańskiego 2, 61-614 Poznań, Poland

[b] Max Planck Institute for Polymer Research, Ackermannweg 10, 55128 Mainz, Germany

[c] Analytical Chemistry – Center for Electrochemical Sciences, Faculty of Biochemistry and Chemistry, Ruhr-University Bochum, Universitätsstrasse 150, D-44780, Bochum, Germany

[d] School of Biochemistry, Biomedical Sciences Building, University of Bristol, University Walk, Bristol, BS8 1TD, UK

[#] A.R. Present Address: PPG Business Support GmbH, PPG Packaging Coatings, Erlenbrunnenstr. 20, 72411 Bodelshausen. Germany

*Corresponding authors: RB: rafal.bialek@amu.edu.pl, KG: krzysztof.gibasiewicz@amu.edu.pl

Abstract

Biohybrid photoelectrochemical systems in photovoltaic or biosensor applications have gained strong attention in recent years. While the photoactive proteins engaged in such systems usually maintain an internal charge separation quantum yield of nearly 100 %, the subsequent steps of electron and hole transfer beyond the protein often limit the overall system efficiency and their kinetics remain largely uncharacterized. In order to reveal the dynamics of one of such charge transfer reactions, we report on the reduction of *Rhodobacter sphaeroides* reaction centers (RCs) by Os-complex modified redox polymers (P-Os) characterized using transient absorption spectroscopy. RCs and P-Os were mixed in buffered solution in different molar ratios in the presence of a water soluble quinone as an electron acceptor. Electron transfer from P-Os to the photo-excited RCs could be described by a three-exponential function, the fastest lifetime of which was of the order of a few microseconds, which is a few orders of magnitude faster than the internal charge recombination of RCs with fully separated charge. This was similar to the lifetime for reduction of RCs by their natural electron donor, cytochrome c_2. The rate of electron donation increased with an increasing concentration ratio of polymer to protein. It is proposed that P-Os and RCs engage in electrostatic interactions to form complexes, the sizes of which depend on the polymer to protein ratio. Our findings throw light on the processes within hydrogel-based biophotovoltaic devices and will inform future design of materials optimally suited for this application.

Acknowledgements

RB acknowledges support from the Ministry of Science and Higher Education, Poland (project entitled: “Construction of solar cells based on purple bacteria reaction centers and polymer hydrogels” no. 0129/DIA/2016/45). KG acknowledges support from the National Science Center, Poland (project entitled “Bio-semiconductor hybrids for photovoltaic cells” no.

2012/07/B/NZ1/02639). WS and AR thank the Deutsche Forschungsgemeinschaft (DFG) under Germany's Excellence Strategy EXC-2033 (project number 390677874) for financial support. MRJ acknowledges support from the BrisSynBio Synthetic Biology Research Centre at the University of Bristol (BB/L01386X/1). The authors thank Dr. Sabine Alsaoub for the synthesis of the redox silent polymer backbone.

Abbreviations

RC – reaction center

Rba. – Rhodobacter

TA – transient absorption

P-Os – osmium-complex modified redox polymer (poly(vinyl imidazole-co-allyl amine)-[Os(bpy)$_2$Cl]Cl with bpy = 2,2' bipyridine)

PVI – redox silent poly(vinyl imidazole) based polymer

DADS – decay associated difference spectrum/spectra

Introduction

Research into biohybrid solar energy conversion devices has expanded significantly over the last couple of decades, with a wide variety of device designs reported.[1–6] The biological component is has usually been a photosynthetic protein such as Photosystem I, Photosystem II or the reaction center (RC) from a purple photosynthetic bacterium, however, recently there is a rise of usage of whole living organisms such as cyanobacteria immobilized directly on electrodes.[5] A much wider variety of non-biological components have been used as electrode substrates and electron acceptors or donors, including inorganic semiconductors, metals,[7,8] conductive polymers and redox polymers. In addition to their sustainability, natural photosystems are attractive materials for solar energy conversion because of the very high quantum yields (event per photon absorbed) of both excitation energy transfer among their light harvesting pigments and photochemical charge separation within the RC component. The benefit of the high yield of charge separation is sustained by rapid reduction of the redox center carrying the electron hole by an external donor, preventing wasteful charge recombination within the RC.[9]

A photoprotein that has been used extensively for fabrication of biohybrid electrodes and devices is the RC from the purple bacterium *Rhodobacter* (*Rba.*) *sphaeroides*. This relatively simple RC conducts charge separation with a quantum yield of nearly 100 %.[10] This functionality is provided by a set of cofactors buried inside an amino-acid scaffold, namely: four bacteriochlorophylls (BChl; two of them are coupled in a so-called special pair and form the primary electron donor (P) and two are accessory BChls, B_A and B_B), two bacteriopheophytins (BPhe; H_A and H_B), two quinones (Q_A and Q_B), and one carotenoid (Car; see Figure 1A).[11] The absorption spectrum of the RC is characterized by bands which are attributed to different chromophores (Figure 1B). This allows for distinct spectral signatures in transient absorption (TA) spectroscopy, facilitating the analysis of the photophysical pathways. The chromophores form two quasi-symmetric branches (A and B), but only one (branch A) is active in an electron transfer process (Figure 1A). After light absorption, the excitation energy within the RCs is typically transferred to P forming the excited state P*. This triggers charge separation resulting in the state $P^+H_A^-$. In this situation the next step depends on the state of RCs, described in literature as “open” or “closed”.[12] Open RCs are those with all cofactors in their neutral state, and thus able to conduct charge through the protein. In closed RCs the electron transfer is blocked beyond H_A, either by reduction of Q_A or its removal. In the closed state the only possibility for the separated charges on P^+ and H_A^- is to recombine. Usually they relax back to the ground state of P, but there is also a low probability that a triplet excited state (^TP) can be formed (with a 15 % yield in wild-type purified RCs [13–15]) leading finally to the formation and decay of a ^{T}Car state. On the other hand, in open RCs the electron from H_A^- is transferred to Q_A within ~200 ps resulting in the $P^+Q_A^-$ state (which can recombine to the ground neutral state PQ_A within ~100 ms) and next from Q_A^- to Q_B within ~100-1000 µs resulting in the $P^+Q_B^-$ state (which can recombine to the state PQ_B within ~1 s). If the Q_B site is not occupied by a quinone in the purified RC the final charge separated state is $P^+Q_A^-$.[12,16]

The converted energy made available to *Rba. sphaeroides* through highly quantum-efficient charge separation within its RCs is secured by transferring the separated electron and hole to external acceptors and donors before they can recombine. The reduced quinone dissociates from the Q_B pocket in RC and is replaced by an oxidized quinone from an intra-membrane pool, whilst the electron hole is transferred from P^+ to a water soluble cytochrome c_2 (cyt c_2). This latter reaction is possible due to formation of a transient complex between a RC and a cyt c_2 mediated largely by electrostatic interactions [17,18]). Within this complex, cyt c_2 is oxidized on a ~1 µs timescale.[19–23] This is several orders of magnitude faster than internal $P^+(Q_AQ_B)^-$ charge recombination in open RCs (0.1-1 s), stabilizing a high yield of charge separation.

Although a great deal is known about the kinetics, energetics and structural bases of individual steps of charge separation and stabilization in *Rba. sphaeroides* RCs in solution, and in native membranes and cells, very little detail is known about how these proteins operate on electrodes or in device settings. In general, only macroscopic parameters such as photocurrents and photovoltages have tended to be reported for RC biohybrid systems,[1,2,24] and to date only a few attempts have been made to model the electron transfer mechanism in such devices.[25–27] Precise modelling requires knowledge of the various parameters of the system, some of which can be accessed by employing electrochemical[24] or steady-state spectroelectrochemical[28] methods. However, the electron transfer rate between the protein and the immediate external donor or acceptor has not yet been studied in detail. Transient absorption (TA) spectroscopy is the ideal tool for characterizing the rates of photoinduced electron transfer reactions, and has already been extensively used for the study of photoinduced charge separation and recombination dynamics in photosynthetic systems as well as in synthetic materials for solar energy conversion.[29–35]

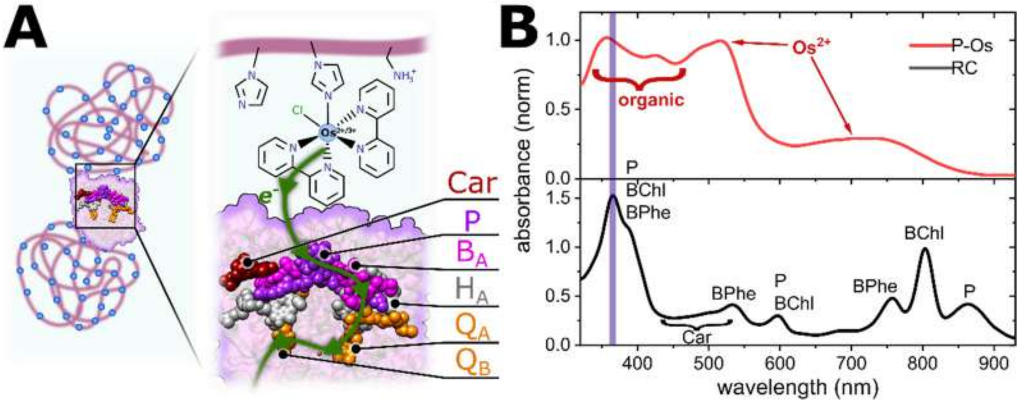

Figure 1 (A) Schematic of a possible complex of a RC and P-Os chains with an electron flow pathway. Os-complexes are marked as blue dots in the zoomed-out view. (B) Steady-state absorption spectra of P-Os and RCs in solution with band attributions. The 365 nm excitation wavelength is marked by a purple line.

Os-complex modified redox polymers (P-Os) have been found to effectively wire photoactive proteins such as Photosystem I,[36–38] Photosystem II[36,39–41] and *Rba. sphaeroides* RCs[28] to electrode surfaces. An efficient electron transfer within these systems is possible due to proper redox potential of the P-Os. Moreover, when the protein is immobilized in the polymer matrix it can stabilize the protein complex and enhance its lifetime.[39,40] An intimate contact between the oppositely charged proteins and polymers can be achieved using charged polymer matrices, favoring a good electron exchange due to short electron pathways between enzyme and redox polymer.[42–44] Moreover, in addition to ensuring a good interaction with the enzyme, the positive or negative charged groups within the redox polymer enable good water solubility and a high concentration of freely diffusing polymer chains in aqueous media. This effect is used for the production of redox polymer based aqueous flow batteries with high charge density.[45] In this work we have used a polymer with a mainly positive charge at pH 8 (see Figure 1A), which in principle is well suited to an interaction with mainly negatively charged RCs. Moreover, Os-complex modified redox polymers show absorption properties that are outside the main absorption region of the *Rba. sphaeroides* RC and thus they can be distinguished spectroscopically (Sokol et al. 2018; Figure 1B).

The combination of the P-Os polymer and *Rba. sphaeroides* RCs in a biophotoelectrode architecture has already been shown to give a relatively high internal quantum efficiency (~50 %) of photon to electron conversion.[28] This number implies a very good electrical contact between the P-Os and RCs immobilized inside this polymer matrix. In the present contribution the dynamics and mechanism of electron transfer between P-Os and bacterial RCs that underlies the high observed efficiency are explored. Since transient optical signals from the thin layer of a biophotoelectrode are extremely low, instead we have investigated mixtures of P-Os and RCs suspended in solution. TA spectroscopy has been used to demonstrate effective electron transfer between RCs and P-Os in solution, the kinetics of which depend strongly on the molar concentration ratio between the P-Os and RCs. Steady-state experiments have also been conducted in order to understand the nature of the interaction between the proteins and polymer chains at different molar ratios.

Experimental

RCs purification

His$_{10}$-tagged *Rhodobacter sphaeroides* RCs were purified as described in detail previously[46,47] using *N*,*N*-dimethyldodecan-1-amine oxide (LDAO; Sigma-Aldrich) as the solubilizing detergent and a combination of nickel affinity chromatography and size exclusion chromatography. Purified RCs were stored at -60°C in 20 mM Tris (pH 8.0)/0.1 % LDAO.

Polymer synthesis

Syntheses of the positively charged redox-silent polymer poly(vinyl imidazole-co-trimethyl aminoethyl methacrylate) (dubbed PVI; see Figure S1) and of the Os-complex based redox polymer poly(vinyl imidazole-co-ally amine)-$[Os(II)(bpy)_2Cl]^+$ (dubbed P-Os) were as described previously.[48,49]

Solution preparation

Samples for TA measurements were prepared in a quartz cuvette with 2 mm optical path length (Gallab) from stock solutions diluted in 20 mM Tris (pH 8.0)/0.1 % LDAO directly prior to the TA experiment. Stock solutions used were: 10.0 ± 0.8 mg/ml polymer (either P-Os or PVI), 20.9 ± 1.4 mg/ml RCs, 15 mM Q_0 (2,3-dimethoxy-5-methyl-*p*-benzoquinone; Sigma-Aldrich), and 1 M sodium ascorbate (Sigma-Aldrich). Five experimental samples (named I-V) were prepared from stock solutions of RCs, P-Os, and Q_0, along with several control samples as detailed in Table 1. Where present, the concentration of Q_0 was kept constant at around 1.5 mM to enable efficient electron acceptance from RCs.[28] More detailed information on sample composition and preparation is given in section S2 of SI.

Solutions for steady-state experiments with centrifugation were prepared as for samples I-V for TA measurements but without Q_0 (the same amount of pure H_2O was used instead).

Table 1 Sample compositions.

Sample (P-Os:RC)[a]	**Final concentration**				
	RCs (µM)	polymer chains (µM)	Os-complexes (µM)	Q_0 (mM)	ascorbate (mM)
I (3.1:1)	1.52 ± 0.10	4.7 ± 0.7	141 ± 17	1.48	-
II (1.23:1)	1.54 ± 0.10	1.9 ± 0.29	56 ± 7	1.48	-
III (0.64:1)	1.55 ± 0.10	0.99 ± 0.15	29.4 ± 3.6	1.49	-
IV (6.4:1)	0.75 ± 0.05	4.8 ± 0.7	142 ± 17	1.49	-
V (1.25:1)	3.76 ± 0.25	4.7 ± 0.7	139 ± 17	1.51	-
RCs only	3.43 ± 0.22	-	-	-	-
RCs + ascorbate	4.54 ± 0.30	-	-	-	9.7
RCs + P-Os	2.28 ± 0.15	3.9 ± 0.6	115 ± 14	-	-
RCs + PVI + Q_0	1.52 ± 0.10	?[b]	-	1.48	-
P-Os only	-	5.3 ± 0.8	158 ± 19	-	-
P-Os + Q_0	4.04 ± 0.26	-	-	1.50	-
Q_0 only	-	-	-	1.53	-

[a] value in parentheses is the molar ratio of P-Os:RC.

[b] unknown due to unknown polymer molecular weight

Steady-state experiments

Steady-state absorption measurements were conducted using a Jasco V-770 spectrophotometer with an integrating sphere (ILN-925) in the same cuvette as used for TA measurements. Centrifugation was performed in 1.5 ml Eppendorf tubes in an Eppendorf MiniSpin® centrifuge at 8000 rpm for 10 min. Absorbance spectra of polymer/protein mixtures were fitted with the sum of spectra of the P-Os and RC components with correction for scattering[50] to deconvolve their contribution using a script written in Python using the scipy.optimize module.[51]

Transient absorption

TA experiments were conducted using the EOS extension in a Helios Fire pump-probe apparatus (Ultrafast Systems), paired with a regeneratively amplified 1030 nm laser (Light Conversion, Pharos, 200 fs). The effective laser repetition rate was set via an internal pulse picker. The pump (photoexcitation) pulse was generated with an optical parametric amplifier (Light Conversion, Orpheus-F). The broadband probe light was generated via a photonic crystal fiber (IRF < 1 ns). The parameters were as follows (if not stated otherwise): excitation wavelength – 365 nm, repetition rate – 100 Hz (and thus the time window ~10 ms), excitation energy per pulse was 0.35 µJ (see Figure S6 for amplitude vs excitation energy plot). Sample solutions were stirred with a magnetic stir bar at the slowest possible speed in order to provide a fresh sample between laser pulses.

The raw absorbance change data were fitted using Glotaran software for a global analysis.[52,53] The resulting fitting function was the following:

$$\Delta A(\lambda, t) = \sum_{i=1}^{n} A_i(\lambda)\, e^{-\frac{t}{\tau_i}} \tag{1}$$

where $\Delta A(\lambda, t)$ – fit of absorbance change at wavelength λ and time t, $A_i(\lambda)$ – i-th preexponential factor, τ_i – i-th lifetime component, and n – number of exponential components. Thus, for each wavelength, the absorbance change kinetics were fitted with sum of exponential decay functions, but the lifetimes were shared among all wavelengths. The analysis yielded a set of spectra of preexponential factors, $A_i(\lambda)$, associated with particular lifetimes. These spectra are referred to as decay associated difference spectra (DADS).

Results and discussion

Evidence of electron transfer from polymer to protein in solution

Application of TA spectroscopy on a milliseconds time scale to RCs in buffer without any additional components produced a P^+/P difference spectrum. This had distinctive negative signals round 870 and 600 nm attributable to the bleach of P ground state absorbance and electrochromic blue- and red-shifts at around 800 and 760 nm coming from the accessory BChls and BPhes, respectively (Figure S2). The apparent shortening of the lifetime of the P^+ state obtained in this paper (11 ms) in comparison to lifetimes from the literature (~100 ms in the absence and ~1 s in the presence of Q_B [12]), was likely due to depletion of RCs in the charge separated state in the small focal volume of the laser beam. This was caused by stirring which moved photoexcited proteins out of the focal volume (see Figure S3 for comparison).

Addition of sodium ascorbate to the solution of RCs causes their closing by formation of reduced Q_A (Q_A^-). That this had occurred was evidenced (Figure S5) by the appearance of faster decay components attributable to $P^+H_A^-$ charge recombination (of the order of ~10 nanoseconds [54,55]) and ^TCar formation and decay (nanoseconds and microseconds, respectively [56,57]).

Addition of P-Os (reduced form, Os(II)-species) to the solution of RCs rather than ascorbate resulted in spectra and lifetimes (Figure S6) that were similar to those obtained with ascorbate (Figure S5). As P-Os alone did not show any TA signals in the studied time range (not shown), we conclude that the P-Os is able to reduce P^+ in the RC, creating a closed state. This observation is novel, as so far this kind of process was observed only in RC or Photosystem I based biohybrid electrodes, but not in a mixture of proteins and polymer in solution.[28,36–38] It validates that P-Os and RCs are properly paired for electron transfer between them, suggesting good pairing also while immobilized on the electrode. However, it is important to note that immobilization can change the properties of the material, such as redox potentials,[28] thus *in situ* methods should be used on biohybrid devices for final verification. The fully reduced initial state of the P-Os and a concentration of species were favorable for reduction of RCs by P-Os (there are at least 20 times more Os-complexes than RCs in solutions; Table S3). However, this reduction leads to the closing of RCs prior to the TA experiment so it is impossible to measure its rate in the described type of experiment. An equivalent experiment with the PVI backbone polymer which acts as a redox silent mimic for P-Os did not produce nanosecond/microsecond decay components (Figure S4), and shows only RC charge recombination occurring on the millisecond time scale as in the absence of ascorbate (Figure S2).

In order to measure the kinetics of electron transfer from the P-Os to P^+ it was necessary to keep RCs in their open state to get long enough lifetime of the P^+ state (~100 ms in open RCs vs ~10 ns in closed RCs). In order to keep RCs in their open state the excess electrons have to be taken away from Q_A^- by adding an external electron acceptor. Addition of a water soluble ubiquinone (Q_0) allowed the following reaction to be monitored:

$$P\text{-}Os(II) + PQ_A + Q_0(ox) \xrightarrow{laser\ pulse} P\text{-}Os(II) + P^+Q_A^- + Q_0(ox) \\ \longrightarrow P\text{-}Os(III) + PQ_A + Q_0(red)$$

The water soluble Q_0 has already proven its usefulness in biohybrid devices as an electron acceptor from the Q-side of RCs, replacing naturally functioning ubiquinone-10 within the membrane.[58] Its usefulness comes from the fact that quinone reduction is coupled with protonation, thus its reaction with bare electrode is relatively inefficient, while its interaction with RCs is fast due to its specific (enzymatic) nature.[59]

The presence of Q_0 in the solution alone or with the P-Os did not give any TA signals in the studied time range.

Kinetics of electron transfer from polymer to protein

Mixtures of RCs, P-Os and Q_0 were prepared at five different molar ratios of P-Os:RC (Table 1). For all samples the difference spectrum just after laser excitation resembled that of oxidized P (in the charge separated state $P^+(Q_AQ_B)^-$; Figure S2) and the spectrum then evolved over time. To observe the kinetics of the P^+ decay, band integrals (kinetics of the raw TA signal integrated over selected wavelength range) were calculated in the range 830-950 nm, corresponding to the bleach of P ground state absorption (Figure 2). Band integrals (BI) were used instead of single wavelength kinetics to increase the signal-to-noise ratio. For data that were not normalized (Figure 2A) the starting amplitude of the signal depended on the concentration of RCs, while the shape of the decay curve also depended on the concentration of P-Os. After normalizing to the initial signal amplitude (Figure 2B), it was evident that for all concentrations of P-Os the decay was faster than that for a reference sample without P-Os electron donor. Moreover, a faster rate of decay of P^+ exhibited a direct correlation with a higher concentration of P-Os and an opposite correlation with the increasing concentration of RCs, suggesting that P^+ decay was caused by its reduction by the P-Os.

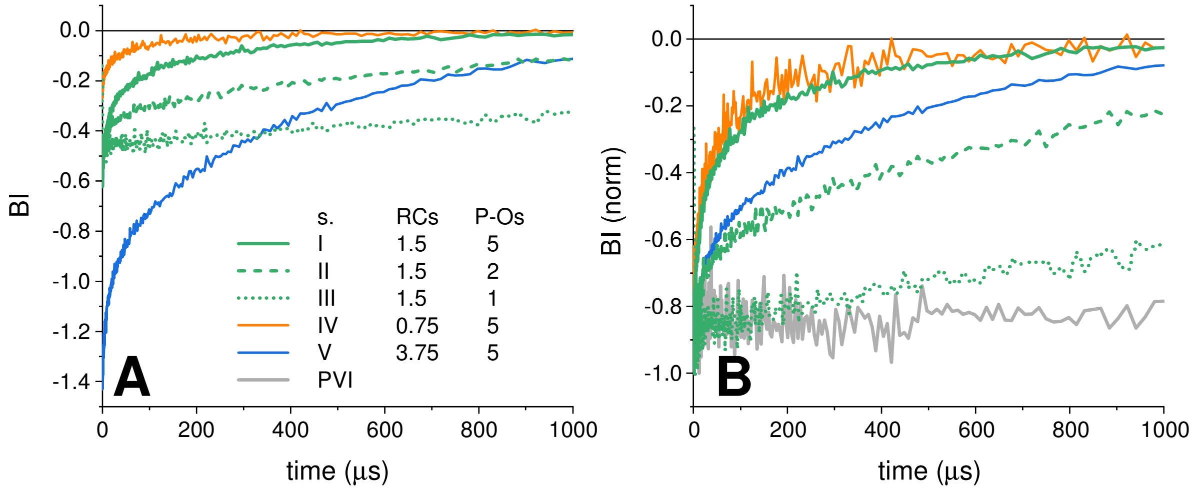

Figure 2 (A) Band integral (BI) kinetics for the first 1 ms. Band integrals were constructed in the 830-950 nm range. (B) The same data normalized to -1 at minimum. Values in the legend represent rounded molar concentrations of RCs and P-Os (in µM unit; for exact values see Table 1). Kinetics reveal rates of electron transfer from the polymer to the protein.

TA spectra averaged over a 4-6 ms delays revealed which species remained at the end of the period monitored (Figure 3, spectra at other delays are shown in Figures S8-S12). For most samples the main features were negative signals centered at ~520 nm and ~740 nm. These can be attributed to bleaches arising from the oxidation of Os(II) to Os(III) in the P-Os.[28] The exception was sample III, which had the lowest concentration of P-Os and lowest ratio of Os-complexes per RC. The spectrum of this sample showed a mixture of RCs and P-Os signal (compare it to pure RCs signal in sample with PVI, Figure 3). The data confirmed the hypothesis that there is an electron transfer from the Os-complexes in the polymer to P^+ in the RCs, showing that nearly 100% of photoexcited RCs, which were in open state before the excitation flash, could be reduced provided that the relative concentration of Os-complexes was sufficiently high. If it was not then P^+ reduction was inefficient, either because the electron transfer was not that efficient under these conditions or it was slower than the time window. Under the conditions of the TA experiment the signal completely vanished within 10 ms due to the excited species gradually escaping from the observed focal volume of the sample, hampering the resolution of slow reduction processes.

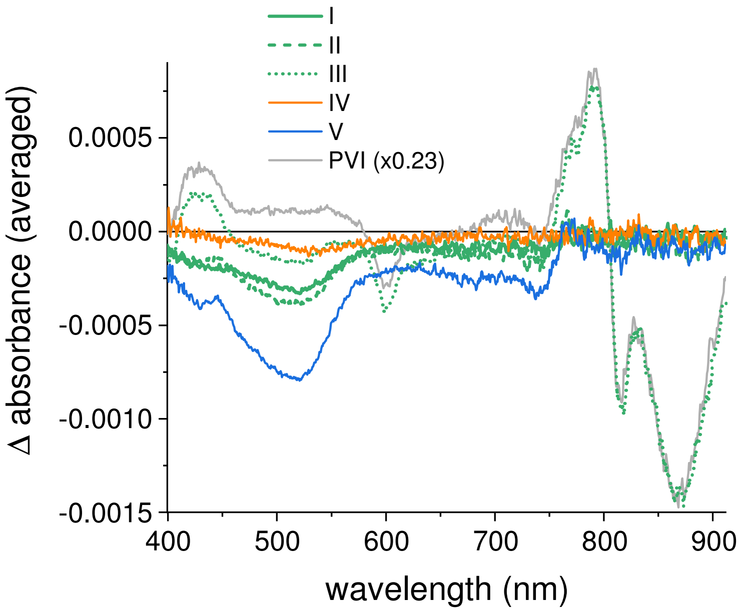

Figure 3 Averages of transient absorption spectra at delay times of 4-6 ms. The averaged spectrum for the PVI sample (redox silent polymer) was scaled to match the sample III spectrum in the long-wavelength region to show its polymer and RCs (P/P$^+$) contributions in the latter spectrum. All the remaining spectra are dominated by the signal from the polymer. Averaging over the 4-6 ms window was performed to improve the signal-to-noise ratio.

Kinetic phases of electron transfer from polymer to protein

Global analysis produced sets of DADS and associated lifetimes. Shapes of DADS were similar for samples I, II, IV and V, differing mainly in amplitude. A representative set for sample I is shown in Figure 4 and the remainder in Figures S13-S16. The best fit was obtained from a four-exponential model with all lifetimes set to be free. Three fastest DADS were similar in shape to one another and corresponded well to the P/P$^+$ difference spectrum.[28] The slowest DADS represented escape of the excited sample from the laser focal volume rather than the real decay of an observed state. In general, this escape is not a simple exponential function but a single exponential was sufficient to fit the data at the present level of noise. Thus the slowest component can be treated as a non-decaying signal left after former reactions and showed mostly photobleaching of ground state P-Os absorbance, suggesting that the three faster DADS should include features of P-Os oxidation process. For sample III (Figure S14) this fitting procedure did not give a fully acceptable result, as the two slowest components clearly compensated one another. However, when fewer exponential components were used the fitting seemed to omit the P-Os signal completely (not shown). The compensation for the two slowest DADS suggests that the lifetime of the electron transfer in this case was very similar to that of the photoexcited part of the sample escaping the focal volume (*i.e.* ~4-5 ms). Thus, for this sample, the amplitudes of the two slowest DADS were not suitable for further analysis.

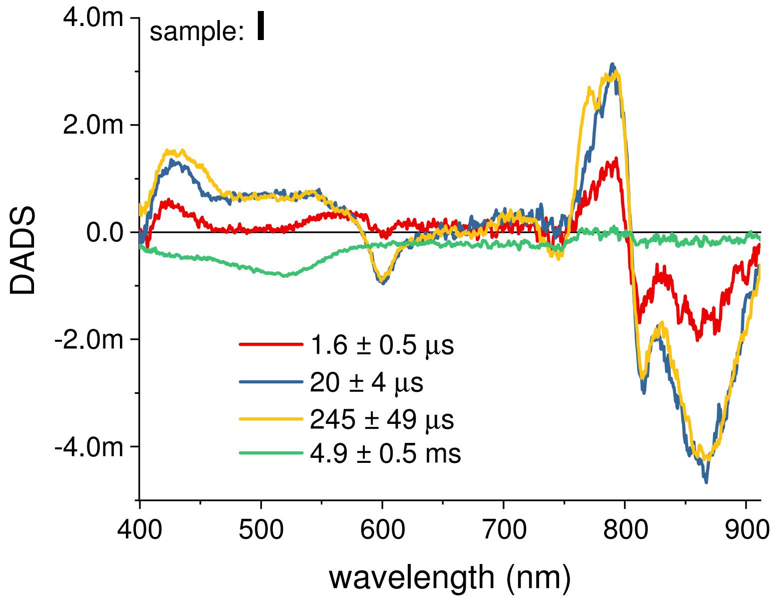

Figure 4 DADS for sample I and associated lifetimes. Individual spectra contain contributions from protein and/or polymer.

To look for a contribution of P-Os oxidation in the first three DADS, a P/P$^+$ differential spectrum in the form of the DADS from the RC-only sample (Figure S2) was subtracted from all of them. This P/P$^+$ differential spectrum was scaled in amplitude such that the signal in the resulting difference spectra in the range 780 – 900 nm was as close to zero as possible (for verification of this see Figures S21-S25). It was achieved using script written in python using scipy.optimize module [51]. The resulting "ΔDADS" for sample I are shown in Figure 5 and for the remainder see Figures S17-S20. The fastest ΔDADS had a maximum around 600 nm and was slightly negative at 500 nm. It resembled the shape of the difference spectrum expected for Car triplet decay (see Figure S5 for comparison) with the possible addition of some oxidation of P-Os causing a shallowing of the ~500 nm valley visible in Figure S5. The reason why a ^{T}Car state was observed is likely to be because the added Q_0 might not be fully efficient in accepting electrons from the Q-side of RCs between laser shots, leading to formation of ^{T}Car in "closed" RCs in the state PQ_A^-. Moreover, it is conceivable that access of Q_0 to the Q-side of the protein in some RCs may have been locked by the adsorbed polymer (see below). Accordingly, the fastest ΔDADS is attributed to a mixture of ^{T}Car decay (expected lifetime ~2.5-4 µs) [56,57] and P-Os→P$^+$ electron transfer. However, the main amplitude of this decay lays in the >750 nm region, where the signal comes almost exclusively from P/P$^+$, and thus P-Os→P$^+$ electron transfer has the dominating contribution to this lifetime. Taking into account equivalent details for the remaining samples (Figures S17-S20), it is concluded that the fastest electron transfer from P-Os to P$^+$ occurred on the time scale of 0.5-5 µs. The next two ΔDADS with lifetimes of 20 and 245 µs in Figure 5 had a prominent positive amplitude around 515 nm attributable to formation of the oxidized state of P-Os. The slowest ΔDADS, attributed to the sample escaping the focal volume, matched the spectral signature of loss of oxidized P-Os, also consistent with electron transfer from P-Os to P$^+$ occurring over a microsecond time scale.

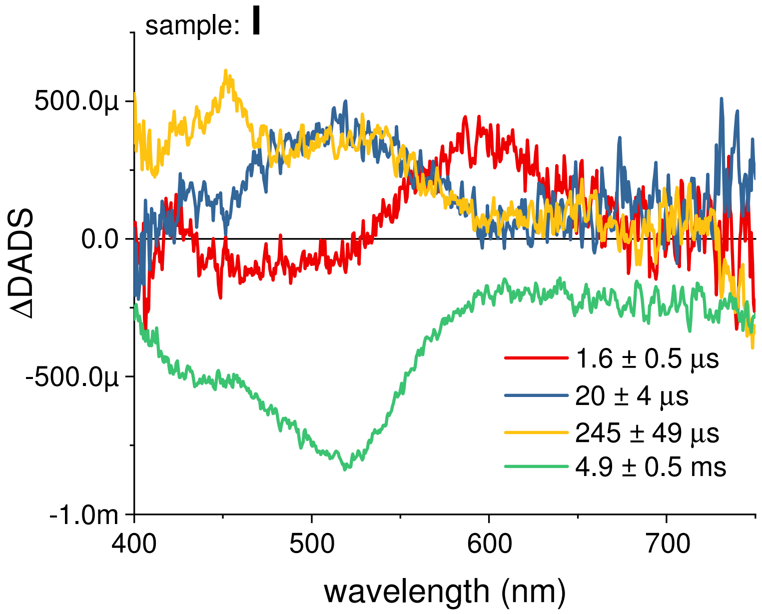

Figure 5 ΔDADS for sample I obtained by subtracting RC contributions from the DADS in Figure 4. Subtraction was performed primarily in order to reveal formation of the oxidized form of the polymer.

Mechanism of electron transfer from polymer to protein

The sample compositions allowed exploration of the dependence of the electron transfer rates on the concentrations of both RCs and P-Os (Figure 6). At a fixed concentration of P-Os (Figure 6A), a higher concentration of RCs resulted in a lower rate constant (slower electron transfer). At fixed concentration of RCs (Figure 6B), a higher concentration of P-Os gives an opposite effect with a higher rate constant (faster electron transfer). As shown in Figure 6C, the rate of all three components of the electron transfer accelerated as the ratio of P-Os:RC increased.

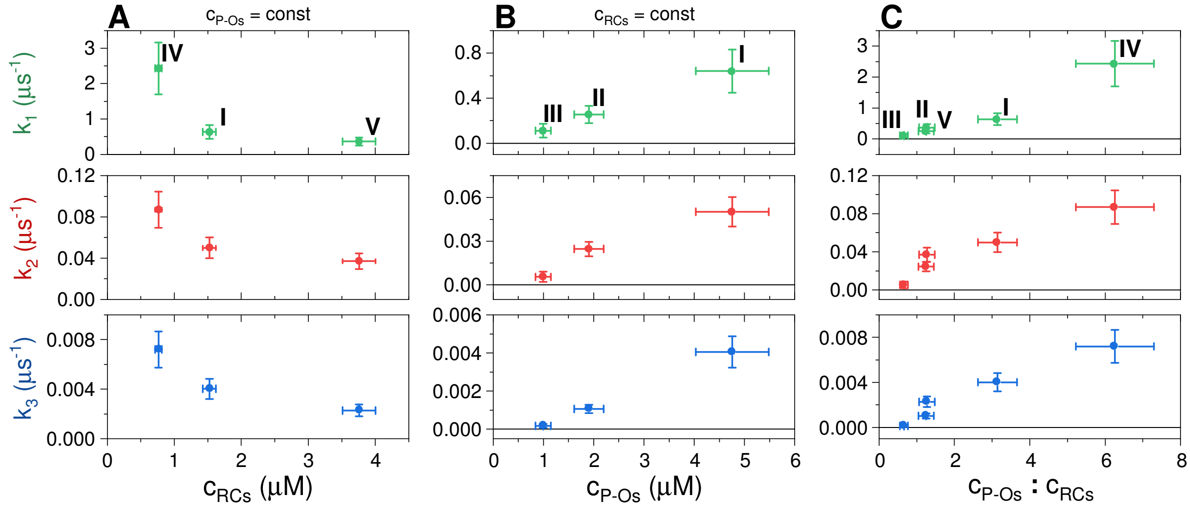

Figure 6 Dependence of electron transfer rate constants (reciprocals of lifetimes) on (A) concentrations of RCs for constant concentration of P-Os, (B) concentration of P-Os for constant concentration of RCs and (C) molar ratio of P-Os chains to RCs. Note that all rate constants increase with increasing ratio of the polymer to protein concentrations.

Analysis of the amplitudes associated with the DADS (Figure 7A) showed that there was an increase in the relative contribution of the two faster components with an increasing P-Os:RCs molar ratio, thus accelerating the overall process. There are two possible descriptions of this behavior.

Collisional model. The simplest description of the electron transfer reaction would be collisional interactions of RCs with aggregates of P-Os of different sizes or structures, producing different electron transfer rates. For this type of interaction, the kinetics of electron transfer would be governed by equation (2):

$$\frac{d[P]}{dt} = k[P\text{-}Os(II)][P^+] \tag{2}$$

During the reaction, the concentration of P-Os(II) remained almost constant (the amplitude of the slowest DADS was no more than 0.5 % of the amplitude of the steady-state absorbance of P-Os). Thus, this reaction can be treated as pseudo-first order with the apparent first-order rate constant (k_{app}) given by equation (3).

$$k_{app} = k[P\text{-}Os(II)] \tag{3}$$

Although this would explain the dependence of the electron transfer rate on the concentration of P-Os, it does not explain its dependence on the concentration of RCs. This indicates that there must be interactions other than collisions occurring, such as the creation of quasi-stable complexes between RCs and P-Os in solution.

Complexing model. Electron donation to P^+ in RCs in solution has been studied in depth for the natural electron donor, cyt c_2, and has been reported to be biexponential.[19–23,60] To account for this a model incorporating the creation of semi-stable complexes has been proposed.[19,22] The faster component (lifetime ~1 µs) was attributed to the electron transfer rate within a RC:cyt c_2 complex, while the slower component was attributed to the diffusionally-limited creation of complexes convolved with direct electron transfer. The finding that the faster component of reduction of P^+ by cyt c_2 was independent of concentration is in contrast with our findings for the RC/P-Os system. Moreover, it was reported that the rate of P^+ reduction increased with increasing cyt c_2 concentration and increased with the concentration of RCs, which is opposite to the effect observed in the present paper.[22,23,60] Thus, the model constructed for cyt c_2 cannot be directly used in the system with P-Os and RCs. However, it is interesting to note that the fastest lifetime for electron transfer between RCs and P-Os is of the same order as that for RCs and cyt c_2. This informed the hypothesis that RCs create complexes with P-Os and at least some of them are as efficient in electron donation as natural cytochrome c_2. The similar behavior of all lifetimes (Figure 6) suggests that they arise from complexes with different compositions that produce different electron transfer rates.

To examine whether complexes form between RCs and P-Os, mixtures were centrifuged at 8000 rpm for 10 min, a treatment which resulted in part of both the RC and P-Os population being spun down from solution. This indicated that, in all samples, there had been formation of complexes large enough to be centrifuged out. The fraction of both RCs and P-Os to be pelleted increased as the molar ratio of P-Os:RC increased (Figure 7B,C), suggesting that more or larger complexes had been formed. The finding that higher concentration ratios also produced a decrease in the contribution of the slowest component of the electron transfer (Figure 7A) suggests that such conditions produce more complexes with a favorable orientation of P-Os and RCs.

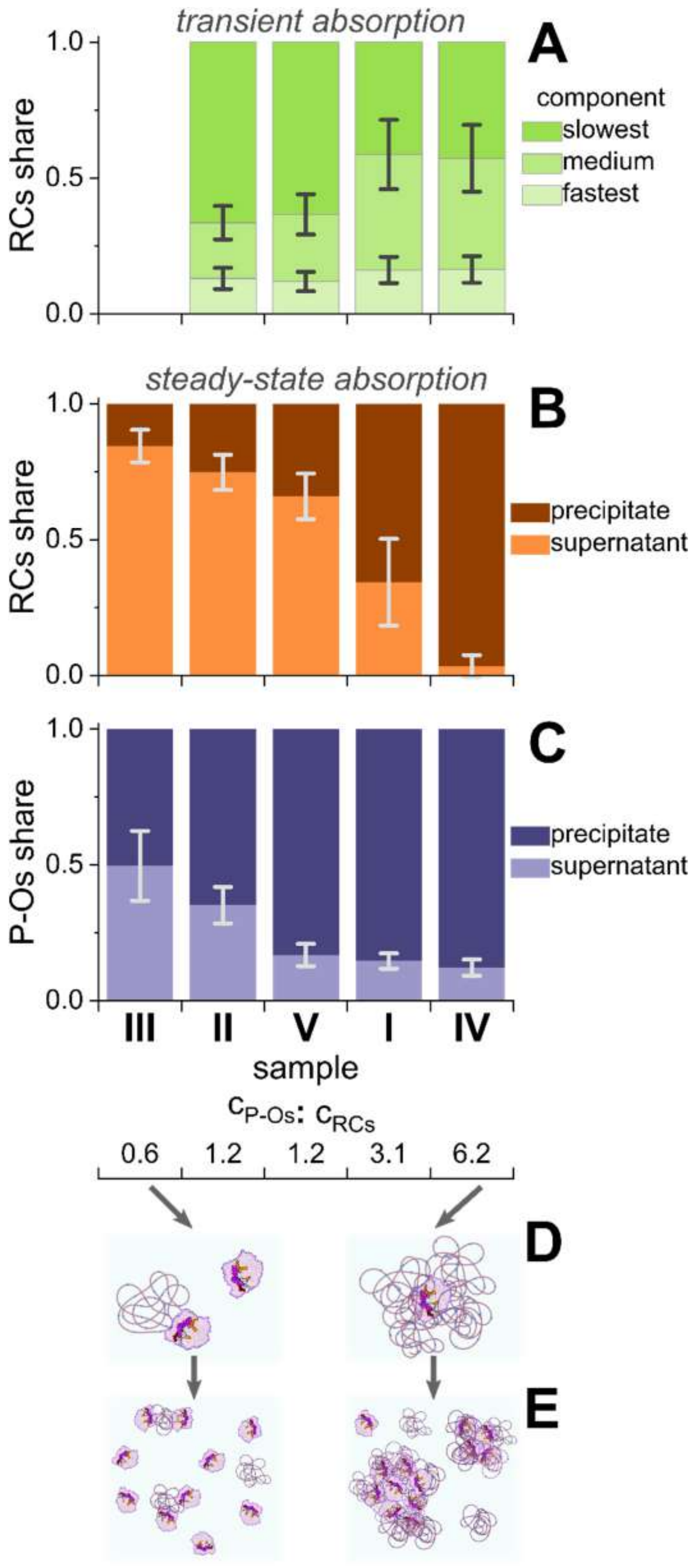

Figure 7 (A) Relative contributions of the three DADS components from TA experiments to the overall process as a function of molar ratio of P-Os:RC. (B) Relative amount of RCs in the precipitate and supernatant, determined from steady-state absorption measurements on centrifuged samples, as a function of molar ratio of P-Os:RC. (C). Relative amount of P-Os in the precipitate and supernatant, determined from steady-state absorption measurements on centrifuged samples, as a function of molar ratio of P-Os:RC. (D and E) Schemes of complex formation for lower and upper limits of polymer to protein ratios (see text for details). Note that the higher polymer to protein ratio, the stronger the effect of complexes formation (B-E).

There remains a question about a nature of complexes formed between RCs and the P-Os. The interaction between the RC and cyt c_2 is primarily electrostatic with the cytochrome being positively charged and its binding site on the RC negatively charged[17,18] under native pH conditions (pH 8; Figure 8). The charge of the P-Os is determined by the states of its component groups in its structure (Figure 1A). Os-complexes remain positively charged independently of the pH of the solution. However, it has been reported that at pH 8 most of the imidazole and primary amino groups remain in an unprotonated, uncharged state.[37] Thus, P-Os is mainly positively charged at pH 8 due to the presence of positively charged Os-complexes. It is known that P-Os has a tendency to form loosely bound agglomerates in solution at pH 6.5, with the smallest particles being of the order of 16 nm in radius.[40] It was also reported that for pH ≥ 7, films made of P-Os collapse.[37] Thus, in the conditions studied in this paper, P-Os entities exist most probably as particles with a hydrodynamic radius of no bigger than 16 nm, or loosely bound agglomerates of such particles, and are positively charged. This would be consistent with net anionic RCs and cationic P-Os particles forming complexes through electrostatic interactions.

For cyt c_2, an additional factor contributing to formation of a complex with RCs in the proper mutual orientation is the shape of the protein. The cytochrome binds in a highly specific manner to a site on the periplasmic (P-side) of the RC that has a complementary shape and charge. For a polymer this shape factor is more random, and it is conceivable that P-Os could attach to any part of the RC protein on either the P-side or Q-side that has a suitable surface charge (Figure 8). The most optimal interaction would be one where a P-Os attached to the P-side of the RC with one of its Os-complexes as close as possible to the P bacteriochlorophylls at the surface of the protein. The least optimal attachment would be at the Q-side, producing very slow electron transfer that would compete poorly with charge recombination internal to the RC. In addition, binding of P-Os to the Q-side could conceivably hamper access of the Q_0 electron acceptor to the Q_B pocket. Enhanced recombination would be observable on the studied time scale as triplet state formation (see section "Kinetic phases of electron transfer from polymer to protein"). When the polymer to protein molar ratio is close to, or even smaller than 1:1 the electron transfer is slowest (see Figure 6C). This ratio means that there is one polymer chain per protein on average and, as it can be attached at random sites of RCs, the observed electron transfer might be expected to be relatively slow. For higher polymer to protein ratios there might be more than one polymer chain attached to the RC, increasing the probability of one occupying an optimal position that leads to better wiring between the polymer and RC, and thus increases the observed electron transfer rate. This scenario is depicted schematically in Figure 7D. On the other hand, we speculate that with increasing number of polymer chains per protein, the probability of formation of large aggregates increases, with polymers acting like an electrostatic "glue" (Figure 7E). This would explain why in centrifugation experiments the amount of precipitate containing both polymers and proteins increases with an increasing molar ratio of P-Os:RC (Figure 7B and C).

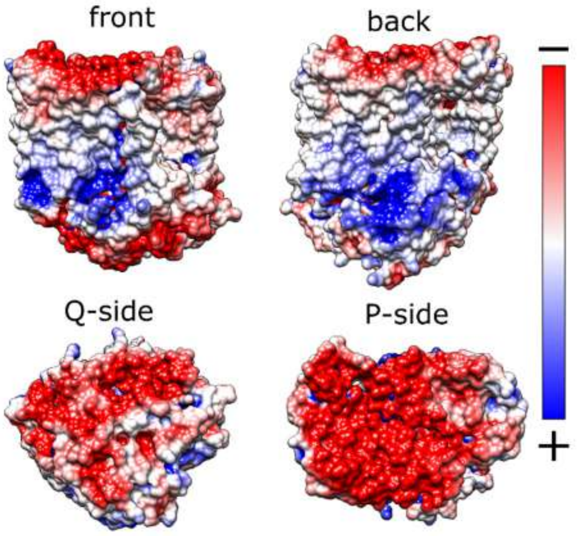

Figure 8 Distribution of the surface charge on RCs at pH 8.0. Simulation was done using PDB2PQR and APBS software with the 1PCR structure from PDB[61] at default settings.[62,63] Negatively charged surfaces preferentially interact with the polymer.

Mechanistic significance and conclusions

The TA data demonstrate that P-Os and RCs interact strongly in solution despite being sparsely dispersed compared to those in a hydrogel on an electrode surface. The P-Os polymer is capable of reducing photoinduced P^+ with time constants distributed over a range of a few microseconds to around one millisecond. The fastest electron transfer from P-Os to P^+ occurred on the time scale of 0.5-5 µs, values that are similar to the ~1 µs lifetime of the natural electron transfer between complexed RCs and cyt c_2.[19–23] This demonstrates that P-Os in the proper conformation can perform as efficiently as a natural donor in terms of electron transfer rate. The exact value of the time constant depended on the concentration ratio between P-Os and RCs, being fastest for the highest ratios. The data allowed derivation of a hypothesis that P-Os and RCs create complexes in solution through an electrostatic interaction, and it is suggested that the lifetime of electron transfer for a single complex depends mostly on its detailed conformation and, in particular, precisely where on the protein surface the polymer binds.

Irrespective of sample composition, all three lifetimes for electron transfer from the polymer to protein were orders of magnitude faster than naturally occurring charge recombination of the $P^+(Q_AQ_B)^-$ state (0.1-1 s), and so it was at least 100 times more probable for this electron transfer to occur rather than charge recombination. This promising finding is one of the explanations for the relatively high (~50 %) internal quantum efficiency of a biophotoelectrode consisting of RCs and P-Os reported previously.[28]

These results explain the relatively high efficiencies of photoelectrodes based on redox hydrogels and RCs in comparison to other architectures with RCs. They show that surface properties (e.g. electrostatic) that govern the interactions between natural and synthetic components in a biohybrid material are at least as important as the proper matching of redox levels. Moreover, the TA technique presented in this study may in principle be used to monitor electron transfer rates *in situ* in an operational device. Such approach enables better understanding of the electron transfer process by obtaining exact values of reaction rate constants, which are necessary for precise modelling and identifying possible bottlenecks limiting the performance of the devices.

Supporting Information

The Supporting Information is available free of charge at ….

- Structure of the redox-silent polymer, detailed information on the sample preparation, reference experiments results, difference spectra at chosen delays and results for samples omitted in the main text. (PDF)

References

(1) Ravi, S. K.; Tan, S. C. Progress and Perspectives in Exploiting Photosynthetic Biomolecules for Solar Energy Harnessing. *Energy Environ. Sci.* **2015**, *8* (9), 2551–2573.

(2) Friebe, V. M.; Frese, R. N. Photosynthetic Reaction Center-Based Biophotovoltaics. *Curr. Opin. Electrochem.* **2017**, *5* (1), 126–134.

(3) Milano, F.; Punzi, A.; Ragni, R.; Trotta, M.; Farinola, G. M. Photonics and Optoelectronics with Bacteria: Making Materials from Photosynthetic Microorganisms. *Adv. Funct. Mater.* **2019**, *29* (21), 1–17.

(4) Musazade, E.; Voloshin, R.; Brady, N.; Mondal, J.; Atashova, S.; Zharmukhamedov, S. K.; Huseynova, I.; Ramakrishna, S.; Najafpour, M. M.; Shen, J. R.; et al. Biohybrid Solar Cells: Fundamentals, Progress, and Challenges. *J. Photochem. Photobiol. C Photochem. Rev.* **2018**, *35*, 134–156.

(5) Kornienko, N.; Zhang, J. Z.; Sakimoto, K. K.; Yang, P.; Reisner, E. Interfacing Nature's Catalytic Machinery with Synthetic Materials for Semi-Artificial Photosynthesis. *Nat. Nanotechnol.* **2018**, *13* (10), 890–899.

(6) Nagy, L.; Magyar, M.; Szabó, T.; Hajdu, K.; Giotta, L.; Dorogi, M.; Milano, F. Photosynthetic Machineries in Nano-Systems. *Curr. Protein Pept. Sci.* **2014**, *15* (4), 363.

(7) Friebe, V. M.; Delgado, J. D.; Swainsbury, D. J. K. K.; Gruber, J. M.; Chanaewa, A.; van Grondelle, R.; Von Hauff, E.; Millo, D.; Jones, M. R.; Frese, R. N. Plasmon-Enhanced Photocurrent of Photosynthetic Pigment Proteins on Nanoporous Silver. *Adv. Funct. Mater.* **2016**, *26* (2), 285–292.

(8) Kowalska, D.; Szalkowski, M.; Sulowska, K.; Buczynska, D.; Niedziolka-Jonsson, J.; Jonsson-Niedziolka, M.; Kargul, J.; Lokstein, H.; Mackowski, S. Silver Island Film for Enhancing Light Harvesting in Natural Photosynthetic Proteins. *Int. J. Mol. Sci.* **2020**, *21* (7), 2451.

(9) Blankenship, R. E. *Molecular Mechanisms of Photosynthesis*; Blackwell Science Ltd: Oxford, UK, 2002.

(10) Wraight, C. A.; Clayton, R. K. The Absolute Quantum Efficiency of Bacteriochlorophyll Photooxidation in Reaction Centres of Rhodopseudomonas Spheroides. *Biochim. Biophys. Acta - Bioenerg.* **1974**, *333* (2), 246–260.

(11) Allen, J. P.; Feher, G.; Yeates, T. O.; Komiya, H.; Rees, D. C. Structure of the Reaction Center from Rhodobacter Sphaeroides R-26: The Cofactors. *Proc. Natl. Acad. Sci.* **1987**, *84* (16), 5730–5734.

(12) Woodbury, N. W.; Allen, J. P. The Pathway, Kinetics and Thermodynamics of Electron Transfer in Wild Type and Mutant Reaction Centers of Purple Nonsulfur Bacteria. In *Anoxygenic Photosynthetic Bacteria*; Blankenship, R. E., Madigan, M., Bauer, C. E., Eds.;

Kluwer Academic Publishers: Dordrecht, 1995; pp 527–557.

(13) Parson, W. W.; Cogdell, R. J. The Primary Photochemical Reaction of Bacterial Photosynthesis. *Biochim. Biophys. Acta - Rev. Bioenerg.* **1975**, *416* (1), 105–149.

(14) Michel-Beyerle, M. E.; Scheer, H.; Seidlitz, H.; Tempus, D. Magnetic Field Effect on Triplets and Radical Ions in Reaction Centers of Photosynthetic Bacteria. *FEBS Lett.* **1980**, *110* (1), 129–132.

(15) Schenck, C. C.; Blankenship, R. E.; Parson, W. W. Radical-Pair Decay Kinetics, Triplet Yields and Delayed Fluorescence from Bacterial Reaction Centers. *Biochim. Biophys. Acta - Bioenerg.* **1982**, *680* (1), 44–59.

(16) Okamura, M. Y.; Feher, G. Proton-Coupled Electron Transfer Reactions of QB in Reaction Centers from Photosynthetic Bacteria. In *Anoxygenic Photosynthetic Bacteria*; Blankenship, R. E., Madigan, M., Bauer, C., Eds.; Kluwer Academic Publishers: Dordrecht, 1995; pp 577–593.

(17) Tiede, D. M.; Vashishta, A. C.; Gunner, M. R. Electron-Transfer Kinetics and Electrostatic Properties of the Rhodobacter Sphaeroides Reaction Center and Soluble c-Cytochromes. *Biochemistry* **1993**, *32* (17), 4515–4531.

(18) Miyashita, O.; Onuchic, J. N.; Okamura, M. Y. Continuum Electrostatic Model for the Binding of Cytochrome C2 to the Photosynthetic Reaction Center from Rhodobacter Sphaeroides. *Biochemistry* **2003**, *42* (40), 11651–11660.

(19) Abresch, E. C.; Gong, X. M.; Paddock, M. L.; Okamura, M. Y. Electron Transfer from Cytochrome C2 to the Reaction Center: A Transition State Model for Ionic Strength Effects Due to Neutral Mutations. *Biochemistry* **2009**, *48* (48), 11390–11398.

(20) Overfield, R. E.; Wraight, C. A.; Devault, D. Microsecond Photooxidation Kinetics of Cytochrome C2 from Rhodopseudomonas Sphaeroides: In Vivo and Solution Studies. *FEBS Lett.* **1979**, *105* (1), 137–142.

(21) Tetreault, M.; Rongey, S. H.; Feher, G.; Okamura, M. Y. Interaction between Cytochrome C2 and the Photosynthetic Reaction Center from Rhodobacter Sphaeroides: Effects of Charge-Modifying Mutations on Binding and Electron Transfer. *Biochemistry* **2001**, *40* (29), 8452–8462.

(22) Farchaus, J. W.; Wachtveitl, J.; Mathis, P.; Oesterhelt, D. Tyrosine 162 of the Photosynthetic Reaction Center L-Subunit Plays a Critical Role in the Cytochrome C2 Mediated Rereduction of the Photooxidized Bacteriochlorophyll Dimer in Rhodobacter Sphaeroides. 1. Site-Directed Mutagenesis and Initial Characterizati. *Biochemistry* **1993**, *32* (40), 10885–10893.

(23) Moser, C. C.; Dutton, P. L. Cytochrome c and C2Binding Dynamics and Electron Transfer with Photosynthetic Reaction Center Protein and Other Integral Membrane Redox Proteins. *Biochemistry* **1988**, *27* (7), 2450–2461.

(24) Plumeré, N.; Nowaczyk, M. M. Biophotoelectrochemistry of Photosynthetic Proteins. In *Advances in biochemical engineering/biotechnology*; 2016; Vol. 123, pp 127–141.

(25) Białek, R.; Swainsbury, D. J. K.; Wiesner, M.; Jones, M. R.; Gibasiewicz, K. Modelling of the Cathodic and Anodic Photocurrents from Rhodobacter Sphaeroides Reaction Centres Immobilized on Titanium Dioxide. *Photosynth. Res.* **2018**, *138* (1), 103–114.

(26) Buesen, D.; Hoefer, T.; Zhang, H.; Plumeré, N. A Kinetic Model for Redox-Active Film Based Biophotoelectrodes. *Faraday Discuss.* **2019**, *215* (i), 39–53.

(27) Milano, F.; Ciriaco, F.; Trotta, M.; Chirizzi, D.; De Leo, V.; Agostiano, A.; Valli, L.; Giotta, L.; Guascito, M. R. Design and Modelling of a Photo-Electrochemical Transduction System Based on Solubilized Photosynthetic Reaction Centres. *Electrochim. Acta* **2019**, *293*, 105–115.

(28) Białek, R.; Friebe, V.; Ruff, A.; Jones, M. R.; Frese, R.; Gibasiewicz, K. In Situ Spectroelectrochemical Investigation of a Biophotoelectrode Based on Photoreaction Centers Embedded in a Redox Hydrogel. *Electrochim. Acta* **2020**, *330*, 135190.

(29) Gibasiewicz, K.; Pajzderska, M.; Dobek, A.; Karolczak, J.; Burdziński, G.; Brettel, K.; Jones, M. R. Analysis of the Temperature-Dependence of P+HA− Charge Recombination in the Rhodobacter Sphaeroides Reaction Center Suggests Nanosecond Temperature-Independent Protein Relaxation. *Phys. Chem. Chem. Phys.* **2013**, *15* (38), 16321.

(30) Gibasiewicz, K.; Białek, R.; Pajzderska, M.; Karolczak, J.; Burdziński, G.; Jones, M. R.; Brettel, K. Weak Temperature Dependence of P + H A − Recombination in Mutant Rhodobacter Sphaeroides Reaction Centers. *Photosynth. Res.* **2016**, *128* (3), 243–258.

(31) Pan, J.; Saer, R.; Lin, S.; Beatty, J. T.; Woodbury, N. W. Electron Transfer in Bacterial Reaction Centers with the Photoactive Bacteriopheophytin Replaced by a Bacteriochlorophyll through Coordinating Ligand Substitution. *Biochemistry* **2016**, *55* (35), 4909–4918.

(32) Faries, K. M.; Dylla, N. P.; Hanson, D. K.; Holten, D.; Laible, P. D.; Kirmaier, C. Manipulating the Energetics and Rates of Electron Transfer in Rhodobacter Capsulatus Reaction Centers with Asymmetric Pigment Content. *J. Phys. Chem. B* **2017**, *121* (29), 6989–7004.

(33) Zabelin, A. A.; Khristin, A. M.; Shkuropatova, V. A.; Khatypov, R. A.; Shkuropatov, A. Y. Primary Electron Transfer in Rhodobacter Sphaeroides R-26 Reaction Centers under Dehydration Conditions. *Biochim. Biophys. Acta - Bioenerg.* **2020**, *1861* (10), 148238.

(34) Lanzani, G. *The Photophysics behind Photovoltaics and Photonics*; Wiley-VCH Verlag GmbH & Co. KGaA: Weinheim, Germany, 2012.

(35) Szewczyk, S.; Białek, R.; Giera, W.; Burdziński, G.; van Grondelle, R.; Gibasiewicz, K. Excitation Dynamics in Photosystem I Trapped in TiO2 Mesopores. *Photosynth. Res.* **2020**, *144* (2), 235–245.

(36) Kothe, T.; Plumeré, N.; Badura, A.; Nowaczyk, M. M.; Guschin, D. A.; Rögner, M.; Schuhmann, W. Combination of A Photosystem 1-Based Photocathode and a Photosystem 2-Based Photoanode to a Z-Scheme Mimic for Biophotovoltaic Applications. *Angew. Chemie Int. Ed.* **2013**, *52* (52), 14233–14236.

(37) Kothe, T.; Pöller, S.; Zhao, F.; Fortgang, P.; Rögner, M.; Schuhmann, W.; Plumeré, N. Engineered Electron-Transfer Chain in Photosystem 1 Based Photocathodes Outperforms Electron-Transfer Rates in Natural Photosynthesis. *Chem. - A Eur. J.* **2014**, *20* (35), 11029–11034.

(38) Zhao, F.; Wang, P.; Ruff, A.; Hartmann, V.; Zacarias, S.; Pereira, I. A. C.; Nowaczyk, M. M.; Rögner, M.; Conzuelo, F.; Schuhmann, W. A Photosystem i Monolayer with Anisotropic Electron Flow Enables Z-Scheme like Photosynthetic Water Splitting. *Energy Environ. Sci.* **2019**, *12* (10), 3133–3143.

(39) Badura, A.; Guschin, D.; Esper, B.; Kothe, T.; Neugebauer, S.; Schuhmann, W.; Rögner, M. Photo-Induced Electron Transfer Between Photosystem 2 via Cross-Linked Redox Hydrogels. *Electroanalysis* **2008**, *20* (10), 1043–1047.

(40) Sokol, K. P.; Mersch, D.; Hartmann, V.; Zhang, J. Z.; Nowaczyk, M. M.; Rögner, M.; Ruff, A.; Schuhmann, W.; Plumeré, N.; Reisner, E. Rational Wiring of Photosystem II to Hierarchical Indium Tin Oxide Electrodes Using Redox Polymers. *Energy Environ. Sci.* **2016**, *9* (12), 3698–3709.

(41) Sokol, K. P.; Robinson, W. E.; Warnan, J.; Kornienko, N.; Nowaczyk, M. M.; Ruff, A.; Zhang, J. Z.; Reisner, E. Bias-Free Photoelectrochemical Water Splitting with Photosystem II on a Dye-Sensitized Photoanode Wired to Hydrogenase. *Nat. Energy* **2018**, *3* (11), 944–951.

(42) Pishko, M. V.; Katakis, I.; Lindquist, S. -E; Ye, L.; Gregg, B. A.; Heller, A. Direct Electrical Communication between Graphite Electrodes and Surface Adsorbed Glucose Oxidase/Redox Polymer Complexes. *Angew. Chemie Int. Ed. English* **1990**, *29* (1), 82–84.

(43) Heller, A. Electrical Connection of Enzyme Redox Centers to Electrodes. *J. Phys. Chem.* **1992**, *96* (9), 3579–3587.

(44) Teanphonkrang, S.; Janke, S.; Chaiyen, P.; Sucharitakul, J.; Suginta, W.; Khunkaewla, P.; Schuhmann, W.; Ruff, A.; Schulte, A. Tuned Amperometric Detection of Reduced β-Nicotinamide Adenine Dinucleotide by Allosteric Modulation of the Reductase Component of the p -Hydroxyphenylacetate Hydroxylase Immobilized within a Redox Polymer. *Anal. Chem.* **2018**, *90* (9), 5703–5711.

(45) Janoschka, T.; Martin, N.; Martin, U.; Friebe, C.; Morgenstern, S.; Hiller, H.; Hager, M. D.; Schubert, U. S. An Aqueous, Polymer-Based Redox-Flow Battery Using Non-Corrosive, Safe, and Low-Cost Materials. *Nature* **2015**, *527* (7576), 78–81.

(46) Swainsbury, D. J. K.; Friebe, V. M.; Frese, R. N.; Jones, M. R. Evaluation of a Biohybrid Photoelectrochemical Cell Employing the Purple Bacterial Reaction Centre as a Biosensor for Herbicides. *Biosens. Bioelectron.* **2014**, *58*, 172–178.

(47) Liu, J.; Friebe, V. M.; Frese, R. N.; Jones, M. R. Polychromatic Solar Energy Conversion in Pigment-Protein Chimeras That Unite the Two Kingdoms of (Bacterio)Chlorophyll-Based Photosynthesis. *Nat. Commun.* **2020**, *11* (1), 1542.

(48) Conzuelo, F.; Marković, N.; Ruff, A.; Schuhmann, W. The Open Circuit Voltage in Biofuel Cells: Nernstian Shift in Pseudocapacitive Electrodes. *Angew. Chemie - Int. Ed.* **2018**, *57* (41), 13681–13685.

(49) Alsaoub, S.; Ruff, A.; Conzuelo, F.; Ventosa, E.; Ludwig, R.; Shleev, S.; Schuhmann, W. An Intrinsic Self-Charging Biosupercapacitor Comprised of a High-Potential Bioanode and a Low-Potential Biocathode. *Chempluschem* **2017**, *82* (4), 576–583.

(50) Owen, T. *Fundamentals of Modern UV-Visible Spectroscopy*; Agilent Technologies: Germany, 2000.

(51) Jones, E.; Travis, O.; Peterson, P. SciPy: Open Source Scientific Tools for Python http://www.scipy.org/ (accessed Jan 28, 2019).

(52) van Stokkum, I. H. M.; Larsen, D. S.; van Grondelle, R. Global and Target Analysis of Time-Resolved Spectra. *Biochim. Biophys. Acta - Bioenerg.* **2004**, *1657* (2–3), 82–104.

(53) Snellenburg, J. J.; Laptenok, S. P.; Seger, R.; Mullen, K. M.; van Stokkum, I. H. M. Glotaran : A Java-Based Graphical User Interface for the R Package TIMP. *J. Stat. Softw.* **2012**, *49* (3), 1–2.

(54) Gibasiewicz, K.; Pajzderska, M.; Dobek, A.; Brettel, K.; Jones, M. R. Analysis of the Kinetics of P + H A – Recombination in Membrane-Embedded Wild-Type and Mutant Rhodobacter Sphaeroides Reaction Centers between 298 and 77 K Indicates That the Adjacent Negatively Charged Q A Ubiquinone Modulates the Free Energy of P + H A . *J. Phys. Chem. B* **2013**, *117* (38), 11112–11123.

(55) Gibasiewicz, K.; Pajzderska, M.; Ziółek, M.; Karolczak, J.; Dobek, A. Internal Electrostatic Control of the Primary Charge Separation and Recombination in Reaction Centers from Rhodobacter Sphaeroides Revealed by Femtosecond Transient Absorption. *J. Phys. Chem. B* **2009**, *113* (31), 11023–11031.

(56) Mandal, S.; Carey, A.-M.; Locsin, J.; Gao, B.-R.; Williams, J. C.; Allen, J. P.; Lin, S.; Woodbury, N. W. Mechanism of Triplet Energy Transfer in Photosynthetic Bacterial Reaction Centers. *J. Phys. Chem. B* **2017**, acs.jpcb.7b03373.

(57) Białek, R.; Burdziński, G.; Jones, M. R.; Gibasiewicz, K. Bacteriopheophytin Triplet State in *Rhodobacter Sphaeroides* Reaction Centers. *Photosynth. Res.* **2016**, *129* (2), 205–216.

(58) Friebe, V. M.; Swainsbury, D. J. K.; Fyfe, P. K.; van der Heijden, W.; Jones, M. R.; Frese, R. N. On the Mechanism of Ubiquinone Mediated Photocurrent Generation by a Reaction Center Based Photocathode. *Biochim. Biophys. Acta - Bioenerg.* **2016**, *1857* (12), 1925–1934.

(59) Wraight, C. A.; Gunner, M. R. The Acceptor Quinones of Purple Photosynthetic Bacteria — Structure and Spectroscopy. In *The Purple Phototrophic Bacteria*; Neil Hunter, C., Daldal, F., Thurnauer, M. C., Beatty, J. T., Eds.; Springer, 2009; pp 379–405.

(60) Overfield, R. E.; Wraight, C. A. Oxidation of Cytochromes c and C2 by Bacterial Photosynthetic Reaction Centers in Phospholipid Vesicles. 1. Studies with Neutral Membranes. *Biochemistry* **1980**, *19* (14), 3322–3327.

(61) Ermler, U.; Fritzsch, G.; Buchanan, S. K.; Michel, H. Structure of the Photosynthetic Reaction Centre from Rhodobacter Sphaeroides at 2.65 å Resolution: Cofactors and Protein-Cofactor Interactions. *Structure* **1994**, *2* (10), 925–936.

(62) Dolinsky, T. J.; Nielsen, J. E.; McCammon, J. A.; Baker, N. A. PDB2PQR: An Automated Pipeline for the Setup of Poisson-Boltzmann Electrostatics Calculations. *Nucleic Acids Res.* **2004**, *32* (WEB SERVER ISS.), 665–667.

(63) Baker, N. A.; Sept, D.; Joseph, S.; Holst, M. J.; McCammon, J. A. Electrostatics of Nanosystems: Application to Microtubules and the Ribosome. *Proc. Natl. Acad. Sci.* **2001**, *98* (18), 10037–10041.

TOC graphics

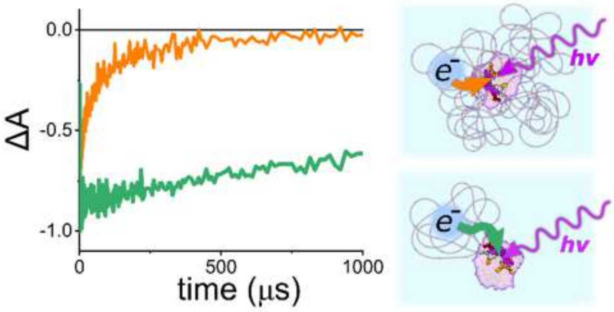

Supporting Information

Insight in the Electron Transfer from Redox Polymers to a Photoactive Protein

Rafał Białek[a]*, Kalyani Thakur[b], Adrian Ruff[c#], Michael R. Jones[d], Wolfgang Schuhmann[c], Charusheela Ramanan[b] and Krzysztof Gibasiewicz[a]*

[a] Faculty of Physics, Adam Mickiewicz University, Poznań, ul. Uniwersytetu Poznańskiego 2, 61-614 Poznań, Poland

[b] Max Planck Institute for Polymer Research, Ackermannweg 10, 55128 Mainz, Germany

[c] Analytical Chemistry – Center for Electrochemical Sciences, Faculty of Biochemistry and Chemistry, Ruhr-University Bochum, Universitätsstrasse 150, D-44780, Bochum, Germany

[d] School of Biochemistry, Biomedical Sciences Building, University of Bristol, University Walk, Bristol, BS8 1TD, UK

[#] A.R. Present Address: PPG Business Support GmbH, PPG Packaging Coatings, Erlenbrunnenstr. 20, 72411 Bodelshausen. Germany

*Corresponding authors: RB: rafal.bialek@amu.edu.pl, KG: krzysztof.gibasiewicz@amu.edu.pl

S1. REDOX SILENT POLYMER

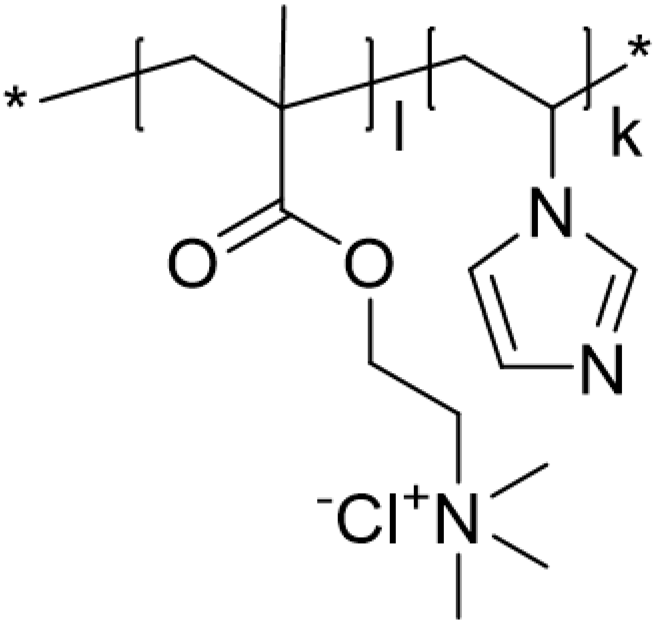

Figure S1 Structure of the redox-silent polymer poly(vinyl imidazole-co-trimethyl aminoethyl methacrylate).

S2. SAMPLE PREPARATION

2.1 COMPOSITION

For preparation of samples, the following stock solutions were used:

- buffer: 20 mM Tris-HCl pH 8.0 with addition of 0.1 % LDAO (*N*,*N*-dimethyldodecan-1-amine oxide)
- RCs: $OD_{800\,nm,1\,cm} = 58 \pm 2.5$ ($c_w \cong 20.9 \pm 1.4\, mg/ml$, $c_m = 201 \pm 13\, \mu M$) in abovementioned buffer
- polymer: $c_w = 10 \pm 0.8\, mg/ml$ (for P-Os and PVI), $OD_{515\,nm,1\,cm} = 55.0 \pm 2.5$ (for P-Os)
- Q_0 (2,3-dimethoxy-5-methyl-*p*-benzoquinone): 15 mM in H_2O
- ascorbate (sodium): 1 M in H_2O

Table S1 shows volumes of each of the stock solutions used for preparation of the samples for TA measurements. All samples were prepared directly in the 2-mm cuvette directly prior to experiment.

Table S1 Volumes of stock solutions used for preparation of samples for TA measurements.

Sample	Polymer type	**Volume of stock solution (µl)**				
		buffer	RCs	polymer	Q_0	ascorbate
I	P-Os	300	2.60	6.85	34.0	0
II	P-Os	300	2.60	2.70	33.5	0
III	P-Os	300	2.60	1.40	33.5	0
IV	P-Os	300	1.30	6.85	34.0	0
V	P-Os	300	6.50	6.85	35.0	0
RCs only	---	300	5.20	0	0	0
RCs + ascorbate	---	300	7.00	0	0	3
RCs + polymer	P-Os	600	7.00	10.00	0	0
RCs + polymer + Q_0	PVI	300	2.60	6.85	34.0	0
polymer only	P-Os	300	0	6.85	0	0
polymer + Q_0	P-Os	300	6.85	0	34.0	0
Q_0 only	---	300	0	0	34.0	0

2.2 CONCENTRATIONS

It has been reported previously[1] that for P-Os: the amount of Os-complexes is 0.67 ± 0.05 mmol Os per g of polymer, the molecular weight of the polymer backbone is 26 ± 3 kDa, and the molecular weight of the polymer with Os-complexes is 44 ± 5 kDa. Steady-state absorption measurements of diluted solution of P-Os (see Figure 1B) show that the absorbance of the stock solution (10.0 ± 0.8 mg/ml) at 515 nm is equal to 55.0 ± 2.5. Moreover, it is known that RCs extinction coefficient is equal to: 288,000 ± 14,000 $M^{-1}cm^{-1}$ at maximum ~800 nm[2] and their molecular weight is equal to 103.75 kDa.[3] From all above data, a conversion table was prepared (Table S2) and it was estimated that there are 29 ± 4 Os-complexes per P-Os chain. Using this conversion table, the exact concentrations of each of the solution compositions were calculated (Table 1 and S3).

Table S2 Values of molar and weight concentrations per 1 unit of absorbance at depicted wavelength for depicted species.

species	wavelength (nm)	molar concentration (µM)	weight concentration (mg/ml)
RCs	800	3.47 ± 0.17	0.360 ± 0.018
P-Os	515	4.1 ± 0.6	0.181 ± 0.017
Os-complexes	515	122 ± 14	0.074 ± 0.019

Table S3 Molar ratios of components of the solutions used for experiments.

Sample	**Molar ratio**	
	polymer chains per RC	Os-complexes per RCs
I	3.1 ± 0.5	93 ± 13
II	1.23 ± 0.2	37 ± 5
III	0.64 ± 0.11	18.9 ± 2.6
IV	6.2 ± 1	185 ± 26
V	1.25 ± 0.21	37 ± 5
RCs only	-	-
RCs + ascorbate	-	-
RCs + P-Os	1.69 ± 0.28	50 ± 7
RCs + PVI + Q_0	3.1 ± 0.5	93 ± 13
P-Os only	-	-
P-Os + Q_0	-	-
Q_0 only	-	-

S3. REFERENCE EXPERIMENTS

3.1 OPEN RCS

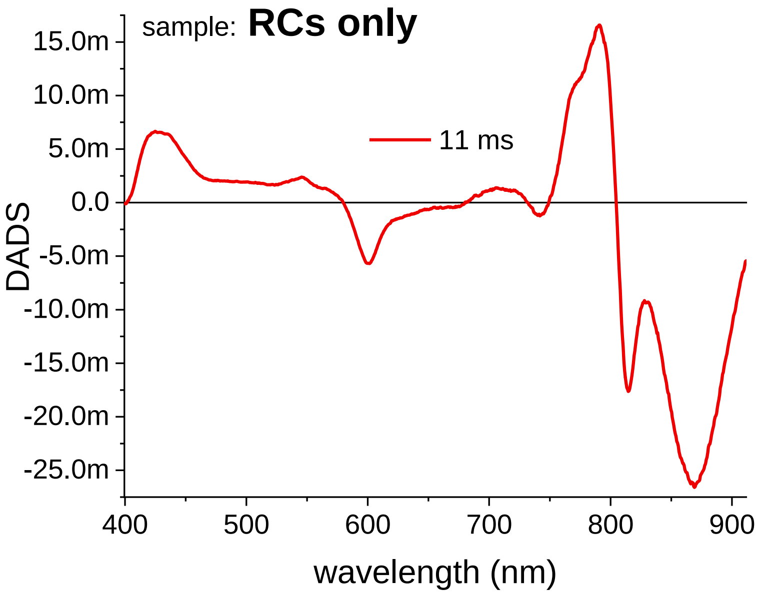

Figure S2 DADS for RCs in buffer only measured with 10-Hz laser pulses over a 100 ms time window. The lifetime is longer than the slowest one for samples I-V due to a wider time window. The excitation wavelength was 365 nm. The 11-ms lifetime reflects depletion of RCs in the charge separated state ($P^+Q_A^-$) from the focal volume of the laser beam due to stirring and diffusion.

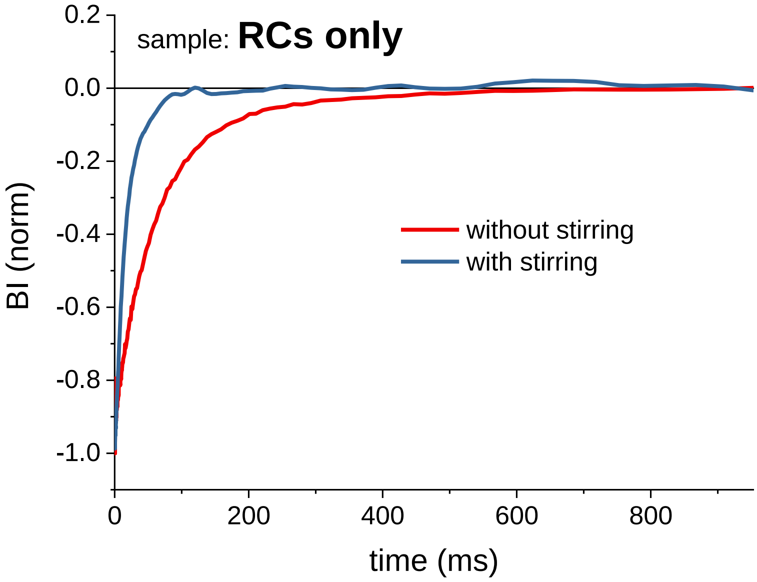

Figure S3 Normalized band integral (BI) kinetics of the RCs in buffer only sample (with and without stirring) excited at 800 nm at 1 Hz repetition rate. Band integrals were constructed in the 830-950 nm range. In this range the negative signal is proportional to the concentration of the oxidized P_{870}.

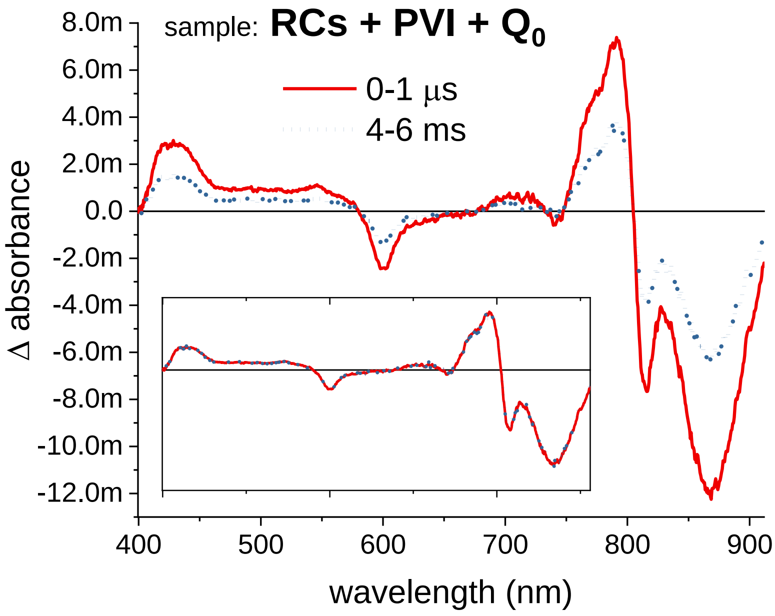

Figure S4 Transient absorption spectra for a sample with RCs, PVI, and Q_0. Values in the legend show delay times for which each spectrum was averaged. Inset shows the same data but normalized, showing that there is just decay of the oxidized primary donor without the creation of any other species. The excitation wavelength was 365 nm.

3.2 CLOSED RCS

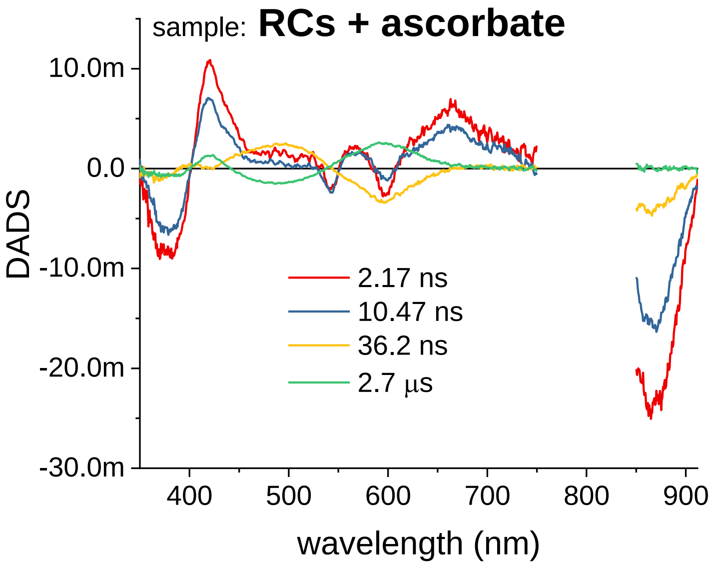

Figure S5 DADS of RCs with the addition of 10 mM sodium ascorbate. The excitation wavelength was 800 nm. The longest DADS is the decay of the Car triplet. The ~2-ns and ~10-ns components are assigned to $P^+H_A^-$ recombination, and the ~36-ns and 2.7-µs components to formation and decay, respectively, of the ^{T}Car state.

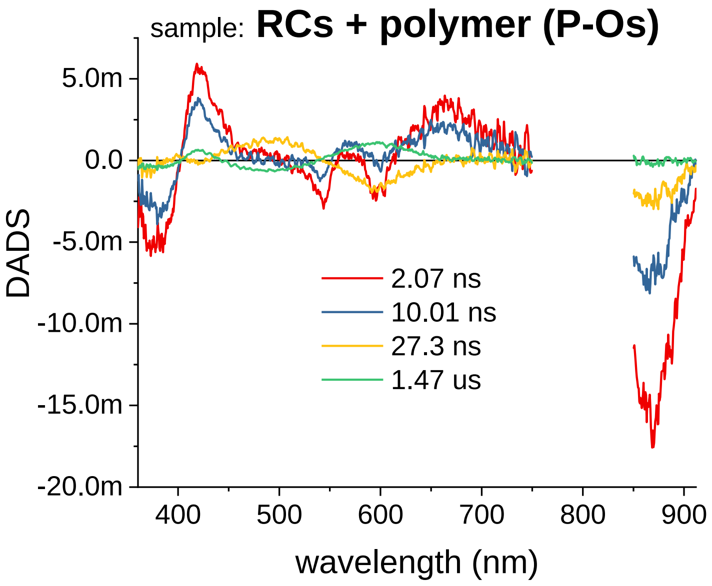

Figure S6 DADS of RCs with the addition of P-Os. The excitation wavelength was 800 nm. The assignment of DADS is as in Figure S5.

3.3 AMPLITUDE VS EXCITATION ENERGY

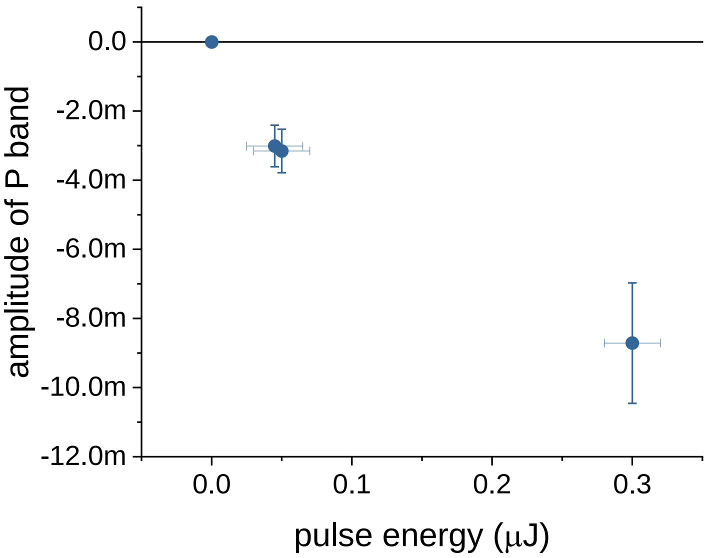

Figure S7 Dependence of the amplitude of the P band at ~870 nm averaged over first 1 μs of the signal as a function of the laser pulse energy. The measurements were conducted using sample II. The point at (0,0) was added to show the trend (there is no signal without laser pulse).

S4. SPECTRA AT CHOSEN DELAYS

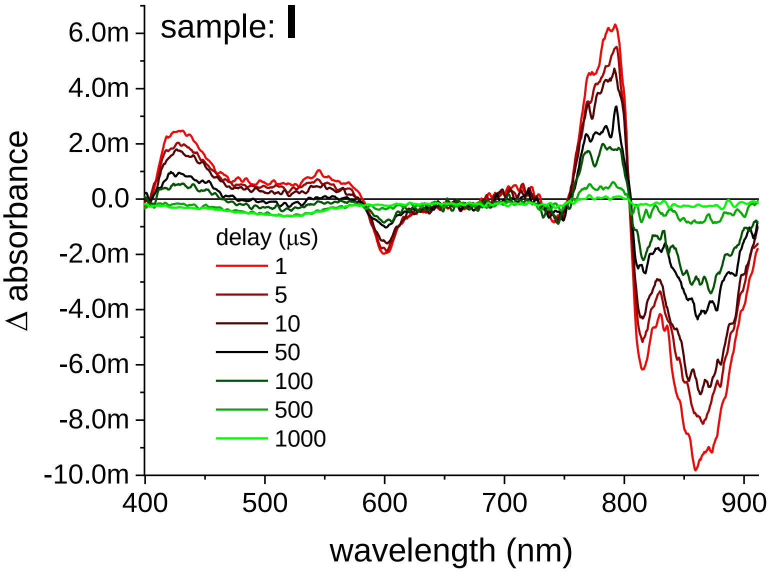

Figure S8 Transient absorption spectra for the indicated delays for sample I.

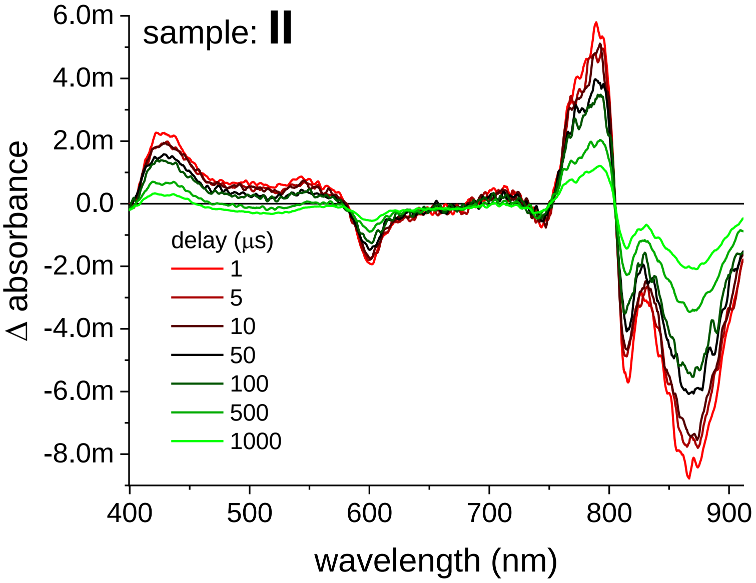

Figure S9 Transient absorption spectra for the indicated delays for sample II.

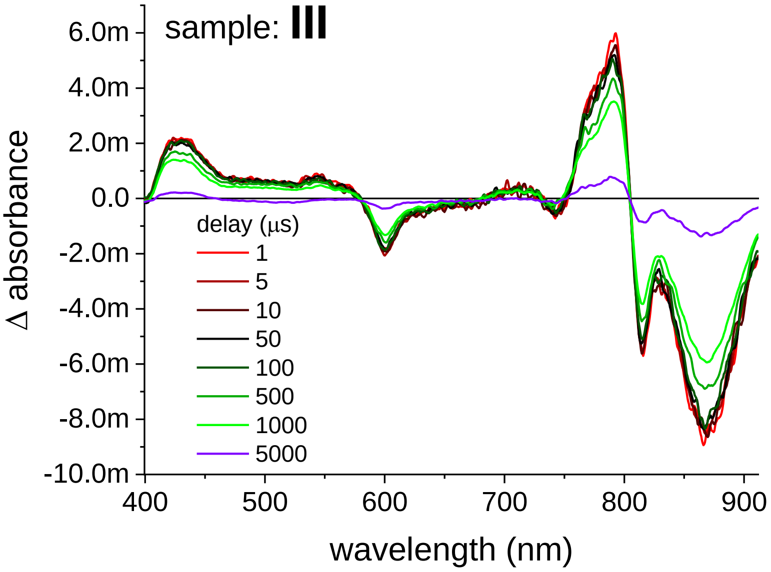

Figure S10 Transient absorption spectra for the indicated delays for sample III.

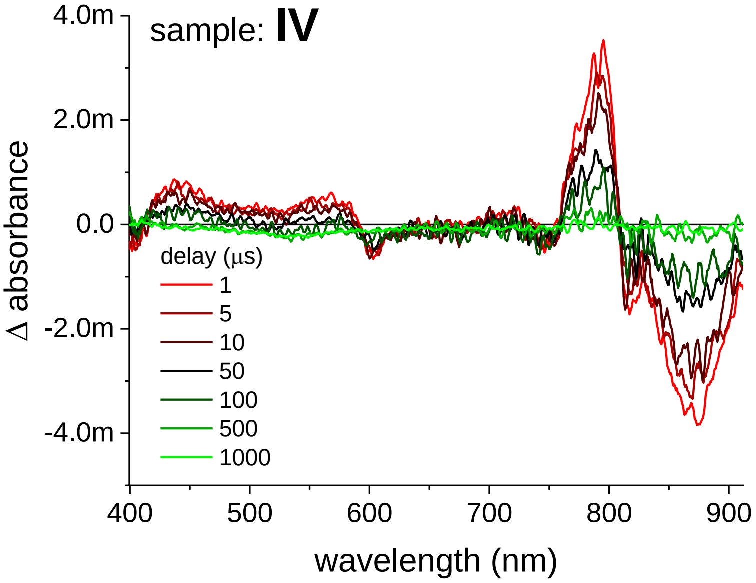

Figure S11 Transient absorption spectra for the indicated delays for sample IV.

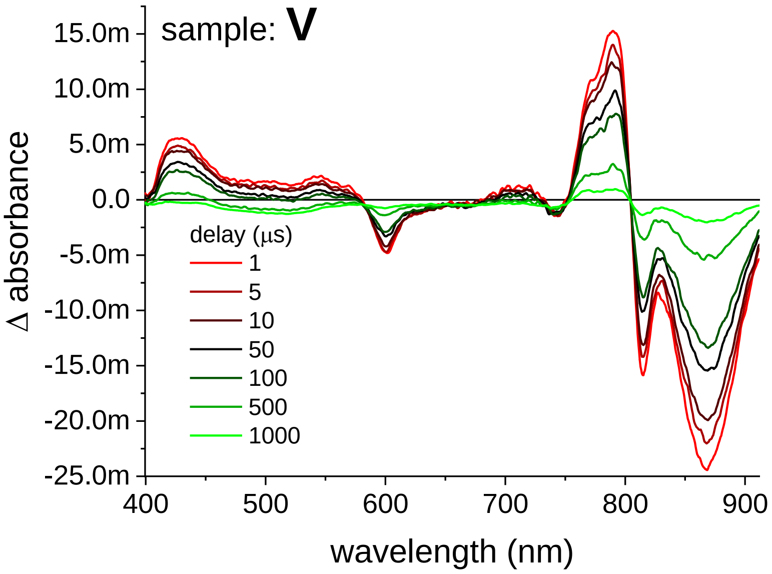

Figure S12 Transient absorption spectra for the indicated delays for sample V.

S5. DECAY ASSOCIATED DIFFERENCE SPECTRA

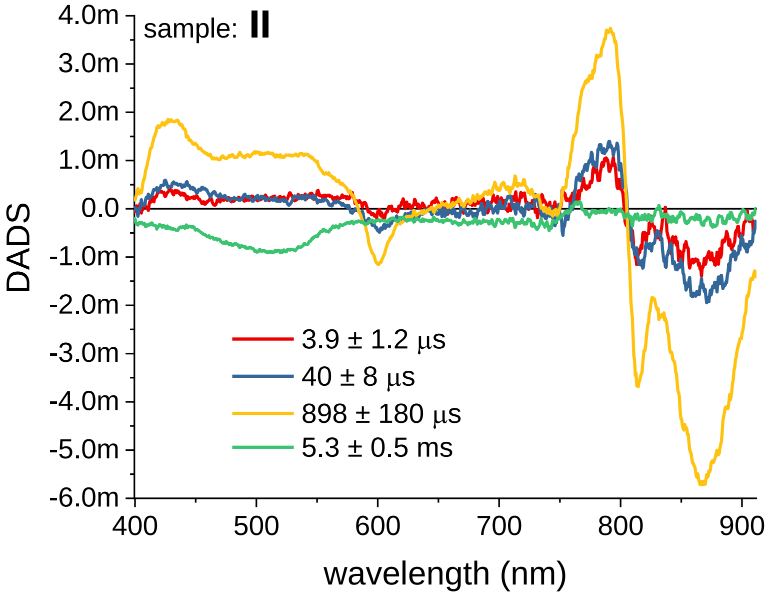

Figure S13 Results of the global analysis for sample II.

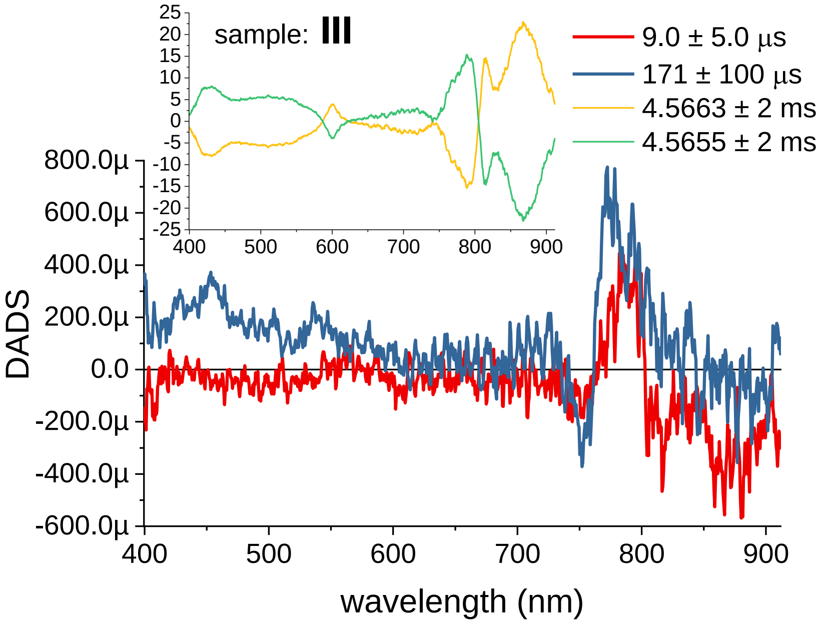

Figure S14 Results of the global analysis for sample III.

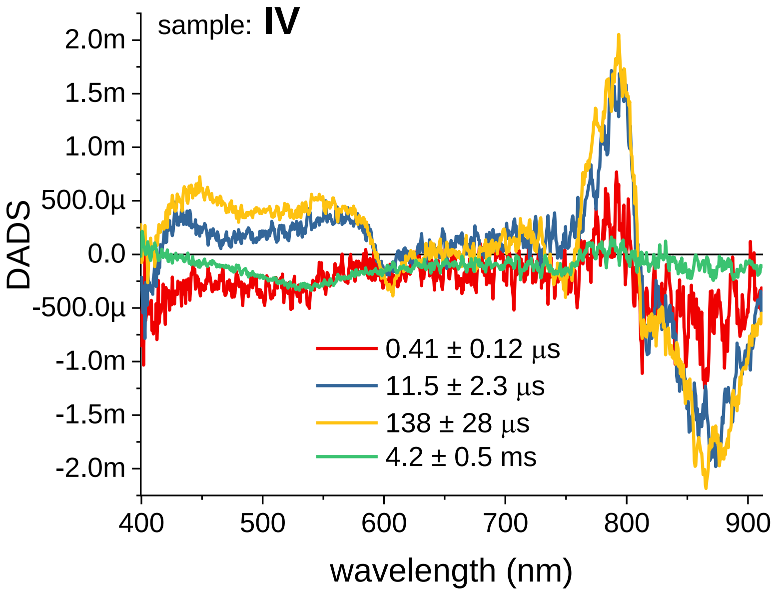

Figure S15 Results of the global analysis for sample IV.

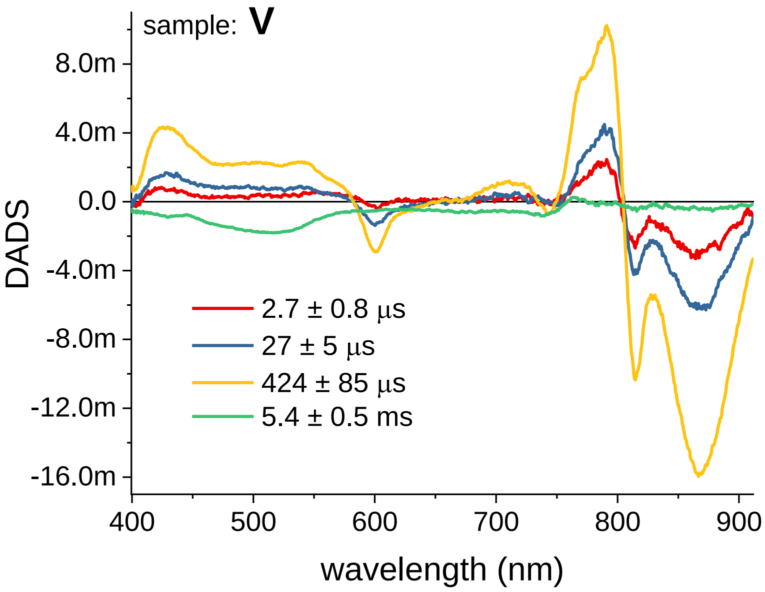

Figure S16 Results of the global analysis for sample V.

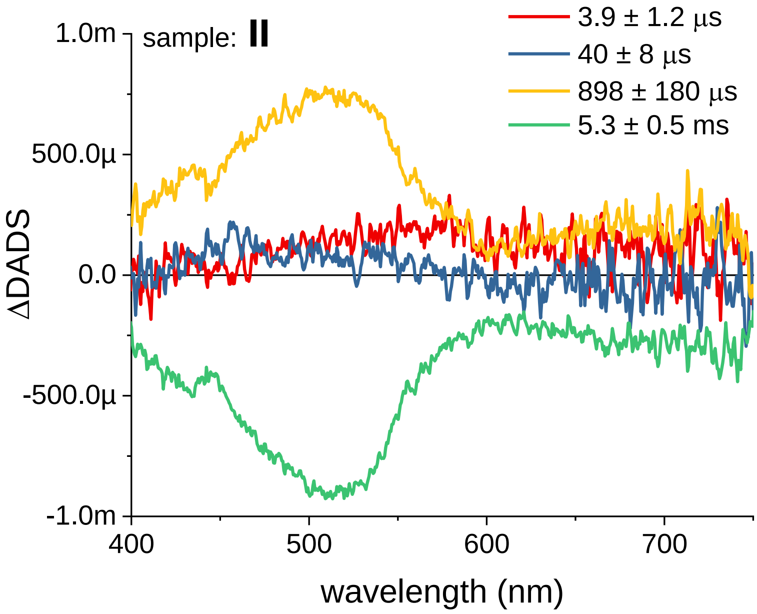

Figure S17 P-Os contribution to DADS for sample II.

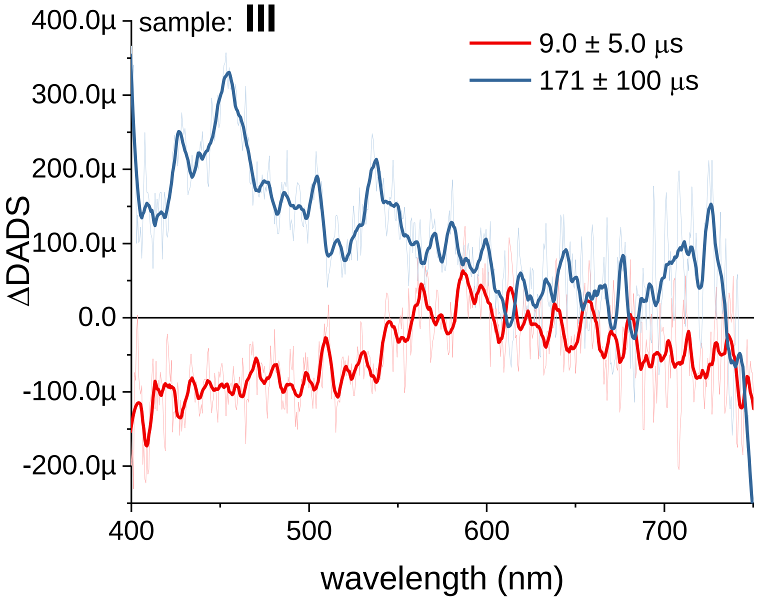

Figure S18 P-Os contribution to DADS for sample III. Data were additionally smoothed with a Savitzky-Golay procedure with a 20 point window (lighter color shows original data). Slower DADS were omitted due to their compensating nature.

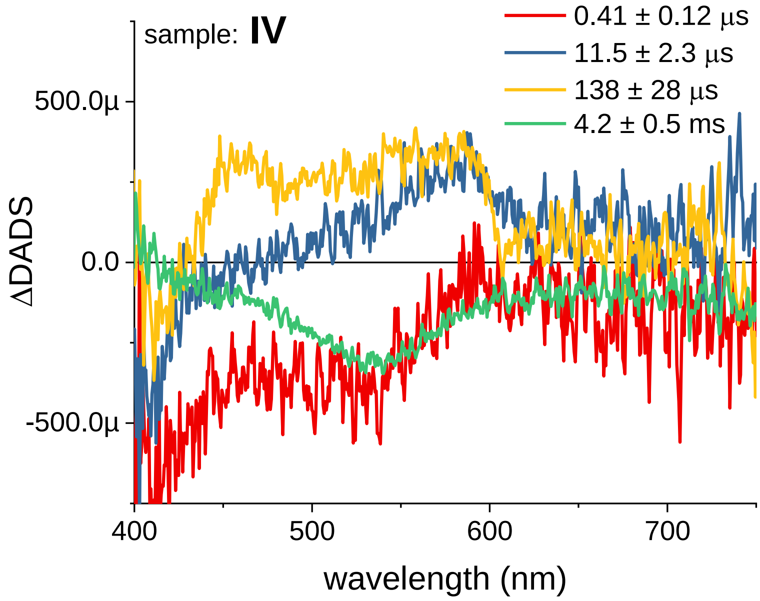

Figure S19 P-Os contribution to DADS for sample IV.

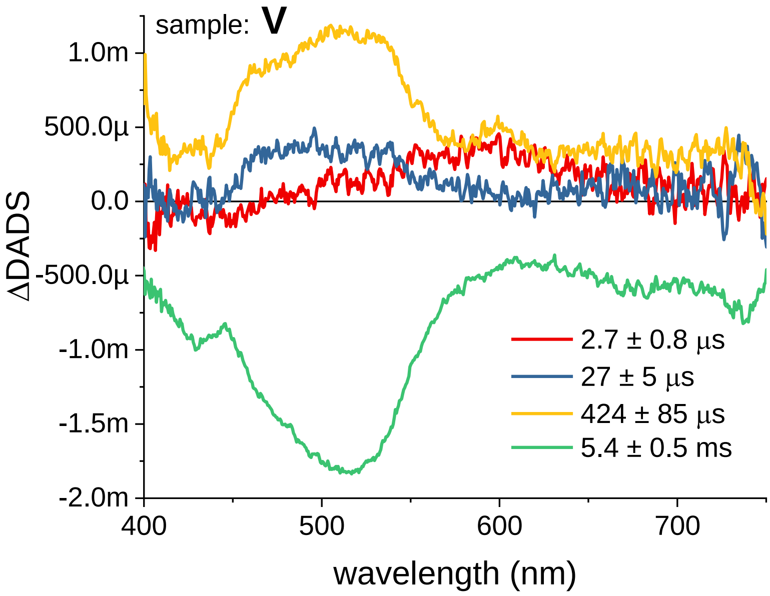

Figure S20 P-Os contribution to DADS for sample V.

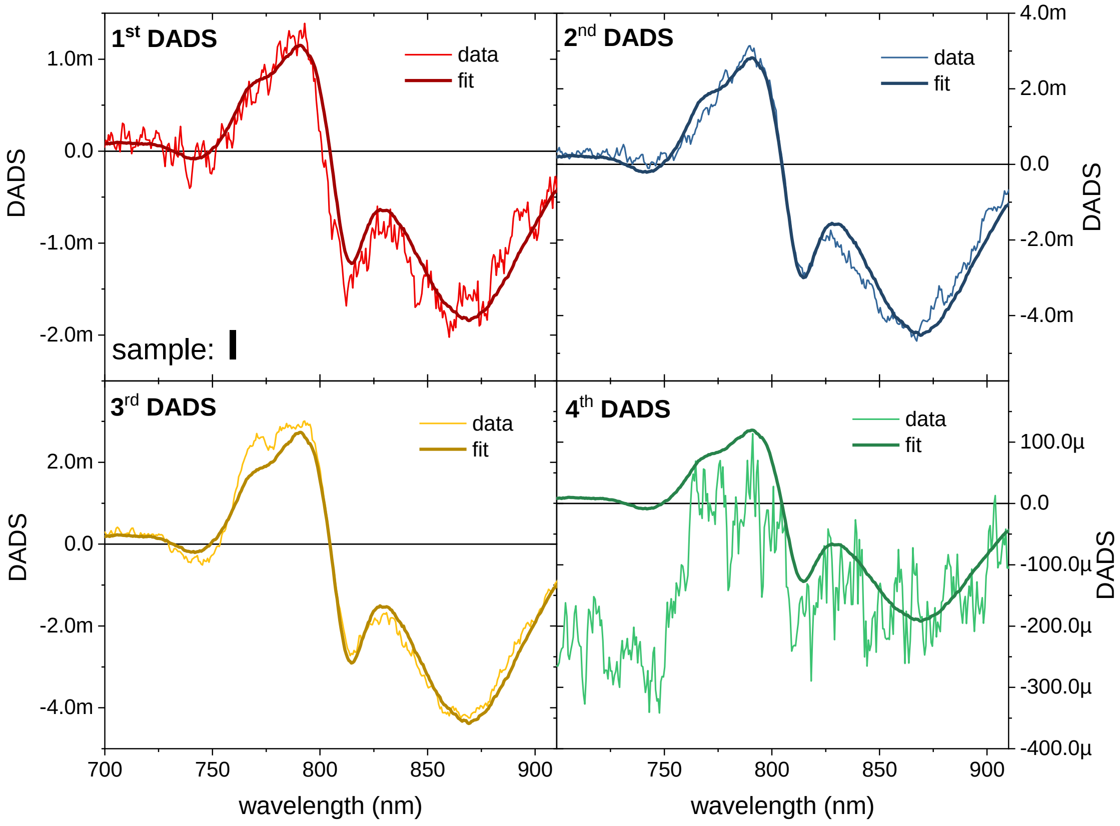

Figure S21 Quality of fit of the P/P⁺ contribution to the DADS of sample I.

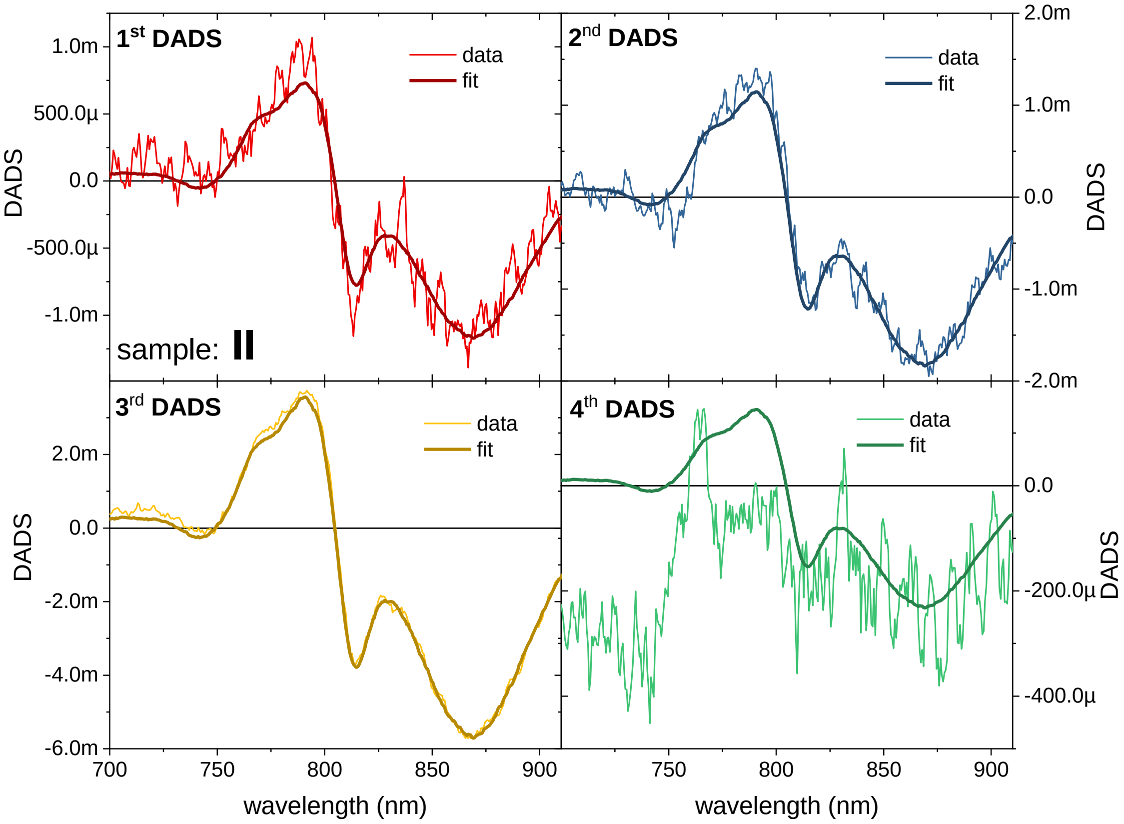

Figure S22 Quality of fit of the P/P⁺ contribution to the DADS of sample II.

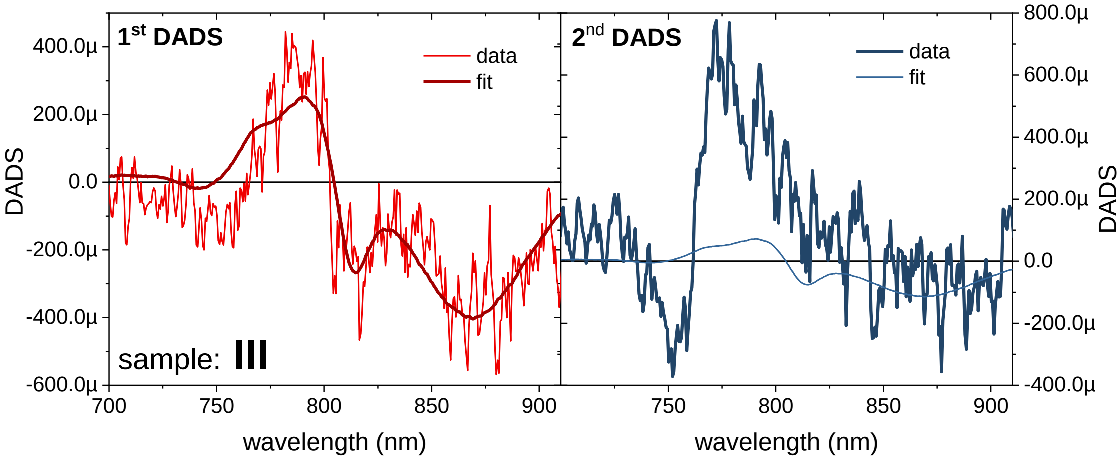

Figure S23 Quality of fit of the P/P⁺ contribution to the DADS of sample III. Slower DADS were omitted due to their compensating nature.

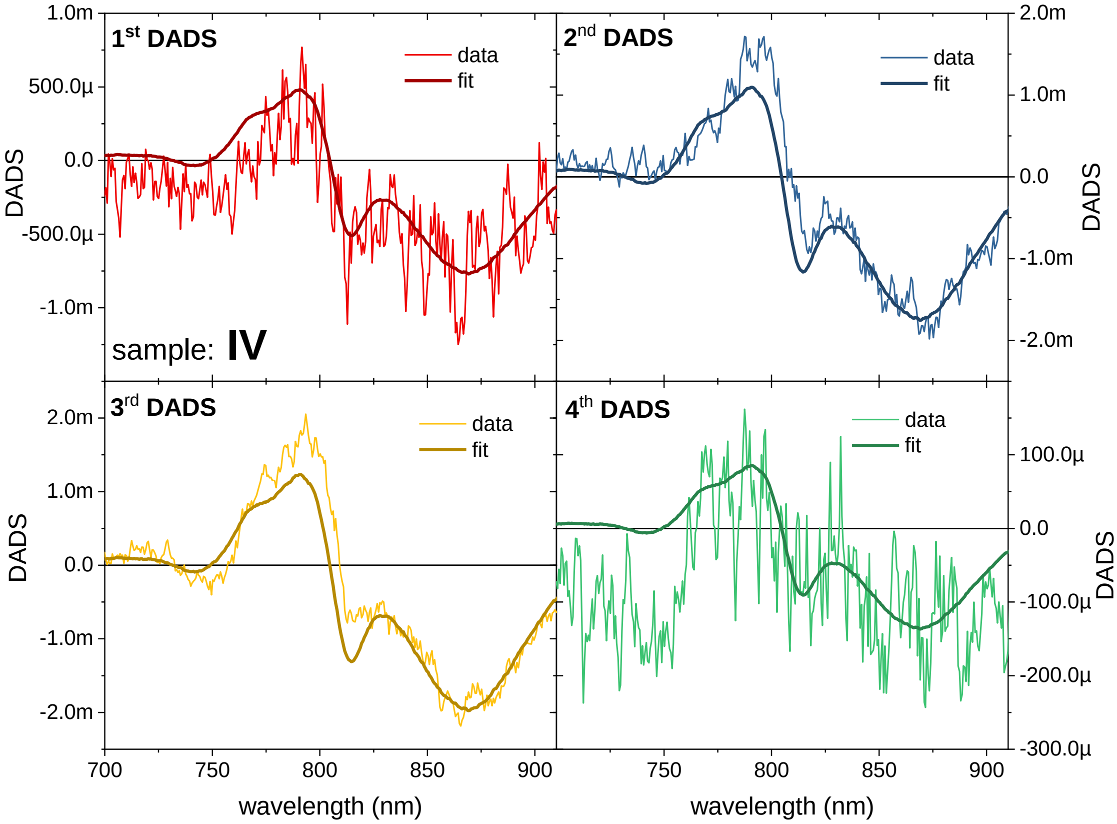

Figure S24 Quality of fit of the P/P⁺ contribution to the DADS of sample IV.

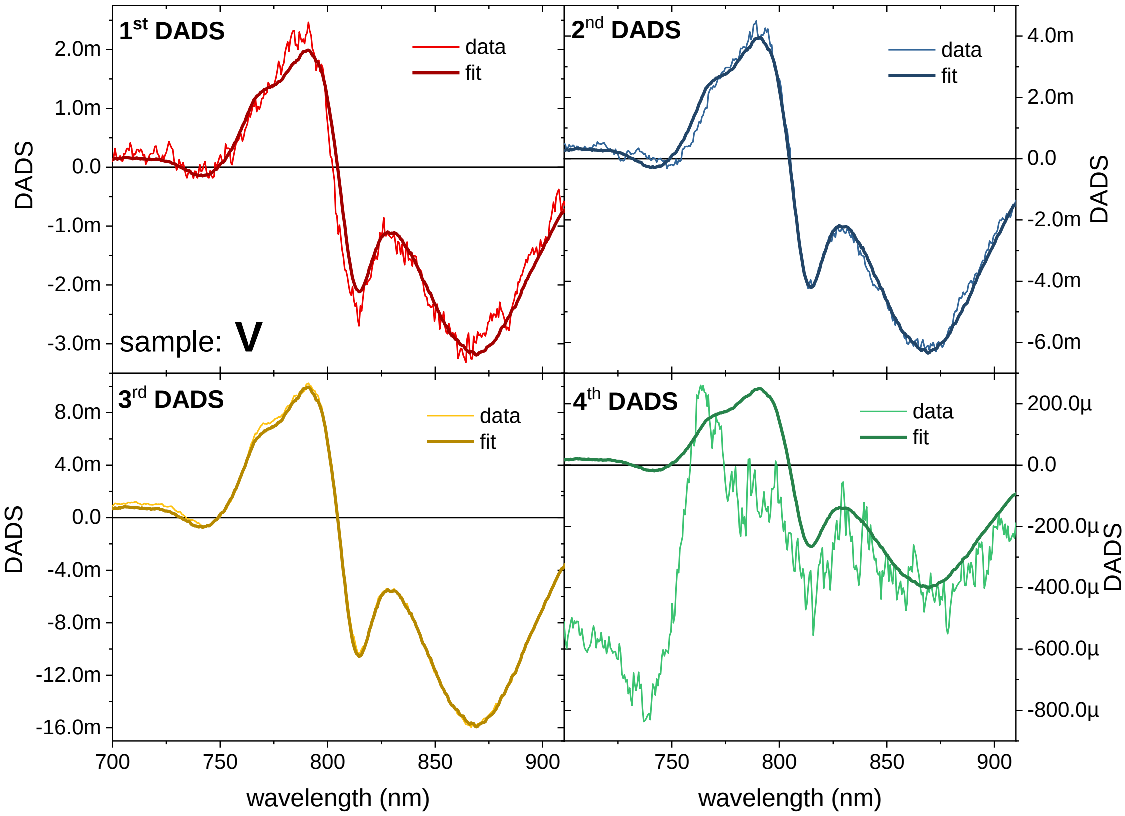

Figure S25 Quality of fit of the P/P⁺ contribution to the DADS of sample V.

S6. REFERENCES

(1) Sokol, K. P.; Mersch, D.; Hartmann, V.; Zhang, J. Z.; Nowaczyk, M. M.; Rögner, M.; Ruff, A.; Schuhmann, W.; Plumeré, N.; Reisner, E. Rational Wiring of Photosystem II to Hierarchical Indium Tin Oxide Electrodes Using Redox Polymers. *Energy Environ. Sci.* **2016**, *9* (12), 3698–3709. https://doi.org/10.1039/C6EE01363E.

(2) Straley, S. C.; Parson, W. W.; Mauzerall, D. C.; Clayton, R. K. Pigment Content and Molar Extinction Coefficients of Photochemical Reaction Centers from *Rhodopseudomonas Spheroides*. *Biochim. Biophys. Acta - Bioenerg.* **1973**, *305* (3), 597–609. https://doi.org/10.1016/0005-2728(73)90079-0.

(3) Ermler, U.; Fritzsch, G.; Buchanan, S. K.; Michel, H. Structure of the Photosynthetic Reaction Centre from Rhodobacter Sphaeroides at 2.65 å Resolution: Cofactors and Protein-Cofactor Interactions. *Structure* **1994**, *2* (10), 925–936. https://doi.org/10.1016/S0969-2126(94)00094-8.

STATEMENTS OF THE CO-AUTHORS

mgr Rafał Białek
Faculty of Physics
Adam Mickiewicz University, Poznań
ul. Uniwersytetu Poznańskiego 2
61-614 Poznań, Poland
e-mail: rafal.bialek@amu.edu.pl

Contribution statement

Hereby, I declare my contribution to the following publications:

1. Gibasiewicz, K.; Białek, R.; Pajzderska, M.; Karolczak, J.; Burdziński, G.; Jones, M. R.; Brettel, K. Weak Temperature Dependence of $P^+H_A^-$ Recombination in Mutant *Rhodobacter sphaeroides* Reaction Centers. *Photosynth. Res.* **2016**, *128* (3), 243–258.

In this publication I have:

- derived fitting equations,
- performed all data analysis, including fitting of nanosecond data, global and target analysis of femtosecond data with additional model constraints,
- prepared all the figures containing experimental and fitting results,
- prepared the parts of the manuscript text about data analysis and equation derivation.

2. Białek, R.; Swainsbury, D. J. K.; Wiesner, M.; Jones, M. R.; Gibasiewicz, K. Modelling of the Cathodic and Anodic Photocurrents from *Rhodobacter sphaeroides* Reaction Centres Immobilized on Titanium Dioxide. *Photosynth. Res.* **2018**, *138* (1), 103–114.

In this publication I have:

- fabricated the TiO_2 paste and final biohybrid electrodes,
- designed and built the experimental setup,
- performed all spectral and electrochemical experiments,
- assisted in electron microscopy experiments,
- performed all the data analysis,
- prepared the model and optimized its parameters,
- prepared all figures,
- prepared most of the text of the manuscript,
- served as one of the two corresponding authors.

3. Białek, R.; Friebe, V.; Ruff, A.; Jones, M. R.; Frese, R.; Gibasiewicz, K. In Situ Spectroelectrochemical Investigation of a Biophotoelectrode Based on Photoreaction Centers Embedded in a Redox Hydrogel. *Electrochim. Acta* **2020**, *330*, 135190.

In this publication I have:

- fabricated the final biohybrid electrodes,
- designed and built the experimental setup,
- performed all the experiments,
- prepared software for data analysis,
- performed data analysis,
- prepared all figures except for the scheme in Figure 1,
- prepared most of the text of the manuscript,
- served as one of the two corresponding authors.

4. Białek, R.; Kalyani, T.; Ruff, A.; Jones, M. R.; Schuhmann, W.; Ramanan, C.; Gibasiewicz, K. Insight in the Electron Transfer from Redox Polymers to a Photoactive Protein. *Journal of Physical Chemistry B*, doi:10.1021/acs.jpcb.0c08714 just accepted

In this publication I have:

- prepared solutions for spectral measurements,
- performed all the experiments except for reference transient absorption experiments with PVI polymer,
- prepared software for data analysis,
- performed all data analysis,
- prepared all figures,
- prepared most of the text of the manuscript,
- served as one of the two corresponding authors.

Date Signature

13.11.2020 Rafał Białek ……………………………

dr hab. Krzysztof Gibasiewicz, prof. UAM
Faculty of Physics
Adam Mickiewicz University, Poznań
ul. Uniwersytetu Poznańskiego 2
61-614 Poznań, Poland
e-mail: krzyszgi@amu.edu.pl

Contribution statement

Hereby, I declare my contribution to the following publications:

1. Gibasiewicz, K.; Białek, R.; Pajzderska, M.; Karolczak, J.; Burdziński, G.; Jones, M. R.; Brettel, K. Weak Temperature Dependence of $P^+H_A^-$ Recombination in Mutant *Rhodobacter sphaeroides* Reaction Centers. *Photosynth. Res.* **2016**, *128* (3), 243–258.

In this publication I have:

- led the work from experiments, through data analysis towards the final manuscript,
- taken part in performing of experiments,
- prepared most of the manuscript text,
- served as a corresponding author.

2. Białek, R.; Swainsbury, D. J. K.; Wiesner, M.; Jones, M. R.; Gibasiewicz, K.
Modelling of the Cathodic and Anodic Photocurrents from *Rhodobacter sphaeroides* Reaction Centres Immobilized on Titanium Dioxide. *Photosynth. Res.* **2018**, *138* (1), 103–114.

In this publication I have:

- supervised all the work performed,
- taken part in writing of the manuscript with comments and corrections,
- served as one of the two corresponding authors.

3. Białek, R.; Friebe, V.; Ruff, A.; Jones, M. R.; Frese, R.; Gibasiewicz, K.
In Situ Spectroelectrochemical Investigation of a Biophotoelectrode Based on Photoreaction Centers Embedded in a Redox Hydrogel. *Electrochim. Acta* **2020**, *330*, 135190.

In this publication I have:

- supervised all the work performed,
- taken part in writing of the manuscript with comments and corrections,
- served as one of the two corresponding authors.

4. Białek, R.; Kalyani; Ruff, A.; Jones, M. R.; Schuhmann, W.; Ramanan, C.; Gibasiewicz, K. Insight in the Electron Transfer from Redox Polymers to a Photoactive Protein. *Journal of Physical Chemistry B*, manuscript accepted for publication.

In this publication I have:

- supervised all the work performed,
- taken part in writing of the manuscript with comments and corrections,
- served as one of the two corresponding authors.

Date	Signature
12 XI 2020	Gibasiewicz

University of BRISTOL

Dr Michael R. Jones
Reader in Biochemistry
School of Biochemistry
Medical Sciences Building
University Walk
Bristol, BS8 1TD
Tel: +44 (0) 117 3312135
Fax: +44 (0) 117 3312168
m.r.jones@bristol.ac.uk
www.bris.ac.uk/biochemistry/research/mrj.html

Contribution statement

Hereby, I declare my contribution to the following publications:

1. Gibasiewicz, K.; Białek, R.; Pajzderska, M.; Karolczak, J.; Burdziński, G.; Jones, M. R.; Brettel, K. Weak Temperature Dependence of $P^+H_A^-$ Recombination in Mutant *Rhodobacter sphaeroides* Reaction Centers. *Photosynth. Res.* **2016**, *128* (3), 243–258.

In this publication I have:

- prepared the biological samples,
- taken part in writing of the manuscript with comments and corrections and provided text for the sections on biological sample preparation.

2. Białek, R.; Swainsbury, D. J. K.; Wiesner, M.; Jones, M. R.; Gibasiewicz, K. Modelling of the Cathodic and Anodic Photocurrents from *Rhodobacter sphaeroides* Reaction Centres Immobilized on Titanium Dioxide. *Photosynth. Res.* **2018**, *138* (1), 103–114.

In this publication I have:

- prepared the biological samples,
- taken part in writing of the manuscript with comments and corrections and provided text for the sections on biological sample preparation.

3. Białek, R.; Friebe, V.; Ruff, A.; Jones, M. R.; Frese, R.; Gibasiewicz, K. In Situ Spectroelectrochemical Investigation of a Biophotoelectrode Based on Photoreaction Centers Embedded in a Redox Hydrogel. *Electrochim. Acta* **2020**, *330*, 135190.

In this publication I have:

- prepared the biological samples,
- taken part in writing of the manuscript with comments and corrections and provided text for the sections on biological sample preparation.

4. Białek, R.; Kalyani, T.; Ruff, A.; Jones, M. R.; Schuhmann, W.; Ramanan, C.; Gibasiewicz, K. Insight in the Electron Transfer from Redox Polymers to a Photoactive Protein. *Journal of Physical Chemistry B*, manuscript submitted and after 1st review round

In this publication I have:

- prepared the biological samples,
- taken part in writing of the manuscript with comments and corrections and provided text for the sections on biological sample preparation.

......11/11/2020........................ M. R. Jones ..

Date Signature

......

dr hab. Krzysztof Gibasiewicz, prof. UAM
Faculty of Physics
Adam Mickiewicz University, Poznań
ul. Uniwersytetu Poznańskiego 2
61-614 Poznań, Poland
e-mail: krzyszgi@amu.edu.pl

Contribution statement

Due to the death of dr Jerzy Karolczak, hereby, I, as a corresponding author, declare his contribution to the following publication:

> Gibasiewicz, K.; Białek, R.; Pajzderska, M.; Karolczak, J.; Burdziński, G.; Jones, M. R.; Brettel, K. Weak Temperature Dependence of $P^+H_A^-$ Recombination in Mutant *Rhodobacter sphaeroides* Reaction Centers. *Photosynth. Res.* **2016**, *128* (3), 243–258.

In this publication he has:

- prepared the experimental setup for femtosecond transient absorption measurements,
- assisted in performing of femtosecond transient absorption experiments.

Date	Signature
12 XI 2020	Gibasiewicz

dr Maria Pajzderska
e-mail: mpajzder@gmail.com

Contribution statement

Hereby I declare my contribution to the following publication:

> Gibasiewicz, K.; Białek, R.; Pajzderska, M.; Karolczak, J.; Burdziński, G.; Jones, M. R.; Brettel, K. Weak Temperature Dependence of $P^+H_A^-$ Recombination in Mutant *Rhodobacter Sphaeroides* Reaction Centers. *Photosynth. Res.* **2016**, *128* (3), 243–258.

In this publication I have:

- conducted femtosecond and nanosecond transient absorption measurements,
- performed initial processing of femtosecond transient absorption data.

Date	Signature
08.11.2020	M. Pajzderska

dr hab. Gotard Burdziński, prof. UAM
Faculty of Physics
Adam Mickiewicz University, Poznań
ul. Uniwersytetu Poznańskiego 2
61-614 Poznań, Poland
e-mail: gotardb@amu.edu.pl

Contribution statement

Hereby, I declare my contribution to the following publication:

Gibasiewicz, K.; Białek, R.; Pajzderska, M.; Karolczak, J.; Burdziński, G.; Jones, M. R.; Brettel, K. Weak Temperature Dependence of $P^+H_A^-$ Recombination in Mutant *Rhodobacter sphaeroides* Reaction Centers. *Photosynth. Res.* **2016**, *128* (3), 243–258.

In this publication I have:

- prepared the experimental setup for femtosecond transient absorption measurements,
- assisted in performing of femtosecond transient absorption experiments,
- read the manuscript and introduced minor corrections.

Date Signature

October 11th 2020

Dr Klaus Brettel
Université Paris-Saclay, CEA, CNRS,
Institute for Integrative Biology of the Cell (I2BC)
91198 Gif-sur-Yvette, France

Contribution statement

Hereby I declare my contribution to the following publication:

> Gibasiewicz, K.; Białek, R.; Pajzderska, M.; Karolczak, J.; Burdziński, G.; Jones, M. R.; Brettel, K. Weak Temperature Dependence of $P^+H_A^-$ Recombination in Mutant *Rhodobacter sphaeroides* Reaction Centers. *Photosynth. Res.* **2016**, *128* (3), 243–258.

In this publication I have:

- prepared the experimental setup for nanosecond transient absorption measurements,
- assisted in performing of nanosecond transient absorption experiments,
- read the manuscript and introduced corrections.

Date	Signature
08/11/2020	Kl. Brettel

Dr David Swainsbury
Department of Molecular Biology and Biotechnology
The University of Sheffield
Sheffield, S10 2TN, UK
e-mail: d.swainsbury@sheffield.ac.uk

Contribution statement

I declare my contribution to the following publication:

Białek, R.; Swainsbury, D. J. K.; Wiesner, M.; Jones, M. R.; Gibasiewicz, K.
Modelling of the Cathodic and Anodic Photocurrents from *Rhodobacter sphaeroides* Reaction Centres Immobilized on Titanium Dioxide. *Photosynth. Res.* **2018**, *138* (1), 103–114.

For this publication I have:

- Prepared a genetically-engineered strain of *Rhodobacter sphaeroides* and purified modified reaction centers from it.
- Contributed to the writing of the manuscript, specifically providing details on the production and biochemical characterization of the engineered reaction centers, and assisting with corrections.

Date	Signature
09/11/2020	

dr hab. Maciej Wiesner, prof. UAM
Faculty of Physics
Adam Mickiewicz University, Poznań
ul. Uniwersytetu Poznańskiego 2
61-614 Poznań, Poland
e-mail: mwiesner@amu.edu.pl

Contribution statement

Hereby, I declare my contribution to the following publication:

Białek, R.; Swainsbury, D. J. K.; Wiesner, M.; Jones, M. R.; Gibasiewicz, K.
Modelling of the Cathodic and Anodic Photocurrents from *Rhodobacter sphaeroides* Reaction Centres Immobilized on Titanium Dioxide. *Photosynth. Res.* **2018**, *138* (1), 103–114.

In this publication I have:

- performed SEM measurements,
- taken part in writing of the manuscript with comments, corrections and details on the SEM measurements.

Date	Signature
09.11.2020.	

Dr Adrian Ruff
Analytical Chemistry – Center for Electrochemical Sciences
Faculty of Biochemistry and Chemistry
Ruhr-University Bochum
Universitätsstrasse 150
D-44780, Bochum, Germany
e-mail: adrian.ruff@ruhr-uni-bochum.de

present address:
PPG Packaging Analytical Labs
PPG Deutschland Business Support GmbH
Erlenbrunnenstr. 20
72411 Bodelshausen, Germany
Email: aruff@ppg.com

Contribution statement

Hereby, I declare my contribution to the following publications:

1. Białek, R.; Friebe, V.; Ruff, A.; Jones, M. R.; Frese, R.; Gibasiewicz, K.
   In Situ Spectroelectrochemical Investigation of a Biophotoelectrode Based on Photoreaction Centers Embedded in a Redox Hydrogel. *Electrochim. Acta* **2020**, *330*, 135190.

In this publication I have:

- performed synthesis of the redox-active polymer,
- taken part in preparation of manuscript by comments and corrections as well as writing parts about redox-active polymers.

2. Białek, R.; Kalyani, T.; Ruff, A.; Jones, M. R.; Schuhmann, W.; Ramanan, C.; Gibasiewicz, K.
   Insight in the Electron Transfer from Redox Polymers to a Photoactive Protein. *Journal of Physical Chemistry B*, manuscript submitted and after 1st review round

In this publication I have:

- performed synthesis of the redox-active polymer,
- taken part in preparation of manuscript by comments and corrections as well as writing parts about redox-active polymers.

Date Signature

10.11.2020 A. Ruff

Dr Vincent Friebe
Department of Physics and Astronomy
LaserLaB Amsterdam
VU University Amsterdam
De Boelelaan 1081,
Amsterdam, 1081 HV, the Netherlands
e-mail: vincent.friebe@vu.nl

Contribution statement

Hereby, I declare my contribution to the following publication:

Białek, R.; Friebe, V.; Ruff, A.; Jones, M. R.; Frese, R.; Gibasiewicz, K.
In Situ Spectroelectrochemical Investigation of a Biophotoelectrode Based on Photoreaction Centers Embedded in a Redox Hydrogel. *Electrochim. Acta* **2020**, *330*, 135190.

In this publication I have:

- optimized the procedure of hydrogel with protein deposition on electrode,
- prepared scheme in Figure 1,
- taken part in discussion during data analysis,
- taken part in preparation of manuscript text, especially in abstract, introduction and conclusion parts.

Date
11.13.2020

Signature
Vincent Friebe

Kalyani Thakur
Max Planck Institute for Polymer Research
Ackermannweg 10
55128 Mainz, Germany
e-mail: kalyanik@mpip-mainz.mpg.de

Contribution statement

Hereby, I declare my contribution to the following publications:

> Białek, R.; Kalyani, T.; Ruff, A.; Jones, M. R.; Schuhmann, W.; Ramanan, C.; Gibasiewicz, K. Insight in the Electron Transfer from Redox Polymers to a Photoactive Protein. *Journal of Physical Chemistry B***,** manuscript submitted and after 1st review round

In this publication I have:

- performed reference transient absorption experiments,
- taken part in preparation of manuscript with comments and corrections.

Date	Signature
11.11.2020	Kalyani
…………………………..	…………………………..

Dr. Charusheela Ramanan
Max Planck Institute for Polymer Research
Ackermannweg 10
55128 Mainz, Germany
e-mail: ramanan@mpip-mainz.mpg.de

Contribution statement

Hereby, I declare my contribution to the following publications:

Białek, R.; Kalyani, T.; Ruff, A.; Jones, M. R.; Schuhmann, W.; Ramanan, C.; Gibasiewicz, K. Insight in the Electron Transfer from Redox Polymers to a Photoactive Protein. *Journal of Physical Chemistry B,* manuscript submitted and after 1st review round

In this publication I have:

- supervised transient absorption experiments,
- taken part in results discussion,
- taken part in preparation of manuscript with comments and corrections.

Date Signature

Charusheela Ramanan
Digitally signed by Charusheela Ramanan
DN: cn=Charusheela Ramanan, c=DE, o=Max-Planck-Gesellschaft, ou=AK-BLOM, email=ramanan@mpip-mainz.mpg.de
Date: 2020.11.12 17:48:55 +01'00'

……………………………… ………………………………

Prof. Dr. Wolfgang Schuhmann
Analytical Chemistry – Center for Electrochemical Sciences
Faculty of Biochemistry and Chemistry
Ruhr-University Bochum
Universitätsstrasse 150
D-44780, Bochum, Germany
e-mail: wolfgang.schuhmann@rub.de

Contribution statement

Hereby, I declare my contribution to the following publications:

1. Białek, R.; Kalyani, T.; Ruff, A.; Jones, M. R.; Schuhmann, W.; Ramanan, C.; Gibasiewicz, K. Insight in the Electron Transfer from Redox Polymers to a Photoactive Protein. *Journal of Physical Chemistry B*, manuscript submitted and after 1st review round

In this publication I have:

- supervised synthesis of the redox-active polymer,
- taken part in preparation of manuscript by comments and corrections.

Date Signature
9/11/2020 W. Schuhmann

DECLARATION

I hereby declare that except where specific reference is made to the work of others, the contents of this dissertation are original and have not been submitted in whole or in part for consideration for any other degree or qualification in this, or any other university. This dissertation is my own work and all the contents of the dissertation have been obtained by legal means.

Rafał Białek

………………………………….

mgr Rafał Białek